Institut für Wasserbau · Universität Stuttgart

Mitteilungen

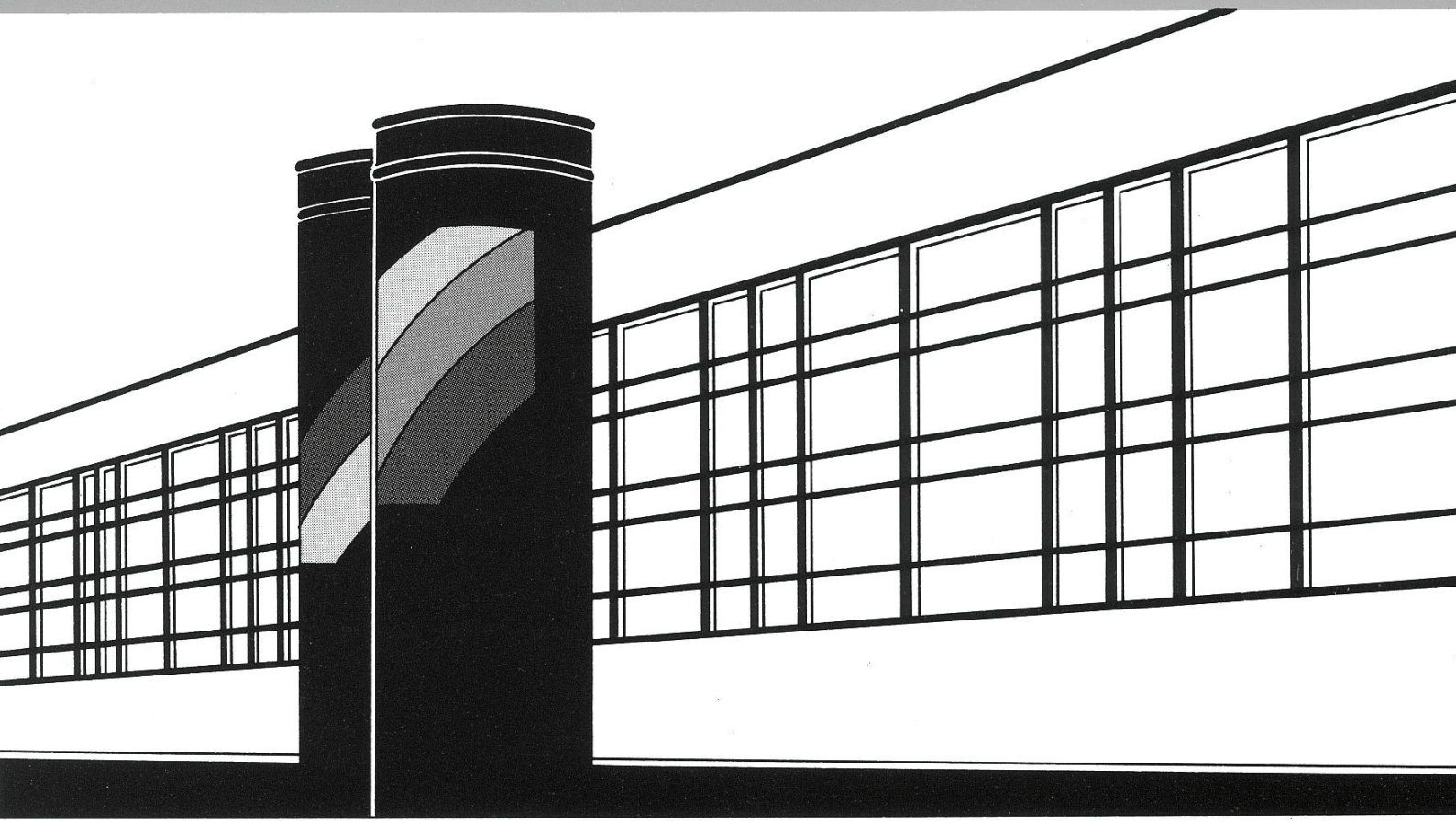

Heft 200

Min Liu

Study of Topographic Effects on Hydrological Patterns and the Implication on Hydrological Modeling and Data Interpolation

Study of Topographic Effects on Hydrological Patterns and the Implication on Hydrological Modeling and Data Interpolation

Von der Fakultät Bau- und Umweltingenieurwissenschaften der Universität Stuttgart zur Erlangung der Würde eines Doktor-Ingenieurs (Dr.-Ing.) genehmigte Abhandlung

Vorgelegt von

Min Liu

aus Suizhou / China

Hauptberichter:	Prof. Dr. rer. nat. Dr. -Ing. András Bárdossy
Mitberichter:	Prof. Dr. -Ing. Erwin Zehe

Tag der mündlichen Prüfung: 29. November 2010

Institut für Wasserbau der Universität Stuttgart
2011

Heft 200

Study of Topographic Effects on Hydrological Patterns and the Implication on Hydrological Modeling and Data Interpolation

von
Dr.-Ing.
Min Liu

Eigenverlag des Instituts für Wasserbau der Universität Stuttgart

D93 Study of Topographic Effects on Hydrological Patterns and the Implication on Hydrological Modeling and Data Interpolation

Bibliografische Information der Deutschen Nationalbibliothek
Die Deutsche Nationalbibliothek verzeichnet diese Publikation in der Deutschen Nationalbibliografie; detaillierte bibliografische Daten sind im Internet über http://www.d-nb.de abrufbar

Liu, Min:
Study of Topographic Effects on Hydrological Patterns and the Implication on Hydrological Modeling and Data Interpolation / von Min Liu.
Institut für Wasserbau, Universität Stuttgart. - Stuttgart: Inst. für Wasserbau, 2011

(Mitteilungen / Institut für Wasserbau, Universität Stuttgart: H. 200)
Zugl.: Stuttgart, Univ., Diss., 2011
ISBN 978-3-942036-04-7
NE: Institut für Wasserbau <Stuttgart>: Mitteilungen

Herausgegeben 2011 vom Eigenverlag des Instituts für Wasserbau
Druck: Document Center S. Kästl, Ostfildern

Acknowledgement

I feel greatly honored to express my utmost thanks to Prof. András Bárdossy, who has offered me the opportunity to conduct my research under his supervision, and make this work possible. His inexhaustible yet unique ideas always motivate me throughout my PhD work. His capability in capturing the essence of a problem, acuteness in mining valuable massage out of information ores, and spirit in seeking for real scientific advancement, has been engraved in this research work, and will inspire me forever. I also appreciate his support and encouragement of my activities in IAHR besides my research. My special thanks go to Prof. Erwin Zehe from Technische Universität München for his warmhearted support and valuable suggestions during my PhD work. His extensive expertise in hydrology in combination with profound knowledge in physics, has provided a unique view angle for the hydrological problems, and more advanced solutions to them. I am very proud of having written my thesis under the joint supervision of Prof. András Bárdossy and Prof. Erwin Zehe, a mathematician and a physicist.

I would like to acknowledge ENWAT (International Doctoral Program of Universität Stuttgart) for providing the academic framework for this research piece. A lot of thanks to Dr.-Ing. Gabriele M. Hartmann for the warmhearted helps she offered to me.The financial support by IPSWaT scholarship program of German Federal Ministry of Education and Research (BMBF) has enabled my research and life in Germany.

I would extend my thanks further to Prof. Rainer Helmig and Dr. Holger Class for their supervision of my master thesis and constant encouragement of my PhD, Prof. Helmut Kobus and Prof. Silke Wieprecht for his motivation of my duty as president in IAHR-BW (International Association of Hydro-environment Engineering and Research - Baden-Württemberg Chapter), Prof. Zhijia Li from Hohai University for his collaboration and hosting my research visit in China.

Many many hearty thanks to all my friends in Stuttgart, Mahboob, Schailesh, Bakim, Pawan, Wei, Helen, Jane, Henning, Henry, Onur, and many other friends and colleagues at the Institut für Wasserbau, who have gave me helpful advices for my work and made this pleasant working atmosphere.

Throughout this work and my stay in Germany, my wife Jing has been a great inspiration for me. It would not have been possible for me to go through the seven-year time in Stuttgart, and bring this work into forth without her love, care, and support. My parents, my sister, and parents-in-law in China, half way across the globe, have done whatever they can to support me, and deserve my deepest gratitude.

Contents

List of Figures

List of Tables

List of symbols

List of Latin symbols

Symbol	Definition	Unit
a_{ap}	Angström-Prescott coefficient	[−]
a_k	Kasten coefficient	[−]
a_u	Unit upslope area	[L]
B	Beam (direct) radiation	[E L^{-2}]
b	Beam (direct) radiance	[E $L^{-2}T^{-1}$]
C_{can}	Canopy conductance	[LT^{-1}]
C_{at}	Atmospheric conductance	[LT^{-1}]
C_h	Covariance function	[−]
C_k	Cloudness index	[okta]
c_a	heat capacity of air	[$EM^{-2}T^{-1}$]
c_p	Specific heat capacity	[E $M^{-1}\Theta^{-1}$]
CC_t	Melting rate caused by temperature	[L $T^{-1}\Theta^{-1}$]
CC_g	Melting rate caused by shortwave radiation	[L $T^{-1}\Theta^{-1}$]
b_{ap}	Angström-Prescott coefficient	[−]
b_k	Kasten coefficient	[−]
D	Diffuse radiation	[E L^{-2}]
d	Diffuse radiance	[E $L^{-2}T^{-1}$]
d_n	Julien day number	[−]
EA	Actual evaporation of soil in vegetated area	[L]
e_a	Actual vapor pressure	[M $L^{-1}T^{-2}$]
e_s	Saturate vapor pressure	[M $L^{-1}T^{-2}$]
ETP_w	Potential evapotranspiration of wet crop	[L]
ETP_d	Potential evapotranspiration of dry crop	[L]
EP_s	Potential evaporation of bare soil	[L]
EP	Potential evaporation of soil in vegetated area	[L]
f_c	Coefficient for cloud cover	[−]
f_{cor}	Coriolis parameter	[T^{-1}]
F_d	Diffuse angular function	[−]
g	Gravitational acceleration	[L T^{-2}]
G	Global radiation	[E L^{-2}]
G_n	Net shortwave radiation	[E L^{-2}]
h	hydraulic head, water depth or elevation	[L]

Symbol	Definition	Unit
h_suc	soil water suction head	[L]
H	Sensible heat flux	[E L^{-2}]
H_0	Radiation in absence of atmosphere	[E L^{-2}]
HU	Humidity	[−]
$I_{0\beta}$	Hourly extraterrestrial radiation on inclined surface	[E $L^{-2}T^{-1}$]
I_{0h}	Hourly extraterrestrial radiation on horizontal surface	[E $L^{-2}T^{-1}$]
i_e	Effective precipitation	[L T^{-1}]
$\dot{I}_{SC}$	Solar constant	[E $L^{-2}T^{-1}$]
k_{a1}	empirical coefficient for ground surface albedo	[−]
k_{a2}	empirical coefficient for ground surface albedo	[−]
K_b	Direct radiation transmittance	[−]
K_c	Clear-sky index	[−]
K_c^b	Beam component of clear-sky index	[−]
K_c^d	Diffuse component of clear-sky index	[−]
K_d	Diffuse fraction	[−]
K_e	Effective hydraulic conductivity	[L T^{-1}]
K_{hay}	Hay's sky-clarity index	[−]
k_p	Rainfall enforcement constant	[−]
k_R	Ratio of energy received on inclined surface to horizontal surface	[−]
K_{sat}	Saturated hydraulic conductivity	[L T^{-1}]
K_t	Clearness index	[−]
K_n	Normal direct transmittance index	[−]
l	Horizontal distance	[L]
l_{root}	plant root density	[−]
L_n	Net longwave radiation	[E L^{-2}]
$L\downarrow$	Downward longwave radiation	[E L^{-2}]
$L\uparrow$	Upward longwave radiation	[E L^{-2}]
LE	Latent heat flux	[E $L^{-2}T^{-1}$]
m_r	Relative optical mass	[−]
m_{vg}	Parameter of pore-size distribution	[−]
n_c	Cloud index	[−]
n_d	Actual sunshine duration	[T]
N_d	Potential sunshine duration	[T]
n_m	Manning-Strickler's coefficient	[−]
n_{vg}	Parameter of pore-size distribution	[−]
R_l	Reflected radiation	[E L^{-2}]
R	All-wave radiation	[E L^{-2}]
R_{gc}	Gas constant	[E L^{-2}]
r_g	Groundwater recharge rate	[L T^{-1}]
RX	root water extraction rate	[−]
s	Optical path length	[L]
SD	Storage deficit	[L]

Symbol	Definition	Unit
S_e	Effective saturation	$[-]$
S_f	Friction slope	$[-]$
S_m	Snow melt rate	$[\mathrm{L\ T^{-1}}]$
S_o	Ground surface slope	$[-]$
t	Time	$[\mathrm{T}]$
TA	Actual transpiration	$[\mathrm{L}]$
T	Temperature	$[\Theta]$
T_a	Daily mean air temperature	$[\Theta]$
T_0	Threshold temperature of snowmelt initiation	$[\Theta]$
T_θ	Potential temperature	$[-]$
TP	Potential transpiration	$[\mathrm{L}]$
T_d	Diffuse transmission coefficient	$[-]$
T_w	Hydraulic transmissivity	$[\mathrm{L^2T^{-1}}]$
T_{Ln}	Linke turbidity	$[-]$
P	Pressure	$[\mathrm{M\ L^{-1}T^{-2}}]$
P_0	Reference pressure	$[\mathrm{M\ L^{-1}T^{-2}}]$
P_r	Total precipitation	$[\mathrm{L}]$
P_l	Liquid precipitation	$[\mathrm{L}]$
q_u	Discharge per unit contour length	$[\mathrm{L^2T^{-1}}]$
u_g	Geostrophic u wind	$[\mathrm{L\ T^{-1}}]$
v_g	Geostrophic v wind	$[\mathrm{L\ T^{-1}}]$
wi	Topographic wetness index	$[-]$

List of Greek symbols

Symbol	Definition	Unit
α	Solar altitude	$[\mathrm{L}]$
α_r	Root extraction reduction factors under stress	$[-]$
α_{vg}	Parameter related to the modal pore size	$[-]$
β	Surface slope	$[\mathrm{L}]$
δ_i	Optical depth of a given substance	$[-]$
δ_r	Rayleigh optical depth	$[-]$
δ	Solar declination angle	$[-]$
Δ_v	Slope of the vapor pressure curve	$[\mathrm{ML^{-1}T^{-3}}]$
ϵ	Eccentricity correction factor	$[-]$
ϵ_a	Emissivity of the atmosphere	$[-]$
ϵ_{vs}	Emissivity of vegetation and soil	$[-]$
γ	Aspect of the surface	$[-]$
γ_h	Variogram	$[-]$
γ_{pc}	psychrometric constant	$[\mathrm{ML^{-1}T^{-3}}]$

Symbol	Definition	Unit
λ_v	Latent heat of vaporization	$[\mathrm{EL^{-2}T^{-1}}]$
λ_{vg}	Shape parameter	$[-]$
κ_i	Attenuation coefficient	$[-]$
ω	Solar hour angle	[L]
ω_s	Sunrise(sunset) hour angle for horizontal surface	[L]
ω_{sr}	Sunrise hour angle for inclined surface	[L]
ω_{ss}	Sunset hour angle for inclined surface	[L]
ϕ	Solar azimuth angle	[L]
ψ	Geographic latitude	[L]
ρ	Density	$[\mathrm{M\ L^{-3}}]$
ρ_a	Air density	$[\mathrm{M\ L^{-3}}]$
ρ_{at}	Atmospheric albedo	$[-]$
ρ_c	Apparent albedo of the heaviest cloud	$[-]$
ρ_g	Apparent albedo of the ground under clear skies	$[-]$
ρ_o	Apparent albedo of observed by the satellite sensor	$[-]$
ρ_s	Apparent albedo of snow	$[-]$
ρ_w	Water density	$[\mathrm{ML^{-3}}]$
σ_{sb}	Stefan-Boltzmann constant	$[\mathrm{E\ L^{-2}\Theta^{-4}}]$
τ_i	Transmittance coefficient	$[-]$
θ	Solar azimuth angle of inclined surface	[L]
θ_e	Effective volumetric water content	$[\mathrm{L^3/L^3}]$
θ_{res}	Residual volumetric water content	$[\mathrm{L^3/L^3}]$
θ_{sat}	Saturated volumetric water content	$[\mathrm{L^3/L^3}]$
θ_z	Solar zenith angle of horizontal surface	[L]

List of sub- and superscripts

Symbol	Definition
x	x Direction of coordidnation system
y	y Direction of coordination system
$\cdot$	Values in normal direction
a	Actual value
p	Potential value
i	List of substances, stations, time intervals, etc.
e	Effective value
h	Horizontal surface
c	Clear sky
β	Inclined surface
b	Cloudy sky (bewölkt in German)

Abstract

Hydrological patterns demonstrate spatial and temporal variability and organization of hydrological responses in the catchment, and contain rich information of underlying hydrological processes. Observed patterns or patterns interpolated properly from point data are ideal sources for distributed model input and perfect references for model calibration and validation, whereas simulated patterns can reflect the effects of spatial land use and climate change and provide insight into the underlying hydrological processes. Investigation of these patterns can deepen our understanding of catchment hydrology, so that we can improve our interpolation methods and hydrological models to produce more realistic patterns for decision making in water resources management. Hydrological patterns may appear to be random, but in many cases they are highly organized and exhibit deterministic structures superimposed with some random variation, because the fundamental driving forces for the catchment evolvement - solar radiation, wind, and precipitation, are strongly related to topographic features - elevation, aspect and slope, and thus highly organized. Topographic variation exists at different scales: at large-scale, earth surface features are caused mainly by geological movements and glacial carving, and referred as *macro-topography* in this monograph, whereas at small scale, *micro-topography* caused by gully incision and other secondary processes dominates. The effects of topography on catchment process may change with the scale, depending on the process under study. The direct topographic dependence of catchment processes, such as radiation, wind, drainage network, and precipitation, are referred as *primary* topographic effects in this monograph, based on which the *secondary* topographic effects governing the spatial patterns of evapotranspiration (ET), soil moisture content (SMC), snow melting, soil properties, vegetation etc., can be derived. The main objective of the study is to illustrate how topography affects these hydrological patterns at different scales through the primary and secondary effects, and how the understanding of spatial processes can advance hydrological modeling concept as well as improve spatial data interpolation. To assure the generality of the research, this study applies globally available data wherever possible. The work also exploited the three main general research methodologies in hydrology: physically-based modeling, conceptual models, and statistical analysis.

The study first simulates the solar radiation pattern and wind pattern under topographic modification, with the *r.sun* model and the METRAS-PC model respectively. The radiation and wind patterns show a strong spatial variability related to topography. Taking these patterns as inputs, the Soil-Water-Atmosphere-Plant (SWAP) model is used to generate the spatial ET/SMC patterns, which are highly organized with a significant spatial difference.

The work further investigates the topographic effects on snow melting. The correlation analysis of solar radiation with binary snow cover data from Moderate Resolution Imaging Spectroradiometer (MODIS) confirms a high dependence of snow melting on radiation

during the clear days. Several different adaptations of radiation index degree-day model in both multiplicative and additive form have been calibrated with station data, and validated spatially against MODIS data. The results show that the incorporation of topographic parameters into the model concept improves the model performance.

Precipitation is affected by topography at large-scale through orographic effects, and at small-scale through wind drift. The presence of mountains causes local anisotropy of the spatial precipitation as a random field from the geostatistical point of view. This study tries to account for the local anisotropy caused by topographic effects by applying the curvature distance along the ground surface in the geostatistical interpolation methods. The kriging methods with multi-dimensional scaling (MDS) transformed curvature distances shows in some cases improvement to the original horizontal distances. To reflect the outweighing of vertical distance to horizontal distance, the vertical distance is scaled with a given factor.

This work also investigates the spatial precipitation variability caused by narrow-steep valleys which are usually neglected by hydrologists at small-scale. Because physically-based precipitation modeling is very site- and event-specific, instead of purely physical approach, statistical analysis based on high-density rain gauge data under the consideration of atmospheric circulation patterns (CPs) is undertaken. Both parametric (One-way Analysis of Variance) and non-parametric (Kolmogorov-Smirnov test) statistical analysis of precipitation time series for the valley and non-valley stations reveals that, when the valley station is isolated from the moisture air flow, it receives comparable amount of precipitation as the neighboring mountain stations. Such valley effects that are usually disregarded in the spatial interpolation procedures, are considered in the external drift kriging (EDK) by applying selective directional smoothing of DEM in this work.

Through the study of the 6 topographic dependent patterns - radiation, wind, precipitation, ET, soil moisture, and snow melting, this study delivers two important messages: first, among all the elements within a catchment, topography is the major source of variability, and this variability can be quantified to a large extent; second, pattern investigation may reveal the hidden principles of hydrological processes, is therefore key to the iterative loop of observation-understanding-modeling in hydrological study. Because for part of the study, physically justified modeling approach and globally available data are used, the methods are applicable to other areas, thus it also contributes the PUB initiation.

Zusammenfassung

Einführung

Diese Arbeit ist von der Untersuchung zweier Oberflächenabflussmuster, abgeleitet. Das eine ergibt sich aus dem gesättigten TOPMODEL(unterflächenabflussbasiert) und das andere aus dem hortioanischen CASC2D Modell(oberflächenabflussbasiert). Die Ähnlichkeit der simulierten Oberflächenabflussmuster von zwei komplett verschiedenen Modellen zeigt, dass die Topographie der maßgebende Faktor in der Wasserbewegung bzw. dem Wasserkreislauf ist. Die Topographie, die durch das Digitale Höhenmodell(DHM) vertreten ist, beinhaltet wichtige räumliche Informationen und ist in den meisten Fällen die Hauptquelle der räumlichen Variabilität in hydrologischen Prozessen, wie Verdunstung, Bodenfeuchtegehalte(BFG), Temperatur, etc. Hydrologische Muster weisen die Organisation und Struktur der zugrunde liegenden hydrologischen Prozesse auf und beinhalten wichtige Informationen, um den Prozess zu verstehen. Desweiteren sind sie der ideale Input für räumlich verteilte Modelle und der perfekte Bezug beim Einstellen und Bewerten von Modellen. Hydrologische Muster können den Eindruck erwecken zufällig zu sein, sind aber in vielen Fällen hochgradig organisiert und weisen deterministische Strukturen auf, die mit einer zufälligen Variation überlagert sind. Dies rührt daher dass die Muster der fundamentalen Antriebskräfte des Verhalten des Einzugsgebiets - Sonneneinstrahlung, Wind und Niederschlag - stark abhängig von topographischen Eigenschaften - Höhe, Ausrichtung und Neigung - sind. Topographische Variationen existieren auf unterschiedlichen Skalen: auf großer Skala entstanden die Eigenschaften der Erdoberfläche größtenteils aus geologischen Bewegungen und Gletscherabrieb und werden im Folgendem als *Makrotopographie* bezeichnet. Auf kleiner Skala hingegen, wird *Mikrotopographie* von Rinnenbildung und anderen sekundären Prozessen verursacht. Die Auswirkungen der Topographie auf Einzugsgebietsprozesse können sich zusammen mit der Skalaändern. In dieser Monographie wird die direkte topographische Abhängigkeit auf Einzugsgebietsprozesse, wie Einstrahlung, Wind und Niederschlag, als *primäre* topographische Effekte bezeichnet auf denen die *sekundären* topographischen Effekte basieren, aus denen die die räumlichen Muster der Evapotranspiration(ET), Bodenfeuchtegehalt(BFG), Schneeschmelze, Bodeneigenschaften, Vegetation, etc. hergeleitet werden können. Das Hauptziel der Arbeit ist es darzustellen wie die Topographie diese hydrologischen Muster auf unterschiedlichen Skalen über ihre primären und sekundären Effekte beeinflusst und wie das Verständnis der räumlichen Prozesse hydrologische Modellkonzepte und -praxis voranbringen und räumliche Dateninterpolation verbessern kann. Um die Allgemeingültigkeit dieser Forschung zu gewährleisten wurden wo es möglich war frei verfügbare Daten benutzt. Für die Arbeit wurden die drei hauptsächlich in der Hydrologie verwendeten Forschungsmethoden verwendet: physikalisch-basierte Modellierung, konzeptuelle Modelle und statistische Analyse.

Die Arbeit besteht aus 6 Teilen:

1. physikalische Modellierung der räumlichen Solarstrahlung im komplexen Gelände mit Fernerkundungsdaten im Vergleich zur empirischen Modellierung der Sonnenscheindauer;
2. Simulation des Windfeldes des meso-skallierten meteorologischen Modell METRAS PC mit NECP/NCAR Reanalysis Daten;
3. Simulation von Verdunstung und Erdfeuchte mit dem SWAP Modell;
4. Einführung des Solarstrahlungsindex in das Grad-Tag Modell und Vergleich; verschiedener Varianten;
5. Anwendung der von multi-dimensionalen Skalierung (MDS) umgewandelte Abstand zur Behandlung die von Topographie verursachten lokalen Anisotropie;
6. Statistische Untersuchung der räumlichen Variabilität des Niederschlags in schmalen und steilen Täler, im Zusammenhang mit atmosphärischer Zirkulation (CP) und der Anwendung von DGM Glättung zur Verbesserung des External-Drift-Kriging.

Modellierung der Solarstrahlung

Die Solarstrahlung erhält das Leben auf der Erde und ist ebenfalls für die räumliche und zeitliche Variation der hydrologischen Bestandteile, wie Vegetation, Biologie und Wasser verantwortlich. Sowohl für die Meteorologie, als auch für die Hydrologie ist die präzise Bestimmung der räumlichen Solarstrahlung auf der Erdoberfläche von fundamentaler Bedeutung. Die Globalstrahlung ist durch das Zusammenspiel der Solar-Erde-Geometrie(Solare Positionierung, Oberflächenneigung, Geländeschattierung, usw.), den Geländeeigenschaften(Albedo, Saugfähigkeit, usw.) und den atmosphärischen Eigenschaften(atmosphärische Dämpfung, Wolken, usw.) bestimmt. Die geometrische Beziehung zwischen der Sonne und der Erde sind hauptsächlich von den Variationen der Topographieparameter bestimmt. Dabei wären die Bodenerhebungen, -neigung, -expositionen, welche totale Unterschiede der Solarstrahlung auf lokaler Ebene verursachen können, zu nennen. Die Oberfläche und die atmosphärischen Bedingungen können physikalisch oder empirisch parametrisiert werden. Um das Potential(unter klarem Himmel) und die tatsächliche(unter bewölkten Bedingungen) Strahlung zu parametrisieren und zu berechnen, wurden Modelle unterschiedlicher Algorithmen und Komplexität entwickelt. Diese Modelle reichen von der einfachen empirischen Gleichung bis hin zur prozessbasierten physikalischen Verfahren.

Dieses Kapitel gibt einen Überblick über das allgemeine Vorgehen der Modellierung von Solarstrahlung sowie über die üblichsten Verfahren. Für die operative Raumstrahlungsmodellierung wurden zwei Verfahren mit kleinstem Datenbedarf ausgewählt: das GIS-basierte, physikalisch parametrisierte, fernerkundungsorientierte Heliosat-2-Modell (Rigollier et al., 2004) sowie das sonnenscheindauerbasierte Angström-Prescott-Regressionsmodell (Angström, 1924). Die Leistungsfähigkeit der Modelle für Strahlungssimulation auf horizontaler Oberfläche wurden durch beobachtete Daten überprüft. Des

weiteren ist die Gültigkeit der Modelle zur Modellierung geneigter Flächen durch den Vergleich der Modelleergebnisse unterteinander nachgewiesen. Die Skalenempfindlichkeit der Modelle und die Schatteneffekte sind mit unterschiedlichen DHM Auflösungen untersucht worden. Starke Auswirkungen der Topographie auf die räumliche Solarstrahlung unter klarem Himmel in komplexem Gelände wurden mit dem Punkt-Vergleich dargestellt. Eine Fallstudie mit einem kleinen Einzugsgebiet zeigt ebenfalls die räumliche Variabilität der Solarstrahlung unter wolkigem Himmel. Die räumliche Variabilität der Solarstrahlung ist besonders im Winter sehr hoch, was wahrscheinlich starke Auswirkungen auf die Schneeschmelze hat. Im weiteren Verlauf der Arbeit werden die Auswirkungen der durch Topographie abgeleiteten ungleichmäßigen Solarstrahlung auf Verdunstung, Bodenfeuchte und Schneeschmelze untersucht. Dieses Kapitel hat das Potential der beiden Modelle bezüglich des Downscaling der räumlichen Solarstrahlung, und der Möglichkeit der Anwendung von Fernerkundung zur Modellierung der Solarstrahlung in komplexem Gelände für die hydrologische Anwendung, bestätigt.

Windmodellierung mit METRAS PC

Dieses Kapitel wendet das massenbeständige mesoskalige Windmodell, MEsoscale TRAnsport and fluid (Stream) Model, PC version (METRAS PC) (Schlünzen et al., 2001) an, um vom geostrophischen Wind zu einem täglichen lokalen Windfeld zu gelangen. Das Modell beruht auf den physikalischen Erhaltungsgleichungen, die in Flußform dreidimensional gelöst werden. Prognostisch werden Wind, potentielle Temperatur und Feuchte sowie die Oberflächentemperatur und Oberflächenfechte berechnet. Die Eingangsdaten des geostrophischen Windes für das Modell sind aus NCEP/NCAR Reanalysis-Daten abgerufen worden. Simulationen sind mit den tatsächlichen täglichen Daten kontinuierlich über ein Jahr und mit gruppierten Winddaten aus über 48 Jahren (1960~2007) mit Clusteranalyse erstellt, durchgeführt worden. Es wurde eine in zwei Schritte aufgebaute Cluster-Analyse verwendet: zuerst mit dem k-mean Algorithmus und dann mit Ward's Clustering im zweiten Schritt. Damit wurden die Daten über 48 Jahre in 200 repräsentative Cluster klassifiziert, und der Rechenaufwand von täglichen Windsimulationen verringert werden kann. Die generierten Windfelder zeigen, dass sie von Topographie und Landnutzung beeinflusst werden. Die Ergebnisse werden anschließend für die Verdunstungsmodellierung verwendet und können darüber hinaus für andere hydrologische Anwendungen eingesetzt werden, wie z.B, Analyse der Abdrift von Niederschlägen, Schnee, usw.

Verdunstung- und Bodenfeuchtemodellierung mit SWAP

Um die räumliche Variabilität der Verdunstung(ET), die Bodenfeuchtegehalte(BFG) sowie die durch die Topographie verursachte räumliche Variabilität von Wind und Strahlung zu quantifizieren, werden numerische Experimente mit dem Soil Water Atmosphere Plant-Modell (SWAP) (van Dam et al., 1997) durchgeführt. Das eindimensionale SWAP-Modell

wurde in einer verteilten Weise unter Annahme linearer Grundwasserspiegel, und anderen identischen Randbedingungen in Abwesenheit von "lateral-flow"für jedes Raster angewandt. Das SWAP-Modell verwendet einen umfassenden Penman-Monteith(PM) Ansatz, um die Verdunstung zu berechnen. Dieser Ansatz bezieht meteorologische Faktoren, Bodenbedeckungen und den artenabhängigen Leaf Area Index(LAI) mit ein. Desweiteren beinhaltet das SWAP-Modell die Richard's Gleichung, um den Bodenwasserfluss in der ungesättigten Zone unter verschiedenen Bodeneigenschaften zu berücksichtigen. Es werden sowohl potentielle als auch tatsächliche ET, sowie die einzelnen Komponenten der Verdunstung und Transpiration von dem Modell berechnet. Um die Skaleneffekte zu bewerten, wurden die numerischen Experimente mit zwei verschiedenen Auflösungen ($100\,\mathrm{m}$ and $1000\,\mathrm{m}$) durchgeführt. Um die räumliche Variabilität von ET durch Wind und Strahlung zu unterscheiden, wurden numerische Experimente durchgeführt. Dabei wurden die Annahmen, dass nur räumlich heterogene Strahlung auftritt oder dass der Wind mit sämtlichen Parameter homogen ist, getroffen. Die numerischen Experimente mit variierendem Wind und Strahlung zeigen die umfassende Wirkung der Topographie auf die Verdunstung. In einem weiteren Experiment wurde die Variabilität der ET, verursacht durch Vegetation, durch Eingabe des landnutzungsspezifischen LAI aus MODIS(Moderate Resolution Imaging Spectroradiometer) betrachtet. Experimente mit Böden unterschiedlicher Beschaffenheit zeigen, dass die Bodenarten die Trennung zwischen Verdunstung und Transpiration wesentlich beeinflussen und einen beschränkten Einfluss auf den totalen ET haben.

Das Ergebnis zeigt eine starke räumliche Variabilität innerhalb der Einzugsgebiete bei täglichen und jährlichen totalen ET und eine geringe Variabilität der Bodenfeuchte. Die räumliche Variabilität der ET ist verbunden mit einem Unterschied der totalen generierten Menge des Abflusses, was möglicherweise zu signifikanten Auswirkungen des Wasserhaushalts der Einzugsgebiete führen kann.

Vergleich den Adaptierten Grad-Tage-Schnee Modellen

Die Temperatur-Index Methode ist eine sehr beliebte Methode, bei der die Temperatur als Surrogat des Energieaufwands genutzt wird, um die Schneeschmelze zu modellieren. Obwohl die Methode in einigen Fällen recht gut funktioniert, ist sie jedoch nicht in der Lage, die räumliche Variabilität des Energieeintrags durch räumliche Topographie zu berücksichtigen, mit der Ausnahme des Temperaturgradients in einer verteilten Modell-Struktur. Dieses Kapitel versucht die räumliche Variabilität der Strahlung, die durch Topographieeffekte hervorgerufen wird, in das Grad-Tage Modell einzuführen. Sowohl in die additive als auch in die multiplikative Formulierungen. Unterschiedliche Strahlungskomponenten wurden ebenfalls untersucht. Von der potentiellen Solarstrahlung über die aktuelle Solarstrahlung zur ganzwelligen Strahlung. Die eingebetteten Grad-Tage-Modelle werden an den Stationen mit den binären MODIS Schneebedeckungsausmaß Daten, die beobachtete Temperatur- und Niederschlagsdaten kalibriert. Validierung der Modelle geschieht mit den räumlich interploierten Temperatur- und Niederschlagsdaten, und MODIS Daten. Der Vergleich der Ergebnisse der angeglichenen Modelle mit dem Standard Grad-Tag Modell zeigt eine Verbesserung der Modellleistung.

Kriging mit MDS Umgewandelten Abständen

Die Anwesenheit von Bergen kann eine lokale Anisotropie der regionalisierten hydrologischen Variablen wie z.B Temperatur, Wind und Niederschlag hervorrufen. Im Gegensatz zur globalen Anisotropie, welche durch verschachtelte Variogramme oder linear transformierte Koordinatensysteme modelliert werden kann, ist die lokale Anisotropie schwer zu bestimmen. Dieses Kapitel beschreibt den Versuch, solche topographieabhängige Anisotropien durch nichtlineare Transformation des Bogenabstands mit MultiDimensionaler Skalierung(MDS) zu modellieren. Weil der vertikale Abstand ausgeprägtere Effekte als der horizontale Abstand hat, ist ein Skalierungsfaktor für die Höhe eingeführt worden. Dieser dient der besseren Angleichung der topographieverursachten räumlichen Variabilität. Im Bewusstsein der potentiellen Verzerrung der Koordinaten aufgrund erhöhter Eingabe von Punkten in MDS, ist ein lokales MDS für die nächsten Nachbarpunkte, die für das Kirging ausgewählt wurden, durchgeführt worden. Die MDS Transformation wurde sowohl für das Ordinary Kirging (OK) als auch für das External Drifting Kirging(EDK) angewandt. Um das Ergebniss statistisch abzusichern, wurden für den Vergleich Tagesdaten über 7 Jahre von Temperatur und Niederschlag benutzt. Die Kreuzvalidierung zeigt eine Verbesserung des Ordinary Krigings der Temperaturdaten und eine geringere Verbesserung in den anderen Fällen. Der Grund dafür liegt möglicherweise im multidimensionalen Skalierungsprozess, welcher zwischen entfernten und nahen Punkten nicht unterscheidet.

Täle-Effekte auf Niederschlag und Kriging mit Geglätteten DHM

Die kleinskalige ($1\sim10\,\mathrm{km}$) räumliche Variabilität des täglichen Niederschlags im Alpenraum von Süddeutschland wird mit den hochauflösenden täglichen Niederschlagsmessungen über einen Zeitraum von 40 Jahren untersucht. Unter Berücksichtigung der täglichen großskaligen Zirkulation(CPs), welche durch den SLP(sea level pressure) oder durch 500 or $700\,\mathrm{hPa}$ geopotentiale Höhenanomalie definiert wird. Der tägliche Niederschlag in den schmalen Tälern wird mit dem der benachbarten Stationen auf den Bergkämmen bezüglich deren Mittelwert (mit one-way ANOVA) und deren kumulativer Wahrscheinlichkeitsverteilung (Kolmogrov-Smirnav test) verglichen. Die statistischen Tests wurden speziell für jeden CP durchgeführt, im allgemeinen jedoch auch ohne dessen Berücksichtigung. Das Ergebnis zeigt, dass es zwei Effekte gibt, die die räumliche Niederschlagsverteilung auf zwei verschiedenen Skalen beeinflussen, auf der einen Seite den orthographische Effekt, wodurch der Niederschlag mit zunehmender Höhe ansteigt, und auf der anderen Seite den als "schmale Täler Effekt"bekannten Effekt, wodurch der Niederschlag in schmalen Tälern vergleichbar mit dem Niederschlag auf dem Bergkamm wird, wenn das Tal vom Feuchtigkeitsfluss, welcher durch die großskalige Zirkulation angetrieben wird, abgeschirmt wird. Die Arbeit bestätigt das Phänomen, dass der Niederschlag in den schmalen Tälern "blind"ist, was oft in hydrologischen Anwendungen unbeachtet bleibt. Zum Beispiel bei der Interpolation der Niederschläge aufgezeichneter Daten. Ein Glättungsalgorithmus, der den DHM innerhalb eines Fensters glättet, wurde angewandt, um die topographische Daten zu glätten und um die schmalen Täler zu füllen. Mit Rücksicht auf die Interaktion von CP und den

Tälern, anisotrope Glättung in der Richtung der CP ist ausprobiert. Dies wurde als Hilfsinformation für das externe drift kriging(EDK) und Detrended Kriging (DTK) genutzt. Die Ergebnisse der Kreuzvalidierung zeigen, dass EDK mit DHM, anisotrop geglättet durch eine bestimmte Fenstergröße, eine bessere Leistung bringt als mit dem ursprünglichen DHM in Bezug des Mittelwerts und des systematischen Fehlers.

Schlussfolgerungen

Diese Arbeit hat durch die systematische Untersuchung von Solarstrahlung-, Wind-, Verdunstung-/Bodenfeuchte-, Schneeschmelze- und Niederschlagmuster die topographischen Effekte auf die hydrologischen Prozesse demonstriert. Diese Effekte wurden angewandt, um die hydrologische Modellierungskonzepte und die Interpolation von räumlichen Daten zu verbessern. Zum Beispiel bringt die Einführung des Solarstrahlungsterms in das Grad-Tag Modell, sowie die Anwendung geglätteter DHM mit externen drift kriging eine höhere Leistung. Des weiteren hat diese Arbeit die drei Hauptmerkmale einer hydrologischen wissenschaftlichen Arbeit: physikalisch-basiertes Modellieren, konzeptionelle Modelle und statistische Analysis. Fernerkundungsdaten, wie zum Beispiel Wolkendaten von Meteosat oder Schnee- und Vegetationsdaten von MODIS werden extensiv benutzt. Die umfangreiche Anwendung von global verfügbarer Daten durch PUB(Prediction in Ungauged Basin) hat eine datenarme Modellierungsannäherung ermöglicht.

Zusammenfassend wird diese Arbeit der hydrologischen Forschung in folgenden Aspekten beitragen:

1. Diese Arbeit wird unser Verständnis der räumlichen Hydrologie wie zum Beispiel die hydrologische Reaktion auf räumliche Veränderungen vertiefen;
2. Die Kenntnis der räumlichen Variabilität kann uns dabei helfen, Ergebnisse von großskaligen Modellen, wie z.B. das Land-Oberflächen-Modell, runter zu skalieren, und die beobachtete Stationdaten zur genaueren räumlichen Daten zu interpotieren;
3. Die Topographischen Effekte können in hydrologische Modelle eingebaut werden, um das Modellkonzept zu verbessern;
4. Viele Modelle, die diese Arbeit verwenden werden, sind selbst hydrologische Modelle und können für beliebte Einzugsgebiete eingesetzt werden.

1 General Introduction

Pattern are everywhere in nature and in science. Mathematics is commonly referred as the "science of patterns" (Steen, 1988); in computer science the design pattern is a general solution for objective-oriented programming; in physics from the cosmos down to the crystal, their structure all compost recurring patterns. Devlin (1997) notes that patterns can be "either real or imagined, visual or mental, static or dynamic, qualitative or quantitative". The existence of patterns is not only to impress people, but is also key to understand the principles behind them. By exploiting the information that resides in the myriad of patterns, people advance the understanding about nature and put the science forward. For example, Johannes Kepler developed the famous Kepler's laws in cosmology by continuous seeking for the perfect geometric patterns.

Observation and interpretation of spatial patterns are also fundamental to hydrology, although the hydrologists have since long time avoided confronting the challenge of spatial variability by focusing on streamflow as an integral (Grayson and Blöschl, 2000). Recently the importance of the patterns for gaining insight into hydrological behavior has been widely recognized (Grayson et al., 2002a; Schröder, 2006), because they can be used to "inform model development and reduce model uncertainty"(Grayson and Blöschl, 2000). This study itself is inspired by the following pattern investigation of the overland flow patterns.

1.1 Motivation from Pattern Comparison

Hydrological modeling, also called rainfall-runoff modeling, deals mainly with the rainfall runoff generation processes, as its name suggests. Whether the model concept reflects properly the runoff generation mechanism, is a matter to the model correctness, more important to the fit test. Historically three types of runoff generation mechanisms have been experimentally confirmed and well established, they are *Hortonian overland flow* (HOF), *subsurface storm flow* (SSF) and *saturated overland flow* (SOF). The Hortonian overland flow, also known as infiltration excess flow states that surface runoff is primarily a result of rainfall surplusing the infiltration capacity which decreases as a function of cumulative infiltration depth or time. It is the dominating runoff generation process in arid and semi-arid region with thin soil and low infiltration capacity (Horton, 1933; Betson, 1964). The Green-Ampt equation (Green and Ampt, 1911), Horton equation(Horton, 1933), Philip equation(Philip, 1957), Smith-Parlange equation(Smith and Parlange, 1978) are all models belonging to this family. The CASC2D model (Downer et al., 2002) applies also this runoff generation concept. For subsurface storm flow, water are connected through the preferential flow paths, and surface runoff is rarely observable. It occurs where shallow permeable soil resides on impeding bed

layer with steep slopes (Weyman, 1973; Harr, 1977). Another type of SSF is the piston type of flow, i.e. old water are mobilized by pressure propagation of fresh water input of rainfall (Zehe et al., 2010). Saturated overland flow is the runoff generated when the soil is saturated up to the earth surface from the groundwater table (Hewlett and Hibbert, 1967; Dunne and Black, 1970). It is usually the dominating process in humid area with shallow groundwater. Because the saturation area always expand from the river course to the flood plain, it's also named as *variable source area* mechanism. The widely used TOPMODEL by Beven et al. (1995) is based on this mechanism.

An experimental study of the overland flow depth with the two conceptually distinct models - CASC2D and TOPMODEL was carried out at the beginning of this study, in order to seek for hints to improve the runoff generation concept. The results are very inspiring, and have directed the study to the topographic effects and pattern investigation. In the following, a brief introduction about the two models will be presented, followed by the enlightening results.

1.1.1 CASC2D Model

CASC2D is a physically-based watershed model simulating exclusively the surface HOF (Julien et al., 1995). Although the reduction of the effective rainfall by infiltration is included in the model, but the infiltrated water is assumed to be depleted by evapotranspiration, and no subsurface flow is considered at all. The exclusion of baseflow render the model incapable to simulate continuously the hydrograph, but only the flood events. The core part of the model is essentially the diffusive flow equations implemented in explicit finite difference scheme for channel flow in 1-dimension and for overland flow in 2-dimension. The overland flow comprises the following diffusion wave equations:

$$\text{Continuity equation:} \qquad \frac{\partial h}{\partial t} + \frac{\partial q_x}{\partial x} + \frac{\partial q_y}{\partial y} = i_e \tag{1.1}$$

$$\text{Momentum equation:} \qquad S_f = S_o - \frac{\partial h}{\partial l} \tag{1.2}$$

$$\text{Manning equation:} \qquad q = \frac{1}{n_m} S_f^{\frac{1}{2}} h^{\frac{5}{3}} \tag{1.3}$$

with

	h	:	surface flow depth [L]
	q_x	:	unit discharge in x direction [$\mathrm{L^2T^{-1}}$]
	q_y	:	unit discharge in y direction [$\mathrm{L^2T^{-1}}$]
	i_e	:	effective precipitation rate [$\mathrm{L\ T^{-1}}$]
	t	:	time [T]
	S_f	:	friction slope in x or y direction [$-$]
	S_o	:	ground surface slope in x or y direction [$-$]
	l	:	distance in x or y direction [m]
	α	:	ground surface slope in x or y direction [$-$]
	n_m	:	Manning-Strickler coefficient [$-$]

Here only the basic idea of the model is presented. Detailed formulation of the CASC2D model and its applications can be founded in Julien et al. (1995); Sánchez (2002); Marsik and Waylen (2006).

1.1.2 TOPMODEL Model

TOPMODEL is, in contrast to the surface flow routing based CASC2D model, derived from the groundwater Darcy Equation. The streamflow is generated by first subsurface downhill flow, and when area close to the river starts to get saturated, also by the surface water input onto this saturated contributing area. The TOPMODEL theory is based on the following assumptions:

- Groundwater is in steady state with a spatially homogeneous recharge rate r_u $[\mathrm{LT}^{-1}]$. Over an unit upslope area a_u [L], the flow per unit contour length q_u $[\mathrm{L}^2\mathrm{T}^{-1}]$is:

$$q_u = r_u \, a_u \tag{1.4}$$

- The effective hydraulic gradient Δh $[-]$ is equal to the local surface slope $\tan\beta$:

$$\Delta h = tan\beta \tag{1.5}$$

- The transmissivity T_w $[\mathrm{L}^2\mathrm{T}^{-1}]$ is spatially homogeneous and locally decrease exponentially with local storage deficit SD' [L] with a controlling parameter m_T [L]:

$$T'_w = T_w \exp\left(-SD'/m_T\right) \tag{1.6}$$

The core part of the model is the analytically derived topographic wetness index:

$$wi = ln(\frac{a_u}{T_w tan\beta}) \tag{1.7}$$

A detailed description can be found in Beven (2001). One thing to be mentioned is that, TOPMODEL does not explicitly simulate the river flow, but consider it as part of the overland flow, whereas CASC2D simulates the river flow separately by considering the river channel geometry. Therefore, the overland flow result simulated by CASC2D in the following section has excluded the channel part.

1.1.3 Model Results and Enlightenment

In this work, the two models have been applied to the Goodwin Creek Watershed of around $21.5\,\mathrm{km}^2$, for a rainfall event lasted 4.8 hours. The catchment and dataset used here are the original data used to calibrate the CASC2D model, for a detailed description of them, the readers can refer to Sánchez (2002). Fig.1.1 shows the overland flow depth at the half time of the rainfall duration simulated by the two models. Fig.1.1(a) shows the overland

flow depth modeled by CASC2D, the water depth in the channel modeled with the detailed channel geometry is excluded, is thus all zero. Overland flow is presented over all area within the catchment, and the high overland flow "branches"look like channel extensions. Fig.1.1(b) shows the result from TOPMODEL without considering the channel geometry, and the high water depth are mainly presented in the channel part and some overland "branches"connected to the channel. The overland flow depth of CASC2D is much higher than TOPMODEL, because CASC2D has excluded the subsurface flow, and all water are flowing overland. Although the overland flow depth of the two models differ, the overland flow pattern, i.e. the locating of high water depth ("branches") are very similar.

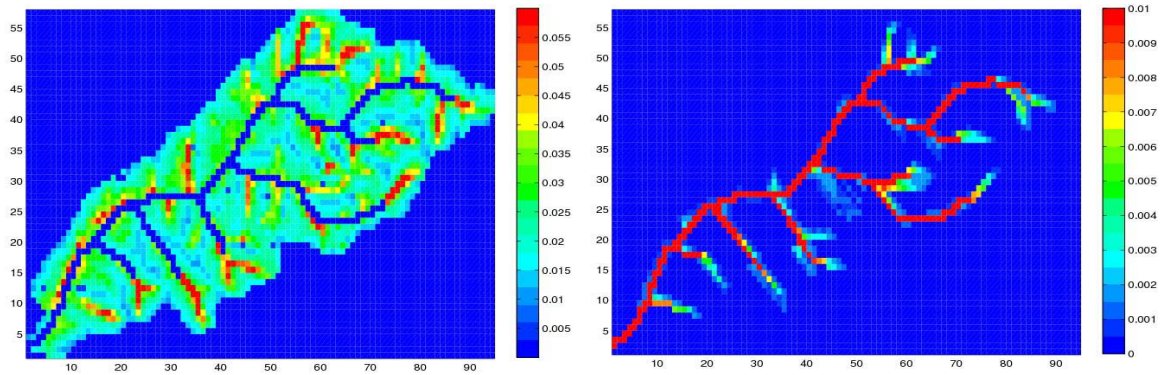

(a) Overland flow depth of CASC2D

(b) Overland flow depth of TOPMODEL

Figure 1.1: Comparison of overland flow patterns of CASC2D and TOPMODEL

Two models of completely different mechanisms generate surprisingly similar overland flow patterns. Is it accidental or deterministic? Does it mean that soil type does not matter, or there is something more dominating? It obviously can be explained by the topography-induced lateral flow, which controls the runoff generation process. No matter water are flowing surface or subsurface, it is controlled by the topography. The control of topography on water movement is fundamental to hydrology, but its regulation on other energy and mass input to the earth surface, i.e. wind, radiation, and precipitation which are the driving force of the hydrological cycle, are also very critical. Such effects, especially wind and radiation patterns resulted from topography, are neglected by most hydrological models, except a few, such as WaSiM-ETH (Schulla and Jasper, 2007) and CATFLOW (Zehe et al., 2001). Therefore some questions are rising here, namely:

- How does topography affect the vertical water transfer? Are they negligible or not?
- Since the assumption of TOPMODEL is "more convenient than true"(Beven, 1997), can we find some other more physical and viable explanation through topographic related energy and mass input and output?
- Does topography also affect other hydrological processes, which and how?
- Are there any systematic patterns in these topography-dependent hydrological processes, like the topographic wetness index?

Neither the questions are new, nor the answers. Still searching for satisfactory answers leads us to further exploit the interaction between topography and hydrological processes, and their co-evolution. The action of topography on hydrological processes are mostly known as short-term and more dominant, whereas the reaction of topography to hydrological forces are very chronic and indiscernible. Also from prospect of hydrological modeling, the effect of topography on hydrological processes are more important. The focus of this work is to study the effect of topography on hydrological processes, and to search for systematic hydrological patterns for improving hydrological model concept and data interpolation accuracy.

1.2 Topography, Processes and Patterns

1.2.1 Topography

Topography stands for the surface shape and features of the catchment, which varies across scale. At large scale, earth surface features are caused mainly by geological movements and glacial carving, and referred as *macro-topography* in this monograph, whereas at small scale, *micro-topography* caused by gully incision and other secondary processes dominates. In certain sense, the topographic scale is related to the Strahler Stream Order (Strahler, 1952) - the micro-topography is associated with the first several orders of the streams and the macro-topography is associated with the higher orders of the streams. In this work, the topographic scale is differentiated in a very general sense without a clearly defined threshold of Strahler Stream Order.

Topography is usually represented by digital elevation model (DEM). Geographic Information System (GIS) has made DEM a readily available information, and provided advanced DEM techniques to meet the demand of distributed hydrological modeling. There are three principal DEM data structures:

- Raster grid: raster surfaces are in grid format consisting of a rectangular array of uniformly spaced cells.
- Triangulated Irregular Network (TIN): elevation are sampled at irregular points, usually points with special features, such as peaks, ridges, etc.
- Vector-based contour: contour lines of each specified elevation are stored in form of points on the contour line.

Raster grid is the most widely used DEM technique because of its easy compute implementation and computational efficiency. Based on DEM, many other topographic attributes can be derived. Moore et al. (1991) has classified the topographic attributes into primary and secondary (or compound) attribute, based on whether it can be directly calculated from elevation data. A good example example of the secondary attributes is the topographic index in TOPMODEL. In this work, only the three basic primary attributes will be used: elevation, slope and aspect. GIS software packages, such as ArcGIS and GRASS greatly reduce complexity of the digital handling of topographic attributes. However, the users should keep in mind that the definitions of the attributes in different softwares are not identical.

1.2.2 Hydrological Processes and Patterns

Pattern is defined as spatial or temporal structure that is significantly different from a random one (Schröder, 2006). Because pattern comprises an organized or ordered structure, it can be detected and recognized without difficulty. Except some special components, such as lakes, reservoirs, most elements in hydrological cycle are spatially distributed, no matter the environment variables (soil, vegetation), or state variables (soil moisture, groundwater level, discharge, etc.). The spatial hydrological process are normally superimpositions of random variation onto a deterministic base, thus showing the characteristics of a pattern. When a hydrological model is implemented for the sake of hydrological system representation and prediction, patterns are concerned in every part and phase of the modeling procedure. They can be either model inputs, outputs or parameters, and they can be used to calibrate or validate models. Model outputs in the form of patterns also offer more thorough and straightforward information for decision making for water resources management.

Dependent on the underlying processes, patterns span a wide range of space and time scales. Small scale patterns, such as overland flow, can be observed at the hillslope scale, which appears and disappears rapidly. Patterns of large scale processes are spatially more coherent and slowly varying (Grayson and Blöschl, 2000). Blöschl and Sivapalan (1995) has provided an wonderful schematic overview of the time and spatial scales of hydrological processes.

From the nature of its origin, patterns can be classified as *observed*, *interpolated*, and *simulated*. *Observed* patterns are the first-hand field data, which is the most valuable and ideal source for process investigation. Unfortunately the formidable cost and efforts of a detailed sampling limits the observed patterns rather uncommon. Interpolation offers a solution to circumvent the lacking of detailed observations. Different interpolation techniques, mainly geostatistical methods, provide the possibility to obtain a spatial data from the point data. Nevertheless, a good interpolation is based on the process understanding, as discussed later in Chapter 6 and 7. Because most interpolation techniques are linear, they are not able to capture the strong nonlinearity of underlying hydrological processes. *Simulated* patterns from physically-based modeling provide more process-oriented spatial information, which is more realistic than interpolation results, and more complete than the point observations, such as catchment integrated discharge. Development in measurement technology, interpolation techniques, especially in remote sensing, have made an unprecedented amount of pattern information available. Grayson et al. (2002b) summarized the pattern information into the following three types:

- Lots of points (LOP): a sufficiently dense array of point measurements can construct a spatial pattern. Some soil moisture map measured by time domain reflectrometry (TDR) are reported in literatures (Bárdossy and Lehmann, 1998; Western and Grayson, 1998; Zehe et al., 2010). But still patterns from direct point measurements are very rare.
- Binary data: spatial qualitative data is a trade-off between detailed patterns and point quantitative data. Binary patterns, such as flood inundation, snow cover, cloud cover, etc., are also very important data for hydrological purpose.
- Surrogate data: Surrogates are variables that show some degree of correlation to the pattern of interest that are not readily measurable. Topographic wetness index is a

typical example. Grayson et al. (2002b) also classify all kinds of quantitative remote sensing images derived from the spectral information as surrogate data. But identification of surrogate data means always proper assumption and hypothesis about the underlying hydrological conditions and/or processes, for example, hillslope position, soil type, etc. (Zehe and Flühler, 2001).

All these patterns are generated not to impress people, but to give hints for understanding and diagnosing the underlying hydrological processes. On the other hand, the advances of hydrological knowledge can help to produce more realistic predictive patterns for decision making.

1.2.3 Topographic effects on process patterns

Topography is known to have a major effects on the hydrological, geomorphological, and ecological processes active in the landscape. Hydrological responses and patterns are affected by topography both directly and indirectly, and the effects of topography on catchment process may change with scale, depending on the process. The direct topographic effects on catchment processes, such as its control on radiation, wind, and precipitation, water flow, are referred as *primary* effects in this work. "primary"also has another meaning that radiation, wind, and precipitation are the energy and mass input processes that are external to the catchment. Topographic effects on other processes are usually derived from the primary effects, and some times the interaction of two of more primary effects, for example, evaporation, snow accumulation, and snow melting, etc., which are called *secondary* effects in this monograph. This definition is not completely unambiguous, for example, precipitation is also affected indirectly by topography through wind. Some of these effects can be directly expressed as an empirical function of the spatial topographic attributes, allow the corresponding patterns to be mapped easily with analytical or empirical techniques. For some other processes, although the impact of topography is deterministic and decisive, its relationship with topography is highly nonlinear and can not be expressed in simple functional form. In the following an extensive, though not exhaustive overview of the primary and secondary topographic effects will be given.

Primary Effects

Among the primary effects, the fact that water flows downwards driven by the terrain and gravity hardly needs any explanation. It is this fact that leads to the formation of drainage network patterns in the catchment, called fractal, which is a complex issue and major topic of geomorphology (Hallet, 1990). This monograph will focus on the other primary effects, namely radiation, wind and precipitation.

Radiation Solar radiation is the only source of energy input to the earth, thus the ultimate driving force of the catchment evolution and hydrological responses. The globally unbalanced heating resulted from radiation variability causes the atmospheric circulation, and the climate difference at the continental scale. While at global scale, the latitudinal and longitudinal location determines the incidental radiation, at regional and local scale, terrain is

the major factor modifying the distribution of radiation (Hofierka and Suri, 2002). Difference in elevation, surface inclination and orientation, and shadow effects result in a regional variability of solar radiation, which in turn affects dynamics of hydrological, meteorological, and ecological ingredients, such as air temperature and moisture, evaporation, snow melting, soil moisture, weather variations, crop growth, etc. An enormous amount of work have investigated the topographic modification of solar radiation, with the focus on renewable photovoltaic energy. In this work, a topography-based spatial radiation mapping for hydrological purpose will be emphasized.

Wind Local topography can drastically alter the wind patterns that originate from atmospheric circulation. The major driving factors of large scale winds, also called geostrophic wind are the differential heating between the equator and the poles, and the Coriolis forces. The geostrophic wind is modified locally by the topography and ground surface, as well as the local heating difference, and forms a spatially varying local wind pattern. Study of wind patterns has been widely applied in building engineering, transportation engineering, air quality control, wind energy generation. The role of wind in hydrological cycle should not be underestimated. Wind alters the distribution of precipitation (Blocken et al., 2005; Lehning et al., 2008), and redistribute the snow even after it reaches the ground. It is also a very important factor in evapotranspiration and soil moisture dynamics. Not only numerical modeling can be applied to simulate the wind field, Winstral et al. (2009) also shows that the spatial wind pattern can be estimated empirically from the shelter-exposure of the topography. A short but effective review of the existing approaches for wind resource estimation can be found in Landberg et al. (2003). In this work, the wind mapping with meso-scale meteorological model fed with reanalysis data will be applied.

Precipitation Precipitation occurs in two forms, liquid form (rain) and solid form (snow), both are affected by topography. Rainfall is altered by topography by both primary and secondary effects at large and small scale respectively. At larger scale, the primary orographic effects dominate, whereas at smaller scale, wind drift effects prevail. Both effects have been extensively studied with statistical(Basist et al., 1994; Weisse and Bois, 2001; MarquInez et al., 2003) and numerical methods (Sharon and Arazi, 1997; Blocken et al., 2005; Lehning et al., 2008), which have shown a precipitation pattern at different scales (Gerstengarbe and Werner, 2008). This monograph will discuss the spatial interpolation of precipitation while accounting for the spatial non-stationarity caused by larger scale orographic effects, and it will also investigate the precipitation variability at valley scale that have been neglected by the researchers up to now.

Snow is more special than rainfall, because it is more susceptible to wind, even after falling to the ground. Moreover, the spatial snow distribution is complicated by the rain-snow variability at different elevation resulted from the laps rate, and the rain-on-snow conditions. Many studies have acknowledged that snow distribution is the result of interaction between wind, terrain and vegetation (Watson et al., 2008). Since there have been already many models available for snow distribution modeling, this issue will not be touched in this work, but only snowmelt.

Secondary Effects

Through the primary effects, or the interaction of different primary effects, many other hydrological processes will be affected, and exhibit a distinct pattern, such as snowmelt, ET, and soil moisture, erosion, vegetation, etc.

Snowmelt Snow melting results from fluxes of energy and mass across the snow-air and the snow-ground, and involves an array of processes (i.e. thermal radiation, condensation, evaporation, sublimation, refreezing, vapor diffusion, settling and compaction), if the details of the physical processes are concerned. However the most decisive factor of snowmelt is the heat-transfer related solar radiation and wind. In this work, instead of going into detailed physical processes involved in snowmelt, improved radiation index degree-day snow model will be tried to simulate the snow melting processes by matching the residual snow cover patterns.

Evapotranspiration The energy exchange between earth surface and atmosphere is realized in the form of sensible heat and latent heat transfer, and the latter, which is associated to evapotranspiration, releases most of the received energy of the earth to avoid the continuous warming of the earth. The governing factors of ET include radiation, wind, humidity, temperature, vegetation, soil, and water availability, which all show to some extent a spatially organized variability. Therefore, the resulting ET also shows some patterns. In this work, the ET pattern affected by the dominating factors of radiation and wind will be investigated with a agro-hydrological model.

Soil Moisture Soil moisture is related to ET, but it is even more complex and uncertain, because its boundary is in subsurface, which is invisible, unknown, and extreme heterogeneous. On the other hand, it is also more important in the hydrological cycle, because rainfall runoff generation process is to a large extent depending on the soil moisture state, called antecedent moisture index (AMI). Soil moisture shows a high spatial and temporal variability at different scales Western et al. (2002). But because soil moisture change is an cumulative process, in a shorter time span, it shows certain temporal stability (Mohanty and Skaggs, 2001). Spatial soil moisture distribution is resulted from both lateral and vertical soil-water flow. The representative soil moisture mapping based on lateral flow is the TOPMODEL, which specifies that in the bottom of the hillslope or basin is always wetter than the upper slope. But how about the variability caused by water flow in the vertical direction? How will the interaction of topography, local atmospheric factors (precipitation, radiation, temperature, humidity, pressure, etc.), soil characteristics and vegetation covers, which are all spatially heterogeneous, influence the soil moisture pattern through vertical water transfer? This will also be questions to be treated in this work.

Vegetation Although the spatio-temporal dynamics of snowmelt (onset, duration), ET, soil moisture, etc., clearly depend on the specific weather conditions, their spatial differences are mainly influenced by the topography and thus remain relatively stable over the years. Such long-term patterns however, determine the vegetation distribution, biodiversity, and the landscape-scale mechanisms of soil-vegetation and atmospheric exchange processes Mohanty and Skaggs (2001). Although the vegetation pattern has been confirmed by many

studies, its dependence on topography and other factors is site-specific, and very complex. The work will not touch this issue.

Soil Soil plays an important role in hydrology. The father of soil science, Vasily Dokuchaev (1846-1903) states that in long term soil is not inert and stable, but develops under the influence of topography, climate, vegetation from a given geological substrate. Dokuchaev developed, and Jenny (1941) further refined the so-called functional factorial approach of pedogenesis. Both deterministic model (Phillips, 1993) and mechanistic model (Minasny and McBratney, 1999) have been tried to predict the soil properties, but the success is very limited. This work will not get into this complex issue.

1.3 Objective and Methodology

This work is going to investigate the primary and secondary effects of topography on spatial hydrological variabilities with the example of radiation, wind, ET/SMC, snowmelt, and precipitation, and exploit the corresponding hydrological patterns. The main objectives of this research are:

- simulating the topographic effects on spatial radiation and wind variability;
- quantifying the effects of topography induced spatial radiation and wind on ET/SMC;
- investigating the topographic effects on precipitation distribution in complex terrain at different scales;
- exploring the possibility of improving the interpolation procedure to account for the topographic effects at both regional and local scale;
- adapting the conceptual degree-day model to include the topographic modified spatial radiation.

The objective of the study is to quantify the topographic effects in general, namely any arbitrarily selected catchment or region, and the quantifying methods should be applicable no matter it is a gauged or ungauged basin. Attention have been paid to the *validity* and *generality* of the methodology. To ensure the validity of the methods, physically-based process modeling approaches are applied wherever possible. For those processes, where the physical descriptions are very site-specific, e.g. precipitation and snowmelt, compromise has to be made - instead of physically-based models, conceptual models and statistical analysis are used. But still the conclusion and findings of these methods are transferable to other areas.

The general applicability is fulfilled by applying globally available data, including processed open-source data archives, such as NCEP/NCAR reanalysis data, and remote sensing data, such as MODIS, Meteosat, etc. However, station data are required to validate the physically-based models fed with global data.

1.4 Study Area and Data

1.4.1 Study Area and Observed Data

To validate the physically-based approaches and to enable the conceptual and statistical analysis, South Germany with very good data availability are selected as the study area of this work. Depending on the hydrological process under examination, the corresponding data demand and data availability, study area or catchment are selected considering the availability of different data sources and the computing efforts, which will be listed in the respective chapters.

1.4.2 Remote Sensing Data

Remote sensing has provided a novel means for collecting hydrological data, and aided the developing of hydrological models. In this work the Moderate Resolution Imaging Spectroradiometer (MODIS) data from US National Aeronautics and Space Administration (NASA)and Meteosat data from European Organization for the Exploitation of Meteorological Satellites (EUMETSAT) have been used.

MODIS

MODIS is a key instrument aboard on NASA's EOS Terra satellite launched on 18 December 1999, and Aqua satellite launched on 4 May 2002. The MODIS sensors scan the earth in 36 spectral bands ranging from the wavelength of $0.4\,\mu\mathrm{m}$ to $14.4\,\mu\mathrm{m}$. Different bands acquire data in three native spatial resolutions: $50\,\mathrm{m}$ (bands 1~2), $500\,\mathrm{m}$ (bands 3~7), $1000\,\mathrm{m}$ (bands 8~36). Because the visible and infrared scanning spectrum of MODIS is far too short to penetrate the cloud, MODIS data are not available for cloud covered area. The revisit time of MODIS varies from 1 to 2 days depending on the latitude, and it provide data on daily base, as well as composite data of 8-day, 16-day, monthly, quarterly and yearly. MODIS provides 4 groups of data (atmosphere, land, cryosphere, ocean) processed at different levels:

- Level-1A: raw data, radiance counts
- Level-1B: calibrated, geo-located radiance
- Level-2: derived geophysical variables at the same resolution and location as level-1 source data (swath products)
- Level-2G: level-2 data mapped on a uniform space-time grid scale (Sinusoidal)
- Level-3: gridded variables in derived spatial and/or temporal resolutions
- Level-4: model output or results from analyses of lower-level data

Data used in this study include Leave Area Index (LAI) and snow cover data. The vegetation data are combined data of 16-day interval with a resolution of $1000\,\mathrm{m}$, and snow data used in this work is $500\,\mathrm{m}$ resolution daily snow cover data.

Meteosat

The Meteosat satellites are a series of geostationary meteorological satellites covering Europe and Africa, operated by EUMETSAT since 1977. With a continuous upgrade, the Meteosat satellites have experienced three generations, the Meteosat First Generation (MFG), the Meteosat Second Generation (MSG), and the Meteosat Third Generation (MTG) which is going to be launched in 2015. The Meteosat Visible and Infrared Imager (MVIRI) of MFG acquire data every $30\,\mathrm{min}$ in 3 spectral channels of visible (VIS) (0.5~$0.9\,\mu\mathrm{m}$), infrared (IR) (10.5~$12.5\,\mu\mathrm{m}$), and water vapor (WV) (5.7~$7.1\,\mu\mathrm{m}$), and the Spinning Enhanced Visible and Infrared Imager (SEVIRI) of MSG significantly improved the system by reducing the scanning period to $15\,\mathrm{min}$ and adding another 8 spectral channels and 1 high resolution (HR) visible channel. The VIS channel of Meteosat are $4.8\,\mathrm{km}$ spatial resolution. Because it is sensitive to the reflection of solar radiation by clouds, it enables the detection of cloud conditions, which can be used for solar radiation calculation. Instead of direct Meteosat data, this study uses the processed cloud and radiation data by SoDa (`http://www.soda-is.com`).

1.4.3 NCEP/NCAR Reanalysis Data

NCEP/NCAR Reanalysis is a continually updating reanalysis data set representing the state of earth atmosphere (temperature, wind, pressure, humidity, etc.) produced jointly by the National Centers for Environmental Prediction (NCEP) and the National Center for Atmospheric Research (NCAR) with data assimilation techniques (Kalnay et al., 1996). The data is distributed in Netcdf and GRIB format, and can be downloaded from `http://www.esrl.noaa.gov/psd/data/gridded/data.ncep.reanalysis.html` free of cost. Data assimilation aims at accurate estimation and prediction of an unknown true state of a time series by incorporating observations into a model. At each time step, observations of the current state of the system are combined with the results from a numerical weather prediction (NWP) model (forecast), with the uncertainty in the observation and forecast being balanced. The result is called *analysis*, and is considered as the best estimation of the current state of the system with minimum uncertainty. When *analysis* is applied not to current data, but to historical data, it is called *reanalysis*. There are several international reanalysis data sets, and the most widely used are NCEP/NCAR Reanalysis and ECMWF (European Center for Medium-Range Weather Forecasts) Reanalysis.

1.5 Organization of the Thesis

In line with the scope and objective of this work, this work is structured in eight chapters. Chapter 2 will review the steps and algorithms of potential and actual spatial radiation mapping, and compare two methods with the least data requirement, one based on remote sensing data and the other one based on sunshine duration observations. Chapter 3 is dedicated to downscaling spatial wind pattern from NCEP/NCAR Reanalysis data with meso-scale wind model METRAS PC. Chapter 4 will combine the spatial radiation and wind difference, and evaluate the resulted spatial ET/SMC variability with grid application of the

SWAP model. Chapter 5 deals with spatial heterogeneity of snowmelt caused by radiation with different adaptations of radiation index degree-day model. Chapter 6 attempts to explore the possibility of applying multidimensional scaling (MDS) transformed distance in kriging to account for the local anisotropy caused by topography. In Chapter 7, the valley effect on spatial precipitation variability is investigated, and it reveals that when the narrow-steep valleys are isolated from the circulation pattern, the valley will receive comparable precipitation as the mountain does. This discovery is implemented in the external drift kriging procedure to improve the interpolation accuracy by an anisotropic smoothing of DEM in the CP direction. Chapter 8 presents a summary of this work, and proposes some interesting points for future research.

2 Solar Radiation Modeling

Solar radiation sustains the lives on the earth, and it also causes the spatial and temporal variation of hydrological ingredients, such as vegetation, biology, and water. Precise quantification of spatial solar radiation incident to the earth surface, is fundamental to both meteorology and hydrology. The global radiation is determined by the interaction of solar-earth geometry (solar positioning, surface inclination, the terrain shading, etc.), surface properties (albedo, absorptivity, etc.), and atmospheric characteristics (atmospheric attenuation, cloud type, etc.). Solar-earth geometrical relationship are mainly determined by the variations in topographic parameters, i.e. elevation, slope, aspect, which can cause substantial difference in solar radiation at local scale. The surface and atmospheric conditions can be parameterized physically or empirically. Models with different algorithm and of different complexity, from the simple empirical equations to process-based physical approach, have been developed to parameterize and calculate the potential (under clear sky condition), as well as actual radiation (under overcast cloudy condition). This chapter will present an overview of the general steps of solar radiation modeling and the most popular modeling approaches. Two models with least data requirements are selected for operational spatial radiation modeling: the GIS-based, physically parameterized, remote-sensing oriented Heliosat-2 model, and the sunshine duration based Angström-Prescott regression model. The capability of the models for radiation simulation on horizontal surface are verified with observed data, and the validity of the models for modeling inclined surface are tested by comparing the models with each other. The scale sensitivity of the models and shading effects are examined with different DEM resolution. Dominating effects of topography on spatial solar radiation variation under clear-sky in complex terrain have been illustrated with point comparison. A case study with a small catchment also demonstrate the spatial solar radiation variability under cloudy conditions. The study confirms the potential of the two models in mapping/downscaling spatial solar radiation, and the feasibility of applying remotely sensed data for mapping global radiation in complex terrain for hydrological application.

2.1 Introduction

Solar radiation is practically the only energy source of the terrestrial system. It affects all the physical, chemical and biological processes on the earth, and sustains the living agents on the global. It is also regarded as one of the most important alternatives of clean and renewable energy. In hydrology, the importance of solar radiation can be witnessed by the fact that, the spatial and temporal varying solar radiation determines the spatial dynamics of many hydrological and landscape processes, e.g. temperature, photosynthesis and evapotranspiration, soil moisture, and snow melting. These processes in turn affects the

regional water balance (Fox et al., 2000), drought and flood occurrence (Danny Marks and Garen, 2001), as well as landscape-scale distribution of vegetation (Urban et al., 2000; Dymond and Johnson, 2002). Mapping of spatial solar radiation is an important prerequisite for many solar radiation related application. For locating solar energy system, monthly maps maybe enough (Janjai et al., 2005), but for hydro-meteorological and hydro-ecological study concerning rapid changing processes, such as snowmelt, wind, vegetation growth etc., radiation variation at finer time scale, such as daily and hourly information is often required (Wang et al., 2002).

Solar radiation mapping may concern the individual radiation components or the total radiation amount, under clear or overcast sky condition, on horizontal or incline surface. The fact is that, due to the interaction of topography, ground surface, and atmosphere, the solar radiation is varying strongly in space and over time. Different approaches, i.e. observations/interpolation, statistical methods, physical techniques, or the combination of them have developed to quantify the spatial radiation. The mapping techniques also differ in terms of spatial and temporal scale. Recent development in geostationary satellite, such as Meteosat (Cano et al., 1986; Rigollier et al., 2004), GEOS (Dubayah and Loechel, 1997), and MODIS (Liang et al., 2006) offers new possibility in solar radiation mapping.

This work will present a review of the most popular solar radiation modeling and mapping concepts. Application and comparison with selected methods will be demonstrated within a small catchment. The objective is to investigate the topographic effects, and find an operational radiation model with minimum observational data requirements, which can be used to facilitate the development and application of distributed hydrological modeling at different resolutions.

2.2 Basics and Terminology

Solar radiation accounting is an important issue of energy balance modeling, which is the core part of many hydro-meteorological process models, such as Land Surface Models (LSM) (Liang et al., 1994), process-based evapotranspiration models (Allen et al., 2007; Kafle and Yamaguchi, 2009) and snowmelt models (Lehning et al., 2006; Reijmer and Hock, 2008). The surface energy balance system can be broken down into two parts regarding the radioactive energy flow (see Fig.2.1): solar energy incoming and terrestrial energy outgoing. Solar radiation is the eletromagnetic energy propagation at wavelengths less than $4\,\mu\mathrm{m}$, therefore it is also called shortwave radiation, in contrast to the longwave radiation emitted by the earth surface, aerosols, and clouds. The spectral radiation arriving outside the earth's atmosphere is called *extraterrestrial radiation*. For a surface perpendicular to the solar rays, the rate of the extraterrestrial radiation fluctuate very slightly, and can be taken as a pseudo constant. The value of this constant flux at a distance of 1 astronomical unit (roughly the mean solar-earth distance) from the sun, is defined as *solar constant* (Eq.2.1).

$$\dot{I}_{SC} = 1353\ W\,m^{-2} = 4871\ kJ\,m^{-2}\,h^{-1} \tag{2.1}$$

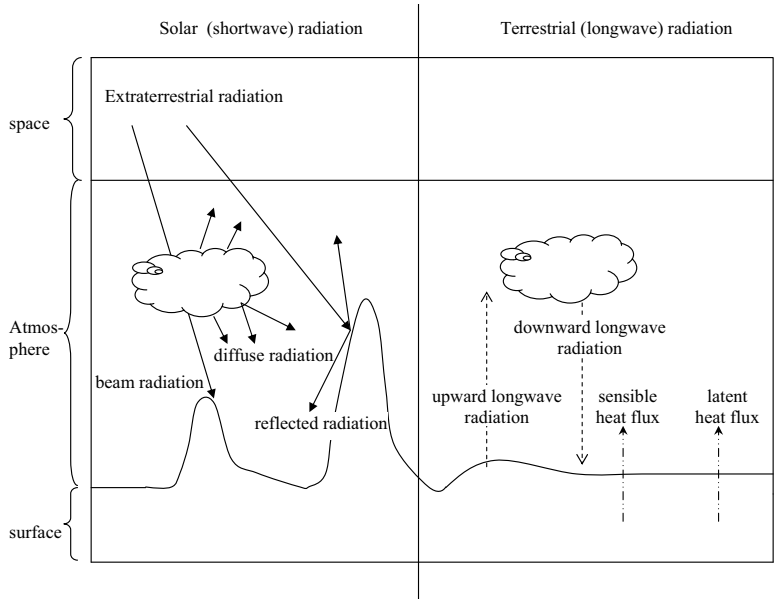

Figure 2.1: Earth radiation and energy balance

Here the difference between units expressing quantity of energy and those denoting rate of energy has to be noticed. Hereafter the widely accepted WMO (2008) terminology will be adopted in this paper – the term *irradiation* and *radiation* are used to refer to the amount of energy falling on unit area over a given time interval, while *irradiance* and *radiance* is used to denote radiant flux or intensity, which is the instantaneous solar power received by unit area per unit time.

When solar radiation passes through the atmosphere, it will be attenuated by various constituents in the earth atmosphere, by means of scattering and absorption. The attenuation is a function of the mass of an attenuating substance the solar ray has to traverse. The air mass in a column of unit cross section is called optical air mass, and the ratio of the optical air mass along the oblique trajectory ds to the mass in the zenith direction dz is called relative optical mass m_r (see Eq.2.2). The length of the solar ray trajectory is called optical path length s, which is different from the atmospheric depth at the zenith direction z.

$$m_r = \int_0^\infty \rho ds / \int_0^\infty \rho dz \tag{2.2}$$

Here ρ is the air density. The residual radiation that reaches the ground surface is called *beam radiation* or *direct radiation*, denoted as B in this work. The amount of beam radiation incident to a surface is depending on the inclination of the surface. A portion of the scattered radiation goes back to space, and the rest reaching the ground is referred as *diffuse radiation* D. The earth surface also receives *reflected radiation* R_l from the surrounding terrain, which is generally a very small portion, and is usually neglected in literatures. The actual amount of radiation incidental the earth surface, defined as *global radiation* G, is the sum of the beam, diffuse and reflected radiation (see Eq.2.3).

$$G = B + D + R_l \tag{2.3}$$

To keep its temperature from continually rising, the earth releases the energy it receives from solar radiation through longwave radiation, sensible and latent heat transfer. The net longwave radiation L_n added to the ground surface is a balance of upward longwave radiation $L\uparrow$ emitted by the ground surface, and downward longwave radiation $L\downarrow$ sent off by the atmosphere. The total energy balance and the longwave balance can be expressed as:

$$L_n = L\downarrow + L\uparrow \tag{2.4}$$

$$LE = G + L_n - Gr - H + A_\omega - \frac{\Delta Q}{\Delta t} \tag{2.5}$$

with

LE	:	latent heat flux [E $\mathrm{L}^{-2}\mathrm{T}^{-1}$]
G	:	global radiation (net shortwave radiation) [E $\mathrm{L}^{-2}\mathrm{T}^{-1}$]
Gr	:	net ground heat exchange [E $\mathrm{L}^{-2}\mathrm{T}^{-1}$]
H	:	sensible heat exchange [E $\mathrm{L}^{-2}\mathrm{T}^{-1}$]
A_ω	:	water-advected energy [E $\mathrm{L}^{-2}\mathrm{T}^{-1}$]
ΔQ	:	change in heat storage [E L^{-2}]
Δt	:	the studying time period [T]

Radiation can be measured by radiometers which are designed to be sensitive to a specified range of wavelength (WMO, 2008). The longwave radiation, direct radiation, and global radiation can be measured by pyrgeometer, pyrheliometer, and pyranometer respectively. For an accurate solar radiation measurement, the devices has to be mounted according to the view-limiting geometry to capture exactly the desired radiation components, and regular calibration and adjustment is also required. The calibration of pygeometer also requires quite some efforts (Reda et al., 2003). The high requirements for calibration and maintenance render the radiation measurement network very sparse, for example, in Germany, altogether only 113 solar radiation stations are available, 13 of which measure in addition the longwave radiation. Moreover, radiation measurement is very site-specific, because of the high spatially variability caused by heterogeneous surface and atmospheric conditions. It is therefore more usual and simple to measure *sunshine duration*, n_d, which is defined as the time period with direct solar irradiance exceeds $120\,\mathrm{W\,m^{-2}}$.

The radiation pattern mapped from the sparse radiation network captures only spatial variability at the national or regional scale, but hydrological or hydro-ecological study often requires very detailed spatial radiation variability, therefore radiation modeling has been brought into forth to meet this demand.

2.3 Solar Radiation Modeling

A good solar radiation model should be capable to handle an arbitrary oriented surface (horizontal and inclined) under all sky conditions (clear-sky and overcast-sky), by properly representing and parameterizing the factors that affect the interactions of solar, atmosphere and ground surface. These factors include: (Hofierka and Suri, 2002):

1. the sun-earth position, revolution and rotation;

2. topography: elevation, surface proposition and inclination, shading;
3. atmospheric characteristics: gases, water(liquid, solid, vapor), particles
4. overcast condition: spatial and temporal cloud cover

The first two groups of the above factors can be modeled by trigonometry with high level of accuracy. The atmospheric attenuation, which is the attenuation effects under clear sky conditions, can only be modeled by parameterization with less but relatively good accuracy, because the composition of atmosphere is relatively stable. The most difficult issue is the cloud accounting, even the observed cloud data can be problematic due to the spatial and temporal changing weather conditions, and the 3D structure of cloud. Nevertheless, many models and softwares have been developed to model the global solar radiation, and some of them are included as a standard package for the GIS software, e.g. *r.sun* in GRASS (Hofierka and Suri, 2002), the Solar Analyst in Arcview and Arcgis (Fu and Rich, 2002), the SRAD in TAPEG (Wilson and Gallant, 2000). Models differentiate themselves in terms of the approaches for geometric modeling, attenuation parameterization, and overcast concept, which will be discussed in the following respectively.

2.3.1 Solar-Earth Geometric Modeling

The geometric modeling concerns the sun position, solar incidence angle and shading. The basic sun positioning algorithm (SPA) and solar incidence angle calculation are very well known. With the geometrical solar-earth relationship, the theoretical solar irradiance, hourly or daily irradiation in absence of earth atmosphere can be calculated numerically or analytically. The analytical solution of daily and hourly solar radiation is shown in Appendix I. Shading can be caused by the inclination of the surface itself or the adjacent terrain. It modifies the direct radiation by changing its projection or blocking it. It also reduce the scope of the sky that scatters diffuse radiation to the ground, and on the other hand, it may add reflected radiation from the blocking terrain to the ground.

Two main shading algorithms are available: the solar-based and the ground-based method. For the solar-based method, shading test is conducted for a given solar altitude at each time step for all points. The elevation of each ground point lying on the sun-point line projection will be checked to ensure that it does not obstacle the sun-light. The GRASS solar radiation package *r.sun* applies this method. The ground-based method calculates the hemispherical viewing area (viewshed), which is the area that the point of interest is exposed to, based only on the adjacent terrain. Direct and diffuse radiation from this area are not shaded (Dozier and Frew, 1990; Rich et al., 1994). Once the viewshed is constructed, at each time step no other computation but only simple check of whether the sun is lying within the viewshed, is needed, therefore the ground-based method is more computing efficient. This method is represented by Solar Analyst package in ArcGIS and ArcView.

The geometric modeling gives the solar radiation in absence of atmosphere on the ground surface. But this is not the case in the real world, where the presence of air, trace gas, dust, water vapor in the atmosphere will attenuate and deplete the radiation.

2.3.2 Atmospheric Parameterization for Clear Sky

Fundaments of Atmospheric Parameterization

The depletion processes include scattering by air molecular (Rayleigh Scattering), scattering and absorption by aerosols, absorption by ozone layer, absorption by uniformly mixed gases, and absorption by water vapor (Iqbal, 1983). The total atmospheric attenuation effect is the result of interaction between atmosphere conditions and solar-earth revolution, because the relative air optical mass changes with the solar ray direction. Different substances scatter or/and absorb solar radiation at certain spectrum range, and the attenuation processes are substance and spectrum independent, therefore can be treated individually as monochromatic attenuation by each substance and then superimposed together. Both monochromatic and the spectrally integrated attenuation can be described by Lambert's law with 3 mutually convertible parameters: the attenuation coefficient κ_i, the transmittance τ_i, and the optical depth, also called optical thickness δ_i:

$$\dot{I}_i = \dot{I}_{0i} e^{-\kappa\, s_i} \tag{2.6}$$

$$\tau_i = e^{-\kappa\, s_i} \tag{2.7}$$

$$\delta_i = \kappa_i\, s_i \tag{2.8}$$

Here i denotes a given atmospheric substance, which may or may not exist in throughout the whole atmospheric layer, s_i is the optical path length of a given substance i, $\dot{I}_{0i}$ and $\dot{I}_i$ is the intensity of spectral radiation before and after passing through the atmosphere. The attenuation coefficient is an obsolete term, and is nowadays rarely used. Because the processes are independent, for n substances, their effects can be superimposed (see Eq.2.10). For calculating direct radiation, it is also not necessary to differentiate between absorption and scattering, because both effects are the same.

$$\tau_e = \tau_r\ \tau_a\ \tau_o\ \tau_g\ \tau_w = \prod_{i=1}^{i=n} \tau_i \tag{2.9}$$

$$\delta_e = \sum_{i=1}^{i=n} \delta_i \tag{2.10}$$

with
- τ_e : effective transmittance of direct radiation by all atmospheric substances $[-]$
- τ_r : transmittance of Rayleigh (molecule) scattering $[-]$
- τ_a : transmittance of aerosol scattering and absorption $[-]$
- τ_o : transmittance of ozone absorption $[-]$
- τ_g : transmittance of uniformly mixed gas $[-]$
- τ_w : transmittance of water vapor $[-]$
- τ_i : spectrally integrated transmittance of a given substances $[-]$
- δ_e : effective optical depth of all substances $[-]$
- δ_i : spectrally integrated optical depth of a given substances $[-]$

For diffuse radiation, absorption and scattering have to be treated separately, because the forward scattered radiation will continue traveling to the ground, whereas absorbed radiation terminates. Molecule and aerosol have also different scattering effects, namely the molecule scattering is symmetrical in forward and backward direction, while the aerosol has a strong forward scattering. The forward scattered radiation reaching the ground can be expressed with the assistance the atmospheric albedo ρ_{at}, which denotes the diffuse component reflected back to space:

$$\rho_{at} = \tau_o \, \tau_g \, \tau_w \, (0.5(1-\tau_r)\tau_a + (1-f_{af})f_{as}(1-\tau_a)\tau_r) \tag{2.11}$$

$$T_d = 1 - \rho_{at} = \tau_o \, \tau_g \, \tau_w \, (0.5(1-\tau_r)\tau_a + f_{af}f_{as}(1-\tau_a)\tau_r) \tag{2.12}$$

Here f_{af} denotes the portion of forward scattered radiation. f_{as} is scattered fraction out of the total energy attenuated by aerosol. T_d is the diffuse transmission coefficient.

Regression analysis and inversion methods using radiative transfer model (RTM) are used to derive the attenuation parameters, based on measurable meteorological data, such as temperature, solar irradiance, humidity, etc. To be mentioned, these data can be also obtained from satellite observations, i.e. the Heliosat-3 model (Mueller et al., 2004). The objective of RTM is to find out the individual optical depth, the size of the extinction layer, or the equivalent sum.

Besides the aforementioned parameterization for clear-sky direct and diffuse radiation modeling, there are many parameterization methods in literature, a good overview of the most popular ones can be found in Ineichen (2006). Although the parameterization methods are so many that it is even confusing to decide for a proper one, they can be generalized into two groups based on whether individual or integrated parameters are used in the radiation model. The individual parameterization applies several attenuation parameters of each extinction layer (substances) together, which is represented by the Page model (Page, 1997), SOLIS model (Mueller et al., 2004), Bird and Hulstrom model (Bird and Huldstrom, 1980), CPCR2 model (Gueymard, 1993). The second group summarize the different processes into Rayleigh optical depth δ_r and the Linke turbidity T_{Ln}, by which the transmittance of each extinction substance are converted and summed up with reference to the spectrally integrated Rayleigh optical depth of the clean and dry atmosphere (Kasten, 1996). It is used by the European Solar Radiation Atlas (ESRA) model (Rigollier et al., 2000) and the Ineichen model (Ineichen and Perez, 2002). Linke Turbidity can be derived by measurements of the beam irradiance using appropriate but expensive equipment. The typical Linke Turbidity values are widely reported in literature for different parts of the world.

Based on the parameterization schemes, the clear sky radiation on horizontal and inclined surface can be expressed as following respectively. Note, the subscripts h and β are denoting *horizontal* and *inclined* surface respectively, and c and b are used for *clear* and *cloudy* (bewölkt in German) sky conditions.

Clear Sky Model on Horizontal Surface

- Direct radiation:

for integrated parameterization:

$$B_{hc} = \dot{I}_{SC}\ \epsilon\ cos\theta_z exp(-0.8662\ T_{Ln}\ m\ \delta_r(m)) \tag{2.13}$$

or for individual parameterization:

$$B_{hc} = \dot{I}_{SC}\ \epsilon\ cos\theta_z \tau_r\ \tau_a\ \tau_o\ \tau_g\ \tau_w \tag{2.14}$$

- Diffuse radiation:

for integrated parameterization:

$$D_{hc} = \dot{I}_{SC}\ \epsilon\ T_d(T_{Ln})\ F_d(\theta_z, T_{Ln}) \tag{2.15}$$

or for individual parameterization:

$$D_{hc} = \dot{I}_{SC}\ \epsilon\ cos\theta_z\ T_d(\tau_i, f_{as}, f_{af}) \tag{2.16}$$

Here θ_z is the solar zenith angle of horizontal surface, ϵ is the eccentricity correction factor of solar-earth distance. The diffuse transmission coefficient, for the integrated parameterization is a function of Linke Turbidity $T_d(T_{Ln})$, and for individual parameterization it is given by Eq.2.12. The integrated form also includes a diffuse angular function F_d related to zenith angle and Linke Turbidity.

Clear Sky Model on Inclined Surface

For the inclined surface under clear sky, the direct radiation will only be modified by the solar incidence angle (see. Eq.2.17), and the diffuse radiation will be reduced in addition by the reduced skyview fraction ν. Both direct and diffuse radiation on inclined surface can be expressed based on the their counterparts on horizontal surface. For direct radiation on inclined surface, expressed as $B_{\beta c}$, only the incidence angle changed to θ instead of θ_z. Diffuse radiation on inclined surface, denoted $D_{\beta c}$, is usually expressed as a portion of the diffuse radiation on horizontal surface at the same location D_{hc}:

$$B_{\beta c} = B_{hc}\ cos\theta\ /cos\theta_z \tag{2.17}$$

$$D_{\beta c} = D_{hc}\ \psi_\beta \tag{2.18}$$

The formulation of coefficient ψ_β depends on how diffuse radiation is treated. The basic component of diffuse radiation is the isotropic part from all direction of the sky, sometimes called dome or sky irradiation. In addition, two anisotropic components may be considered - circumsolar brightening caused by the strong forward aerosol scattering from approximately 5° around the direct solar beam, and the horizon brightening due primarily to

multiple Rayleigh scattering and retro-scattering in clear atmospheres. The diffuse radiation model may consider only the isotropic component as by Liu and Jordan (1961), or in addition the circumsolar component, for example by Hay (1979), or eventually all three components, i.e. by Perez et al. (1990) and Muneer (1990). There are an array of diffuse radiation models which will not be repeated here. These models are applicable for both clear-sky and overcast conditions. For a complete overview of them, the author suggests the article of Evseev and Kudish (2009). Here the Liu-Jordan model and the Muneer model, which will be used in the next section are given briefly.

1. Liu-Jordan model (1961)

$$\psi_\beta = cos^2(\beta/2) = (1 + cos\beta)/2 \tag{2.19}$$

2. Muneer model (1990)

$$\psi_\beta = T_M(1 - F_M) + F_M\ r_b \tag{2.20}$$

$$T_M = cos^2(\beta/2) + U\ \left[sin\beta - \beta\ \cos\beta - \pi\ sin^2(\beta/2)\right] \tag{2.21}$$

$$U = 0.00263 - 0.712F_m - 0.688F_m^2 \tag{2.22}$$

$$r_b = max\left[0, (cos\theta/cos\theta_z)\right] \tag{2.23}$$

$$F_m = K_{hay} \qquad \text{for sunlit surface and non-overcast sky} \tag{2.24}$$

$$F_m = 0 \qquad \text{for surfaces in shadow} \tag{2.25}$$

$$K_{hay} = B_{hc}/H_{0h} \tag{2.26}$$

Here, β is the slope of the incline surface; K_{hay} is the Hay's sky-clarity index (Hay, 1979); denoting the proportion of beam irradiance and extraterrestrial solar irradiance on horizontal surface; T_M is the Muneer's tilt factor; F_m is a composite clearness function; r_b and U are some auxiliary variables.

In complex terrain, the topography will exert a major influence on the spatial solar radiation, especially under clear-sky condition where the direct radiation dominates. In Section 2.4 two GIS-based clear-sky radiation models - *r.sun* and Solar Analyst, will be compared to check the resolution effect and the shading effect under clear sky conditions.

2.3.3 Cloud Accounting for Cloudy Sky

Cloud is the most critical factor for calculating the actual solar radiation. It is also the most uncertain factor in radiation modeling, due to its temporal and 3D spatial variability. Actual radiation under overcast-sky are usually processed step by step: first obtaining the overcast global radiation on horizontal surface G_{hb} by modeling or observation, then the estimation of direct and diffuse radiation proportion, finally the direct and diffuse solar radiation on the inclined surface, $B_{\beta b}$ and $D_{\beta b}$, will be estimated based on their corresponding horizontal values and summed together to get the global radiation on inclined surface $G_{\beta b}$. From now on unless it is explicitly specified, global radiation means under overcast condition.

Overcast Global Radiation on Horizontal Surface

Detailed physical modeling of cloud field for radiation analysis is beyond the objective of this work, or even beyond the demand of hydrological study. Cloud effects are usually quantified by a parameter called clear-sky index K_c (Kasten and Czeplak, 1980), which is the ratio of actual global radiation on inclined surface to the potential global radiation on horizontal surface under clear sky condition. K_c^b and K_c^d are the respective diffuse and beam components of the clear-sky index. It has to be distinguished from other similar parameters: (1) clearness index K_t, which is the ratio of global radiation to extraterrestrial radiation on horizontal surface, (2) the normal direct transmittance index K_n, which is the ratio of direct normal radiance at the surface to the extraterrestrial direct normal radiation, and (3) the Hay's sky-clarity index K_{hay} mentioned above.

$$K_c = G_{hb}/G_{hc} \tag{2.27}$$

$$K_c^b = B_{hb}/B_{hc} \tag{2.28}$$

$$K_c^d = D_{hb}/D_{hc} \tag{2.29}$$

$$K_t = G_{hb}/H_0 \tag{2.30}$$

$$K_n = \dot{B}_b/\dot{H}_0 \tag{2.31}$$

The clear-sky index can be interpreted as the cloud transmittance, and it can be obtained through, as its definition suggests, the observation of G_{hb}. When no radiation observation is available, K_c is expressed as empirical functions of one of the following parameters: (1) the sunshine duration, (2) the cloudiness index, (3) the cloud index, or (4) some combination of meteorological parameters, i.e. precipitation, temperature, and humidity, etc.

The Sunshine Duration Method

Angström-Prescott equation (Angström, 1924) has suggested that the monthly average daily global radiation on a horizontal surface can be estimated through the sunshine duration as following:

$$G_{hb}/G_{hc} = K_c = a_{ap} + b_{ap}\ n_d/N_{dh} \tag{2.32}$$

Although the original form is proposed for evaluation long-term average daily global radiation, it is proved to be hold for daily radiation as well. There are many nonlinear version of Angström-Prescott equation which will not be listed here.

The Cloudiness Index Method

Cloudness index C_k is the spatial cloud cover in okta. It does not consider the cloud type or thickness. Kasten (1983) proposed the following relationship between cloud cover and clear-sky index:

$$K_c = 1 - (a_k\ (\frac{C_k}{8}))^{b_k} \tag{2.33}$$

The Meteorological Method

There are many attempts trying to relate the clear-sky index to individual meteorological parameters such as temperature T (Paulescu et al., 2006), humidity HU (Yang and Koike, 2002), or precipitation P or the combination of them (Hunt et al., 1998; Liu and Scott, 2001). Some researches relate, instead of the clear-sky index, the clearness index, i.e. the ratio of global radiation to extraterrestrial radiation, to meteorological parameters (Bristow and Campbell, 1984; Hargreaves et al., 1985; Allen, 1997). There are so many of such empirical relations, and all of them are very site-specific, therefore these methods will be not discussed in more details in this work.

$$K_c = f(T, HU, P, ...) \tag{2.34}$$

The Cloud Index Method

Cloud index n_c is defined specifically for each pixel based on albedo data derived from the satellite VIS (visible spectrum range from 0.5 to 0.9 μm) band images, i.e. Meteosat, and K_c is a function of n_c (Cano et al., 1986; Rigollier et al., 2004).

$$n_c = (\rho_o - \rho_g)/(\rho_c - \rho_g) \tag{2.35}$$

$$K_c = f(n_c) \tag{2.36}$$

with ρ_o : the apparent albedo observed by the satellite sensor
ρ_g : the apparent albedo of the ground under clear skies
ρ_c : the apparent albedo of the heaviest clouds

Note albedo increases with the cloud cover, which is bright thus has higher reflection. ρ_g and ρ_c are the minimum and maximum that selected from time series of satellite images at each pixel. This is the method that adopted in the Heliosat-2 method (Rigollier et al., 2004). Actually with the development of meteorological satellites, an alternative of cloud parameterization does not belong to the clearness index family called cloud optical depth (COD) has emerged (Mueller et al., 2004), but is still subjected to improvement.

Once the clear-sky index is known, the overcast global radiation on horizontal surface G_{hb} can be obtained by Eq.2.27, given that G_{hc} is available from observation or model estimation. Then with Eq.2.30, the clearness index K_t can be obtained for further calculation. To be mentioned, for some methods the calculation order of clearness index K_t and overcast global radiation on horizontal surface is inversed - first K_t is directly regressed with sunshine duration n_d (Prescott, 1940; Bahel et al., 1987) or meteorological parameters, such as temperature (Bristow and Campbell, 1984; Allen, 1997), then based on K_t, G_{hb} is calculated. The latter method is supposed to be rougher than the former one, because no physical processes are explicitly considered.

Partition of Direct and Diffuse Radiation on Horizontal Surface

The diffuse and direct radiation on inclined surface under cloud condition are derived from their horizontal counterparts. So at the first step, the beam and diffuse radiation component has to be obtained for the horizontal surface under cloudy conditions. They are usually

estimated by statistical regression of historical observed data, which relate either the direct radiation fraction, usually called direct radiation transmittance K_b (see Eq.2.37), or the diffuse radiation fraction K_d (see Eq.2.38) to the clearness index, the surface albedo, the sun elevation (or say relative air mass), and some other parameters, such as dew point temperature. If the reflected radiation is neglected, K_b and K_d sum to unit, i.e. Eq.2.39 holds.

$$K_b = B_{hb}/G_{hb} \tag{2.37}$$

$$K_d = D_{hb}/G_{hb} \tag{2.38}$$

$$K_b + K_d = 1 \tag{2.39}$$

Direct Radiation Transmittance K_b

The DISC model of Maxwell (1987) first proposed the expression of direct radiation transmittance (normal to the incident surface) as the function of clearness index and relative air mass using regression analysis, but with some physical considerations. Perez et al. (1992) further developed the model into the Drint model, which considers more parameters, such as precipitable water. DirIndex model (Perez et al., 2002) is a further update of Drint.

$$K_b = f(K_t, n_d, ...) \tag{2.40}$$

Diffuse Radiation Fraction K_d

Diffuse Radiation Fraction is a more popular approach in application, and also has longer history. It is expressed as a polynomial function of clearness index (Liu and Jordan, 1961; Ruth and Chant, 1976) or the sun-shine duration (Iqbal, 1983). Logistic functions (Boland et al., 2001) and functions with multiple predictors (Ridley et al., 2010) have also been developed to include more parameters, such as temperature, humidity, turbidity, etc. as a correction of the clearness index or the sun-shine duration. Despite of the functional form, all these equations are mainly regression analysis based on observed data, even though in some cases physical processes may be incorporated. Comparative studies on diffuse radiation modeling can be found in Torres et al. (2010).

$$K_d = f(K_t, n_d, ...) \tag{2.41}$$

Global Radiation on Inclined Surface

The direct and diffuse radiation on a tilted surface can be obtained through the similar procedure of the clear-sky conditions. The beam radiation model in Eq.2.17 and the diffuse radiation model in Eq.2.18 derived for clear sky also hold for cloud conditions. For application, just the subscript c in the two equations need to be replaced with b.

To give a better overview of the global solar radiation modeling, we summarize the modeling steps and options in a pseudo flow chart (see Fig.2.2). This monograph is aiming to provide an introduction and overview of solar radiation modeling, therefore it is impossible

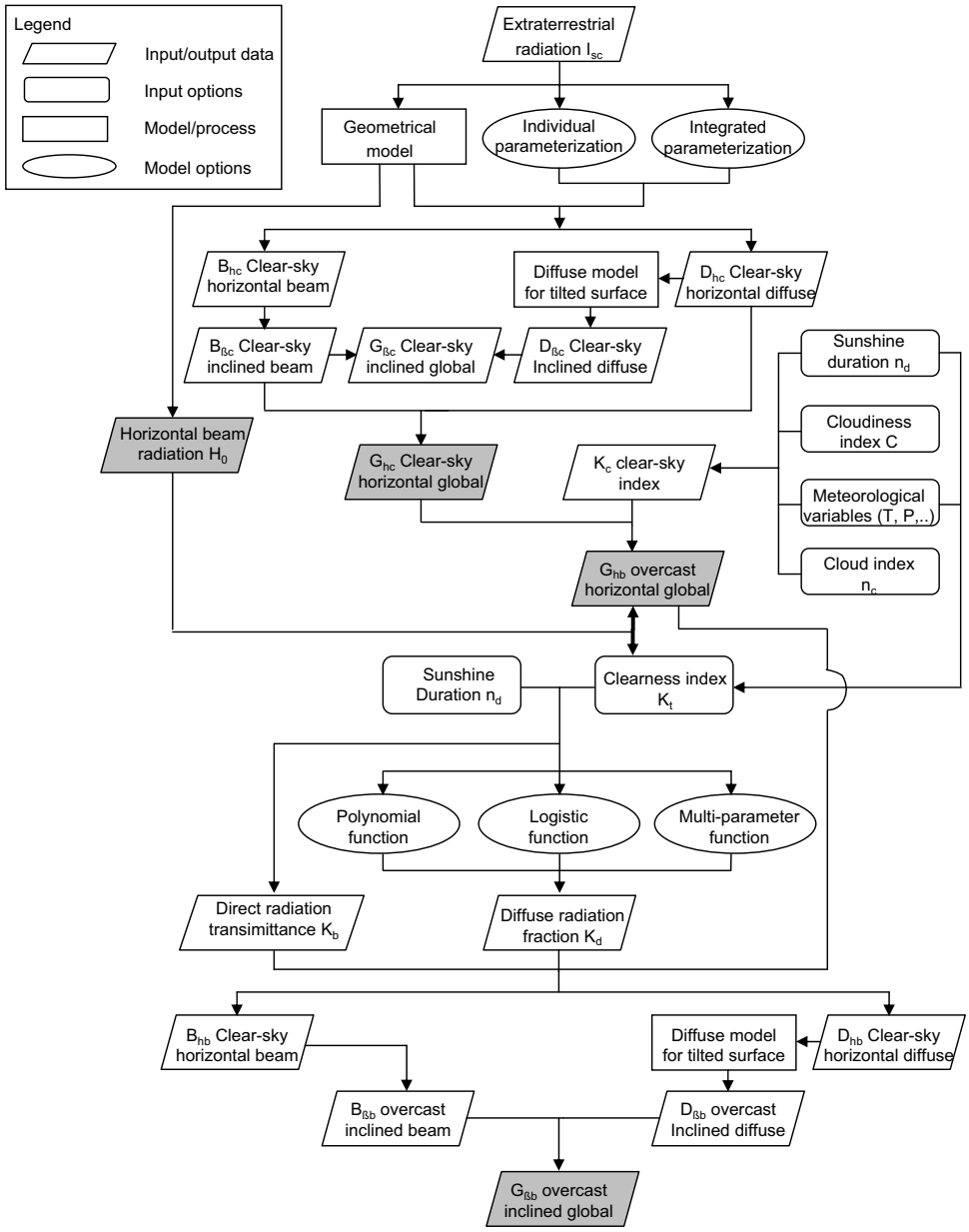

Figure 2.2: Scheme of Global Solar Radiation Modeling

to cover every individual model used in the research community, but just the main steps and alternatives. Models generally comprise of the following steps: horizontal extraterrestrial radiation $H_0 \rightarrow$ clear-sky global radiation on horizontal surface $G_{hc} \rightarrow$ overcast global radiation on horizontal surface $G_{hb} \rightarrow$ overcast global radiation on tilted surface $G_{\beta b}$, and for each step, different alternatives discussed in the previous sections can be selected depending on the data availability.

2.4 Comparison of Selected Models

There are many comparative studies of different modeling approaches listed in Section 2.3 (Evseev and Kudish, 2009; Muneer and Gul, 2000; Wu et al., 2007; Iziomon and Mayer, 2002; Ineichen, 2006; Torres et al., 2010; Trnka et al., 2005), as well as GIS solar radiation modeling software packages (Ruiz-Arias et al., 2009), the readers can refer to the listed literatures for details. This work is specifically focusing on the spatial modeling of solar radiation in complex terrain with least data demand for hydrological application, and how it is influenced by topography. At catchment scale, the cloudy conditions can be assumed to be uniform, but still the topographic modulation render the interpolation methods usually unsuccessful in such region (Batlles et al., 2008). GIS-based models calibrated with station data have been widely applied to model the spatial solar radiation (Batlles et al., 2008; Mckenney, 1999; Ruiz-Arias et al., 2009; Wang et al., 2006; Martínez-Durbán et al., 2009), but these methods always require certain station data, such as observed global radiation, or at least, sunshine duration for cloud parameterization and derivation of diffuse fraction, which limits the transferability of these models in catchment without observations. Cloud parameterization using remote sensing data is an ideal substitute of ground-based data, and provide a solution to this problem. Solar radiation model based on MODIS, GEOS, Meteosat data have shown very promising performance in some past studies (Dubayah and Loechel, 1997; Hammer, 2003; Liang et al., 2006).

In this work one GIS-based, physically parameterized, remote-sensing oriented model Heliosat-2 (Rigollier et al., 2004) and the regressional model based on sunshine duration, Angström-Prescott equation, are selected. Both are representative models of its type. Except the cloud parameterization, other modeling procedures of Heliosat-2 are identical with the *r.sun* (Hofierka and Suri, 2002). At the first step the geometrical modeling of *r.sun* will checked against the Solar Analyst and observations on horizontal surface under clear-sky conditions. The performance of *r.sun* on inclined surface under clear-sky conditions is validated by comparing with Solar Analyst. Then the scale sensitivity of *r.sun* will be tested with $30\,\mathrm{m}$ to $500\,\mathrm{m}$ DEM resolutions. After the clear-sky test, the performance control of the Heliosat-2 and Angström-Prescott model under cloudy conditions will be conducted based on global and diffuse radiation measured on horizontal surface at stations. Because solar radiation observation data for this study are from horizontally mounted instruments, a more advanced model validation on inclined surface under cloudy conditions is not possible. Finally the regional mapping, or in other words, topographic downscaling of solar radiation using two methods will be performed

2.4.1 Test Area

The solar radiation stations in German federal state Baden-Württemberg (see Fig.2.3) are used to test the Heliosat-2 and Angström-Prescott model. There are 3 solar radiation stations within the state - Mannheim, Stuttgart, Freiburg, which provide daily sunshine duration, global and diffuse solar radiation data from 2002 to 2007. For Stuttgart station global radiation data from year 1990 to 1999 is also available. A small catchment within the state

called Talhausen, close to Stuttgart city is used to test the *r.sun* module within the Heliosat-2 model. The Talhausen catchment is around $192\,\mathrm{km}^2$, with elevation varying from $216\,\mathrm{m}$ to $530\,\mathrm{m}$ for a $30\,\mathrm{m}$ DEM. The south part of the catchment is a mountainous area with steep valleys, while in the north it is relatively flat, which meets the requirement of this study, namely a complex terrain. Four points with representative topographic features, $P1{\sim}P4$ are marked for detailed investigation. The selected points are around 10 to 15 kilometers away from the Stuttgart solar station, which is close enough to make a parameter transfer.

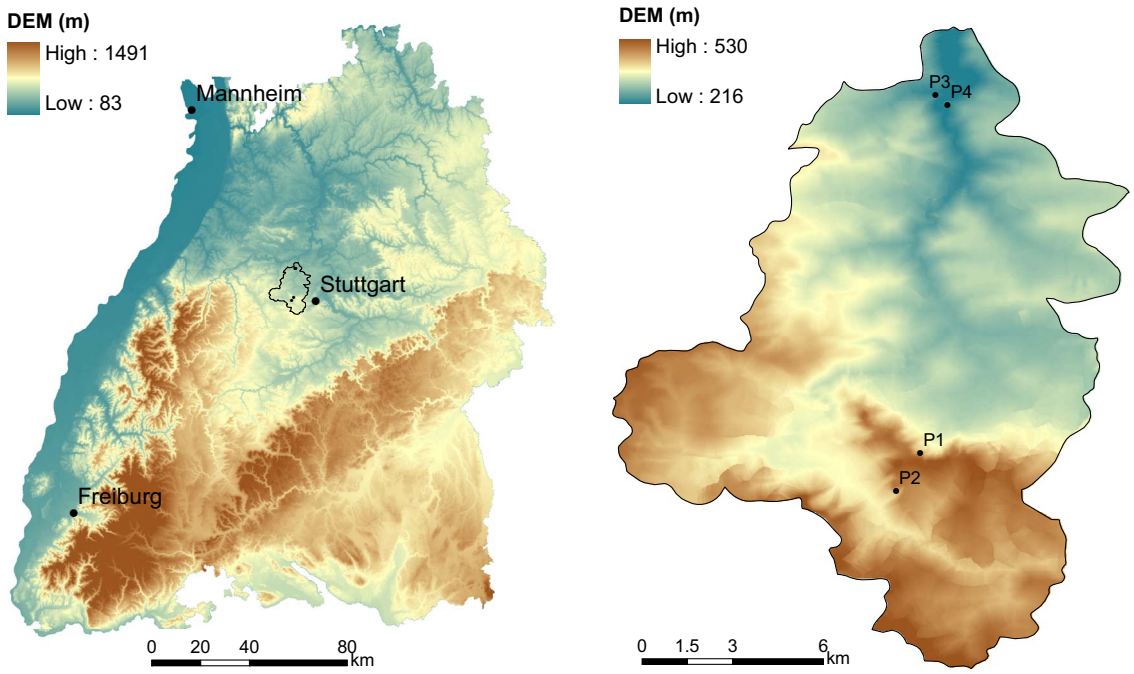

Figure 2.3: Study area of solar radiation (The left figure shows the location of the Talhausen catchment and the meteorological stations, and the right figure shows the DEM of the Talhausen and the selected studying points.)

2.4.2 Test of Geometric Modeling

As discussed in Section 2.3.1, *r.sun* applies the solar-based shading algorithm, and it is conceptually simpler than the hemispheric viewshed algorithm used in Solar Analyst (SA), which is assumed to be more advanced and computationally efficient. Here the performance of the two algorithms are compared for time series of point solar radiation and spatial radiation of a given day under clear sky conditions. The original *r.sun* program in GRASS can only calculate spatial daily irradiation or instantaneous irradiance. For more flexible calculations, such as time series of a given point and spatial time series, *r.sun* is adapted to be a stand-alone program.

Comparison of Point Time Series Radiation

The observed data at Stuttgart station and the following calculation at P1 have been obtained for comparison (see. Fig.2.4):

1. Observed maximum daily global radiation at station Stuttgart for all data available years (blue line with circles): The station measures global radiation at horizontal surface without any shading. The maximum radiation, i.e. the most clear case of a given day over 18 years, are taken to approximate the clear-sky radiation. Although the station is located around 10 km away, it can be taken as the clear-sky approximation for comparing with the calculation, because the clear-sky global radiation on a horizontal surface depends only on the latitude and the atmosphere condition, the difference within the catchment is assumed to negligible;
2. SA simulated clear-sky radiation on horizontal surface with an imaginary flat DEM (green line): both the calculation point and the surrounding DEM are set horizontal to be compared with the observed clear-sky radiation. In SA, the shading effect of surrounding terrains is explicitly included in the program. Simulation without shading is done by setting the terrain flat. The SA clear-sky parameters are set as following: transmissivity=0.75, diffuse portion=0.2 by trial-and-error to maximumly approach the clear-day approximation;
3. SA simulated clear-sky radiation on horizontal surface with actual DEM (orange line): the result shows the shading effects of surrounding terrain addressed by SA;
4. SA simulated clear-sky radiation on inclined surface with actual DEM (purple line): the result shows the shading effects of the surrounding terrain and the inclined surface itself;
5. *r.sun* simulated clear-sky radiation on horizontal surface without shading effect (yellow line): the Linke Turbidity for clear sky is set to 3.0 taken from literature (Kasten and Czeplak, 1980), constant throughout the whole year;
6. *r.sun* simulated clear-sky radiation on horizontal surface with shading effect (brownish line);
7. *r.sun* simulated clear-sky radiation on inclined surface without shading effect (blue line);
8. *r.sun* simulated clear-sky radiation on inclined surface with shading effect (red line);

From the figures we can see that, although for some days no complete clear condition has happened over 18 years, the profile of the maximum daily radiation curve resembles the clear-sky condition very well. SA simulated clear sky radiation on horizontal surface has difficulties to ensemble the observed curve. In comparison, the *r.sun* model with the selected the Linke Turbidity value applied to horizontal surface without shading, has in general given a very good estimation to the clear-day approximation. For 2 or 3 days in July and September, the observed clear-sky radiation is slightly above the simulated value, which may come from the extraordinary sky clearness or some measurement error. When considering surrounding terrain, both SA and *r.sun* gives much lower radiation for winter time,

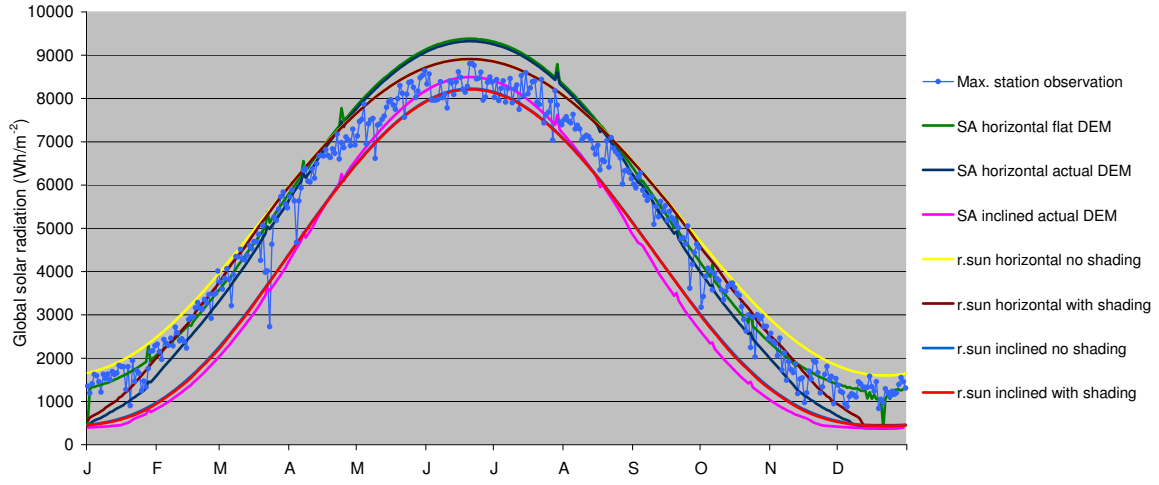

Figure 2.4: Observed and simulated global solar radiation at P1

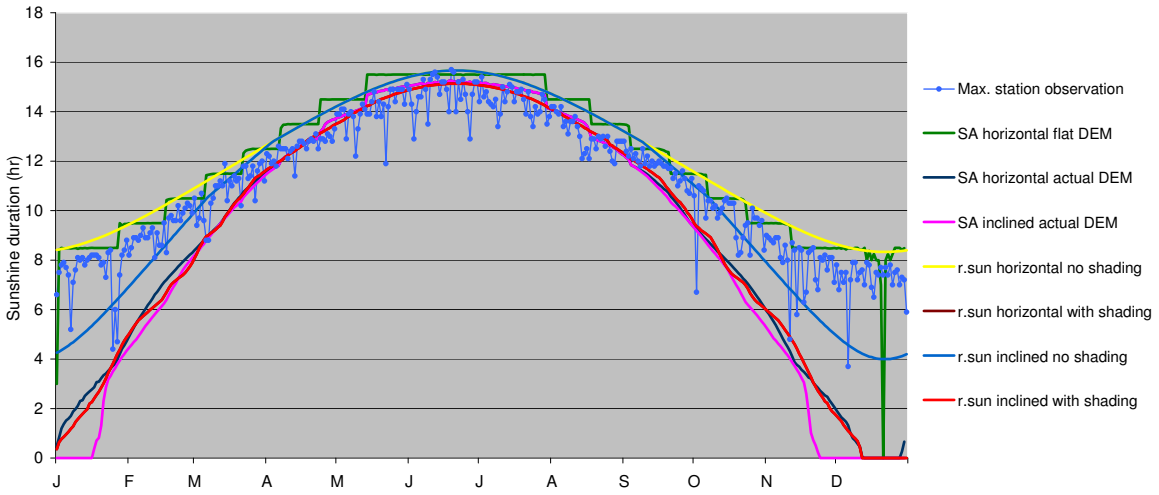

Figure 2.5: Observed and simulated sunshine duration at P1

with SA gives larger difference, which may implies the significance of spatial radiation for snowmelt. Because P1 lies on a backlit slope, the shading is happening in winter time when sun altitude is low. When the surface is inclined, it receives much less radiation than the horizontal surface, which is modeled correctly by both models. One interesting phenomenon is that, for the backlit point P1, the shading of surrounding terrain does cause a big difference in sunshine duration, but little difference in global radiation. The reason is that shading happens at sunrise or sunset time, but at this time because of the surface inclination, the solar incidence angle is very small, therefore the reduced beam radiation is almost compensated by the increased the diffuse radiation due to horizontal brightening. For P1, the sunshine duration for horizontal surface and inclined surface calculated by *r.sun*, under the presence of shading is identical, which means shading is caused by the neighboring terrain, not by the inclination of the surface itself. The corresponding results of SA shows slightly different

illumination time for the horizontal and inclined surface in January and December, which may arise from the accounting of detailed micro-topography of SA.

In general, the results of the two models are consistent with each other, and validation with observed data has shown that both models, especially r.sun, perform reasonably well on horizontal surface under clear-sky conditions. The performance of SA is not as good as *r.sun*. There is also a persistent problem for parameter selection concerning the spatial (sky size) and temporal resolution (discretion interval). The zig-zag of curve is caused by the time-step setting. The authors have tried many combination of parameter sets, still the problem is not solved. SA is specially error prone for the equinox and solstice day, which can be witnessed by the abnormal value on Dec. 22 of the green curves. With simple parameterization *r.sun* gives better results which is more close to the observation. The agreement of the two models on inclined surface can serve as a theoretical validation of the models on inclined surface, because validation with observed data is not possible.

Comparison of Spatial Radiation

The spatial comparison of *r.sun* is conducted for an arbitrarily selected day (as an example day 30 is selected, see Fig.2.6 and 2.7) and the yearly average daily radiation (see Fig.2.8 and 2.9). Both the scatter plot and the differential patterns show that there is a high correlation between radiation and sunshine duration simulated by the two models, except very few outliers. *r.sun* gives in general higher evaluation than SA for global radiation, mainly in the valleys. The reason may lie in the fact that SA considers the micro-topography more in details. For extremely low sunshine duration values, i.e. points that are mostly in shadow, *r.sun* gives lower values than SA. Nevertheless, the strong linear relationship between the two model results implies that by adjusting parameters properly, a good match of the two models are possible. For the yearly average daily radiation, the difference smooths out, and results of the two models become more close (see Fig.2.8).

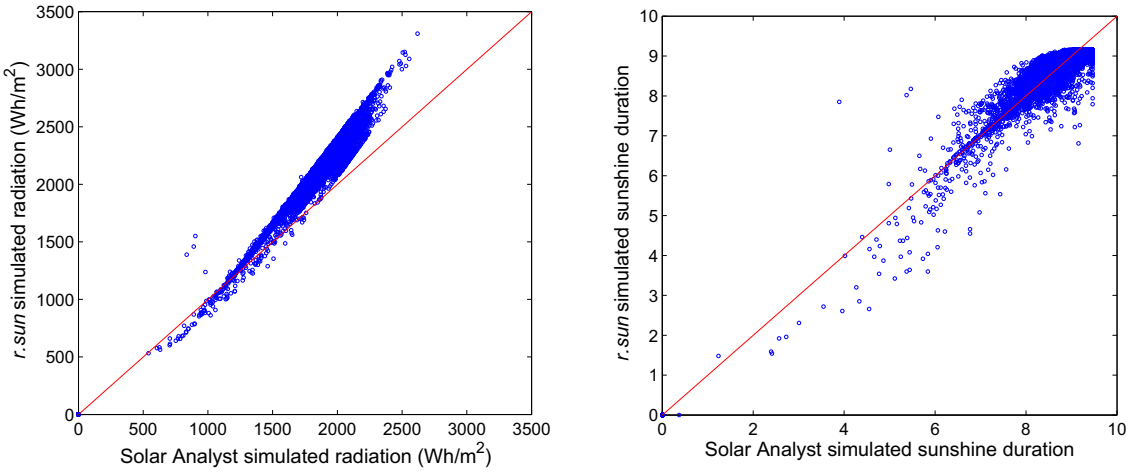

Figure 2.6: Scatter plot of spatial radiation and sunshine duration of day 30

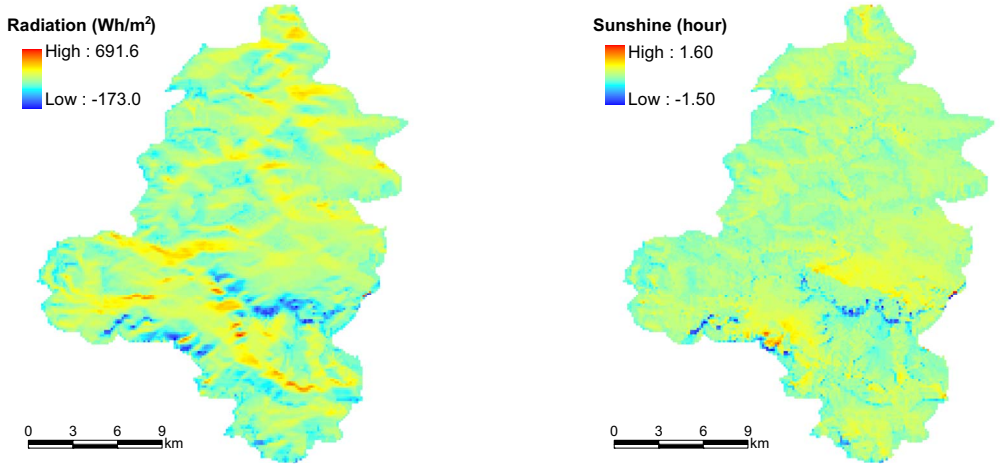

Figure 2.7: Pattern of spatial difference on day 30

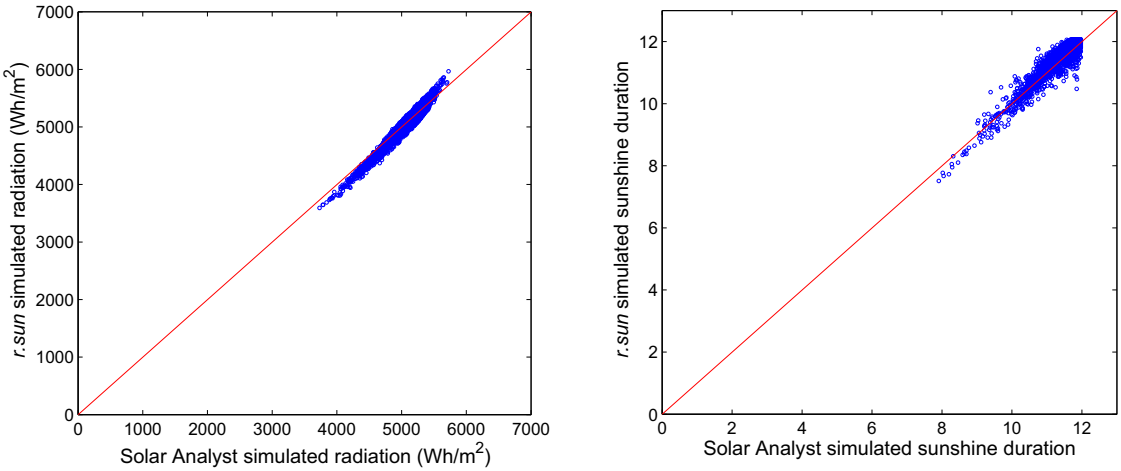

Figure 2.8: Scatter plot of spatial radiation and sunshine duration of yearly average daily

Correlation of Radiation with Topography

Statistical analysis shows there is a positive correlation of radiation with aspect, and negative ones with slope and elevation. Table 2.1 shows the mean daily correlation ρ_{topo} and associated standard deviation σ_{topo} over one year. The aspect starts at north zero, clockwise. The values ranging from 180°~360° have been mirrored to 0°~180° to get monotonic aspect values. To be mentioned in GRASS, the aspect increase counter clockwise, with east as 0 degree.

2.4.3 Test of Scale Sensitivity

In the model the calculation of radiation is based on DEM, therefore it is natural that the resolution of the DEM will affect the result of radiation by modifying the topographic pa-

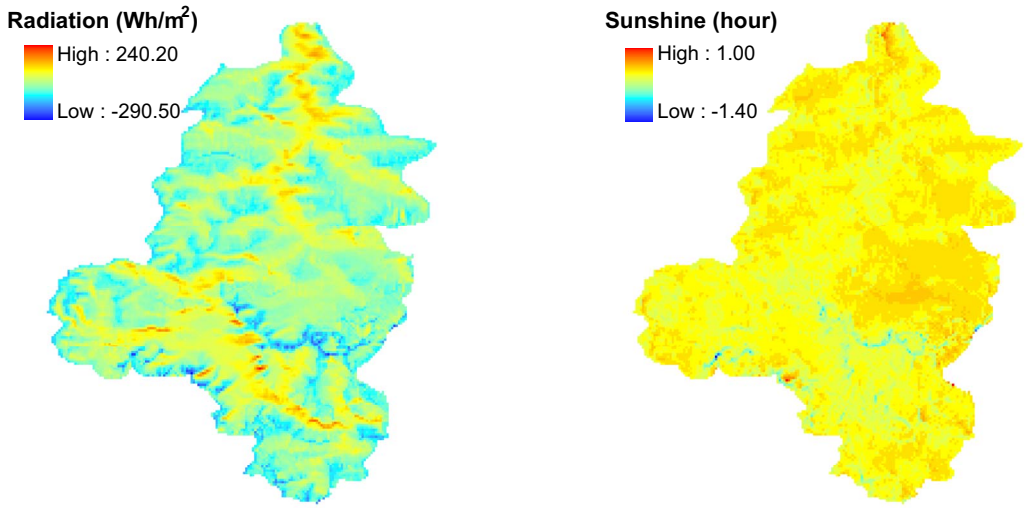

Figure 2.9: Pattern of spatial difference of yearly average daily

Table 2.1: Correlation between the terrain parameters and radiation

	aspect	slope	elevation
ρ_{topo}	0.686	-0.476	-0.111
σ_{topo}	0.117	0.079	0.070

rameters and shading conditions. In the following, the changing of shading effect and the changing spatial variability with scale will be investigated with DEM resolution varying from $30\,\mathrm{m}$, $60\,\mathrm{m}$, $100\,\mathrm{m}$, $150\,\mathrm{m}$, $300\,\mathrm{m}$.

Spatial Radiation Variance with Scale

Fig.2.10 shows the distribution of clear-sky global radiation simulated by *r.sun* at different scales. The spatial variance decrease with increasing grid size. For 30m DEM, the spatial difference can be as large as 4 times (radiation value from less than $1500\,\mathrm{Wh/m^2}$ to $6000\,\mathrm{Wh/m^2}$). But a closer look shows that the extreme low and high values are very few. If these extreme values were excluded, the radiation difference between the highest 10% areas and lowest 10% areas, depending on the resolution, is around $5{\sim}15\%$. To be alerted, there is an artifact in the curve caused by the reduced number of cells as the grid size increases - the differences between the curves are actually exaggerted.

For ecological study, the extreme difference caused by the micro-topography at finer resolution might be important, while in catchment hydrology, people rarely go into that much details. On the other hand, the micro-scale difference may be homogenized out at a larger scale. To check the loss of accuracy during the scale transition, the $30\,\mathrm{m}$ resolution radiation is aggregated into $300\,\mathrm{m}$ to compare with the direct simulation at $300\,\mathrm{m}$. Fig.2.11 shows that simulated at larger scale smooths out the spatial variability, the aggregated radiation tends

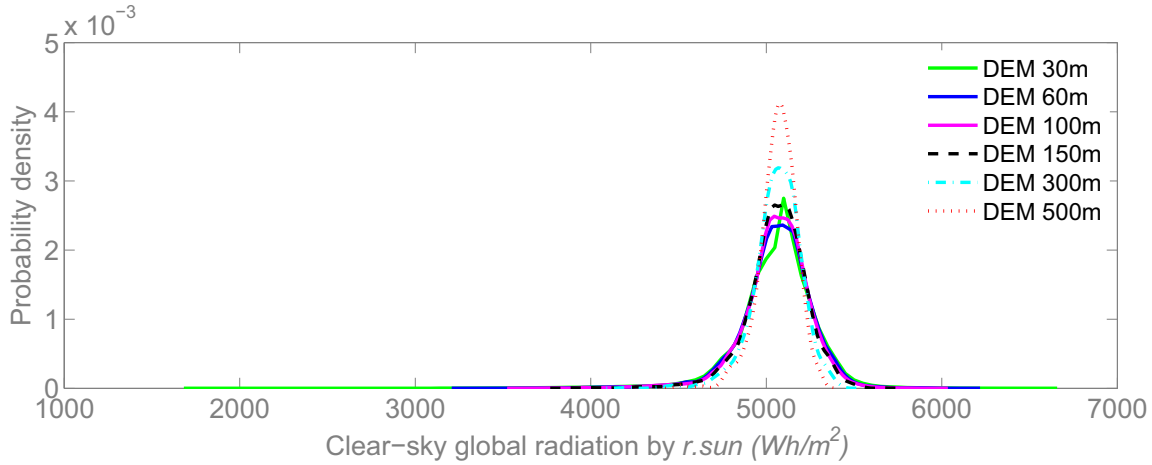

Figure 2.10: Distribution of yearly average daily clear-sky global radiation at different scales

to be lower at low radiation, and higher at high radiation. But the predominantly major points show little discrepancy. In principle, the aggregated and simulated radiation match each other well, with RMSE being $41.5\,\mathrm{Wh/m^2}$, and the correlation coefficient being 0.91. It is subjected to the user to decide whether the simulation at larger resolution is accurate enough for an specific application.

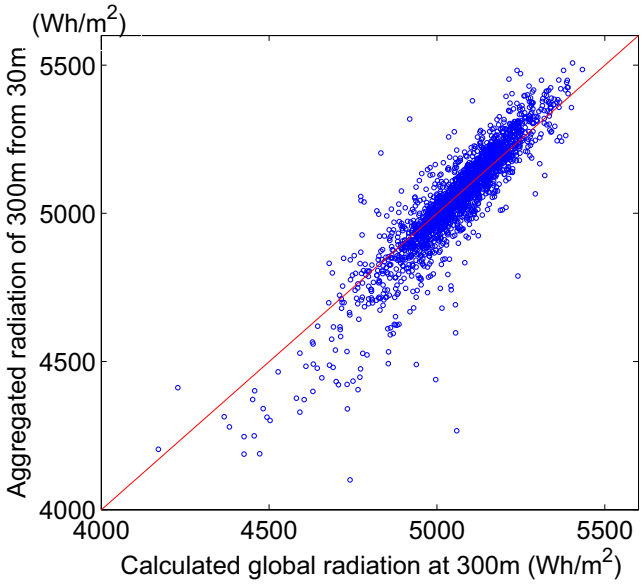

Figure 2.11: Comparison of simulated and aggregated solar radiation

Shading Effect with Scale

Shading will reduce the global radiation of one point in shadow (from G_{ns} to G_s). When the DEM grid size increases, the micro-topographic features which can be reflected at finer resolution, can not be resolved any more, which results in some information lost and thus affect the shading effect, i.e. two points with one is shaded by the other may be merged as

one point in a coarser resolution DEM. Here, the daily average radiation simulated with and without shading effect are compared for 6 DEM resolutions.

The probability density functions (PDF) of relative difference ($\frac{G_{ns}-G_s}{G_{ns}}$) of all grid points of each DEM resolution are demonstrated in Fig.2.12. It shows that, the shading effect is prevails at small resolution. At resolution of $30\,\mathrm{m}$, shading can cause a relative difference more than 50%. When the grid size is larger than $100\,\mathrm{m}$, the shading effect is below 1%, almost neglible.

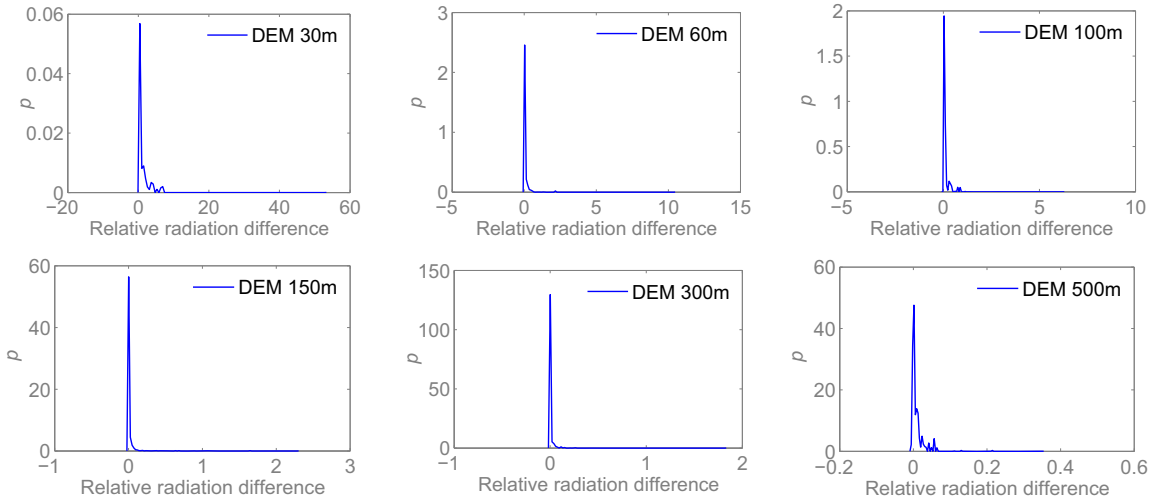

Figure 2.12: Distribution of radiation difference of simulations with and without shading at different scales (the axis in expressed in percentage)

.

Scale Effect over Time

To check the scale effect over time, two pair of points, p1 and p2 in mountain area (Fig.2.13a and 2.13b), p3 and p4 (Fig.2.13c and 2.13d) in flat area are examined without considering shading effect. The results shows that the radiation difference varies at different scale, in general at finer resolution the difference are bigger, and at higher resolution the difference are smaller. For both pairs the scale effect is much stronger in winter than in summer. The radiation difference also depends strongly on the local topographic condition, both the absolute and relative difference between P1 and P2 is much larger than the difference between P3 and P4.

2.4.4 Performance Test on Overcast Horizontal Surface

For testing the model performance on all-sky conditions, the Heliosat-2 model is validated against the station data at Stuttgart, Mannheim, and Freiburg from 2002 to 2007. The Angström-Prescott method using extraterrestrial radiation is also tested against the observations.

Heliosat-2 Method

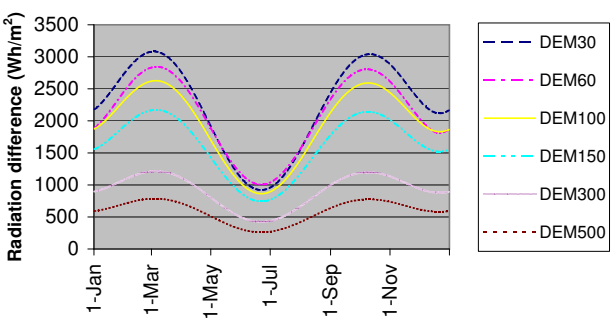

(a) Absolute radiation difference of P1 and P2

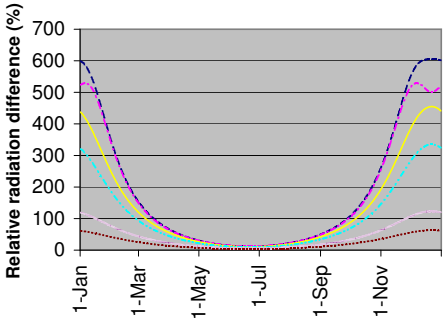

(b) Relative radiation difference of P1 and P2

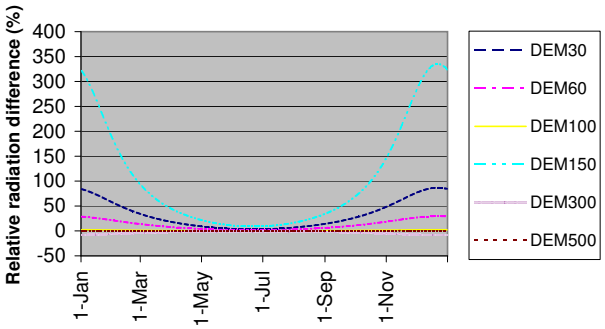

(c) Relative radiation difference of P3 and P4

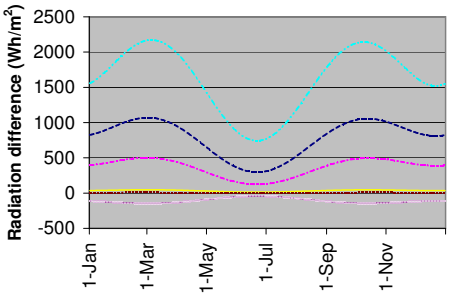

(d) Absolute radiation difference of P3 and P4

Figure 2.13: Point radiation difference at different scales over time

The Heliosat-2 method calculate the cloud index using Eq.2.35. The functional form of deriving clear-sky index K_c from the cloud index n_c (Eq.2.36) is following Rigollier et al. (2004):

$$K_c = \begin{cases} 1.2 & \text{if } n_c < -0.2 \\ 1 - n_c & \text{if } -0.2 \leq n_c < 0.8 \\ 2.0667 - 3.6667\, n_c + 1.6667\, n_c^2 & \text{if } 0.8 \leq n_c \leq 1.1 \\ 0.05 & \text{if } n_c \geq 0.05 \end{cases} \tag{2.42}$$

The overcast radiation G_{hb} is the clear-sky radiation G_{hc} scaled by the clear-sky index K_c. Fig.2.14 shows the simulated result at the three stations comparing with the observations. The correlation coefficients for all the 3 stations are above 0.96 (Stuttgart 0.964, Freiburg 0.968, Mannheim 0.968). But the scatter plots show that there is a bias in the Heliosat-2 estimated radiation, namely the estimation is in general lower than the observation. The estimated value is multiplied with one of the following coefficient to remove the bias: the slope from linear regression or the ratio of mean observed and modeled radiation. For station Stuttgart and Mannheim, the slope adjustment works better, and adjustment with the ratio of mean works better for station Freiburg.

Angström-Prescott

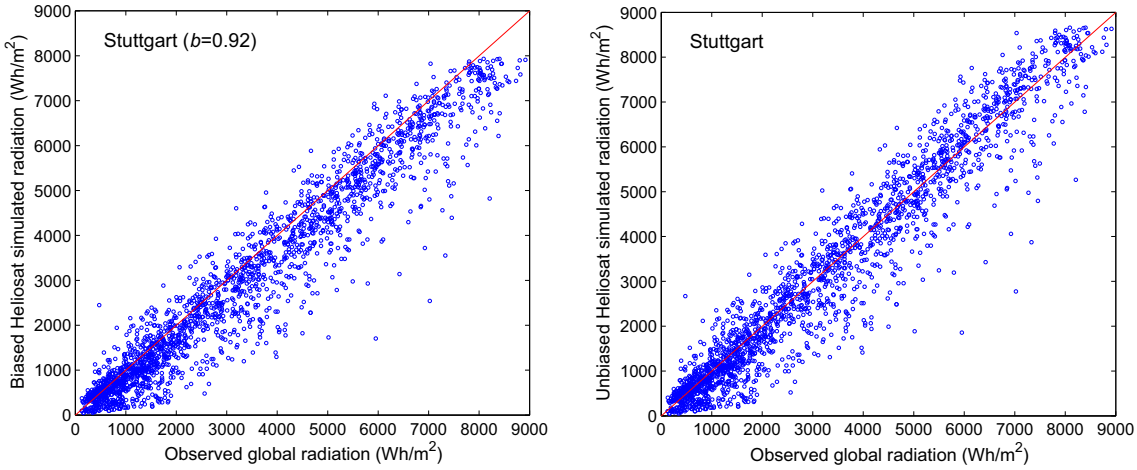

(a) Biased (b) Slope corrected

Figure 2.14: Observations and Heliosat-2 simulated global radiation on horizontal surface 2002~2007

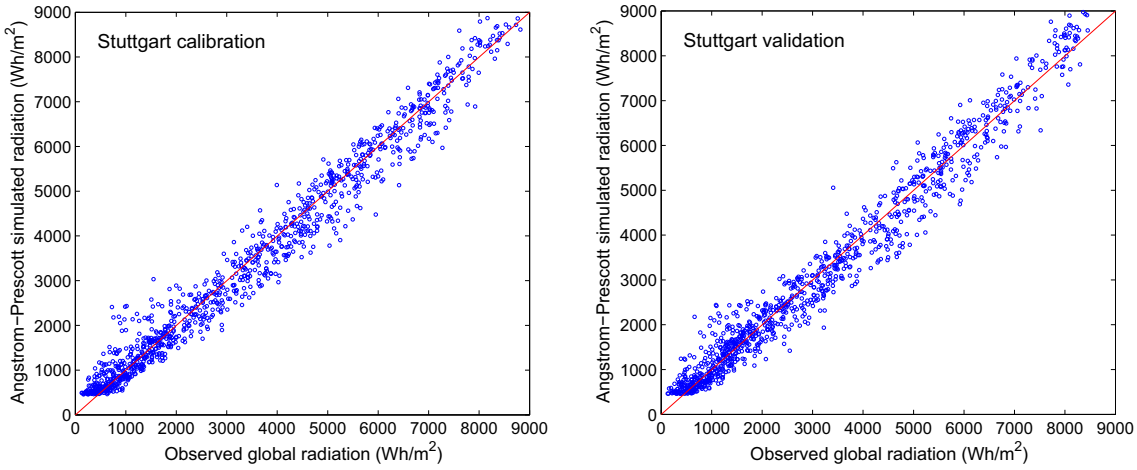

Figure 2.15: Observations and Angström-Prescott simulated global radiation on horizontal surface 2002~2007

The original Angström-Prescott equation (Eq.2.32) can be adapted to the following form using extraterrestrial radiation instead of clear-sky radiation:

$$G_{hb}/H_0 = K_t = a_{ap} + b_{ap}\, n_d/N_{dh} \tag{2.43}$$

The actual daily sunshine duration n_d is obtained from the observations, while the potential daily sunshine duration and extraterrestrial radiation on horizontal surface, N_{dh} and H_0 can be easily calculated from Eq.8.7 and Eq.8.11. To apply the Angström-Prescott equation, the parameters a_{ap} and b_{ap} have to be estimated first. The observation data are split into two time series (of equal length, with 2002~2004 for calibration and 2005~2007 for validation.

The goodness-of-fit is controlled by the Root Mean Squared Error (RMSE) and R-squared (see Table 2.2). It shows that a_{ap} increases and b_{ap} decrease with the latitude, which is consistent to the findings of Glover and McCulloch (1958), and can be regarded as a kind of climatic gradient. Because in our case, the three solar radiation stations are relatively close, the Angström-Prescott coefficients do not change much, a "General"case is applied by fusing the data of the three stations together for calibration, and using individual station for validation. The result from the empirical method and the physically-based methods both offer high quality results, and the former is even slightly better. But one should keep in mind that, the Heliosat-2 method is free of any ground observations, which offers a satisfactory solution for ungauged basins.

$$RMSE = \sqrt{\frac{1}{n}\sum_{i=1}^{i=n}(G_i^{est} - G_i^{obs})} \tag{2.44}$$

$$R^2 = 1 - \frac{\sum_{i=1}^{i=n}(G_i^{est} - G_i^{obs})}{\sum_{i=1}^{i=n}(G_i^{obs} - \overline{G^{obs}})} \tag{2.45}$$

Table 2.2: Simulation results of Heliosat-2 and Angström-Prescott on horizontal surface under all-sky conditions

	Heliosat-2			Angström-Prescott					
	biased		unbiased	calibration				validation	
	RSME	R^2	RSME	a_{ap}	b_{ap}	RSME	R^2	RSME	R^2
Stuttgart	708.58	0.930	640.56	0.214	0.572	392.92	0.972	400.13	0.969
Freiburg	581.36	0.936	581.36	0.194	0.592	416.41	0.967	422.66	0.968
Mannheim	645.47	0.937	613.29	0.201	0.561	373.19	0.973	378.85	0.973
General	645.47	0.937	613.29	0.205	0.564	400.58	0.970	400.30*	0.970*

$*$ Mean value of validation with all three stations.

Because the radiometers for routing measurements of solar radiation are usually mounted horizontally, ground sources for validation of radiation on tilted surface are very scarce. A model test for the inclined surface is not possible due to the data limitation in the study region. Therefore the capability and correctness of Heliosat-2 methods for modeling tilted surface under overcast sky condition has to be assumed.

2.4.5 Spatial Solar Radiation Mapping

Derivation of Diffuse Fraction

For hydrological application, usually spatial patterns of global radiation is desired. In this section, the spatial radiation pattern will be simulated with Heliosat-2 and an adapted Angström-Prescott method respectively. As discussed before, the calculation of radiation components on a tilted surface under overcast condition is similar to the clear-sky condition.

The simulated spatial radiation pattern by Heliosat-2 is taking as a reference to evaluate the adapted Angström-Prescott method.

For calculation of global radiation on tilted surface, the partition of direct and diffuse radiation is necessary. In order to implement a ground-observation free method for Heliosat-2, the Ruth-Chant (Ruth and Chant, 1976) approach has been applied to relate diffuse fraction to clearness index in the following form:

$$K_d = \begin{cases} K_d^c & \text{if } K_t \leq K_t^c \\ p_1\ K_t^{c2} + p_2\ K_t^c + p_3 & \text{if } K_t > K_t^c \end{cases} \tag{2.46}$$

The diffuse fraction is also evaluated as a quadratic function of relative sunshine duration:

$$K_d = p_a\ {n_{rel}}^2 + p_b\ n_{rel} + p_c \tag{2.47}$$

Table 2.3 shows the calibration and validation results of each station with the clearness index method and sunshine duration method respectively. Both functional forms are calibrated and validated with two approaches:

1. split sample approach: calibration and validation with split sample (2002~2004 for calibration, 2005~2007 for validation) for each station;
2. General methods: calibration with data from all 3 stations and validation for each station.

For each station the performance are considerable good, although the parameters varies a bit. Actually the parameter are not very sensitive, so we can use a general parameter set obtained from the data of all three stations. When being validated with each individual stations, the general parameter set gives results which is even superior than the parameters calibrated from the station itself.

Mapping Spatial Global Radiation

Once the global radiation on horizontal surface and the diffuse fraction is available, the beam and diffuse component on the tilted surface can be derived from the horizontal surface by considering the geometric modification. The spatial radiation mapping from the horizontal value can be regarded as a downscaling procedure, by which the radiation on horizontal surface can be considered as the regional value. While the calculation of beam radiation on inclined surface from horizontal radiation is unanimous, there are many different approaches for diffuse radiation modeling as discussed in Section 2.3.2. In fact, some comparative studies have shown that the results of these models do not differ much (Muneer, 1990; Evseev and Kudish, 2009). The author does not have any preference to these models. Since the Muneer model is already adopted by the *r.sun* model, which favors the more physical approach, it is applied to generate the spatial radiation with the Heliosat-2 method. The Muneer model calculates the cloud parameters at hourly interval to include the solar altitude influence and changing sky conditions throughout the day. In our calculation, instead of a hourly changing value for the clear-sky index components K_c^b and K_c^d, they are

Table 2.3: Diffuse fraction obtained from clearness index and sunshine duration

Heliosat-2									
	parameter					calibration		validation	
	K_d^c	K_t^c	p_1	p_2	p_3	RSME	R^2	RSME	R^2
Stuttgart	0.978	0.191	-0.648	-0.839	1.165	0.076	0.922	0.084	0.905
Freiburg	0.984	0.134	-1.369	-0.210	1.034	0.081	0.922	0.089	0.898
Mannheim	0.974	0.153	-1.096	-0.473	1.078	0.081	0.908	0.082	0.909
General	0.975	0.180	-0.903	-0.644	1.120	0.083	0.910		

	Heliosat-2		Angström-Prescott						
	general		parameter			calibration		validation	
	RSME	R^2	p_a	p_b	p_c	RSME	R^2	RSME	R^2
Stuttgart	0.080	0.912	0.237	-1.020	0.974	0.066	0.942	0.072	0.930
Freiburg	0.085	0.912	0.197	-1.002	0.967	0.075	0.932	0.092	0.893
Mannheim	0.082	0.906	0.203	-0.986	0.971	0.067	0.937	0.071	0.931
General			0.229	-1.011	0.972	0.074	0.927	0.072*	0.936*

$*$ Mean values of RSME and R^2 for general parameter sets applied to each station.

assumed to be constant over the day. In *r.sun* model, the modeling concept is expressed in Eq.2.48. The lower case is used to denote the instant value, i.e. irradiance. The mean value of the discretization interval is approximated by the value at the middle time of the interval.

$$\begin{aligned} G_{\beta b}(i,j) &= B_{\beta b}(i,j) + D_{\beta b}(i,j) \\ &= \int_{\omega_{sr}}^{\omega_{ss}} (b_{\beta b}(i,j) + d_{\beta b}(i,j)) d\omega \\ &= \int_{\omega_{sr}}^{\omega_{ss}} (b_{hb}(i,j)\ cos\theta / cos\theta_z + d_{hb}(i,j)\ \psi_\beta) d\omega \\ &= \int_{\omega_{sr}}^{\omega_{ss}} (b_{hc}(i,j)\ K_c^b\ cos\theta / cos\theta_z + d_{hc}(i,j)\ K_c^d\ \psi_\beta) d\omega \end{aligned} \tag{2.48}$$

The geo-latitude and sky condition can be assumed to be constant within the catchment, therefore,

$$\begin{aligned} b_{hc}(i,j) &= b_{hc} \\ d_{hc}(i,j) &= d_{hc} \end{aligned} \quad \forall i,j \tag{2.49}$$

Eventually, Eq.2.48 can be simplified in following form,

$$G_{\beta b}(i,j) = \int_{\omega_{sr}}^{\omega_{ss}} (b_{hc}\ K_c^b\ cos\theta / cos\theta_z + d_{hc}\ K_c^d\ \psi_\beta) d\omega \tag{2.50}$$

The Liu-Jordan model is chosen to be applied in accompany with Angström-Prescott method, because of its simplicity. The Liu-Jordan method estimates only isotropic diffuse

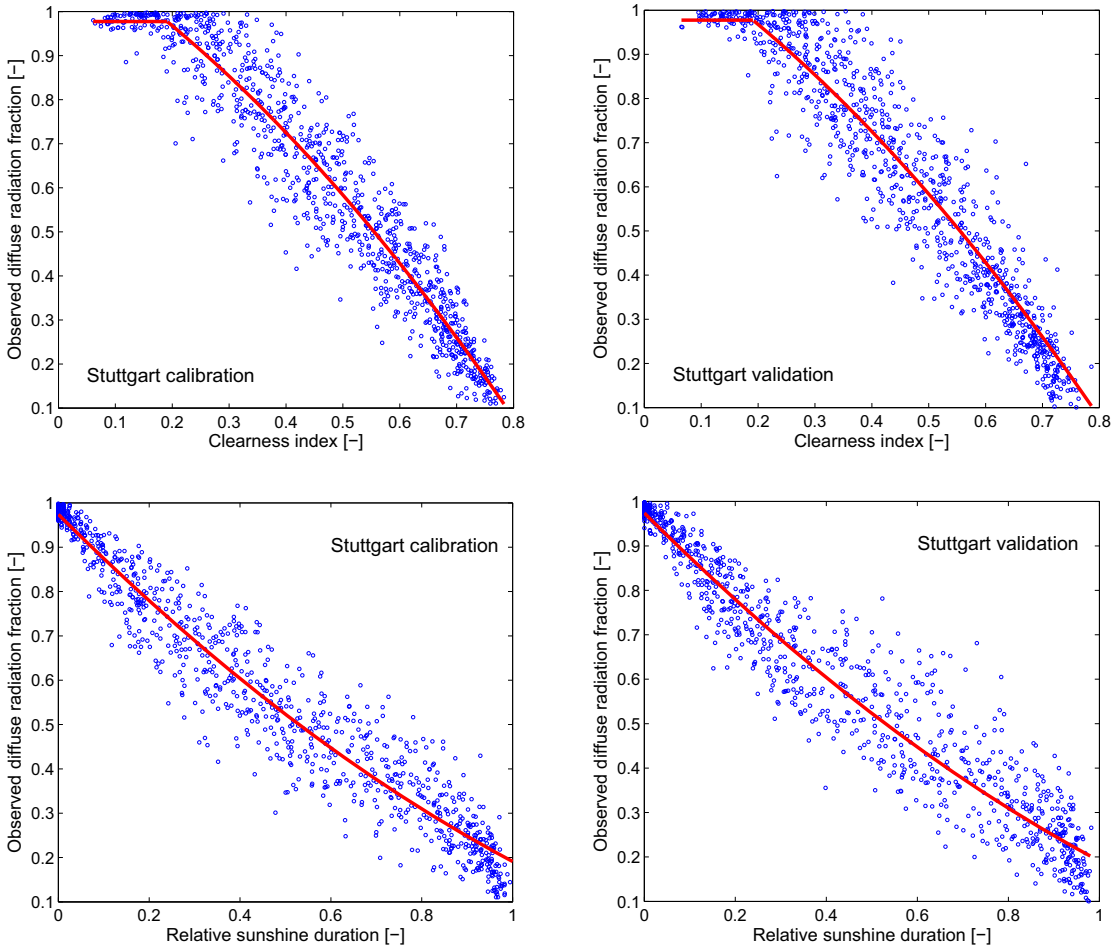

Figure 2.16: Diffuse fraction fitted as a function of clearness index and relative sunshine duration for 2002~2007

component by geometric calculation of the sky exposure of the tilted surface, which is a constant over time. As demonstrated in Section 2.4.3, the shadow effect is anyhow negligible from certain resolution. For application with the empirical Angström-Prescott methods, the author considers this approach to be proper and consistent. The hourly value is integrated analytically to get daily value by assuming constant diffuse fraction throughout the day. Following similar procedure for extraterrestrial radiation in the Appendix 8.2, Eq.2.51 can be obtained.

$$\begin{aligned} G_{\beta b}(i,j) &= \int_{\omega_{sr}}^{\omega_{ss}} (b_{hb}(i,j)\ cos\theta / cos\theta_z + d_{hb}(i,j)\ \psi_\beta) d\omega \\ &= B_{hb} \int_{\omega_{sr}}^{\omega_{ss}} \frac{\cos\theta_z}{\cos\theta} d\omega + D_{hb}(i,j)\ \psi_\beta \end{aligned} \tag{2.51}$$

If the clear-day global radiation on horizontal surface is calculated using Angström-Prescott method, the adapted Angström-Prescott approach for spatial solar radiation mapping is

obtained as following:

$$\begin{aligned} G_{\beta b}(i,j) &= G_{hb}(1-K_d)\,\xi + G_{hb}K_d\,\psi_\beta \\ &= H_0\,(a_{ap}+b\,n_{rel})(1-K_d)\,\xi + H_0\,(a_{ap}+b\,n_{rel})K_d\,\psi_\beta \end{aligned} \tag{2.52}$$

Fig.2.17 shows the comparison of the mapping results of year 2002 with the two methods. The left figure shows the R-square and RMSE of the two methods over the year. The R-square (denoted as circle) is considerably high, most of time over 0.80 except for a short period around month in summer time, even in summer it never goes below 0.60, and the RMSE (denoted as square) is also relatively small, which demonstrates the two methods agree well with each other. The RSEM mainly originate from the deviation of the regional radiation calculated by the two methods. The right figure illustrates the relative variability of the spatial radiation, which is denoted by $\frac{P_{90}-P_{10}}{\mu_s}$, P_{90} and P_{10} is the 90 and 10 percentiles of the spatial values in a specific radiation map, and μ_s is the mean radiation of that map. We do not use the standard deviation, because the distribution of spatial radiation is depending on the topography, and not necessarily normally distributed. It shows that the spatial variability is in general larger in winter, which implies the importance of the spatial effects on seasonal hydrological processes occurring in winter, such as snowmelt.

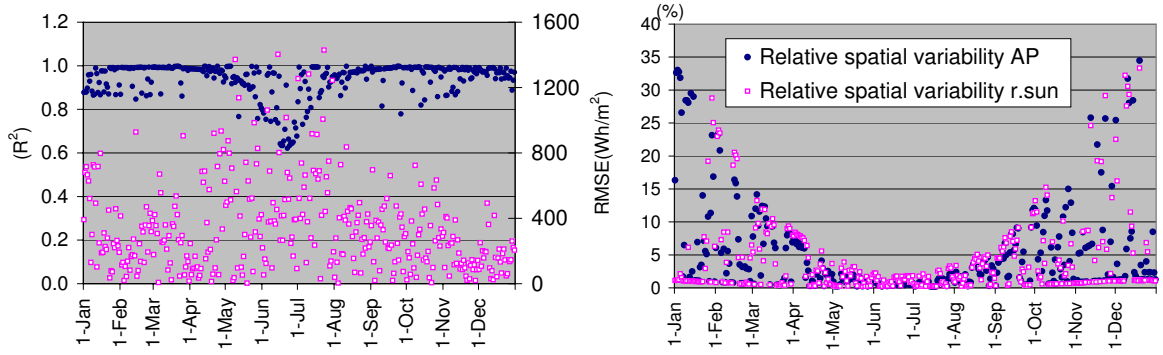

Figure 2.17: Comparing the spatial mapping results of *r.sun* and Angström-Prescott (In the left figure, R-square is denoted as circle and RMSE is denoted as square.)

2.5 Conclusion, Discussion and Outlook

2.5.1 Conclusion

The ultimate goal of this chapter, as stated in the very beginning, is to seek for proper all-sky spatial solar radiation mapping or downscaling methods, which are suitable for hydrological applications. The methods should be on one hand accurate, i.e. be able to account for the spatial topographic effects, and on the other hand, user-friendly, i.e. less data-demanding and computationally efficient.

First an overview of the radiation modeling theory and methods is provided, and the steps for deriving all-sky radiation on an arbitrary oriented surface are summarized. Among all the options, the emphasis is put on the on the remote-sensing oriented Heliosat-2 method, which is implemented considering the detailed spatial topographic features derived from GIS. Since the accuracy of the final results, i.e. all-sky spatial radiation on inclined surface can not be tested due to the problem of data availability, the model is tested in three steps: in the first step the geometric modeling of the model is tested by comparing with Solar Analyst and observed data. Because no observed data on inclined surface is available to test the model performance for inclined surface, the inclined surface modeling can only be verified theoretically and rationally by comparing the model results with each other; in the second step scale sensitivity of the model is tested; in the third step, the models are validated for horizontal surface under cloudy conditions at three weather stations in South Germany.

After the three-step validation, the model is applied to inclined surface under overcast conditions, because the principle of modeling inclined surface under clear and overcast conditions are identical. The Angström-Prescott method based on sunshine duration observation has also been implemented. The comparison of the two methods shows very good agreement. The results show that, both potential and actual radiation demonstrate considerable spatial variability over the year circle, predominantly in winter time, due to the topographic effects. In the following chapter, this effects on hydrological processes will be examined for ET, soil moisture and snowmelt.

2.5.2 Discussion and Outlook

In this chapter the performance of the model on inclined surface can not be verified by observed data, but only be analyzed theoretically and rationally. This is also a general problem for solar radiation research because of the horizontal instrumental mount of routine measurement. In energy oriented research, this problem is not that important, because there the focus is the normal radiation. So a designed observation network to test the inclined surface radiation is highly appreciated.

In this research, the clear-sky index and sunshine duration for the study area is considered to be constant, which is a reasonable assumption for a catchment up to certain area. For a large basin, the weather situation is certainly not spatially even, and should be accounted for. For this problem we can count on the future generation of Meteosat data with high resolutions, which will replace the current $5 \times 5\,\mathrm{km}^2$ resolution data. Another possibility might be the combination of the Meteosat data with MODIS $500 \times 500\,\mathrm{m}^2$ cloud data. Refining the geostationary satellite data with the sun-synchronous satellite data will be a very interesting research work.

3 Topographic Downscaling of Wind

This chapter applies the mass-consistent mesoscale wind model, MEesoscale TRAnsport and fluid (Stream) Model, PC version (METRAS PC) (Schlünzen et al., 2001) to downscale from the geostrophic wind to daily local wind field. METRAS PC model reflects the topographic and land use modification of wind, i.e. sheltering, amplification due to wind-tunnel effect, etc. The input geostrophic wind data is retrieved from NCEP/NCAR Reanalysis data. Simulations are conducted with actual daily data for one year continuously, and with clustered daily wind data over 48 years (1960~2007). Two-step cluster analysis, with k-mean clustering for the first step and Ward's clustering for the second step, are used to classify the 48 years data into 200 representative cases, in order to reduce the computational efforts of a daily wind simulation. The generated wind fields show effects from both topography and land use. The results can be used for hydrological applications, e.g. ET modeling, analysis of wind drift of precipitation, etc.

3.1 Introduction

The impact of wind on hydrological processes, such as ET/soil moisture, precipitation drift, snowpack distribution and melt, is widely recognized. Yet applications of detailed wind data in hydrological study is still not very common, probably due to the lack of detailed wind data. Standard meteorological stations report both the wind speed and wind direction at a height over 10 meters, and averaged over a given time frame, typically 10 min, measured by anemometers. However, the density of such meteorological stations is usually very low, taken Germany as an example, German Weather Service (DWD) provides a measurement network with 175 stations over the whole Germany. Moreover, wind observations can be very inaccurate, because it is a common practice to record the wind force in Beaufort Scale, which rates the wind force qualitatively through depicting the behavior of smoke, trees, waves, etc.

Mesoscale wind simulation has provided an solution to overcome the scare station observations. Wind modeling been widely applied for optimal locating of wind turbines in wind energy research (Finardi et al., 1998; Ayotte, 2008). It is also routinely coupled with chemical transport models to study air pollution (Pielke and Uliasz, 1998). The COST Action 728 (`http://www.cost728.org/`) has provided an overview of the existing integrated mesoscale systems in Europe. But practice of wind modeling for hydrological purpose is, as to the knowledge of the author, still very rare. In this chapter, the METRAS PC model will be applied to downscale wind fields from geostrophic wind data. Fig.3.1 demonstrates the schematic mechanism of wind downscaling with METRAS PC.

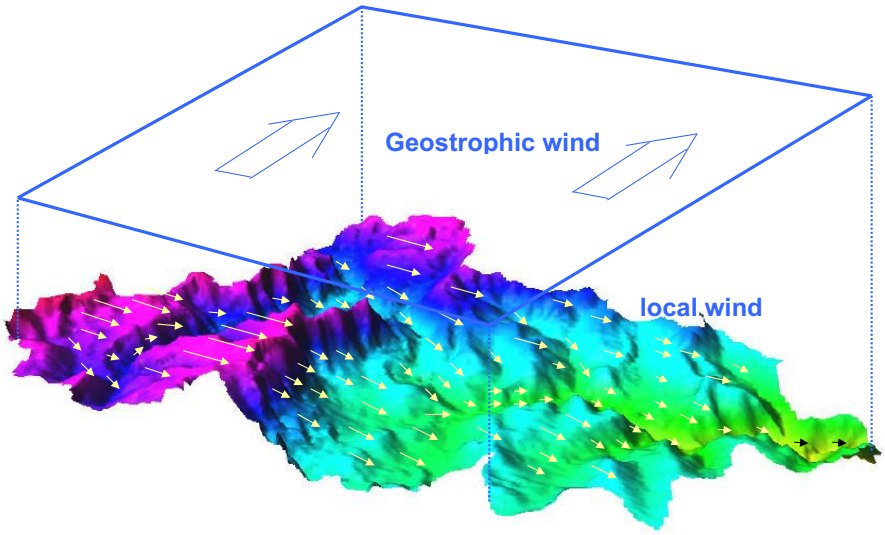

Figure 3.1: Scheme of wind downscaling with METRAS PC

3.1.1 METRAS PC Model Description

METRAS PC is the PC version of the MEsoscale TRAnsport and fluid (Stream) Model (METRAS) (Schlünzen et al., 2001), which is a three dimensional, mass consistent fluid model based on a terrain-following coordinate system (K.H.Schlünzen and Bigalke, 2001a). The model consists of momentum equation, continuity equation, the equations of heat/water/substances conservations, and equations for the ideal gas law and the definition of potential temperature. Only few approximations, such as anelastic assumption, Boussinesq approximation, and constant Coriolis parameter, are applied in the model, which ensure a wide range of model applications. The roughness length is parameterized using Charnock's Formula, with the cloud microphysics being depicted by Kessler-type cloud scheme. The subgrid scale turbulent transport terms in the model equations are parameterized by a first order closure. Two alternative approaches to determine the exchange coefficients above the Prandtl-layer (countergradient closure and TKE-ϵ closure) are provided in the model. METRAS PC is an "up-to-date"mesoscale model with complete functionalities for flow and transport simulation. For a detailed description about the equations and the features of the model, the readers can refer to Schlünzen et al. (2001) and K.H.Schlünzen and Bigalke (2001a,b), here we only present the domain discretization, model input/output and functionalities of the model, which are of interest of the model application.

METRAS PC is capable of simulating wind, temperature, humidity, cloud- and rain-water-content, as well as pollutant concentration field over areas up to $800 \times 800\,\mathrm{km}^2$. It applies a horizontally non-uniform but orthogonal grid, with minimum grid increment of about $20\,\mathrm{m}$, and maximum increments of about $5\,\mathrm{km}$, which allows a detailed study of the process concentrated area. The minimum grid size is around $100\,\mathrm{m}$, smaller grid size may cause problems due to the turbulence parameterization. Vertically the model uses a non-orthogonal terrain-following μ-coordinate system, which can be also non-equidistant, with smaller grid

size close to the ground surface.

The main inputs of the model are the geographic location and the synoptic meteorological data at the initializing point, which include:

- surface pressure
- wind speed (u_g, v_g) and corresponding height
- temperature profile (real temperature (RT) at more than one point, or one real temperature with one or more potential temperature gradient (PTG))
- relative humidity profile (relative humidity at more than one vertical point)

3.1.2 Geostrophic Wind and NCEP/NCAR Reanalysis Data

For this study, the synoptical data is extracted from pressure level data of the NCEP/NCAR reanalysis-I data set (Kalnay et al., 1996). The pressure level data provides four-times daily, daily and monthly values for 17 pressure levels (1000~$10\,\mathrm{mbar}$, some data, such as humidity, has less data levels. The data is available for 2.5×2.5 global grids. In this study the daily data is used, and the pressure levels used are depending on the data. The large-scale wind provided by reanalysis data is the geostrophic wind, which is the theoretical wind that would result from the balance of Coriolis effect and pressure gradient with neglecting the friction force exerted by the ground surface. The theoretical geostrophic wind should prevail above the friction layer, usually above 600 meters, and blow parallel to the isobars, but due to the friction force from the ground and the centrifugal force from curved air flow, it seldom happens in the nature. Nevertheless, geostrophic wind is usually a good approximation for the synoptic scale wind in the mid-latitude. Assuming geostrophic balance, the geostrophic wind components (u_g, v_g) at a given pressure level can be derived from the geopotential height as following:

$$u_g = -\frac{g}{f_{cor}} \frac{\partial Z}{\partial y} \tag{3.1}$$

$$v_g = \frac{g}{f_{cor}} \frac{\partial Z}{\partial x} \tag{3.2}$$

Here, f_{cor} [T^{-1}] is the Coriolis parameter. NCEP/NCAR provides geostrophic wind at different pressure levels. A positive u_g component means that the wind is blowing from west to east, and the positive v_g component indicates the wind originates from south. Following the suggestion of the model inventors, the wind data at the $850\,\mathrm{mbar}$ is chosen as the input, which is lowest level wind that is most likely not affected by lower boundary, Fig.3.2 shows the windrose of the daily geostrophic wind of the 48 years at the first 4 pressure levels. Frank and Landberg (1997) applied the wind data of the same pressure level for simulating the wind climate in Ireland by Karlsruhe Atmospheric Mesoscale Model (KAMM).

Profiles of relative humidity and real temperatures can be obtained from the reanalysis data at different pressure levels. The potential temperature T_θ is defined as the temperature if a

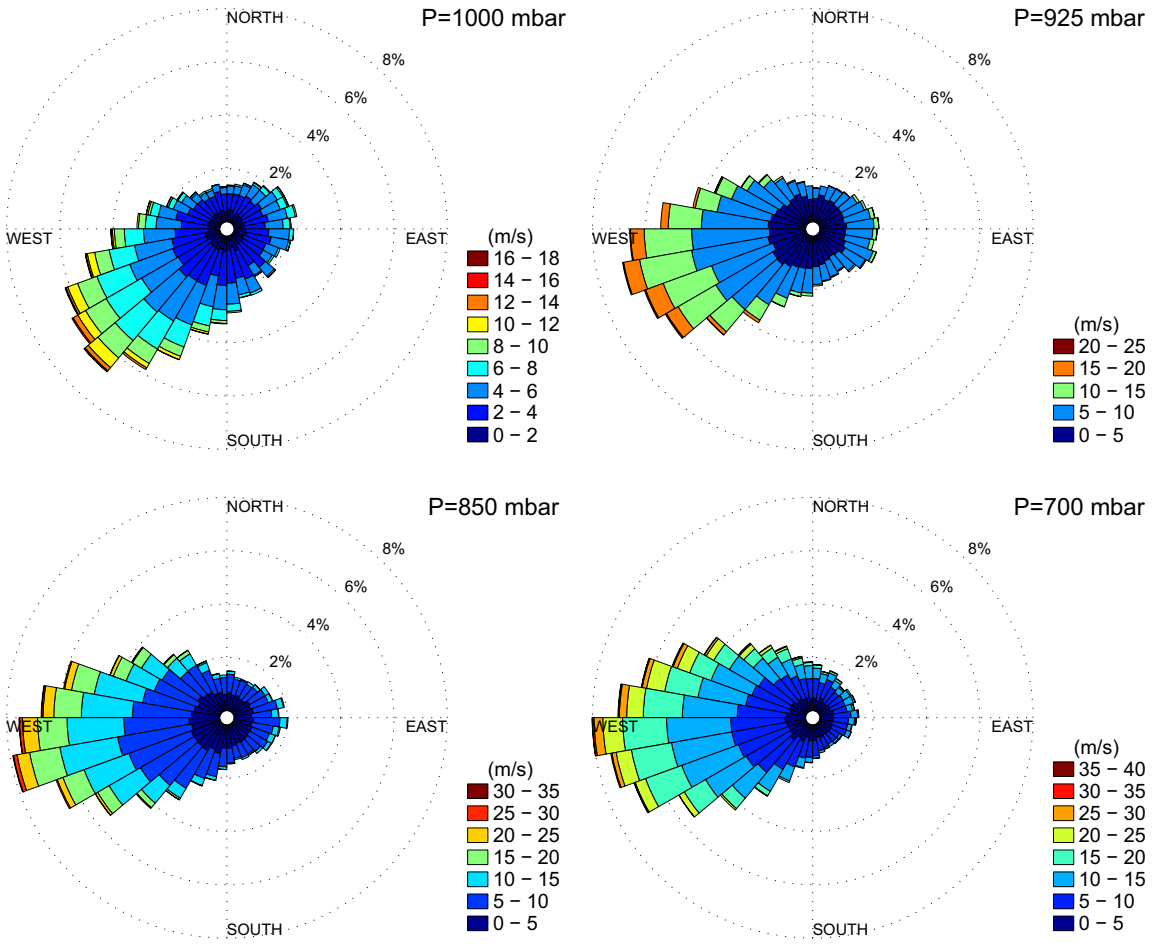

Figure 3.2: Windrose of geostrophic wind from NCEP/NCAR Reanalysis-I data (1960~2007)

parcel of air with temperature T at pressure P is brought to a standard reference pressure P_0 of $1000\,\mathrm{mbar}$ adiabatically, and can be calculated with the Poisson's equation (see. Eq.3.3).

$$T_\theta = T\,(\frac{P_0}{P})^{\frac{R_{gc}}{c_p}} \tag{3.3}$$

Here R is the gas constant, and the c_p is the specific heat capacity at a constant pressure. With the retrieved real temperature and geopotential heights, the potential temperature and the corresponding PTG can be obtained. In this study, the temperature input option is using one real temperature plus two levels of PTGs.

3.2 Cluster Analysis of Wind Data

The wind simulation is very time consuming, and is usually running on super computers. As reported by the model developer, the simulation time of METRAS PC is about 2×10^{-4}

to 5×10^{-4} seconds per grid per time step for 200 MHz CPU power. The model can be run on daily base for short time period. If long time period or statistical result is desired, the input data have to be classified into representative cases. In this work, a two-step cluster analysis is used to classify the more than 40 years data, with k-mean clustering for the first step and Ward's clustering for the second step. Sensitivity tests of the METRAS PC model show that humidity is not a sensitive parameter. Therefore humidity is excluded from the cluster analysis, an arbitrary value will be assigned for the simulation, which will not affect the wind simulation results.

Clustering, or grouping is considered the most important unsupervised learning technique, which deals with finding a structure in a collection of unlabeled high-dimensional data. Clustering is done based on the measure of associations between clusters or original data, which is called similarity or its counterpart dissimilarity. Distance is most popular similarity criterion. Two or more objects belong to the same cluster are "close"in terms of a given distance, e.g. the Minkowski metric,

$$d_p(x_i, x_j) = (\sum_{d=1}^{N} |x_{i,d} - x_{j,d}|^p)^{\frac{1}{p}} \tag{3.4}$$

where N is the dimensionality of the data. The Euclidean distance is the special case of Minkowski metric with $p = 2$.

Clustering methods can be distinguished according to operational methodology into hierarchical and partitional methods. The affiliation of an object to the clusters can be exclusive, overlapping or fuzzy weighted. A complete clustering assigns every object to a cluster, whereas a partial clustering does not (Tan et al., 2005). In this work, the complete exclusive clustering method of both hierarchical and partitional method have been used, and will be discussed in the following.

3.2.1 Ward's Method

Hierarchical clustering creates a hierarchy of clusters in a tree structure called dendrogram. The root of the tree, i.e. the highest level of cluster is a a single cluster containing all data objects, and the lowest level of clusters are the individual data objects. The hierarchical clustering can go "bottom-up", subsequently merge two clusters with smallest distance (agglomerative hierarchical clustering), or "top-down", recursively split the clusters that are farthest (divisive hierarchical clustering). Agglomerative clustering is easy to implemented, thus the most frequently used hierarchical method. For the agglomerative hierarchical clustering, differences may arise depending on the way of defining distance between clusters. The single linkage clustering defines the minimum distance between the closest objects within two clusters as the cluster distance, and the complete linkage uses, on the contrary, the longest object distance. The average group linkage uses the mean of all the distances of all the object pairs formed by the two clusters. The Ward's method specifies the linkage function as the increases in the "error sum of squares"(ESS) after fusing two clusters into a single cluster. Ward's method seeks to merge the clusters while minimizing the increase in ESS at each

step.

$$ESS_j = \sum_{i=1}^{N_j} |x_i^j - c_j|^2 \tag{3.5}$$

$$D(j1, j2) = ESS(j1, j2) - (ESS(j1) + ESS(j2)) \tag{3.6}$$

$$c_j = \sum_{i=1}^{n_j} x_i^j \tag{3.7}$$

$ESS(j1, j2)$ is the error sum of squares, once cluster $j1$ and $j2$ are merged into one cluster. For the agglomerative hierarchical clustering, of course including the Ward's method, all the possible combinations have to be calculated, and stored for comparison, which leads to a large intermittent storage demand. So the methods are only appropriate for small datasets.

3.2.2 k-mean Clustering

k-mean Clustering is the most representative partitional clustering method, which divide the data into a specified number of clusters fixed *a priori*. The algorithm is done in following steps:

1. Define k centroids, one for each cluster $c_j (j = 1, ..., k)$;
2. Associate each data point to the nearest centroid, being denoted as x_i^j;
3. Recalculate the new centroid of the n_j data point of each cluster j: $c_j = \sum_{i=1}^{n_j} x_i^j$;
4. Repeat step 2 and 3, until the location of k centroids do not change any more.

Because a matrix of distance does not have to be determined and stored in the k-mean clustering, therefore it can be applied to much larger data sets. In this study, to classify the more than 40 years daily data, a two-step clustering with the first step using k-mean, and the second step using Ward's method with refinement by k-mean has been applied.

3.2.3 Clustering Results

Before clustering, the different dimensions of the data have been standardized at the first step, the daily real temperature at $1000\,\mathrm{mbar}$ and the lowest two potential temperature gradients (1000~$925\,\mathrm{mbar}$ level and 925~$850\,\mathrm{mbar}$ level) have been classified into 10 groups by k-mean clustering. Fig.3.3 shows the example scatter plot of grouped data between 1960~1970.

In the next step, each temperature class is clustered with Ward's method, and refined by k-mean method. The refinement with k-mean improves the clustering accuracy, and offer the possibility to automatically fix the number of sub-clusters (Hosking and Wallis, 1997). Fig.3.4 shows the example result of the different cluster method for one temperature class. Wind originate from west (horizontal) and south (vertical) are denoted as positive. Fig.3.4a

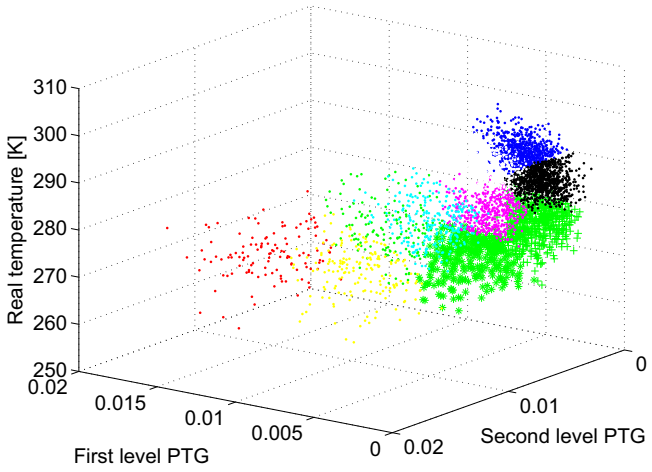

Figure 3.3: Clustering of temperature data of 1960~1970

shows the clustered wind data of one temperature subset by Ward's method without refinement by k-mean clustering, and Fig.3.4b shows the case with refinement. The refined result is more reasonable, for example, some of the data objects in cluster No.8 is more close to cluster No.6 before refinement. One problem can be noticed in both Fig.3.4a and 3.4b is that wind with very diversified directions, even complete opposite directions are classified into one group, which is not proper. Therefore, some constraints on the wind direction for distance calculation are imposed on the clustering algorithm, which shows Fig.3.4c.

The final 200 temperature-wind clusters are shown in Fig.3.5a, and the windrose of the 200 wind clusters are shown in Fig.3.5b. As we can see that by taking the centroid of all data objects, the maximum wind speed of the clusters is smaller than the original data in Fig.3.2. One may also notice that, the windrose is a flip of the clusters in Fig.3.5a, this is because that windrose denotes the originating direction of the wind, whereas in the cluster plot express the wind in the opposite direction as specified before.

3.3 Simulation Results

3.3.1 Results for Clustered Wind

The final result for the Talhausen area is shown in Fig.3.6. Because the wind model requires a rectangular domain, an area cover the Talhausen catchment is used. Fig.3.6a shows the DEM of simulation domain, and Fig.3.6b presents the land use of the simulated area, mixed use is mainly agriculture. Fig.3.6c displays the mean weighted wind strengthen, and in south-east part of the domain the wind pattern resembles the DEM relatively well, i.e. stronger wind at higher elevation. In the west part of the domain, such feature can not be detected. Fig.3.6c,d,e demonstrate the wind rose at the selected points P1, P2, P3 respectively. It shows that the spatial wind is related both to the topography and the surface roughness. Fig.3.7

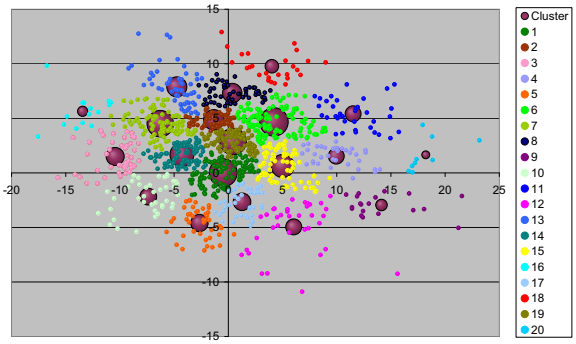

(a) Clustering with only Ward's

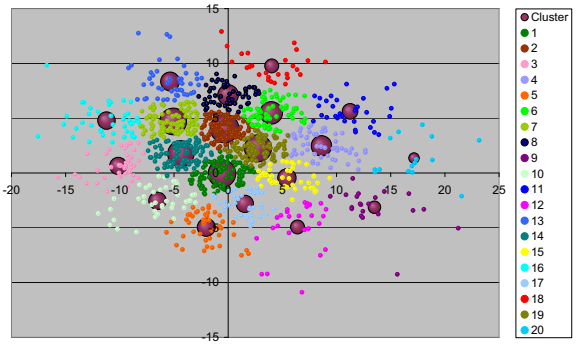

(b) Clustering by Ward's and refined by k-mean

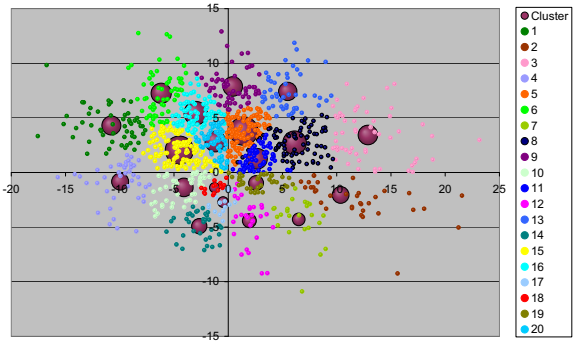

(c) Clustering with wind direction restriction

Figure 3.4: Example cluster results of wind data (The unit of the axes are in m/s. The small circles are the individual data objects, and the big circles stand for the clusters. The centers of the big circles reflect the cluster center, and the area of circles represent the number of the objects belongs to the corresponding clusters.)

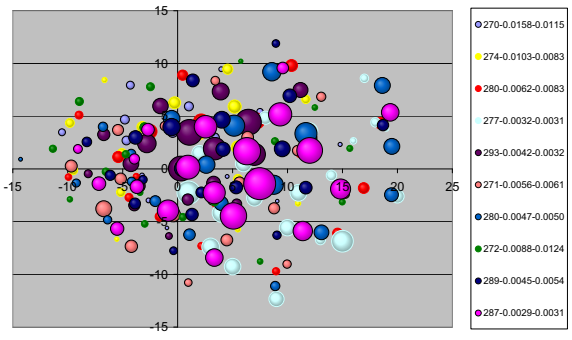

(a) Final wind clusters based on wind and temperature

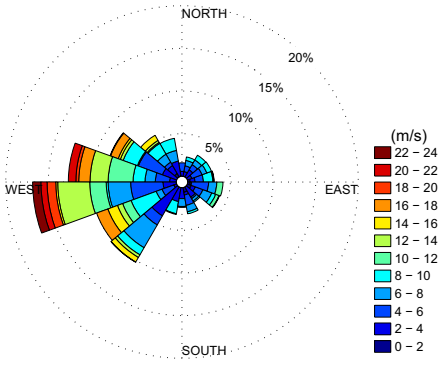

(b) Windrose of the wind speed clusters

Figure 3.5: Temperature-wind clusters and windrose of wind speed clusters

shows the distribution of wind energy for each land use type. It shows that for forest and building area which have a bigger surface roughness, the wind is generally smaller, whereas

for grass and agriculture the wind is stronger.

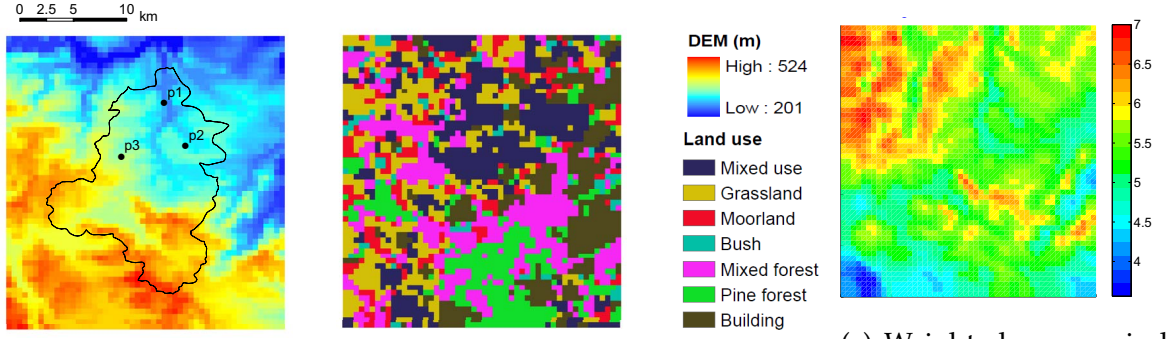

(a) DEM (b) Land use (c) Weighted mean wind pattern

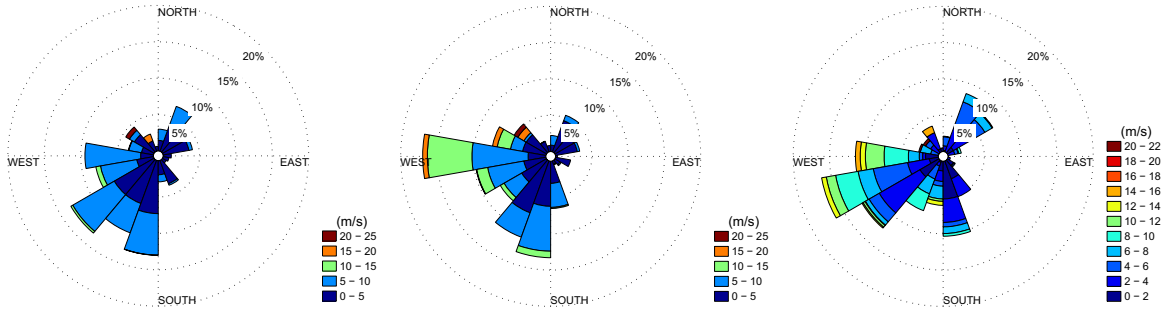

(d) Windrose P1 (e) Windrose P2 (f) Windroes P3

Figure 3.6: Wind simulation results for Talhausen

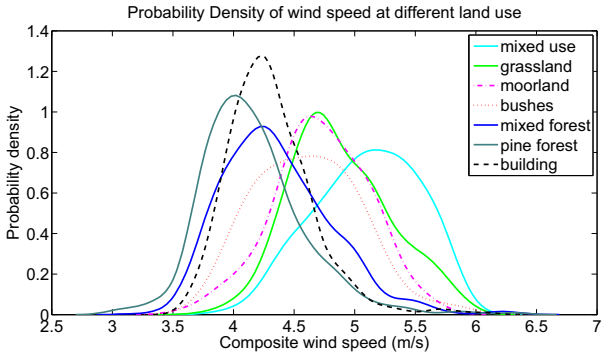

Figure 3.7: Distribution of wind strength of different land use

Table 3.1 shows the statistical results of correlation between the wind speed resulted from each wind cluster and the three topographic parameters. ρ_{wind} is the average correlation coefficient of wind with the individual topographic parameters, and σ_{wind} is the corresponding standard deviation. $\rho_{\overline{wind}}$ is the correlation coefficient of the weighted mean wind with topography. In this case, no correlation between wind and any topographic parameters can be detected. Because wind may not show a linear relationship to topographic aspect, wind strength is classified into 8 categories according to the aspect, and the mean wind of different

Table 3.1: Correlation between the terrain parameters and wind

	aspect	slope	elevation
ρ_{wind}	0.054	0.000	0.140
σ_{wind}	0.014	0.030	0.150
$\rho_{\overline{wind}}$	0.127	0.056	-0.035

aspects are compared. For all days the Null-hypothesis that the mean wind at points with different aspects are the same, is rejected. Fig.3.8 shows the boxplot of the mean daily wind of different aspects. The lower, middle and upper line within the box are the lower quartile (Q1), the median(Q2), and the upper quartile (Q3) respectively. Whiskers extend from the box out to the limits of 1.5 times the interquartile range (IQR). Extreme values out of this range is denotes as crosses. The notches at the median bar indicate the 5% significance level of the median. Notches do not overlap each other means that the medians are significantly different.

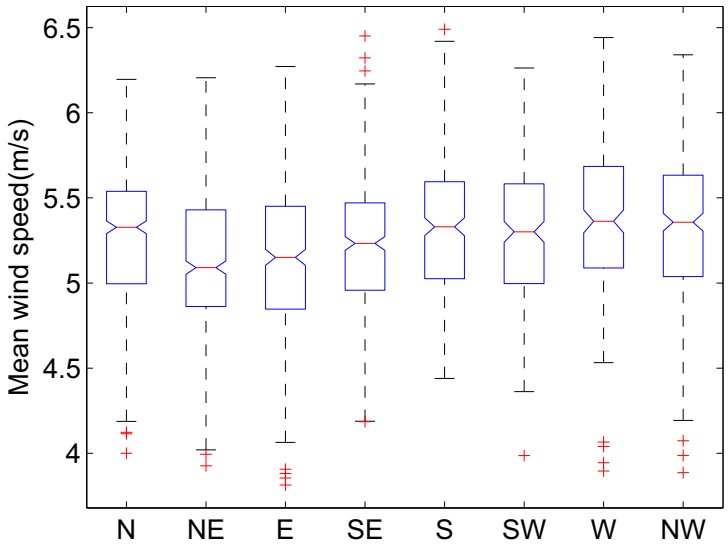

Figure 3.8: Boxplot of wind vs. aspect for mean daily wind

3.3.2 Results for Daily Wind

A continuous simulation fed with daily synoptic wind data of year 2002 is also performed for another bigger area with a resolution of $1000m$, the topographic and land use information of the study area can be found in Chapter 4. Fig.3.9a shows the mean daily wind, which shows a very similar pattern with DEM. The correlation coefficient of mean daily wind speed with DEM is as high as 0.594. The high correlation of wind speed with DEM

is also demonstrated by statistically for multiple days. The DEM dependence of wind force agrees with the results of other statistical study (Winstral et al., 2009) and model simulations (Ayotte, 2008). The missing correlation in the east part in the Talhausen domain, is presumably caused by the small size of the domain, which may not resolve the influence of the neighboring terrain. Table 3.2 shows the statistical results of correlation between daily wind

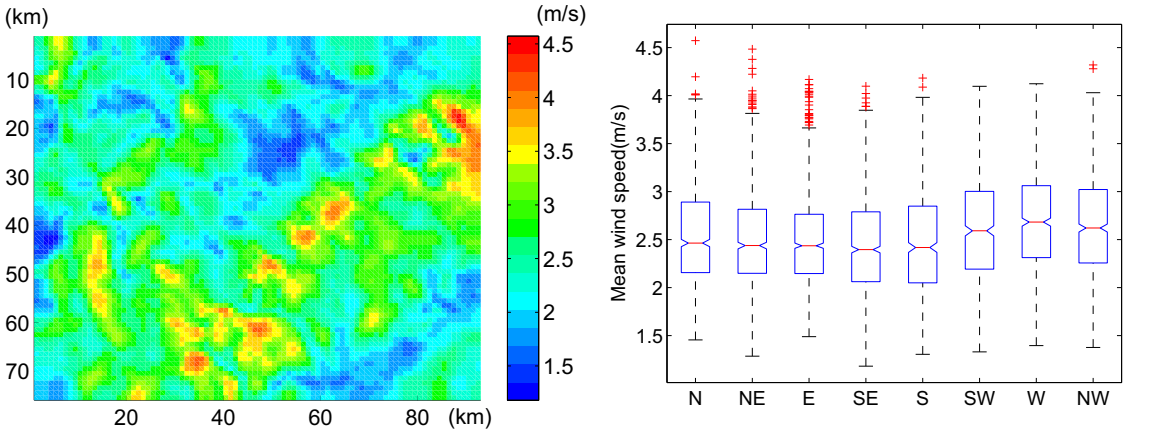

(a) Mean daily wind

(b) Boxplot of wind at locations with different aspects

Figure 3.9: Wind results for continous daily simulation

speed and topographic parameters. Fig.3.9b shows the boxplot of the mean daily wind of different aspects. For this area, wind also demonstrate some influence from aspect.

Table 3.2: Correlation between the terrain parameters and wind

	aspect	slope	elevation
ρ_{wind}	0.066	0.012	0.302
σ_{wind}	0.007	0.011	0.066
$\rho_{\overline{wind}}$	0.127	0.057	0.594

In this chapter, the the local wind patterns have been mapped with a dynamic downscaling approach with mesoscale meteorological model METRAS PC. The statistical wind field show strong spatial difference resulted from topography and land cover modification, which is related by the topography, aspect, and land use. The spatial wind pattern will consequently affect hydrological processes, such as ET, precipitation drift, snow accumulation and snowmelt, etc. In the following chapter, we will demonstrate the wind effects on different hydrological processes.

4 Topographic Effects on ET and Soil Moisture

Numerical experiments with the Soil Water Atmosphere Plant (SWAP) model (van Dam et al., 1997) are applied to quantify the spatial variability of evapotranspiration (ET) and soil moisture content (SMC) caused by topography-induced spatial wind and radiation differences. The field scale SWAP model is applied in a distributed way for each grid, assuming linear groundwater table, identical boundary conditions and in absence of lateral flow. The SWAP model utilizes a comprehensive Penman-Monteith(PM) approach that incorporates meteorological factors, land cover conditions, and species-dependent leaf area index (LAI) to calculate ET, and the Richard's Equation to account for soil water flow in unsaturated zone under different soil characteristics. Both potential and actual ET, as well as the individual components of evaporation and transpiration are calculated by the model. The numerical experiments are conducted for grids with two different resolutions ($100\,\mathrm{m}$ and $1000\,\mathrm{m}$) to evaluate the scale effects. To separate the spatial ET variability caused by radiation and wind, numerical experiments assuming only spatially heterogeneous radiation or wind with all other parameters being homogeneous are performed. Numerical experiment with both spatial varying wind and radiation demonstrates the comprehensive effect of topography on ET. In another experiment, the spatial ET variability caused by vegetation is considered by supporting the model with land use specific LAI obtained from MODIS. Experiments with different soil conditions reveals that the soil type changes mainly the partition between evaporation and transpiration, and has very limited effect on the total ET.

Spatial wind and solar radiation are obtained with the procedures described in previous chapters with globally available data. The results shows a strong spatial intra-catchment variability in daily and annual total ET, and less variability in soil moisture. The spatial variability in ET is associated with a difference in total amount of runoff generated, which may lead to a significant consequence in catchment water balance, snowmelt and rainfall-runoff generation processes.

4.1 Introduction

Evapotranspiration is such an important element in hydrological cycle that it is adopted by Thornthwaite and Mather (1955) as the criteria for climate classification. Globally evapotranspiration amounts to more than 60% of the precipitation that falls on the continents (Dingman, 2002), and in arid and semi-arid regions, it is much higher. At long-term, evapotranspiration determines the regional water balance and hydro-ecological system, whereas

at short-term, it affects the crop growth and yield, as well as the antecedent moisture conditions (AMC) which controls the rainfall-runoff generation processes, thus the hydrologic response of an area. The importance of ET and SMC are witnessed both on small agriculture field scale and in large-scale modelling of land atmosphere interaction. For most climate conditions, soil moisture and evapotranspiration are strongly coupled together, and they are the key parameters for soil water budget, which helps to optimize water balance management and forecast the flash floods (Cassardo et al., 2002; Norbiato et al., 2008). Temporal ET and SMC dynamics also has a strong implication on the interpretation of global climate change.

Several characteristic ET values are available in the literatures, i.e. potential ET (ETP), actual ET (ETA), and reference ET. PET is originally defined as "the amount of water transpired in a given time by a short green crop, completely shading the ground, of uniform height and with adequate water status in the soil profile"by Penman (1948), and it has been generalized to describe the maximum evapotranspiration possible under specific climatic conditions with unlimited water availability in the soil for any vegetation. ETA is the exact water loss by soil and vegetation under water stress conditions. Reference ET is definition adapted by FAO (1990), which refers to "the rate of evapotranspiration from a hypothetical reference crop with an assumed crop height of $0.12\,\mathrm{m}$, a fixed surface resistance of $70\,\mathrm{sec\ m^{-1}}$ and an albedo of 0.23, closely resembling the evapotranspiration from an extensive surface of green grass of uniform height, actively growing, well-watered, and completely shading the ground". In this work, the terms of ETP in general sense and ETA are used.

ET/SMC show a high spatial heterogeneity at different scales (Bresnahan and Miller, 1997; Western et al., 2002), resulted from the interaction of local atmospheric factors (precipitation, radiation, temperature, humidity, pressure, etc.), soil characteristics and vegetation covers, all of which possess a highly heterogeneous nature, and many of which show a dependence on topography. Except radiation, wind, and temperature, for most of these factors, such as soil texture and vegetation features, it is difficult to quantify their spatial distribution with topography. But this does not contradict to the fact that, topography plays an important role in the spatial distribution of ET/SMC. The spatial pattern of ET/SMC gives insight into the spatial water consumption, provides necessary information for water resource allocation and land use management, and helps to understand the spatial rainfall-runoff generation processes. Understanding, monitoring, and quantifying the spatial ET/SMC variability as well as the topographic effects on these variability is important for both theoretical and practical purpose in catchment hydrology.

In contrast to other hydrological parameters such as precipitation and temperature, reliable direct measurement of evapotranspiration and soil moisture is more difficult and expensive. Soil moisture can be measured with gravimetry, lysimetry, radiological techniques such as neutron scattering, or dielectricity based reflectometry (WMO, 2008). ET are usually indirect measured through water budget methods. The direct Pan-evaporation measurement givens only an approximation of free-water evaporation, which need to be adjusted empirically to obtain free-water evaporation under natural conditions. Eddy-correlation measurements are often considered to be the "true"ET rate, however it is not applicable for routine measurement because of its stringent instrumentation requirements. The strong spatial variation

of ET and soil moisture with the local meteorological and hydrological conditions, referred by Western et al. (2002) as scale effect, together with the high cost of measurements, render all types of point measurements impractical for an extensive spatial measurements.

Methods based on remote sensing are nowadays widely deployed to measure soil moisture and to derive evapotranspiration. Three types of microwave sensors with different wavelength are used to capture soil moisture information from space: radiometers, Synthetic Aperture Radars (SARs), and scatterometers. Wagner et al. (2007) conclude that the operational coarse-resolution ($25\sim50\,\mathrm{km}$) soil moisture products can be expected within next few years from radiometer and scatterometer systems, yet operational soil moisture retrieval at finer scale ($\leq 1\,\mathrm{km}$) from SAR still need technological breakthroughs. The main limitations for the operational soil moisture remote sensing are the interfering signal of soil surface roughness and vegetation canopy, and the restricting signal penetration depth (Western et al., 2002). An alternative of inferring evapotranspiration with modeling approach using other remotely sensed parameters, such as land surface temperature (LST), vegetation index (NDVI/EVI), etc. are widely used (Cleugh et al., 2007; Wang et al., 2007; Mu et al., 2007).

Many methods exist for PET evaluation. Empirical equations based on simple meteorological input are widely used to estimate regional ET. Xu and Singh (2000) provided an overview of the temperature and radiation based method. Other empirical methods utilize the remotely sensed LST and vegetation index data to calculate the the actual evapotranspiration, such as triangle method (Price, 1990), B-method (Carlson et al., 1995), temperature/vegetation dryness index (TVDI) (Andersen et al., 2002). A good overview of the remote sensing based techniques can be found in Verstraeten et al. (2008). More physical approaches are based on the conservation of either energy, mass, or both. Penman-Monteith method, also called combination method, because it eliminates the surface temperature and does not need an explicit calculation of sensible heat flux, is the most popular approach used in modeling the physical process of ET. The surface energy balance method, usually applied in land surface models (LSM), on the contrary, try to employ remotely sensed LST data to derive aerodynamic surface temperature, and to explicitly determine sensible heat flux, so that the latent heat flux associated with ET can be calculated as a residual (Bastiaanssen et al., 1998; Su, 2002).

This chapter applies the Soil Water Atmosphere Plant (SWAP) model to investigate the spatial ET/SMC variability originate from spatial wind and radiation difference. First a brief introduction of the SWAP model will be given. Because the SWAP model utilizes a Penman-Monteith approach for ET estimation, a short review of sensitivity analysis of PM equation is summarized prior to the model application, in hope to give some justification of the study of wind and radiation. Then the possibility of the application of MODIS LAI data with the model is examined. Finally the numerical experiments with the SWAP model is performed. To test solely the spatial radiation effect, all other parameters at each grid are holding the station observed values except radiation. So does for the wind. The ET/SMC resulting from the interaction of spatial wind and radiation are also examined with both parameters assuming spatial variant input. The experiment with land-use specific LAI are tested to approximate the topographic induced ET variability under more realistic conditions. The impact of soil type on ET has been also investigated with point experiments.

4.2 Study Area and Data

The study is focusing on the topographic effects on ET/SMC, i.e. the water exchange and transfer in vertical direction, while neglecting the horizontal/lateral flow. A delineated water basin is not necessary. Instead, a region with rich topographic features is required. An rectangular region contains both mountains and flood plains in Southern Germany is taken as the study area for our purpose (see Fig.4.1). On this larger area, simulations are done at $1000\,\mathrm{m}$ resolution. A small area on the north-east mountain part of the study area is taken for detailed study, and simulation are performed at $100\,\mathrm{m}$ resolution.

The original land use of the study area are defined by 16 classes. For wind simulation, the land use is re-classified into 9 groups as specified in the METRAS PC model. To further simplify the parameterization evapotranspiration modeling, similar land use are again merged into one class assigned with unique parameter sets in the SWAP model. The final land use map consists of 5 land use types - grass, agriculture, deciduous forest, coniferous forest, and others, which stands for residence and industrial area in the original land use map. In this study such area are assigned with parameters of bare soil.

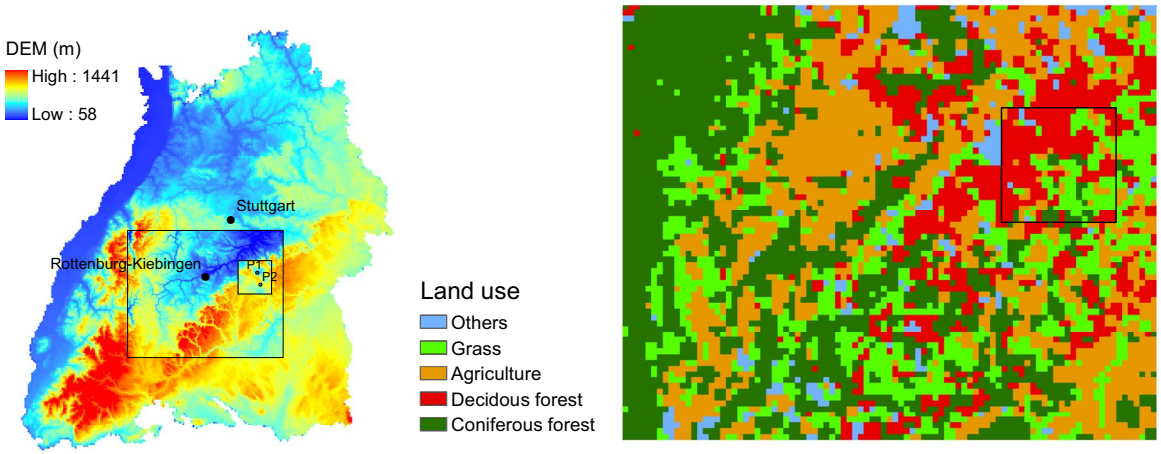

Figure 4.1: The study area (left) and the corresponding land use (right)

4.2.1 Meteorological Data

Daily spatial radiation and wind pattern of year 2002 are obtained with the approaches described in previous chapters with globally available data. The wind field is simulated under the consideration of surface roughness caused by land use difference. Fig.4.2 shows the daily spatial variation expressed by $\frac{P_{90}-P_{10}}{\mu_s}$ over the year. The wind fields of both inner and outer domain are simulated at $1000\,\mathrm{m}$ resolution. For both area, the difference between the lower and upper 10 quartile of wind force can be as high as two times the mean wind force for some days. For radiation, the inner domain is simulated with $100\,\mathrm{m}$ resolution, whereas the outer domain is simulated at $1000\,\mathrm{m}$ resolution. In addition to the variance of actual radiation, the variance of potential radiation is also displayed in the figure by the solid line.

Except in very few winter days, the spatial variation of potential radiation is normally larger than the variation of actual radiation. Because of the finer resolution of the inner domain, the relative radiation difference is up to 90%, whereas the outer domain shows a maximum relative difference of 15%. The avoid the reduced spatial radiation variability resulted from a coarse DEM resolution, the aggregated actual radiation from $500\,\mathrm{m}$ and $100\,\mathrm{m}$ resolution is simulated, and plotted for the sake of comparison. It shows that except in the summer time, the spatial variance of aggregated radiation from $500\,\mathrm{m}$ simulation is almost doubled of the direct $1000\,\mathrm{m}$ simulation, whereas the improvement with aggregation from $100\,\mathrm{m}$ simulation is marginal. In this work, the aggregated radiation from simulation with $500\,\mathrm{m}$ resolution will be used. The spatial variation of both solar and wind are more stable in summer season, and vary strongly in winter season.

Table. 4.1 shows the spatial variation of mean daily radiation and wind of both domains. The mean potential radiation shows a much higher variation then the mean actual radiation. For radiation, because of the finer resolution of the inner domain, the spatial variation of inner domain is much larger than the outer domain. But for wind, under the same resolution, the outer domain shows higher variation, because the outer domain contains more diversified topographic features.

To investigate the spatial ET/SMC variability caused by wind and radiation, all other inputs are assuming spatially homogeneous values, therefore observations at one station is enough. Temperature and precipitation data are obtained from the station Rottenburg-Kiebingen for the year 2002. Because the station does not provide humidity, these data are taken from the nearest meteorological station Stuttgart-Echterdingen. In case humidity data is not available, it can also be estimated with temperature data (Thornton et al., 1997). First dew-point temperature T_d [°C] is approximated by minimum daily temperature T_{min}. Then the ambient vapor pressure e_a can be derived from T_{min}, and the saturated vapor pressure e_s can be evaluated at the mean daily temperature T_a, which can be expressed as a weighted average

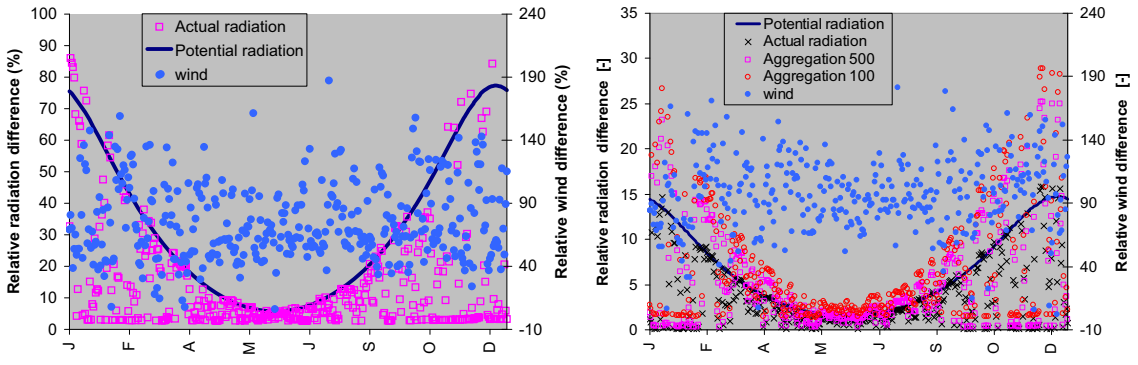

(a) Inner domain (b) Outer domain

Figure 4.2: Spatial variation of wind and radiation over time

Table 4.1: Spatial variability of mean daily wind and radiation

	Potential radiation	Actual radiation	wind
Inner domain	21.16%	12.98%	37.01%
Outer domain	6.51%	3.96%	50.93%

of max daily temperature T_{max} and minimum daily temperature T_{min}.

$$e_a = 0.611\ exp(\frac{17.3\ T_{min}}{237.3 + T_{min}}) \tag{4.1}$$

$$e_s = 0.611\ exp(\frac{17.3\ T_a}{237.3 + T_a}) \tag{4.2}$$

$$T_a = 0.606\ T_{max} + 0.394\ T_{min} \tag{4.3}$$

4.2.2 Land Use Data and LAI

Leave Area Index (LAI) required by the SWAP model are obtained from MODIS 8-day composite data (Yang et al., 2006). A preliminary investigation of the MODIS LAI data shows, the cell-based LAI values show a strong fluctuation, which may come from the data uncertainty. Fig.4.3 shows LAI of two randomly selected points. To remove the strong time variation, the land use specific LAI, which is the spatial average value of the same land use, is applied. As shown in Fig.4.1, the study area are dominated by several land use types, the 16 land use types are aggregated into 5 main land use types: grass, agriculture, coniferous forest, deciduous forest, and others. The right figure in Fig.4.3 shows the land use specific LAI, and the time varying feature is reduced.

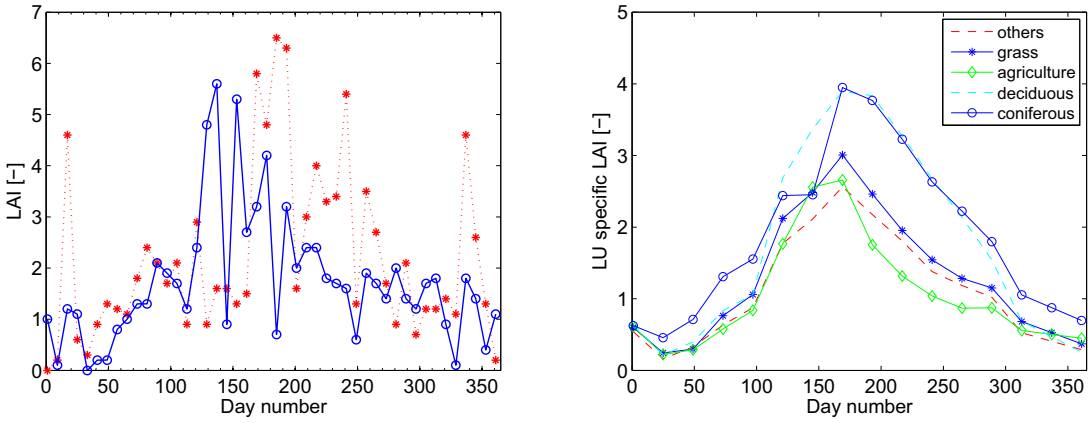

Figure 4.3: Cell-based LAI (left) and land use specific LAI (right)

4.3 SWAP model

The SWAP model is an agro-hydrological model that simulates transport of water, solutes and heat in saturated/unsaturated soils (van Dam et al., 1997). SWAP is designed ideally for field scale study, but it can also be applied to regional scale. It considers a one-dimensional column in the vertical direction, with the lower atmospheric layer being the upper boundary and the unsaturated zone or the upper part of the saturated zone being the bottom boundary. The soil water flow is simulated by the Richard's Equation discretized in a finite difference scheme. Three potential rates are modeled by the Penman-Monteith algorithm (see Appendix 2) by varying the crop resistance, crop height and albedo: potential ET of wet crop (ETP_w), potential ET of dry crop (ETP_d), and potential evaporation of bare soil (EP_s), based on which the actual rates of a fully covered or non-covered surface can be calculated. For partly covered soils, the potential ET of wet or dry crop is partitioned into potential evaporation (EP) and potential transpiration (TP) according to soil cover fraction (SC) as shown in Eq.4.4 or the energy interception by LAI of the vegetated area (see Eq.4.5) .

$$EP = (1 - SC)EP_s \tag{4.4}$$

$$EP = EP_s e^{-\kappa_{gr}\, LAI} \tag{4.5}$$

$$TP = ETP_d - EP \tag{4.6}$$

Here, κ_{gr} is the extinction coefficient for solar radiation. The actual transpiration is the integrated root water uptake of each root layer taking into the reduction due to water and/or salinity stress. In absence of any stress, the total root uptake capacity equals to the potential transpiration rate.

$$RX_p(z) = \frac{l_{root}(z)}{\int_{-D_{root}}^{0} l_{root}(z)dz} TP \tag{4.7}$$

$$RX_a(z) = \alpha_r\, RX_p(z) \tag{4.8}$$

$$TA = \int_{-D_{root}}^{0} RX_a(z)dz \tag{4.9}$$

where $l_{root}(z)$ and $RX_p(z)$ is root density and the potential root water extraction rate at depth z. D_{root} is the root layer thickness. α_r is the reduction factors due to water, salinity stress and frozen conditions. $RX_a(z)$ and TA is the differential and integrated actual transpiration respectively.

Fig.4.4 shows the example of water stress coefficient α_{rw} as a function of soil water pressure head. The water stress caused reduction of transpiration is depicted in Fig.4.4. In the range $h_3 < h < h_2$ root water uptake is optimal. Below h_3 root water uptake linearly declines until zero at h_4 (permanent wilting point). The threshold pressure h_3 increases with potential transpiration rates. For low potential transpiration TP_{low}, the threshold pressure h_{3l} is lower

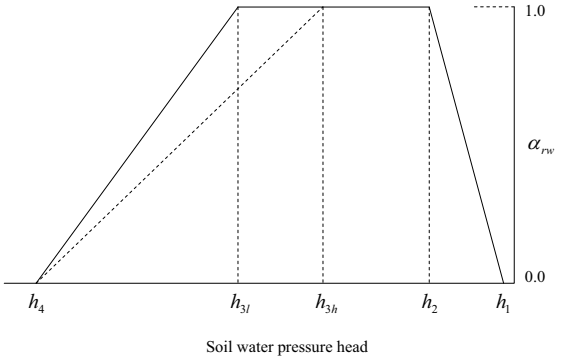

Figure 4.4: Reduction coefficient for root water uptake

than the threshold pressure h_{3h} at high potential transpiration rate TP_{high}. Above h_2 root water uptake linearly decreases due to insufficient aeration until zero at h_1. In this study, the recommended values from SWAP manual is taken, which usually allows a wide range of optimal uptake. The crop specific parameters are listed in Table.4.2.

The maximum soil evaporation E_{max} is restricted by the soil water suction at the top soil layers based on Darcy's law:

$$E_{max} = K_{1/2}(\theta)\ (\frac{h_{atm} - h_1 - z_1}{z_1}) \tag{4.10}$$

where $K_{1/2}(\theta)$ [$cm \cdot d^{-1}$] is the average hydraulic conductivity between the soil surface and the first node as a function of soil water saturation θ [-], h_{atm} is the soil water pressure head [cm] in equilibrium with the air relative humidity, h_1 is the soil water pressure head of the first node, and z_1 is the soil depth [cm] at the first node. SWAP provides also the option to choose empirical evaporation functions of Black et al. (1969) and Boesten and Stroosnijder (1986). In SWAP model, the actual soil evaporation EA is determined by the minimum value of EP, E_{max}, or results of the empirical functions. The soil water head and hydraulic conductivity under unsaturated condition are modeled following the Mualem-van Genuchten

Table 4.2: Crop specific parameters for SWAP modeling

	D_{root} [cm]	characteristic suction heads [cm]				
		h_1	h_2	h_{3h}	h_{3l}	h_4
Natural grass	60	0.0	-1.0	-200.0	-800.0	-8000.0
Maize	5~100	-15.0	-30.0	-325.0	-600.0	-8000.0
Pine forest	70	-0.0	-1.0	-600.0	-600.0	-6000.0
Deciduous forest	100	-1.0	-2.0	-600.0	-600.0	-6000.0

functions as following.

$$S_e = (1 + |\alpha_{vg} h_{suc}|^{n_{vg}})^{-m_{vg}} \tag{4.11}$$

$$m_{vg} = 1 - \frac{1}{n_{vg}} \tag{4.12}$$

$$K_e = K_{sat} S_e^{\lambda_{vg}} (1 - (1 - S_e^{1/m_{vg}})^{m_{vg}})^2 \tag{4.13}$$

$$S_e = \frac{\theta_e - \theta_{res}}{\theta_{sat} - \theta_{res}} \tag{4.14}$$

with
S_e : effective saturation [$-$]
h_{suc}: soil water head [L]
α_{vg} : parameter related to the modal pore size $-$]
n_{vg} : parameter of pore-size distribution [$-$]
m_{vg}: parameter of pore-size distribution [$-$]
K_e : effective hydraulic conductivity [L T^{-1}]
K_{sat}: saturated hydraulic conductivity [L T^{-1}]
λ_{vg} : shape parameter [$-$]
θ_e : effective volumetric water content [L^3/L^3]
θ_{res} : residual volumetric water content [L^3/L^3]
θ_{sat} : saturated volumetric water content [L^3/L^3]

Soil in the study region are mainly clay (soil A) and loam (soil B), their hydraulic parameters are shown in Table.4.3. Besides the actual soil conditions, the study also investigates the effects of soil types on ET/SMC by simulating with a more permeable soil configuration (soil C and soil D in Table.4.3).

4.4 Sensitivity Analysis of Penman-Monteith Based Evapotranspiration

Sensitivity analysis can estimate the relative response of each input factors. Frey and Patil (2002) and Saltelli et al. (2006) provide a good overview of approaches available for sensitivity test. Sensitivity analysis of Penman-Monteith actual ET have been investigated for three

Table 4.3: Soil parameters for SWAP modeling

	θ_{res} [cm^3/cm^3]	θ_{sat} [cm^3/cm^3]	α_{vg} [$-$]	n_{vg} [$-$]	K_{sat} [cm d^{-1}]	λ_{vg} [$-$]
Soil A	0.01	0.42	0.0099	1.288	2.36	-2.244
Soil B	0.01	0.42	0.0191	1.152	13.79	-1.384
Soil C	0.01	0.43	0.0227	1.548	9.65	-0.983
Soil D	0.02	0.38	0.0214	2.075	15.56	0.039

sites in UK by Beven (1979) with the nominal range sensitivity analysis, i.e. by individually varying only one of the model input while holding all other inputs at their nominal or base-case values (Cullen and H.C., 1999). Recently Bois et al. (2008) applied the more advanced Sobol's method, which enables the evaluation of the interaction between the input variables. The Sobol's method decompose the total variance V of the model output into variance with different orders in response to individual or simultaneous variation of the model inputs. For a model with k input variables, $2^k - 1$ variance terms can be obtained:

$$V = \sum_i V_i + \sum_{i<j} V_{ij} + \sum_{i<j<m} V_{ijm} + \cdots + V_{1,2,\ldots,k} \tag{4.15}$$

where V_i is the first-order variance in response to variation of the ith input variable, and V_{ij} is the second-order variance to the simultaneous change of the ith and the jth model input, and so-on. The Sobol's sensitivity index, which measures the model output variance caused the ith model input, including all the possible interactions with other inputs, is defined as:

$$S_{T_i} = \frac{V_i + \sum_j V_{ij} + \sum_{j<m} V_{ijm} + \cdots + V_{i,j,\ldots,k}}{V} \tag{4.16}$$

Bois et al. (2008) have shown that wind speed has a major impact on ET during winter season and solar radiation is more influential during summer, whereas other meteorological parameters show no significant effects. The analysis is achieved with the SIMLAB software (Saltelli et al., 2007), which will not repeated here.

4.5 Numerical Experiments and Results

4.5.1 Model Setup

To simulate the actual ET with SWAP, not only the meteorological input, but also detailed the soil hydraulic information, vegetation leaf and root properties, and groundwater dynamics are required. The soil hydraulic parameters and the vegetation properties are extremely heterogeneous, and are associated with high uncertainty. Spatial acquisition of such data are very expensive, if not impossible. The aim of this work is to seek the theoretical pattern caused by decisive topographic-induced spatial patterns of radiation and wind, therefore a resort of spatial soil-vegetation data is not necessary. Nevertheless, the application of the actual spatial data will lead to a better approximation of the actual spatial ET/SMC patterns, therefore a maximum utilization of the actual data is attempted in this work with the application of remote sensing data. The numerical experiments are conducted at two different resolutions, $100 \times 100\,\mathrm{m}^2$ for the inner domain and $1 \times 1\,\mathrm{km}^2$ for the outer domain to check the scale effect. For all simulations and each grid, the boundary and initial conditions are set to be identical, and are set as following:

- Bottom boundary condition: a shallow groundwater aquifer of $3\,\mathrm{m}$ on top of an impervious layer is assumed for the region, thus each grid, which implies a zero bottom flux

boundary. A simplification of regional groundwater table is assumed - groundwater depth is linearly related to the local elevation, with a groundwater depth of $0.7\,\mathrm{m}$ at the lowest elevation close to the river, and a depth of $1.5\,\mathrm{m}$ at the highest elevation;

- Lateral drainage condition: groundwater dynamics caused by groundwater flow is considered to be equivalent to drainage to surface water with drainage bottom at $5\,\mathrm{cm}$ below the groundwater table;
- Soil hydraulic properties: the upper $2\,\mathrm{m}$ soil consisting of an upper $30\,\mathrm{cm}$ less permeable clay and an underlying $170\,\mathrm{cm}$ more permeable loam (see Table. 4.3), is considered in the simulation.

Meteorological data, such as temperature, precipitation, and humidity are station observations at Rottenburg-Kiebingen. Station radiation and wind data from Stuttgart station is used in case that spatially constant value is required for a given experiment. Both fictitious homogeneous vegetation data and actual remote sensing LAI have been used depending on the experiment objective. Following numerical experiments have been tested:

- Experiment 1: Spatial actual radiation, station wind, homogeneous vegetation of grass;
- Experiment 2: Station radiation, spatial wind, homogeneous vegetation of grass;
- Experiment 3: Spatial actual radiation, spatial wind, homogeneous vegetation of grass;
- Experiment 4: Spatial actual radiation, spatial wind, actual land use;

4.5.2 Simulation Results

Point Results

Two points, P1 and P2 (see Fig.4.1), with distinct topographic features are chosen for comparison. P1 is located at the north side of the mountain foot, whereas P2 is located in south aspect of the mountain peek. The topographic information of the two points are listed in Table 4.4. Fig.4.5 shows the common (see Fig.4.5a) and specific meteorological inputs obtained at $100\,\mathrm{m}$ scale (see Fig.4.5b) at two selected points P1 and P2. P2 receives considerably higher radiation and exposed to stronger wind (see Fig.4.5b). Both points are simulated by assuming a vegetation cover of natural grass. Fig.4.5c and 4.5d show that the soil moisture dynamics of the two points simulated at the spatial resolution of $100\,\mathrm{m}$. The soil moisture profile of the both points are similar, but point P2 is much drier than point P1. The driest period is from March 24 to April 11, during which there is no rainfall in around two weeks.

Table 4.4 shows the simulated water balance at the two points simulated with two different soil configurations, a less permeable soil conditions (soil A & B) and a highly permeable soil conditions (soil C & D). The simulation is done for two different scales, $100\,\mathrm{m}$ and $1000\,\mathrm{m}$. At both scale, more water are evaporated/transpired at P2 than P1. At P1 more water is drained through groundwater and/or surface runoff than at P2. The highly permeable soil allows strong infiltration, therefore most water are drainage through subsurface, and very little

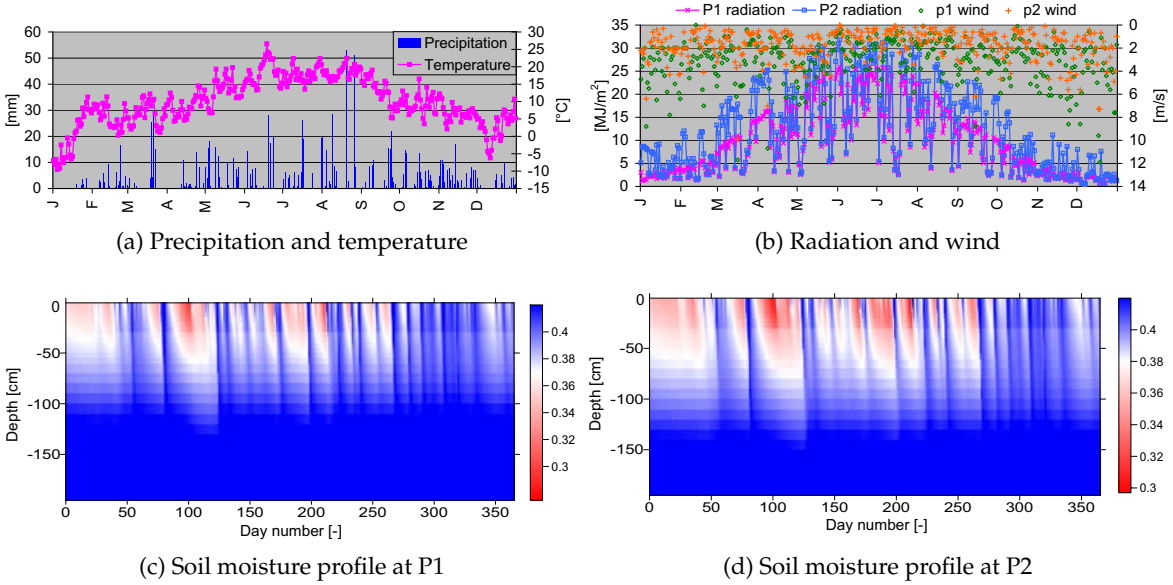

(a) Precipitation and temperature

(b) Radiation and wind

(c) Soil moisture profile at P1

(d) Soil moisture profile at P2

Figure 4.5: Meteorological inputs and simulated soil moisture time series at P1 and P2

surface runoff is generated. There is no big difference between the actual and the potential evapotranspiration, because south Germany is a humid region, and ET is a energy limited process rather than a water availability limited process. The actual transpiration is more close to the potential value, and in the case of more permeable soil conditions, they are even identical, which is resulted from the strong water transportation capacity of plants than soil texture. As shown in the table, simulation at coarser resolution diminishes the difference between the two locations. At $100\,\mathrm{m}$ resolution, the difference of potential and actual ET at the two points are around 23.7% and 20.6% respectively, and at $1000\,\mathrm{m}$ resolution, the difference are around 14.9% and 13.7% respectively. The soil condition does not change the total actual ET much, but the partition between evporation and transpiration. In the case of highly permeable soil, the soil transportation capacity is much weaker than the less permeable clay and loam, therefore the soil evporation is reduced, and the available energy is consumed by plants and increases the amount of tranpiration.

Spatial Results

This section shows the spatial results of the numerical experiments simulated at different scales. Fig.4.6a and 4.6b show the spatial variability of the spatial radiation and wind by the probability density function (PDF). Fig.4.6c, 4.6d, and 4.6e show the PDFs of the yearly total evaporation, transpiration, and evapotranspiration of the respective numerical experiments. The results of Experiment 4 spread much wider than the others because of the variation of vegetation types, they are shown individually in Fig.4.6f to avoid the distortion of other experiment results in the figure. To be mentioned, the negative value in Fig.4.6f is an artifacts coming from the kernel smoothing of the distribution curve, when zero transpiration of bare soil occurs in the data.

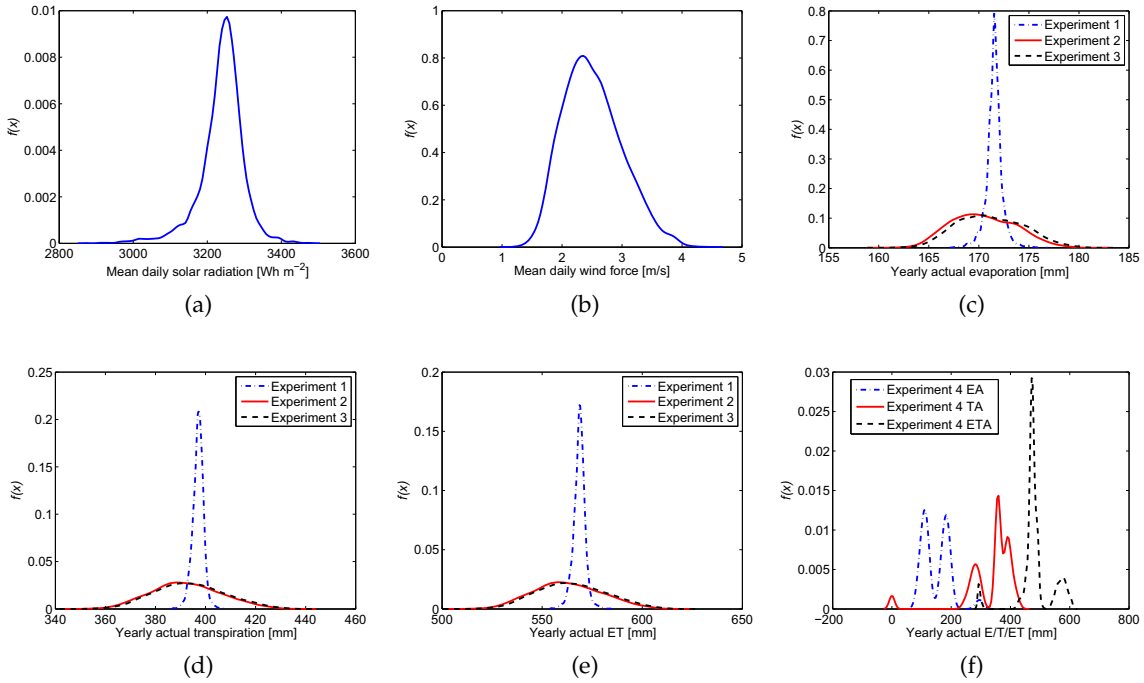

Figure 4.6: Spatial variation of meteorological inputs and ET of outer domain

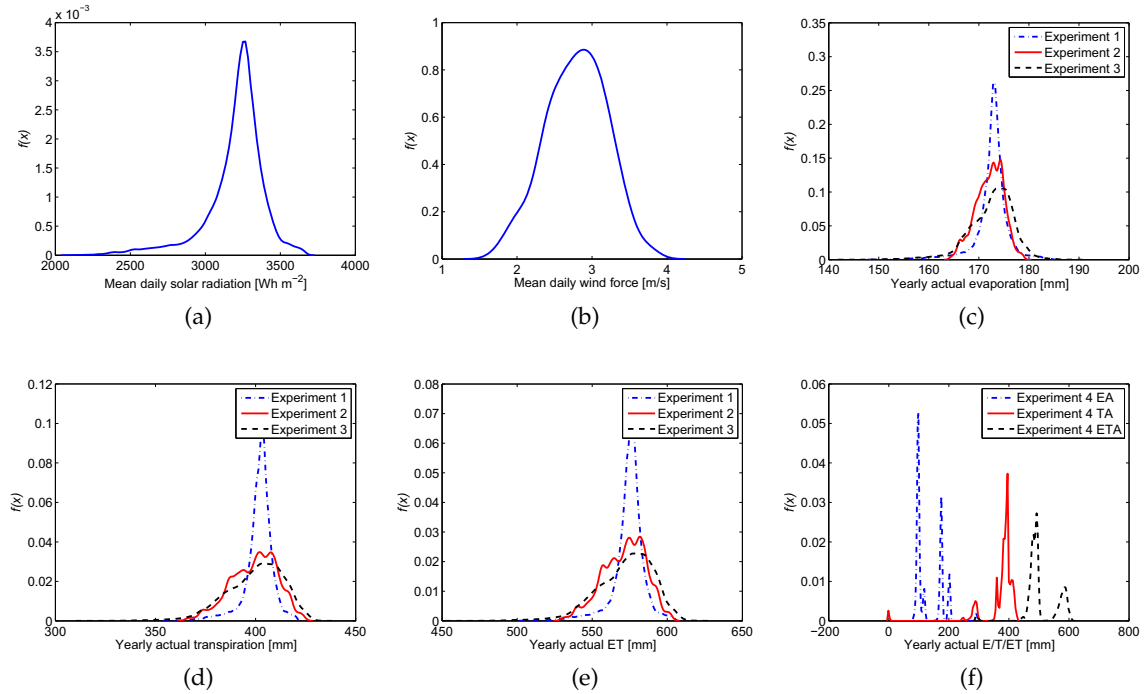

Figure 4.7: Spatial variation of meteorological inputs and ET of inner domain

Table 4.4: Comparison of point simulation results with clay and loam

	P1		P2	
	100m	1000m	100m	1000m
elevation [m]	616	608	820	811
aspect [degree]	315.0	6.92	194.5	188.8
slope [degree]	26.98	5.74	5.97	1.46
mean radiation [MJ/m^2]	9.33	10.54	12.25	11.98
mean wind [m/s]	1.73		3.10	
Acutal soil (Soil A & B)				
Initial water storage [mm]	801.5	802.1	786.0	786.7
transpiration [mm]	339.1(343.1)	357.1(360.9)	417.1(419.6)	414.1(416.6)
evaporation [mm]	154.3(197.4)	161.9(214.7)	177.7(248.8)	176.1(244.9)
drainage [mm]	509.7	486.7	411.5	416.3
runoff [mm]	88.0	85.9	78.7	78.9
Final water storage[mm]	816.8	817.1	807.4	807.8
Test soil (Soil C & D)				
Initial water storage [mm]	654.2	656.1	601.2	603.6
transpiration [mm]	344.3(344.3)	361.9(361.9)	421.7(421.7)	418.7(416.6)
evaporation [mm]	146.6(196.2)	153.2(213.6)	167.3(246.7)	165.8(244.9)
drainage [mm]	600.9	577.5	495.8	500.0
runoff [mm]	0.8	0.2	0.3	0.0
Final water storage[mm]	668.2	669.8	622.6	624.6

Note: The values in the parentheses are potential values.

Fig.4.7 shows the spatial variation of radiation (Fig.4.7a), wind (Fig.4.7b), EA (Fig.4.7c), TA (Fig.4.7d), ETA (Fig.4.7e), and the results with actual land use (Fig.4.7f) for the inner domain at finer scale. The PDF of Experiment 1 which considers only radiation effects, both evaporation and transpiration spread much narrower than the PDF of other experiments. For both domains, especially for the outer domain, the result of Experiment 2 is very close to Experiment 3, which means the wind effects dominate the radiation effects. The variation caused by different vegetation can also be observed through the multiple peeks in the PDFs in Fig.4.6f and 4.7f. Because in general, agriculture field has a higher ET depending on the planted crops, and ET is decreasing in the order of grass, deciduous forest, pine forest, and bare soil, Experiment 4 with actual land use gives less ET than Experiment 3 with natural grass only. The partition of evaporation and transpiration also changes with plant type, forest shows higher transpiration because of the strong root uptake capability and higher vegetation cover of soil.

The spatial variation quantified by $\frac{P_{90}-P_{10}}{\mu_s}$ is shown in Table.4.5 and 4.6. The variation of ET is much smaller than the variation of energy input, i.e. wind and solar radiation, because of the nonlinearity of the process. The inner domain has a larger variation in radiation and a

smaller variation in wind, therefore the resulted variation by radiation of the inner domain is much larger than the outer domain, and *vice versa*, the variation originated from wind is smaller. The inner domain shows also a higher yearly area mean ET than the outer domain, because it is lying on a mountainous region.

Fig.4.8a, 4.8b, 4.8c, 4.8d show the resulted spatial actual ET of the four numerical experiments respectively. The data in the inner catchment are shown in the scale of the outer domain. The strong contrast within the inner domain shows that the fine scale simulation captures the spatial variation better. The extreme low ET represented by the lower tail in the PDFs in Fig.4.6 and 4.7 occurs exclusively the on the north side of steep mountains and in river valleys, where sunshine is shielded. Such small area may not be very significant for rainfall-runoff generation process, but is ecologically very important. Under homogeneous land use, the patterns of ET demonstrate a strong structured feature which is related to the topography. When land use is considered, the heterogeneity of ET is strongly related to land use type (see Fig.4.8d). Fig.4.8e shows the soil moisture of upper $20\,\mathrm{cm}$ on April 8th, which is the end of around two weeks dry weather in the spring. The soil moisture is strongly related to the topography, which comes from the assumption of elevation related groundwater table. Fig.4.9 shows the monthly actual areal ET (see Fig.4.9a) and the spatial variation of actual ET over the year (see Fig.4.9b) for the outer domain resulted from Experiment 3 when both spatial wind and radiation are considered. In the winter time, although the amount of evapotranspiration is relatively small, the variation in terms of $\frac{P_{90}-P_{10}}{\mu_s}$ is as high as 180%, which may also imply a strong effect on snowmelt.

4.6 Discussion

In this chapter, numerical experiments have been applied to a mountainous region at two different scales to simulate the evapotranspiration and soil moisture. The study aims at analyzing the spatial variability of ET/SMC caused by spatial radiation, wind, and their interaction. Simulations with spatial vegetation information obtained from MODIS LAI are also performed to check the effect of spatial vegetation distribution on ET/SMC. The result shows that, under the humid climate condition of the study area, ET is an energy controlled process. A spatial ET pattern exists, and in the case of homogeneous land use, it is well related to topography. When heterogeneous land uses present, ET pattern is strongly con-

Table 4.5: Numerical experiment results of outer domain

	Spatial variation $\frac{P_{90}-P_{10}}{\mu_s}$ (%)							Annual area mean (mm)			
	EA	EP	TA	TP	ETA	ETP	SM*	EA	EP	TA	TP
EX 1	1.02	2.09	1.34	1.10	1.20	1.47	6.53	172.0	236.0	398.1	401.3
EX 2	4.90	6.20	8.95	9.33	7.95	8.00	7.35	170.9	233.9	393.5	396.7
EX 3	5.01	6.77	9.04	9.43	7.34	8.05	8.18	171.6	235.7	395.0	398.3
EX 4	62.23	113.72	33.54	39.69	19.39	24.60	34.65	150.6	228.9	336.1	359.9

∗ Maximum daily spatial soil moisture variation over the year

Table 4.6: Numerical experiment results of the inner domain

	Spatial variation $\frac{P_{90}-P_{10}}{\mu_s}$ (%)							Annual area mean (mm)			
	EA	EP	TA	TP	ETA	ETP	SM*	EA	EP	TA	TP
EX 1	3.57	7.00	3.42	3.53	3.53	4.74	5.45	173.1	237.4	402.8	405.8
EX 2	4.09	5.07	7.14	7.39	6.35	6.36	6.21	172.6	236.7	400.4	403.4
EX 3	6.10	9.30	8.68	9.08	8.12	8.80	6.45	172.9	237.3	400.7	403.7
EX 4	77.53	148.17	28.83	31.65	18.35	22.88	33.34	134.3	180.7	374.7	377.96

∗Maximum daily spatial soil moisture variation over the year

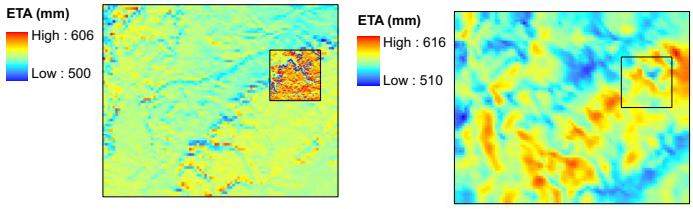

(a) ETA of Experiment 1 (b) ETA of Experiment 2

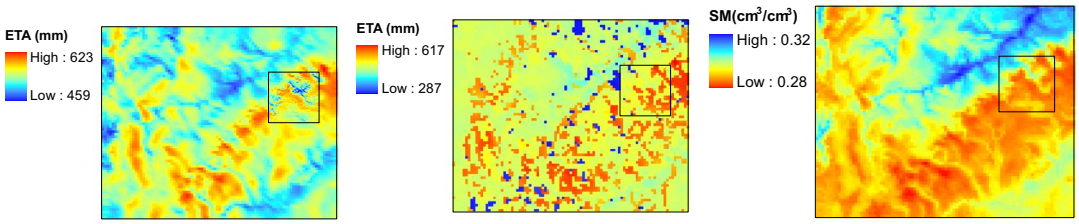

(c) ETA of Experiment 3 (d) ETA of Experiment 4 (e) SMC of Experiment 4 on day 101

Figure 4.8: Spatial actual ET and SMC of the numerical experiments

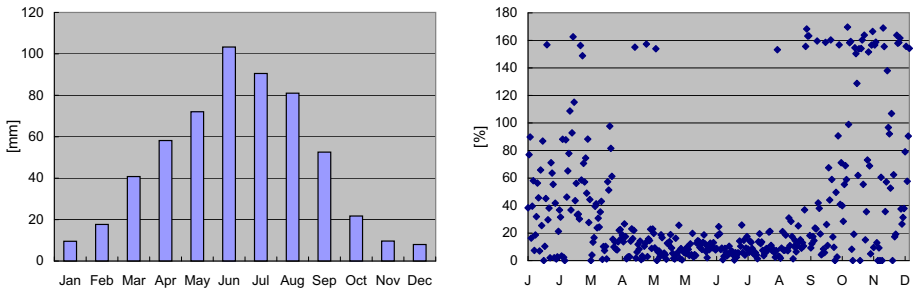

(a) (b)

Figure 4.9: Monthly ET and daily spatial variation of ET

trolled by land use type. Different soil conditions will change the partition between evaporation and transpiration and, partition between surface runoff and subsurface flow, but has very limited impact on total amount of ET and runoff. Radiation causes a stronger spatial variation of ET/SMC at finer scale than at coarser scale, especially for evaporation. But

under homogeneous land use, spatial wind effect is dominating the spatial radiation difference at both scales. Because of the nonlinearity of the evapotranspiration process, the resulted spatial variation is smaller than the variation in the meteorological inputs. The spatial variation is much stronger in the winter time, which may cause a very different snowmelt progress. The spatial difference in ET is offset by the amount of runoff generated, which may have an implication in flood generation.

The SWAP model is applied with radiation and wind data mapped from global data and physically-based model, which demand very few observation data. Because the lack of groundwater data, a linear groundwater table is assumed for the numerical experiments in this study. In order to implement a complete spatial simulation, the SWAP model should be coupled with a groundwater model, to update the groundwater level at each step.

This study has confirmed the effects of topographic induced spatial radiation and wind on ET, and this information may be utilized to improve hydrological concepts in ET/SMC modeling. Moore et al. (1993) derived a dimensionless evaporation scaling ratio based on spatial radiation differences. Vertessy et al. (1990) developed a radiation weighted wetness index, which is a combination of potential solar radiation index (the ratio of the potential solar radiation on a sloping surface to that on a horizontal surface) and wetness index. As we have seen, that the wind effect is much stronger than radiation, so the inclusion of wind effect into the wetness index following a similar approach to Vertessy et al. (1990) is desired in the future.

5 Topographic effects on Snowmelt

Temperature-index method is a very popular method for modeling snowmelt, by which the temperature is used as surrogate of energy input for snowmelt. Although the method performs reasonably well in some cases, the temperature index method is not able to account for the spatial variability of the energy input caused by spatial topography, except for the elevation through the lapse rate in a distributed model structure. This chapter attempts to incorporate the spatial radiation variability caused by topographic effects into the distributed degree-day model, in both additive and multiplicative formulations. Different radiation components are also investigated, from potential solar radiation, to actual solar radiation, to all-wave radiation. The implemented degree-day models are calibrated at the stations with the binary MODIS snow cover extent (SCE) data, observed temperature and precipitation data, and validated with spatially interpolated temperature and precipitation data, as well as MODIS data. Comparison of the results of the adapted models with the standard degree-day model shows an improvement of the model performance.

5.1 Introduction

5.1.1 Review of Physical and Conceptual Snowmelt Modeling

In alpine regions of the mid-latitudes snow accumulation and ablation are often the dominating hydrological processes, thus crucial for water resources management, hydro-power planning, and disaster prevention. In many areas of the world, snowmelt contributes the dominating part of the seasonal or annual runoff. Anderton et al. (2002) demonstrated the importance of spatial accumulation and melt patterns of snow for runoff generation. Consequently, accurate monitoring and modeling of spatial snow properties and dynamics, such as snow cover extent (SCE), snow water equivalent (SWE), and snow depletion curve (SDC), have an important implication in hydrological applications. The snowmelt process is inextricably controlled by various external energy exchange with the surroundings, and conductive heat flux, internal to the snowpack, and involves many sub-processes, such as sublimation/vaporization, ripening, layering, refreezing, etc (Dingman, 2002). These processes are resulted from the interaction of the snowpack metamorphism, the weather conditions, and the underlying soil/vegetation environment (DeWalle and Rango, 2008). Many process-based energy budget models have tried to quantify the snowmelt dynamics by resolving the detailed processes, such as the ISNOBAL model by Marks et al. (1999), the UEB model by Tarboton et al. (1995), the ALPINE3d model by Lehning et al. (2006). To describe the underlying processes, such models generally require very detailed input data, including the

meteorological data(temperature, dew point, vapor pressure, wind, radiation), snow characteristics (snow layering, SWE, albedo), and the underneath soil and vegetation conditions. Such data are usually very site-specific. The data availability has limited the applicability of the process-based models. Moreover, the process-based energy budget approach are exclusively designed for point scale by neglecting the lateral energy and mass transfer, which render the spatial application of such model troublesome (Cazorzi and Fontana, 1996).

The temperature index method, also called degree-day model, offers an option to circumvent the data problem. Since in the process-based method, air temperature is already a predominant variable energy budget equations, it is logical to explore the possibility of removing other variables which are not routinely available, by statistical regression. The method has been adopted by many operational hydrological models, e.g. HBV model (Bergström, 1995), SRM model (Martinec and Rango, 1986), even "physically-based"models, such as the WaSiM-ETH model (Schulla and Jasper, 2007) and the SHE model (Bø ggild et al., 1999). The approach has also been validated out of a complete hydrological model in different spatial and temporal scales, as well as under different climate conditions (Semádeni-Davies, 1997; Singh et al., 2000; Schumann and Lauener, 2005), and is well justified by its simplicity and relatively good performance, even when compared with process-based snowmelt models. Recently, Walter et al. (2005) tried to feed the process-based model with only temperature as site-specific input, with all other missing inputs and parameters being estimated empirically, and the results shew no significant differences from the results obtained from temperature-index method. Debele et al. (2009) also suggests that temperature-index snowmelt estimation model is sufficient in case that net solar radiation is dominating the turbulent heat flux, by comparing the process-based and temperature index based approaches within the SWAT model.

Because the nominal melt-rate coefficient is in principle a synthesis of many factors involved in the snowmelt process which vary spatially and seasonally, it is not a constant. Zuzel and Cox (1975) have pointed out the necessity of including meteorological parameters in addition to temperature. There have been many alternatives of degree-day models to account for the time-dependent environmental effects, e.g. wind, albedo, rain-on-snow etc., and a summary can be found in WMO (1986) and Melloch (1999). Inspired by the combination approach of temperature-index with simple energy balance by Anderson (1973), researchers started to explore the possibility to incorporate radiation into the simple temperature index method (Martinec, 1989; Kane et al., 1997; Kustas et al., 1994; Brubaker et al., 1996). In these models, the temperature term and radiation term are generally expressed in an additive form, namely, the temperature and the radiation are in two separated terms.

$$S_m = \begin{cases} CC_t\ (T_a - T_0) + CC_g\ G & \text{if } T_a > T_0 \\ 0 & \text{if } T_a \leq T_0 \end{cases} \tag{5.1}$$

Here, S_m is snow melt rate in water equivalent [L], CC_t is the degree-day factor [L $\mathrm{T}^{-1}\Theta^{-1}$], T_a is the daily average air temperature [Θ], and T_0 is the threshold temperature for snow melt initiation [Θ]. CC_g is a constant converting energy to water depth [E L^3], and G is the net shortwave radiation [E L^{-2}] (Kane et al., 1997) or the balance of both shortwave and longwave radiation (Martinec, 1989; Kustas et al., 1994; Brubaker et al., 1996). In most of

these study, radiation are obtained from station observations, and in some cases longwave radiation are evaluated from other meteorological data, e.g. temperature, humidity, and cloud information. Nevertheless, radiation is assumed to be spatially constant, even though Kustas et al. (1994) have recognized the importance of "obstruction, reflection, emission from adjacent surface"in complex terrain.

However, as shown in previous chapters, the energy input also show a strong spatial variability caused by the topographic factors. Tappeiner et al. (2001) have demonstrated the significant correlation between snow cover duration with the topographic parameters. Several attempts of accounting for the spatial radiation caused by topographic modification using an adapted degree-day model in a spatially distributed way have appeared in the literature, and were summarized by Hock (2003). Male and Gray (1981) has applied a multiplicative formulation of the radiation effects by scaling the standard melting coefficient on horizontal surface with a factor k_R. k_R is the ratio of radiation received on the inclined surface to the radiation on the horizontal surface. When potential radiation is used, k_R equals to the ξ in Eq.8.25.

$$S_m = \begin{cases} CC_t \; k_R \; (T_a - T_0) & \text{if } T_a > T_0 \\ 0 & \text{if } T_a \leq T_0 \end{cases} \tag{5.2}$$

Male and Gray (1981) applied the Eq.5.2 in a semi-distributed way, i.e. dividing the catchment into several elevation bands and aspect/slope classes. Braun et al. (1994) and Dunn and Colohan (1999) applied similar semi-distributed multiplicative approach, and the radiation used for calculating k_R are monthly mean. Cazorzi and Fontana (1996) proposed a fully-distributed application of multiplicative temperature-index method. They applied again the monthly mean clear-sky solar radiation for calculating k_R, and justified it by showing that k_R is rather time-invariant, which is somehow debatable. In contrary to Cazorzi and Fontana (1996) who suggested using smaller time-step of k_R will not improve the model performance, but rather increase the computation burden, Hock (1999) believe that a hourly varying melt factor according to the spatio-temporal variation of clear-sky direct solar radiation performs better in terms simulation of daily and sub-daily discharge pattern. Except that Hock (1999) has tried the additive formulation, all the other distributed and semi-distributed radiation incorporation follow the multiplicative formulation.

Based on a review of temperature-index methods, (Hock, 2003) concludes that temperature-index models need to be enhanced "in order to bridge the gap between restricted data availability and increasing demand for high resolution estimates of melt rates in space and time". In this work, different formulations of the radiation index in the degree-day model, i.e. multiplicative and additive, shortwave radiation and all-wave radiation, potential and actual radiation, time-invariant and time-dependent radiation index, all implemented in fully-distributed way, will be tested, and their performance will be compared.

5.1.2 Remote Sensing for Snow Modeling

Recent advancement in remote sensing has provided more information for driving, calibrating and validating snow modeling. Immerzeel et al. (2009) used the MODIS SCE data

to drive the Snow Runoff Model (SRM) to investigate the climate change scenarios of Himalayan river basins. Corbari et al. (2009) has successfully applied the elevation corrected MODIS SCE data to calibrate a snow accumulation and melt model. Andreadis and Lettenmaier (2006) assimilated the MODIS SCE and ASMR-E SWE data with Ensemble Kalman filter (EnKF) into the Variable Infiltration Capacity (VIC) model to accommodate both model errors and satellite data errors. Nagler et al. (2008) applied the compensated MODIS SCE data and the radar snow image of Envisat ASAR data in the SRM model. Durand et al. (2008) merged the high temporal resolution MODIS data with the high spatial resolution Landsat Enhanced Thematic Mapper(ETM+) for reconstructing the SWE with model. Tong et al. (2010) used SSM/I SWE in combination of MODIS 8-day composite data to derive the snow distribution.

There is an array of satellite sensors to obtain SCE and SWE data respectively. A good overview can be found in Schmugge et al. (2002). Some frequently used remote sensing snow data are listed in Table 5.1

Table 5.1: List of frequently used remote sensing snow data

Type	Data	Platform	Spatial resolution	Temporal resolution	Launched time
Optical	MODIS	AQUA	500m	daily	2002
		TERRA			2000
	AVHRR	TIROS-N	1.25km	twice daily	1978
	MERIS	ENVISAT	1.20km	3 days	2003
Thermal	TM, ETM+	Landsat	30m	16 days	1972
Active microwave	ASRA	ENVISAT	12.5km	3 days	1995
Passive microwave	SMSR-E	AQUA	25km	daily	2002
	SSM/I	DMSP	25km	daily	1987

In general the optical remote sensing provides data with superior time and spatial resolution, but have problems with cloud cover. Microwave Radar can penetrate the cloud, but has in general very low spatial resolution. Thermal spectrum, instead, has a high spatial resolution but low time resolution. All the sensors except passive microwave provides only the qualitative SCE data. Passive microwave sensors can derive the quantitative SWE, and overcome the cloud problem. But the strongly varying snow and land cover properties severely impairs the data accuracy. Several studies have revealed that MODIS data shows an agreement with observation over 80% (Tekeli et al., 2005; Klein and Barnett, 2003) and in some area up to 95% (Parajka and Blöschl, 2006). The superiority of spatio-temporal resolution and accuracy make it the most frequently used operational remote sensing data, with sometimes other remote sensing sources being used as auxiliary data. Because of the MODIS cloud problem, most studies applying MODIS data have taken only the clear images, e.g. cloud cover less than, for example 20% (Andreadis and Lettenmaier, 2006; Nagler

et al., 2008). In this work, combination of MODIS AQUA and TERRA daily SCE data will be used with no additional processing.

5.2 Methodology

Traditionally the standard degree-day model and the different adaptation of radiation degree-day models are calibrated and validated with snow lysimeter or the hydrography, or the combination of both. The objective of this work is to compare the different formulation of radiation degree-day model. If other runoff generation processes of a hydrological model are involved, and model performance is judged by hydrograph, then the error compensation or propagation of different model components can not be properly evaluated. Therefore, in this study, only the snow accumulation and melt will be simulated, and criteria will be the SCE information. The binary snow pattern is a complementary to the discharge measurement, because it provides the information where the water has originated (Western and Grayson, 1998). Although snow cover information is not a state variable as quantitative as snow depth, SWE or hydrograph, but it is the most objective information, which is not contaminated by any other measurement or modeling errors. Moreover, the snow cover information for a given cell is just an qualitative massage, but the SCE which integrates the information over an area, does offer an quantitative objective function to evaluate the model performance.

In this research, the Heidke Skill Score (HSS)(Heidke, 1926), which is commonly used in quantifying the quality of meteorological forecast, is defined as the objective function, and optimized by simulated annealing. The outcome of the simulation or prediction of a binary system can be expressed as a contingency table 5.2. The cell counts for each of the four possible combinations of simulation/prediction and observed event are represented by a, b, c and d. $n = a + b + c + d$ is known as the sample size. HSS is defined as following (Livezey, 2003):

$$\text{Base Rate:} \quad s = \frac{a+c}{n} \tag{5.3}$$

$$\text{Hit Rate:} \quad H = \frac{a}{a+c} \tag{5.4}$$

$$\text{False Alarm Rate:} \quad F = \frac{b}{b+c} \tag{5.5}$$

$$\text{Proportion Correct:} \quad PC = \frac{a+d}{n} \tag{5.6}$$

$$\text{Expected Proportion Correct:} \quad E = (\frac{a+c}{n})(\frac{a+b}{n}) + (\frac{b+d}{n})(\frac{c+d}{n}) \tag{5.7}$$

$$\text{Heidke Skill Score:} \quad HSS = \frac{PC - E}{1 - E} = \frac{a2(1-s)(H-F)}{s + s(1-2s)H + (1-s)(1-2s)F} \tag{5.8}$$

$$HSS = \frac{a\ d - b\ c}{(a+c)(c+d) + (a+b)(b+d)} \tag{5.9}$$

HSS measures the fraction of correct simulations after eliminating those simulations which would be correct due purely to random chance. (Corbari et al., 2009) applied the correct performance index (CPI) to evaluate the simulation of snow cover, by which the CPI is actually the hit rate. Since the goodness of simulation depends on maximizing the number of hits while minimizing the number of false alarms, the hit rate alone is insufficient for measuring the simulation system.

Table 5.2: Contingency table of simulation or prediction of a binary system

Simulation/	Observed		
Prediction	Yes	No	Total
Yes	a	b	$a+b$
No	c	d	$c+d$
Total	$a+c$	$b+d$	$a+b+c+d=n$

Several researchers tried to reconstruct the MODIS snow cover map using spatial or temporal filter (Parajka and Blöschl, 2008; Gafurov and Bárdossy, 2009), but the author deems that this will introduce additional errors. Therefore in this work, only the combination of original MODIS AQUA and TERRA data are used to avoid any artificial errors from data processing. Since in this work, the different formulations of degree-day model are investigated in a fully-distributed way, the interpolation of spatial temperature and precipitation data will inevitably introduce errors. To minimize the errors introduced by such interpolation, the models are calibrated using station data only. For validation, the spatially interpolated input are used.

Besides the snow cover type, the precipitation type resulted from the snow accumulation routine of the models is also compared with the observed rainfall type data.

5.3 Data

An area from Baden-Württemberg is taken for this study (see Fig.5.1). In this region, there is no persistent annual snow cover, but just event-based snow cover during the winter time. Because the models are not calibrated with discharge, the study area is not necessarily a water basin. The only criteria is that the selected study area is able to address the issue of topographic effects. For the convenience of the data processing, a rectangular area covering part of the Blackforest and part of the Swabian Alps is taken for this study. Precipitation data, both amount and type are available at 125 stations, and 47 out of them provided also temperature. The solid circle in Fig.5.1 shows the precipitation stations, and the double circle shows the temperature data. The study area is constrained within the station covered area to avoid the extrapolation for gridded data. MODIS TERRA data is available since the beginning of 2000, and AQUA data is provided for the time period started from July 2002. In the study, the overlapping time period of AQUA and TERRA data since Fall 2000 is used. The AQUA and TERRA data are simply combined to reduce the cloud cover. For the cells that AQUA and TERRA provide contradictory data, the cell is marked as cloud.

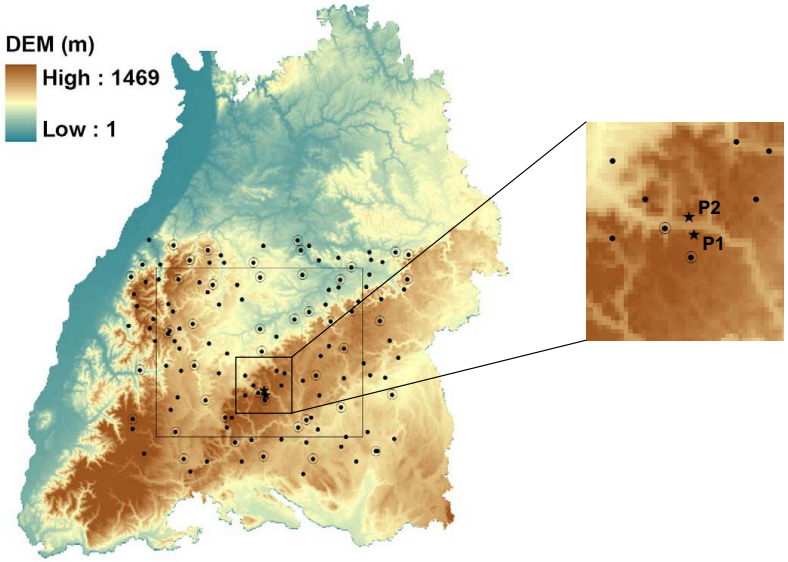

Figure 5.1: Study area and the available observation stations (Solid circle denotes precipitation stations, double circles are temperature stations. P1 and P2 are selected points for detailed investigation.)

5.4 Preliminary Investigation of Radiation on Snow

To check the spatial radiation caused snowmelt variability, a simple statistical analysis of snow cover fraction with potential solar radiation is carried out for the selected very clear days (snow cover area (SCA) fraction larger than 70%) of snowmelt events. Assume an homogeneous spatial snowfall, the SCA fraction of each class during the snowmelt is supposed to be inversely related to the accumulated actual melting energy since the beginning of the snow melt event. Here the mean potential radiation of each class is used as an surrogate of the accumulated actual melting energy. A negative correlation of snow cover with potential solar radiation is expected. Snowmelt event are identified based on the consecutive SCA fractions. Here the snowmelt event in December 2004 is selected. On Dec. 11, the sky is considerably clear, Fig.5.2 shows the corresponding snow cover situation. First, the study area is divided into 10 classes according to the received potential radiation. Then, the SCA fraction of each class on the clear day is calculated. The correlation of the potential radiation of each class with the snow cover fraction of the corresponding class on the day is as high as -0.95. A further correlation analysis considering the land cover type is also conducted for the period 2002~2007, and for each snow melt event such high negative correlations can be found. The simple correlation analysis confirms again the importance of solar radiation in snow melting.

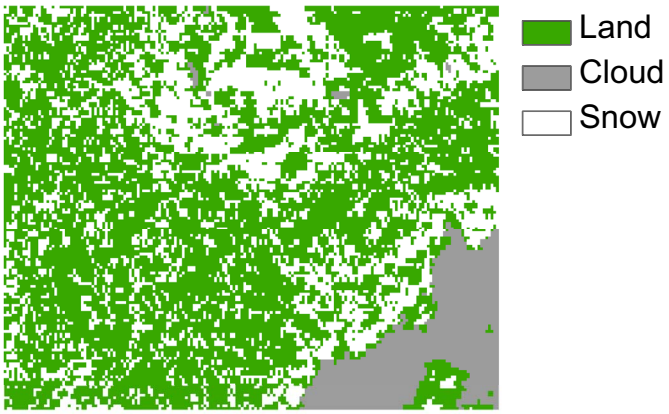

Figure 5.2: MODIS snow cover on Dec. 11, 2004

5.5 Formulations of Different Radiation Degree-Day Model

In the literature, additive and multiplicative formulations of radiation degree-day model considering either extraterrestrial shortwave radiation, actual shortwave radiation, or actual all-wave radiation can be found. In this section we will compare 11 different adaptations of the degree-day model.

Model 1: Simple degree-day model

The degree-day model which considers the melting energy input by rainfall, is taken as the reference degree-day model in this study. The model is expressed as the following mathematical form:

$$S_m = \begin{cases} CC_t(T_a - T_0) & \text{if } T_a > T_0 \\ 0 & \text{if } T_a \leq T_0 \end{cases} \tag{5.10}$$

$$CC_t = min(CC_{max}, CC_0 + k_p\, P_l) \tag{5.11}$$

$$P_l = \begin{cases} P_r & \text{if } T_a > T_0 \\ 0 & \text{if } T_a \leq T_0 \end{cases} \tag{5.12}$$

with	CC_{max}	:	a limiting value to the degree day factor [$\mathrm{mm}\ \Theta^{-1}\mathrm{T}^{-1}$]
	CC_0	:	degree-day factor when there is no rainfall [$\mathrm{L}\ \Theta^{-1}\mathrm{T}^{-1}$]
	k_p	:	rainfall enforcement constant [$\Theta^{-1}\mathrm{T}^{-1}$]
	P_l	:	daily depth of liquid precipitation [L]
	P_r	:	daily depth of total precipitation [L]
	T_a	:	mean daily air temperature [Θ]
	T_0	:	threshold temperature for snow melting [Θ]

Model 2: Multiplicative mid-day radiation index

Model 2 includes a radiation index which is a function of the slope, aspect and the day number (see. Eq.5.16), and the radiation index k_R is approximated by the ratio of extraterrestrial radiation on inclined surface to the extraterrestrial radiation on horizontal surface at noon time(mid-day), i.e. solar hour angle $\omega = 0$. Refer to Eq.8.4 and 8.12, one can obtain k_R through Eq.5.16. The elevation effect is reflected by the lapse rate using the external drift kriging (EDK) of temperature. In model 2, the Eq.5.11 is changed to:

$$CC_t = min(CC_{max}, k_R\, CC_0 + k_p\, P_l) \tag{5.13}$$

$$k_R = \frac{I_{0\beta}}{I_{0h}} \tag{5.14}$$

$$= \frac{cos\theta}{\cos\theta_z}\bigg|_{\omega=0} = cos\beta - sin\beta\ tan(\psi - \delta)\ cos\gamma \tag{5.15}$$

$$= cos\beta - sin\beta\ tan(\phi - \delta)\ cos\gamma \tag{5.16}$$

with
$I_{0\beta}$: extraterrestrial radiance on inclined surface at mid-day [E $L^{-2}T^{-1}$]
I_{0h} : extraterrestrial radiance on horizontal surface at mid-day [E $L^{-2}T^{-1}$]
θ : solar azimuth angle of inclined surface [L]
θ_z : solar azimuth angle of horizontal surface [L]
ω : solar hour angle [L]
β : surface slope [L]
ψ : geographic latitude [L]
δ : solar declination angle [L]
γ : aspect of the surface [L]

The underlying simplifications and assumptions for this formulation include:

1. the longwave radiation is negligible;
2. albedo is considered to be spatially homogeneous;
3. daily potential radiation is approximated by the mid-day radiation, i.e. the hour angle ω and solar azimuth ψ both are equal to zero.

Model 3: Multiplicative mid-day actual radiation index

In model 3, the radiation index is expressed as the ratio of actual solar radiation on the tilted surface($G_{\beta b}$ [E L^{-2}]) to the horizontal surface approximated by mid-day(G_{hb} [E L^{-2}]). That is

$$k_R = \frac{G_{\beta b}}{G_{hb}} \tag{5.17}$$

The actual radiation on inclined surface under cloudy condition can be calculated follow the approach in Chapter 2, i.e., based on the diffuse fraction, which is expressed as linear function of the relative sunshine duration n_{rel} (see. Eq.5.18), instead of a quadratic function as in Eq.2.47 to reduce the number of parameters. The potential sunshine radiation is approximated by the value at horizontal surface, i.e. $n_{rel} = n_d/N_{dh}$, N_{dh} can be obtained through Eq.8.7 in Appendix 8.2, and k_d is an empirical parameter to be optimized.

$$K_d = 1 - k_d\, n_{rel} \tag{5.18}$$

Also, for the simplicity, the diffuse radiation is assumed to be spatially even, i.e. independent from the topography. The actual solar radiation is the sum of direct solar radiation($B_{\beta b}$) and diffuse solar radiation($D_{\beta b}$).

$$G_{\beta b} = B_{\beta b} + D_{\beta b} = G_{hb}(1 - K_d)\frac{cos\theta}{cos\theta_z}\bigg|_{\omega=0} + G_{hb}\ K_d \tag{5.19}$$

Eventually we can get

$$k_R = \frac{G_{\beta b}}{G_{hb}} = 1 + k_d\ n_{rel}(\frac{cos\theta}{cos\theta_z}\bigg|_{\omega=0} - 1) \tag{5.20}$$

The formulation of Model 3 allows the consideration of reduced radiation variability due to cloud, for example, in case of complete overcast day degree-day factor of horizontal and inclined surface will be identical.

Model 4: Multiplicative daily radiation index

Model 4 is an improvement of Model 2, by which the ratio of potential radiation on inclined surface and horizontal surface are using the integrated daily value, $H_{0\beta}$ and H_{0h}. Except k_R in Eq.5.16 is replaced with ξ in Eq.8.25 in Appendix 8.2, all other equations remain the same.

$$k_R = \frac{H_{0\beta}}{H_{0h}} = \xi \tag{5.21}$$

Model 5: Multiplicative daily actual radiation index

Model 5 replaces the mid-day approximation in Model 3 with analytical form of the daily radiation. The modification factor of direct radiation using mid-day approximation $\frac{cos\theta}{cos\theta_z}\Big|_{\omega=0}$ is replaced by the daily integrated value ξ.

$$k_R = 1 + k_d\ n_{rel}(\xi - 1) \tag{5.22}$$

Model 6: Net all-wave radiation degree-day model

Model 6 considers the net all-wave radiation. The snow albedo is included to get the net shortwave radiation (Eq.8.27), and the net longwave radiation is obtained following the FAO approach which utilizes only the mean temperature (FAO, 1990) as in Eq.8.28 in Appendix 8.2. The change in snow albedo with time t (days) is described by an empirical relationship from literature (see Eq.5.25).

$$R_{hb} = G_{hb}(1 - \rho_s) + L_n = H_{0h}(a_{ap} + b_{ap}n_{rel})(1 - \rho_s) + L_n \tag{5.23}$$

$$R_{\beta b} = G_{hb}(1 + k_d\ n_{rel}(\xi - 1))(1 - \rho_g) + L_n \tag{5.24}$$

$$\rho_s = 1 - k_{a1}(1 + e^{-k_{a2}\ t}) \tag{5.25}$$

$$k_R = \frac{R_{\beta b}}{R_{hb}} \tag{5.26}$$

with R_{hb} : all-wave radiation on horizontal surface [E L^{-2}]
$R_{\beta b}$: all-wave radiation on inclined surface [E L^{-2}]
G_{hb} : shortwave radiation on horizontal surface [E L^{-2}]
ρ_s : snow albedo [$-$]
L_n : new longwave radiation [E L^{-2}]
a_{ap} : Angström-Prescott coefficient [$-$]
b_{ap} : Angström-Prescott coefficient [$-$]
k_{a1} : empirical coefficient [$-$]
k_{a2} : empirical coefficient [$-$]
t : number of days after the first snowfall [$-$]

Here a_{ap} and b_{ap} are the Angstrom-Prescott coefficients using the extraterrestrial radiation, which takes values estimated in Chapter 2.

For each multiplicative formulation, there is a corresponding additive alternative. When the additive formulation is used, the absolute quantity of radiation has to be calculated.

Model 7: Additive mid-day potential radiation index

Model 7 is the additive formulation of Model 2, with the snowmelt formulation as Eq.5.1. The rainfall melting reinforcement is considered in the same way as in the multiplicative formulation. The half of the mid-day radiation is used to approximate the daily average radiation R. Again the sunshine duration is approximated by the simple case of horizontal surface. Here the radiation is not the actual value, therefore consideration of snow albedo is not necessary. The "*" means an arbitrary surface, which can be horizontal or inclined.

$$R = 0.5\ I_*0\ N_{dh}\ (cos\beta\ cos(\phi - \delta) + sin\beta cos\gamma\ sin(\phi - \delta) \tag{5.27}$$

Model 8: Additive mid-day actual radiation

Model 8 is corresponding to Model 3. The difference is that in the multiplicative formulation, the snow albedo is canceled off, but for the additive formulation, the snow albedo is kept in the equations.

$$G_{hb} = 0.5\ I_{0h}\ N_{dh}\ (a_{ap} + b_{ap}\ n_{rel}) \tag{5.28}$$

$$G_{\beta b} = G_{hb}\ (1 + k_d\ n_{rel}(\frac{cos\theta}{cos\theta_z}\bigg|_{\omega=0} - 1)) \tag{5.29}$$

$$R = G_{*b}\ (1 - k_{a1}(1 + e^{-k_{a2}\ t})) \tag{5.30}$$

Model 9: Additive daily potential solar radiation

The basic equations of Model 9 are modified based on Eq.5.1, and radiation is taking the analytically integrated daily value of the horizontal surface or inclined surface. The calculation of H_{0*} can be found in Appendix I.

$$R = H_{0*} \tag{5.31}$$

Model 10: Additive daily actual solar radiation

Model 10 is similar to Model 8, but instead of mid-day actual radiation, it uses the analytically integrated daily solar radiation using the Angström-Prescott approach.

$$G_{hb} = H_{0h}\ (a_{ap} + b_{ap}\ n_{rel}) \tag{5.32}$$

$$G_{\beta b} = G_{hb}\ (1 + k_d\ n_{rel}(\xi - 1)) \tag{5.33}$$

$$R = G_{*b}\ (1 - k_{a1}(1 + e^{-k_{a2}\ t})) \tag{5.34}$$

Model 11: Additive daily actual all-wave radiation

Model 11 uses the all-wave radiation in an additive form. The advantage of the additive formulation is that it can account for the negative radiation balance. Under clear skies the incoming longwave radiation is much less than the longwave radiation loss from a melting snowpack, and meanwhile the large portion of incoming solar radiation are reflected by the fresh snow with high albedo. Consequently the net longwave or even the net all-wave exchange could be negative (DeWalle and Rango, 2008), i.e. there is pure energy loss from the snowpack, which may be compensated by conductive energy transfer from air to snowpack, thus reduce the melting rate caused by temperature. The calculation of the radiation is the same as in Model 6.

$$R = G_{*b}\ (1 - k_{a1}(1 + e^{-k_{a2}\ t})) + L_n \tag{5.35}$$

5.6 Results and Discussion

The models are calibrated at the stations, and validated for all grid points. All models are run from August 2002 to the end of 2007, and the performance are calculated only for the winter days, i.e. the from October of previous year to April of the next year. The calibrated parameters and model performance for selected points are listed in Table 5.3, and the spatial calibration and validation results in Table 5.4. The performance criteria of calibration of the model are measured by two HSSs, one for precipitation type and one for snow cover. For calibration, the simulated precipitation type (rainfall or snow) evaluated by the snowmelt temperature threshold are compared with the observed precipitation type. Spatially interpolated precipitation type is very problematic, therefore HSS for precipitation type is not applied for validation. In general the model performances of calibration and validation (both spatially and at P1 and P2) in terms of HSS do not differ much except for Model-1.

Two simulations are applied to the standard degree-day model: simulation with spatially interpolated temperature by external drift kriging (Model-1a), and simulations with spatial mean temperature measured at the stations (Model-1b), which is essentially a lumped model. The significantly lower HSS of Model-1b (0.646 for precipitation type and 0.767 for snow cover) comparing with the other cases shows that, the distributed degree-day model with interpolated temperature does provide higher accuracy than the lumped model. A detailed look into the contingency table and calibrated model parameters gives more information about the model performance. The optimized parameters are also very reasonable. The degree-day factor for all the radiation snow models are of no exception smaller than the

Table 5.3: List of model parameters and point performance at selected points

	parameters								HSS	
	T_0	CC_0	CC_{max}	k_p	k_d	k_{a1}	k_{a2}	CC_r	$P1$	$P2$
Model-1a	0.259	2.454	1.181	0.012	-	-	-	-	0.580	0.753
Model-1b	-0.172	2.099	1.879	0.043	-	-	-	-	-	-
Model-2	0.202	2.265	0.474	0.054	-	-	-	-	0.605	0.759
Model-3	0.210	2.366	1.113	0.014	0.734	-	-	-	0.616	0.767
Model-4	0.217	2.352	0.936	0.018	-	-	-	-	0.605	0.759
Model-5	0.223	2.392	0.276	0.025	0.503	-	-	-	0.616	0.765
Model-6	0.225	2.280	0.710	0.021	0.618	0.377	0.179	-	0.582	0.753
Model-7	-0.495	1.825	1.526	0.020	-	-	-	0.303	0.612	0.778
Model-8	0.286	2.340	1.831	0.015	0.051	0.325	0.203	0.051	0.612	0.766
Model-9	0.514	0.874	1.731	0.012	-	-	-	0.371	0.580	0.758
Model-10	0.188	2.112	1.967	0.021	0.671	0.522	0.282	0.242	0.612	0.777
Model-11	0.062	1.798	2.216	0.001	0.811	0.378	0.305	0.608	0.600	0.778

degree-day factor of the standard model. It is straightforward for the additive formulations, where the introduction of radiation melting term offsets the temperature melting factor. For the multiplicative formulation, the degree-day factor for the standard model can be understood as a spatial average of all cells, while for the radiation snow models, it is the reference melting factor of the horizontal surface. Furthermore, for the multiplicative formulations, models applying actual radiation have an larger degree-day factor than the models applying potential radiation, which is reasonable, because the potential radiation is larger always than the actual radiation.

For a detailed investigation of the model performance, two specific points, P1 and P2, are selected. The two points are lying closely in the same elevation belt, with P1 in north slope and P2 in south slope. The topographic information of P1 and P2 are given in Table 5.5. Because the two points are located closely to each other and in the same elevation, the temperature of the two stations are almost identical. The difference in the melting process at the two points can be considered mainly being resulted from the radiation difference.

The model performance for the selected points are listed in the last two columns in Table 5.3. In general the radiation model improves the HSS at the two points. The simulated SWE by the 11 models are plotted together with the MODIS snow cover information of a snow event between Jan.27 and Mar. 10, 2002 in Fig.5.3. Because some of the model results are somehow similar, only the results of Model-1, Model-2, Model-3, and Model-11 are demonstrated here. First of all, the melting process at the two points reflected by MODIS snow cover data have shown a clear radiation enhancement at the southern slope. Despite the cloud disturbance, the MODIS data shows that, snow persisted at P1 until Mar. 5, while at P2, snow is melted off since Mar. 4. Because Model-1 does not account for the radiation effects, the simulated SWE curve at two points are almost identical (Fig.5.3a). With the potential radiation being approximated by mid-day radiation, the simulated snow cover

Table 5.4: List of model performance of station calibration and spatial validation

	calibration					valibration				
	HSS	a	b	c	d	HSS	a	b	c	d
Model-1a	0.708* 0.814**	1121 210	372 7	290 85	4852 6617	0.661	2283948	923857	625565	8218757
Model-1b	0.646* 0.767**	949 187	462 1	290 108	4934 6623	0.636	1894106	489757	1015407	8652857
Model-2	0.708* 0.814**	1121 210	373 7	290 85	4851 6617	0.694	2193518	619905	715995	8522709
Model-3	0.708* 0.814**	1121 210	373 7	290 85	4851 6617	0.694	2191807	617325	717706	8525289
Model-4	0.707* 0.814**	1120 210	373 7	291 85	4851 6617	0.694	2195864	624463	713649	8518151
Model-5	0.707* 0.814**	1120 210	373 7	291 85	4851 6617	0.694	2192267	617804	717246	8524810
Model-6	0.711* 0.814**	1119 210	363 7	292 85	4861 6617	0.692	2199072	637563	710441	8505051
Model-7	0.713* 0.729**	1078 173	298 1	333 122	4926 6623	0.694	2102981	495859	806532	8646755
Model-8	0.713* 0.814**	1121 210	372 7	290 85	4852 6617	0.694	2204560	636708	704953	8505906
Model-9	0.710* 0.857**	1116 229	361 7	295 66	4863 6617	0.695	2193848	617193	715665	8525421
Model-10	0.707* 0.797**	1106 203	353 7	305 92	4871 6617	0.695	2189767	607473	719746	8535141
Model-11	0.710* 0.789**	1110 199	352 6	301 96	4872 6618	0.696	2203692	624794	705821	8517820

*HSS for snow cover. **HSS for precipitation type.

Table 5.5: List of characteristics of selected points

	alt	asp	slp
P1	937	350.11	9.01
P2	915	187.78	5.91

at P1 lasts longer than at P2 (Fig.5.3b). Because the radiation difference is diminished due to cloud when actual radiation is applied, the melting process are prolongated two or three days, as it can be seen for P1 in case of Model 3 (Fig.5.3c) and Model 11 (Fig.5.3d). Because

Model 11 applies all-wave radiation, so the outgoing long-wave will reduce the total energy input to the snow pack, the snow melting process is again slightly delayed as comparing to Model 3. The radiation signal contained in the curve is not so strong, but still detectable. In general, the introduction of the radiation factor into the degree-day model leads to a more realistic melting process with regarding to the MODIS information. It also models the spatial difference more reasonably.

5.7 Discussion

In this study, different formulations of radiation degree-day models have been compared in terms of their capacity of simulating snow melting process. In general, the radiation models show higher accuracy than the standard degree-day model, and there is little performance difference among the different formulations, no matter additive or multiplicative, actual or potential radiation, shortwave or all-wave radiation. The author still believes there is some difference which can not be detected by the data currently being used. Applying the original MODIS data to calibrate and validate the model is a compromise of data availability. Following problems can be identified for our approach:

- The original MODIS data contains errors, for example, it happens that MODIS shows a no-snow cover condition in between several snow cover conditions, and snow on flat region in a hot summer day. To what extent can we trust the MODIS data is not clear. Additional processing attempt to reduce such errors will always bring new errors;
- The original MODIS data is contaminated by cloud. The discrimination power of our approach relies on the transition days from snow to no-snow. If this transition phase is covered by cloud, then the radiation model tempted to fail;
- The fixed threshold temperature is problematic. Even if only the precipitation type is selected as the objective function, the highest HSS for calibration is 0.875.

Despite these problems, both the spatial validation and the point results show that the adapted radiation models perform better than the standard one. The superiority of the more complex formulation may be proved with higher resolution and more accurate data. All of the models apply routinely available data, i.e. air temperature or in addition, the sunshine duration. As to the author, Model-2 provides a conceptually complete, and computationally simple alternative, with relatively good performance, is therefore a good alternative to the standard model. Still the readers are encouraged to choose the model according to the available data and their own preference.

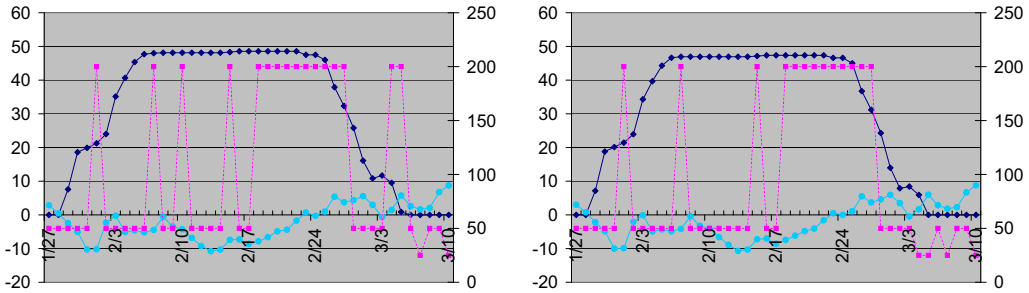

(a) Results of Model 1

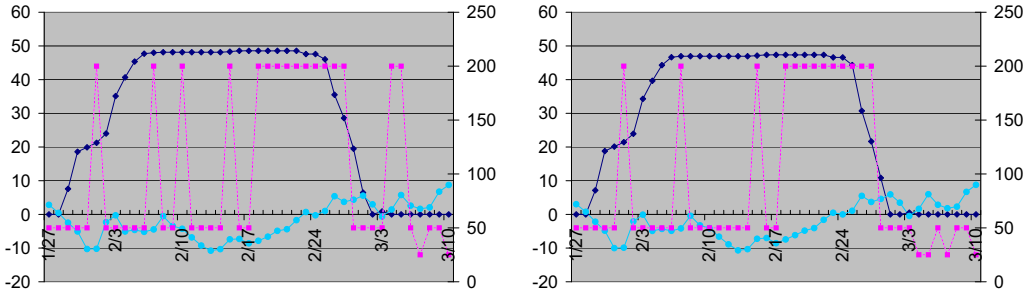

(b) Results of Model 2

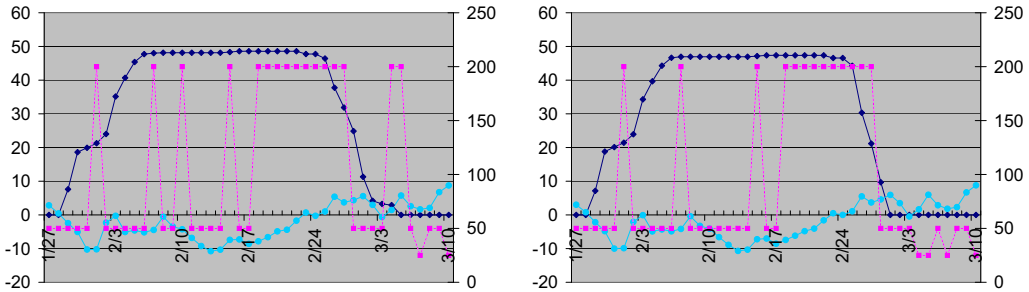

(c) Results of Model 3

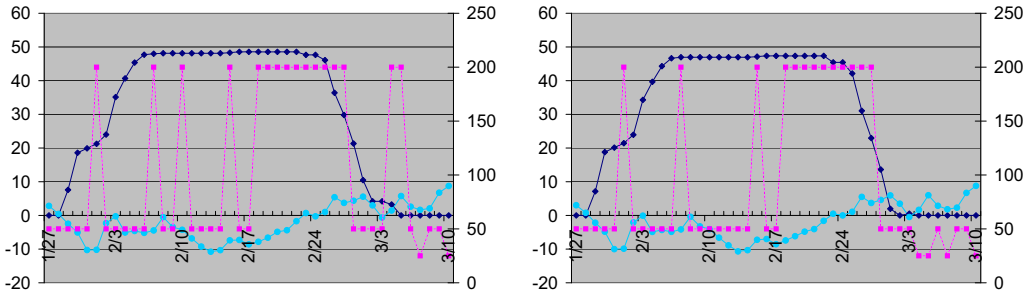

(d) Results of Model 11

Figure 5.3: MODIS snow cover, simulated snow depth and temperature (Figures on the left hand are for P1, and on the right hand side for P2. From the first row to the last row it is in the order of Model-1, Model-2, Model-3, and Model-11. The diamond line to be read at the primary axis is the simulated SWE in mm, and the line with square shows the MODIS snow cover, with 200 for snow, 50 for cloud and 25 for no snow. The circle line represents the temperature.)

6 Space Transformation to Account for Topographic Anisotropy

The presence of mountains can cause local anisotropy for the regionalized variables representing some hydrological parameters (temperature, wind, precipitation). Unlike the global anisotropy which can be modeled by nested variograms or linear transformed coordinate with isotropic variogram, local anisotropy is difficult to quantify. This chapter presents an attempt of modeling such topography-depending anisotropy by nonlinear transformation of the arc distances following the topography with Multidimensional Scaling (MDS) and a global isotropic variogram in the transformed space. Because the vertical distance has more pronounced effects than horizontal distance, a scaling factor of the elevation is introduced to best approximate the topography-induced spatial variability. Being aware to the potential of distortion of coordinates when more points are included in MDS, a local MDS is performed for the nearest neighbors selected for kriging. The MDS transformation is applied to both ordinary kriging (OK) and external drift kriging (EDK). Cross validation results are compared in terms of multi-criteria, such as mean absolute error (MAE), percentage of improved stations (POI), number of days improved (DoI), etc., for standard kriging, kriging with local MDS (LMDS), and kriging with global MDS (GMDS). The comparison is based on 7-year daily temperature and precipitation data to ensure a statistical conclusion.

6.1 Introduction

A prerequisite for any hydrological model is to provide it with the most accurate input data. If these data are of poor quality, then the entire hydrological simulation is flawed from the outset. Although bearing a lot of controversies, distributed hydrological modeling has gradually become a trend for the modeling practice. To provide the model with a spatial input, a proper and accurate interpolation of stations data is indispensable. Particularly in mountainous areas, where complex interactions among topography, vegetation canopies, and climate exist, it is essential that spatial interpolation methods that account for these effects should be applied to estimate the spatial fields of meteorological input (Garen and Marks, 2005).

Kriging is probably the most widely used geostatistical technique to interpolate the spatial variables, and different variants of kriging have been successfully applied in hydro-geology, meteorology, and ecology, etc. (Bárdossy and Lehmann, 1998; Goovaerts et al., 2005; Monestiez et al., 2006). Kriging computes the best linear unbiased estimator at the unobserved location for a given random field based on a spatial dependence model called variogram. The

algorithm considers the underlying spatial variable as random function, and assumes the second order stationarity, i.e. a constant mean over the domain and a distance-depending covariance, which are the prerequisites of applying kriging. But unfortunately many natural parameters do not fulfil the stationarity hypothesis, some non-stationary cases known as drift where the studying variable is a function of some external variables and anisotropy where the stationarity only holds on certain directions, always happen. In case of a globally systematic drift, universal kriging (UK), regression kriging (RK), or external drift kriging (EDK) can be applied (Deutsch and Journel, 1998). Global anisotropy occurs in two major types: geometric anisotropy and zonal anisotropy. The global geometric anisotropy by which the range of variogram changes in different directions with the sill remaining constant can be corrected by a linear transformation of the spatial locations to an equivalent isotropic model, while the zonal anisotropy can be handled by data detrending or a nested variogram model. Local anisotropy is more difficult to deal with, a good summary of methods can be used to deal with the local anisotropy can be found in (Sampson et al., 2001). A usual approach is splitting the domain into globally varying, locally stationary and isotropic sub-regions (Haas, 1990) and smoothing at the boundary of sub-regions (Fuentes, 2001), but dividing the data into small datasets may lead to unreliable statistics (Deutsch and Journel, 1998). Another major group of approaches is nonlinear bijective deformation of the sampling space to a virtual space by multidimensional scaling (MDS), so that in the new space whose dimension may be higher than the original one, the covariance of the samples increases monotonically with distance (Sampson and Guttorp, 1992). The basic idea is to obtain a transformed space which fits the data under the condition of stationarity. So the focus is on achieving a perfect fitting of the data without looking at the physical reason behind the non-stationarity. As we know in the catchment, the spatial distribution of many hydrological variables depends on the topography which affects the heat, air, and moisture transfer. That's why it is not surprising that different weather often appears at two different sides of the mountain. Lehner et al. (2006) has demonstrated the effect of such topographic effects on stationarity, and the possibility to accommodate the topography-induced anisotropy with three different distance functions in an interpolation process similar to but not exactly the same as kriging. Recently Boisvert and Deutsch (2009) have shown a case where the locally varying anisotropy is strictly related to the arc length between two points in some geological formations, and in such cases where the underlying anisotropy is known, they successfully applied MDS to transform the space, and obtained much better results than kriging with original Euclidean distance.

Our approach is an application following the basic idea of Sampson and Guttorp (1992), but we try to address the physical reason, i.e. the anisotropy caused by topography, when transforming the space as done by Boisvert and Deutsch (2009). In normal kriging systems, Euclidean distance or radial distance, i.e. the Euclidean distance is used, which is the length of straight-line path, and does not take into consideration of the topography in between. Lehner et al. (2006) has tried the arc length of convex hull and radial distance plus highest peak in the so-called DayMet interpolation. Because the simple inverse distance interpolation they have used does not require any positive definiteness as required by kriging, the non-Euclidean distances are directly applied without any transformation. In our case, we will define our arc distance, and transform it by MDS. The next section will present the

outline of the method, how the distance is defined, and the criteria applied to evaluate the method. In section 3, the application of different variants of the method will be shown with 7-year daily dataset of temperature and precipitation, and compare the results with standard OK and EDK procedure, which are taken as references. We conclude this study with some theoretical and applied questions for further research.

6.2 Method

6.2.1 Basics of Kriging

Kriging is a group of geostatistical techniques to interpolate the value $Z(x_0)$ of a random field $Z(x_i)$ at an unobserved location x_0 from observations of the neighboring locations $x_i, (i = 1, ..., n)$, based on the spatial dependence model fitted as variogram γ_h or covariance function C_h from the observed data. Kriging computes the best linear unbiased estimator $\hat{Z}(x_0)$ of $Z(x_0)$, as well as the estimation variance $\sigma^2(x_0)$ which is minimized. Kriging has many variants, but here only ordinary kriging (OK) and external drift kriging (EDK) that have been used in this study will be described. The methodology and techniques of the space transformation with MDS described later is general, and can be also applied for other kriging approaches.

For all kriging approaches, the spatial variable $Z(x_i)$ is considered as a random function,

$$Z(x_i) = \mu(x_i) + E_r(x_i) + E_e(x_i) \tag{6.1}$$

where $\mu(x_i)$ represents the expected value of the random field, $E_r(x_i)$ is the random error and $E_e(x_i)$ is the measurement error. For OK it is assumed to be constant over the domain, i.e. $\mu(x_i) = m$, while for EDK it is considered as function of a known external variable, i.e. $\mu(x_i) = a + b\ Y(x_i)$, with a and b being unknown constants. The estimator $\hat{Z}(x_0)$ for any given location is a linear combination of the neighboring points:

$$\hat{Z}(x_0) = \sum_{i=1}^{n} \lambda_i\ Z(x_i) \tag{6.2}$$

$$\text{with} \sum_{i=1}^{n} \lambda_i = 1 \tag{6.3}$$

Under condition of Eq.6.3 called unbiasness condition, the kriging variance

$$\sigma^2(x_0) = Var(\hat{Z}(x_0) - Z(x_0)) = -\sum_{i=1}^{n}\sum_{j=1}^{n} \lambda_i\lambda_j\gamma(x_i, x_j) + 2\ \sum_{i=1}^{n} \lambda_i\gamma(x_i, x_0) \tag{6.4}$$

should be minimized with the Lagrange multiplier to get the weights of λ_i, which results in a linear equation system. Here, $Z(x_0)$ is the true value. When the Euclidean distance is used, and certain legitimated variogram models are applied, the resulting equation system can be proved to be positive definite and solvable. For a given variogram model, the weights λ_i is unique and only depending on the distance, i.e., the configuration of the observation points.

6.2.2 Arc Distance

In standard kriging systems, Euclidean distance is used for both variogram fitting and calculation, which means the spatial dependence and the calculated weights of the neighboring stations in Eq.6.2 is exclusively depending on the Euclidean distance. But two pairs of points with the same Euclidean distance but separated by different topography will have different spatial dependence. So for two points p and q, Euclidean distance is only a function of the point coordinates, i.e. $d_{i,j} = f(p, q)$. To account for the topography between the point pair, we can use distance function suggested by Lehner et al. (2006), i.e. $d_{i,j} = f(p, q, G)$, where G is the elevation function in the domain for all points. In the distance function defined by Lehner et al. (2006), only the surface path between the points is considered, i.e. the intersection of the terrain surface with a vertical plane that contains the two points. This intersection is a planar curve representing the profile of the direct path between the two points along the earth surface, which gives the elevation of any point on the path. Based on the distance function, Lehner et al. (2006) have used different subset of the elevation function G to get different realization of , e.g. arc length of convex hull and radial distance plus highest peak, etc. In this work the whole profile of G will be used for calculating distance. Because the vertical distance has larger effects than horizontal distance, a scaling factor z_s is introduced to the elevation function to amplify the distance in vertical direction so that the topography effects can be reflected properly. Iteration or optimization algorithm can be applied to find the proper scaling factor, but in this work, $z_s = 30$ is applied, based on experimental results.

6.2.3 Multidimensional Scaling (MDS)

As mentioned before, the kriging equation system is positive definite, only if the Euclidean distance is used and proper variogram model is applied. The distance obtained by the distance function $d_{i,j} = f(p, q, G)$ is non-Euclidean, thus if they are directly used in kriging, the resulting equation system will be singular and not solvable. A solution for this problem is to apply Multidimensional Scaling (MDS) to transfer the arc distance into Euclidean space. MDS is the technique to find the coordinates of n points in a p-dimensional geometric space whose inter-point distances approximate the specified dissimilarities of the points (Johnson and Wichern, 1992). The distance function described in the previous section can be considered one type of dissimilarity. Here the detailed mathematics of MDS will not be repeated, the readers can refer to Borg and Groenen (2005) for details. Something deserve to mention here is the difference between *metric* MDS and *non-metric* MDS: *metric* MDS tries to minimize the disagreement of the observed dissimilarities and the inter-point distance in the transformed space, which is sometimes too strict, and the solution may result in points configurations whose rank of distances conflict with the rank of the dissimilarities. Instead of approximate the dissimilarities themselves, *non-metric* MDS tries to preserve the ordering of dissimilarities. Because in kriging, both the absolute distances and the relative distances are important, and absolute distances are more substantial, a metric MDS is applied in this study.

MDS can also be regarded as an optimization algorithm, in the sense that it minimizes the disagreement between the observed dissimilarities or the rank of the dissimilarities in the

transformed space, which is called stress. The most often used stress function is *Kruskal* stress,

$$S_k = \sqrt{\frac{\sum_{i=1}^{n}\sum_{j=1}^{n}(\hat{d}_{ij} - d_{ij})^2}{\sum_{i=1}^{n} d_{ij}^2}} \tag{6.5}$$

Here, d_{ij} and $\hat{d}_{ij}$ is the inter-point distance or dissimilarities of the original space and transformed space respectively. Usually the higher the dimension is, the smaller the stress is, but not always, as we can see later in this study. Usually the dimension where an "elbow"is detected in the scree plot is taken as the optimal dimension.

6.2.4 Cross Validation

Cross validation is used to assess the performance of the interpolation method at the points where observation is available, which can be taken as a proxy of the overall performance. For cross validation, the value at each observation point will be evaluated with the rest data at other points, as if the value at the point under cross validation is unknown, and then compared with the true value (Clark, 1986). Errors from kriging with a valid variogram model should satisfy the following criteria:

$$\frac{1}{n}\sum_{i=1}^{n}(\hat{z}_i - z_i) = 0 \tag{6.6}$$

$$\frac{\frac{1}{n}\sum_{i=1}^{n}(\hat{z}_i - z_i)^2}{\frac{1}{n}\sum_{i=1}^{n}\sigma_i^2} = 1 \tag{6.7}$$

For cross validation, a minimized estimation error is desired. The usually applied error criteria are the mean absolute error (MAE) (Eq.6.8) and the root mean squared error (RMSE) (Eq.6.9).

$$MAE = \frac{1}{n}\sum_{i=1}^{n}|\hat{z}_i - z_i| \tag{6.8}$$

$$RMSE = \sqrt{\frac{1}{n}\sum_{i=1}^{n}(\hat{z}_i - z_i)^2} \tag{6.9}$$

The both are in principle reflecting the same error property. In this study, MAE is chosen as the criteria. Because of the problem of the error compensation among the station estimations, another criteria called percentage of improved stations (PoI), which is, as its name suggested, the percentage of stations whose absolute error have been reduced, is applied. For multi-days results, the number of days that more than 50% stations get smaller error, referred as DoI, is also used.

6.3 Study Area and Data

The study region locates in south-west Germany covering the Swabian Alps, part of the Black Forest and the flood plain of upper Neckar River between them. The presence of two different mountain ranges cause the local anisotropy that are of interest of this study. Because we are interested only in the data, instead of water basin in the hydrological sense, for the convenience in data preparation a rectangular area of about $14,000\,\mathrm{km}^2$ is taken. The elevation in the study area varies from $93\,\mathrm{m}$ a.s.l at the catchment outlet to about $1169\,\mathrm{m}$ a.s.l in the south-west corner of the region (see. Fig.6.1). The climate can be characterized as humid, the long-term average annual precipitation is $950\,\mathrm{mm}$, ranging from $750\,\mathrm{mm}$ in the lower part to over $1200\,\mathrm{m}$ in the Black Forest. A good data coverage is ensured by 47 temperature stations, denoted by squares, and 129 precipitation stations, represented by the solid circles. The data is provided by German Weather Service (DWD) from 2002 to 2007, but due to the station system change, data at a few stations is incomplete. In the worst case, 24 temperature stations and 63 precipitation stations are available, which is still satisfactory. In order to avoid extrapolating, the inner rectangular region is taken for grid interpolation. In case of cross-validation, all stations are checked, and the depth function Rousseeuw and Ruts (1996) is used to find out whether the estimation is interpolation or extrapolation.

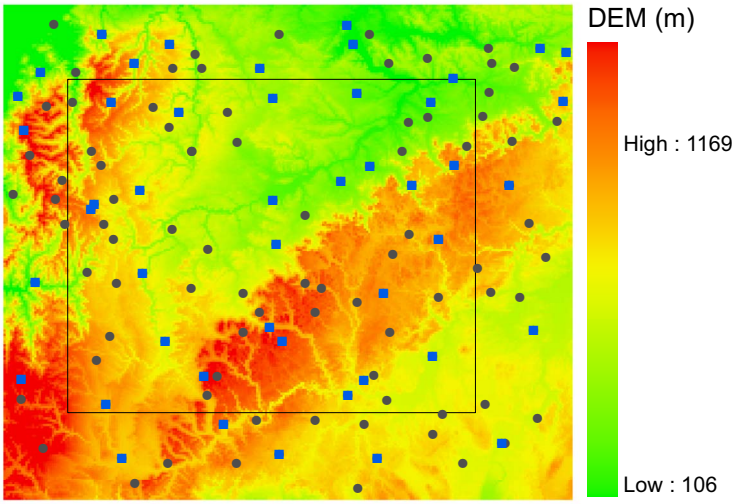

Figure 6.1: Study area and observation stations

6.4 Transformed Space by MDS

The study area is discretized into $1500\,\mathrm{m}$ regular grids. Because the stations may not locate in the centre of one grid, it is shifted to the center for the convenience of arc distance calculation. Due to the micro-topography within the grid, there is some disagreement between the grid elevation and the station elevation within it, but still acceptable ($\pm 100\,\mathrm{m}$).

Fig.6.2a shows the first try of coordinate transformation with MDS, for which all the grids (denoted be blue dots) together with the observed stations (denotes by purple squares) are transformed, and the method is called here global MDS (GMDS). Fig.6.2a-c shows the coordinates in the transformed space for different scaling factors z_s, where a deformation of the original regular grids can be detected.

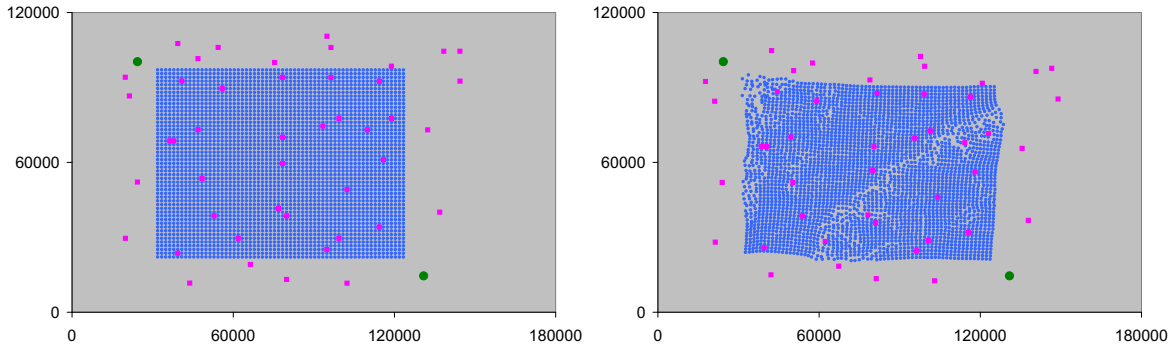

(a) GMDS z_s=1

(b) GMDS z_s=10

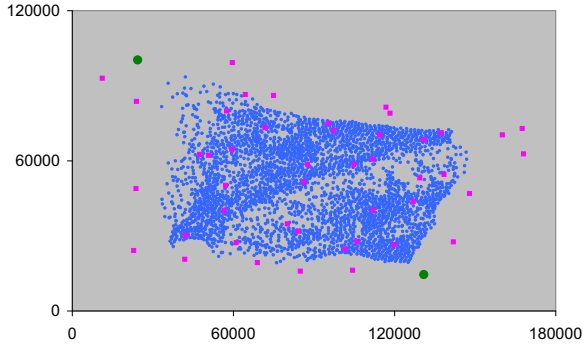

(c) GMDS z_s=30

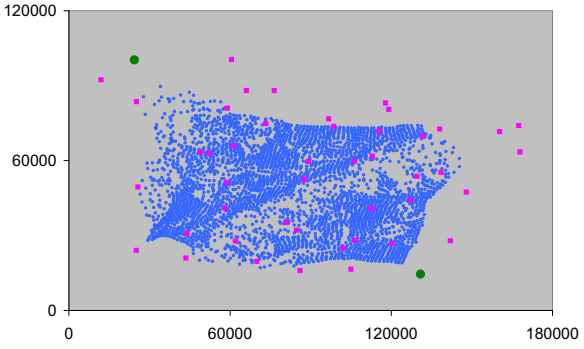

(d) PMDS z_s=30

Figure 6.2: MDS transformed space

The deformation starts from the foot of the hill, i.e. the distance between transition region from flat part to mountain part increases, while the distance of the points within the individual lower and higher region changes much less, which is presumed to be favorable for correct representing topography caused regional difference. As the elevation scaling factor increases, the departure of points at the south-east hill foot can be visualized, and the distortion of the coordinates is more pronounced and the effects of topography are enlarged. To be mentioned, the transformed spaces by MDS may have a different orientation from the original one, and with the introduction of elevation scaling factor, they also differ in size. But what matters for the following kriging process is the relative location of the points, which is kept constant during offsetting, rotating, mirroring, and scaling, defined in this context as *alignment*. Therefore, for the purpose of comparison of the points in different spaces, or what can be called coordinate systems, the resulting spaces from MDS will be again transferred by these alignment techniques with regarding to two reference points, which is denoted as green dots in Fig.6.2.

A problem arises when finer resolution is used, the amount of points will exceed the mem-

ory limit for computation. An alternative to avoid this problem is to transform each grid cell individually with regard to the observed stations, which we call partial MDS (PMDS). An experiment with $z_s = 30.0$ shows that there is little difference between the results of PMDS and GMDS (see Fig.6.2c and Fig.6.2d). For each grid cell, the coordinates of the transformed stations may differ, but the mean standard deviation of the station coordinates is $311\,\mathrm{m}$ in x direction and $260\,\mathrm{m}$ in y direction, which is negligible for the station density in the study area. The similarity of the results of PMDS and GMDS also reveals that the MDS procedure may be dominated by certain pair of points while minimizing the overall stress.

Fig.6.3a demonstrates the change of absolute stress and relative stress (Kruskal stress) for the temperature stations with a scaling factor of 30. The 3-d Scree-plot (Fig.6.3b) regarding both scaling factor z_s and number of dimensions shows that the minimum Kruskal stress is achieved in a 3-dimensional transferred space by MDS when scaling factor is less than a threshold $z_s = 20.0$ in case of the temperature stations. For precipitation stations the threshold is $z_s = 18.0$. Above the threshold value, 4 dimensional MDS gives the optimal result, but for higher dimensional spaces the stress increases slightly. Actually space with lower dimensionality can be regarded as a special case for the high dimensional space. So the increasing stress with dimensionality is a mathematical artifact caused the MDS algorithm. So the 3-dimensional space can be taken as the optimal space with lowest stress.

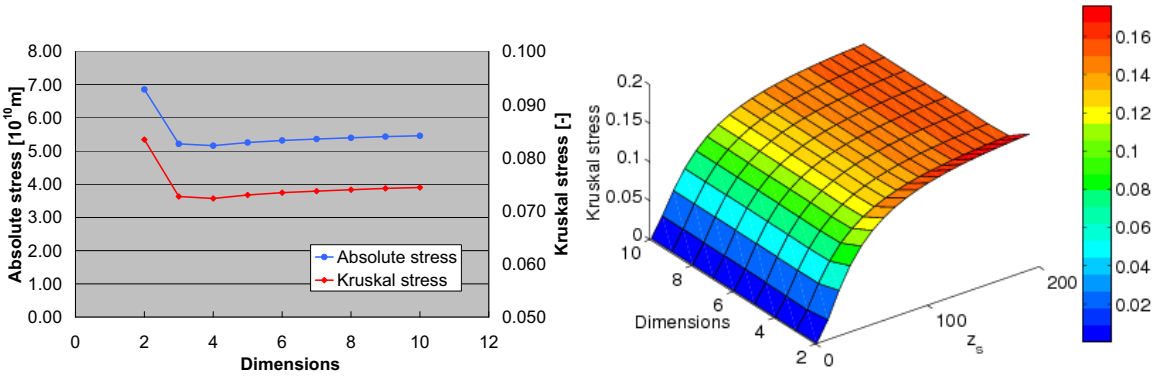

(a) 2D Scree plot plot for $z_s = 30$

(b) 3D Scree

Figure 6.3: Scree plot

A close check of the stress for each pair of distances taking the example of $z_s = 30$ shows that for 32 out of 47 stations, the largest relative stress occurs at one of its 10 closest neighbors, while for 28 out of 47 stations, the smallest relative stress happens to 30 faraway non-neighbors, which means MDS optimizes the overall stress at the expense of distorting small distances. But in Kriging, it is the neighboring points that are important. As a remediation of such undesired distortion of the distances in the transformed space, we propose to use a moving window PMDS (LMDS) instead of the PMDS for the whole domain, which means for each interpolation point, the MDS is done for the point itself together with the neighboring stations that are within the range of the variogram. Given that a certain searching radius and a certain limit is specified for the number of neighbors within the moving window, most points will remain the same with only one or two points being replaced when the window

is shifted, which ensures a smooth transition of coordinates within the domain.

Fig.6.4a demonstrates the different coordinates for LMDS and PMDS with scaling factor $z_s = 30.0$ for the region located in the north-east corner of domain (see Fig.6.4b). The station 2863 is taken as studying points, and all three sets of coordinates are aligned in one coordinate system with keeping the studying point and its closest neighbor 2868 fixed. It shows clear by the figure, that the distortion is smaller by LMPS than by PMDS.

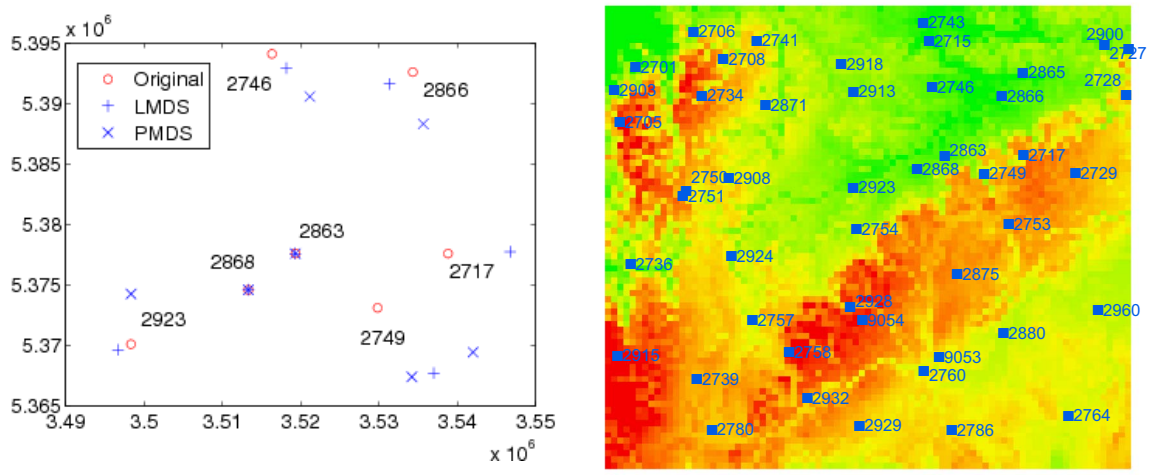

(a) (b)

Figure 6.4: Comparison of tranformed distances by LMDS and PMDS

Table 6.1 shows the original and transformed distances before alignment, as well as the stresses. For both cases, the distances have been increased. The stress, which will introduce errors in kriging process, for PMDS is almost double as in case of LMDS. More important is that, LMDS still keeps the order of the arc distances, while for PMDS the order is changed due to the metric MDS procedure, which shows that with less data included in MDS process, the risk of changing the order of dissimilarities is reduced.

Table 6.1: Comparison of original and MDS-transformed distances for station 2863

Station ID	Euclidean distance	Arc distance	Distance LMDS	Distance PMDS	Rel. stress LMDS	Rel. stress PMDS
2868	6708.2	6950.6	8295.3	9383.7	0.19	0.35
2749	11423.7	25519.6	25034.3	25233.0	-0.02	-0.01
2746	16770.6	18253.4	19011.4	18335.4	0.04	0.00
2717	19500.0	27574.6	33897.7	33737.1	0.23	0.22
2866	21213.2	22002.9	22820.0	27329.4	0.04	0.24
2923	22299.1	26139.0	29699.4	29722.7	0.14	0.14
				$\sum$	0.14	0.17

6.5 Results of Kriging

Correlation analysis of the 6-year data shows that temperature data is highly correlated with elevation, with a mean correlation coefficient of -0.73 and variance of 0.09. No significant correlation between rainfall and elevation has been detected (mean correlation coefficient 0.09 and variance 0.04). In the following the comparison of cross-validation results by PMDS and LMDS with regards to kriging with standard distance will be shown step by step - first the result of one example point, then the result of all points for one day, and finally the statistical results of all points in all days.

6.5.1 Example Results of One Station

A small experiment is done for the station 2863 with its 6 neighbors shown in Fig.6.4 for Jan. 1, 2002 with EDK, the true value (observed value) at station 2863 is -7.1°C. The result shows that the LMDS gives best estimation with smallest error, because the closest point 2868 is getting much closer after transformed by LMDS. The weights of two other nearby stations 2749 and 2717 are reduced comparing with the case of kriging with standard distance, because the two stations are lying on the mountains. The effect of LMDS is that the difference of distance getting larger, i.e. closer points get closer, farther points get further (due to topography), therefore the weights of the points exhibit larger contrast, and consequently the variance is getting larger. Because PMDS has compensated the distance difference among the points, the points which should be physically closer, have been widened. In this case, LMDS generates a better estimation with a larger variance, comparing with PMDS.

Table 6.2: Kriging with original and MDS-transformed distances for station 2863 (Jan. 1, 2002)

Station ID	Temperature (°C)	Weights by std. kriging	Weights by LMDS kriging	Weights by PMDS kriging
2868	-7.0	0.584	0.694	0.555
2749	-9.0	0.328	0.138	0.194
2746	-7.7	0.123	0.091	0.303
2717	-5.2	-0.112	-0.043	-0.080
2866	-6.7	0.108	0.153	0.056
2923	-6.8	-0.032	-0.033	-0.028
	Est.	-7.917	-7.380	-7.732
	Est. var.	0.817	0.821	0.661

6.5.2 Example Results of All Stations

Cross-validation for all stations shows that not all stations get improvement. For an arbitrary selected day (Dec.15,2007) with 24 stations data available, the cross validation results

are shown in Fig.6.5 and Table 6.3. Taking the ordinary kriging with standard distance as reference, for different points, the 4 methods perform differently. The mean absolute error and the percentage of improvement is taken as evaluation criteria. In this case, ordinary kriging with 2 dimensional PMDS transformed distance obtains the lowest overall estimation error, whereas OK with 3 dimensional LMDS has the highest PoI. When other scaling factor values are applied, the results will be changed – a dataset where major points get improvement with one scaling factor may get an overall degradation of in estimation errors with another scaling factor. This shows that a proper scaling factor to reflect the anisotropy properly is important. But at the moment, we have not found a suitable approach to obtain the correct scaling factor. An option might be application of optimization algorithm to for cross-validation to find the best scaling factor and then apply it to interpolation.

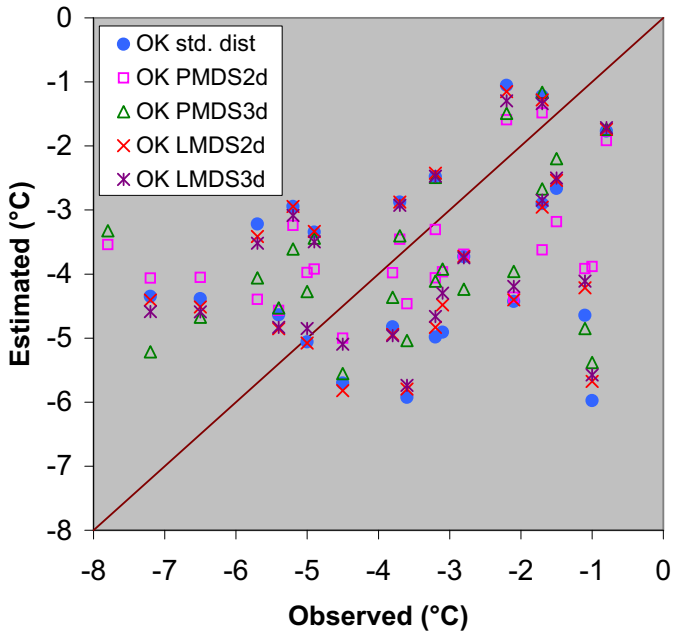

Figure 6.5: Scatter plot of cross validation results for multi-stations

Table 6.3: Kriging with original and MDS-transformed distances for multi-stations (Dec.15, 2007)

Method	MAE	NoI	PoI
OK std. dist	1.840	-	-
OK PMDS 2d	1.414	17	71%
OK PMDS 3d	1.486	19	79%
OK LMDS 2d	1.745	18	75%
OK LMDS 3d	1.631	20	83%

6.5.3 Statistical Results for Multi-stations and Multi-days

The different algorithms are applied to temperature data from Jan.1, 2002 to Dec.31, 2007, in order to draw a statistically significant conclusion. For the 2191 days applying scaling factor $z_s = 30$, following results in Table 6.4. The days for which more than half of the stations get smaller absolute estimation error comparing with the reference case are also counted. Stations are differentiated between interpolation and extrapolation by depth function. When EDK is applied, the kriging results are much better than the corresponding OK, but comparing with the EDK reference case, all methods with MDS transformation show lower performance, except EDK PMDS 3d. The reason might be that part of the non-stationarity or anisotropy is explained by the application of external drift. In general, kriging with MDS transformed distances obtains better results in terms of MAE for OK, and for EDK the MAE of interpolation has been improved. For all cases, the MAE for interpolation are smaller than for extrapolation, but for LMDS, PoI is higher for extrapolation than for interpolation.

Table 6.4: Comparison of kriging with original and MDS-transformed distances for multi-days (temperature)

Method	MAE	MAE(in)	MAE(ex)	PoI	PoI(in)	PoI(ex)	DoI
OK std. dist	1.126	1.080	1.226	-	-	-	-
OK PMDS 2d	1.083	1.041	1.171	0.559	0.564	0.548	1346
OK PMDS 3d	1.054	0.943	1.258	0.554	0.570	0.520	1482
OK LMDS 2d	1.081	0.922	1.469	0.633	0.622	0.658	1443
OK LMDS 3d	1.078	0.928	1.286	0.630	0.607	0.680	1470
EDK std. dist	0.661	0.633	0.721	-	-	-	-
EDK PMDS 2d	0.663	0.631	0.744	0.496	0.496	0.495	913
EDK PMDS 3d	0.653	0.629	0.712	0.508	0.505	0.513	1110
EDK LMDS 2d	0.671	0.632	0.790	0.513	0.512	0.514	553
EDK LMDS 3d	0.665	0.616	0.760	0.518	0.520	0.512	636

The seasonal performance of each method comparing with the standard kriging methods has also been investigated(see Table 6.5), but no significant improvements can be found.

Although no positive conclusion can be drawn from the multi-day results, it shows that PoI for all 4 MDS methods are getting larger for year 2006 and 2007, when only 24 stations instead of 47 stations are available. Fig.6.6 shows the example for OK with 2 dimensional LMDS. This means, when few stations are available in kriging, the MDS approaches work better. It shows that the anisotropy is induced by macro-topography, i.e. large mountains, not by the local micro topography.

6.5.4 Results with Precipitation Data

While the results of temperature data with both OK and EDK show some improvement comparing with kriging with standard distance, the results with precipitation show little

Table 6.5: Seasonal results of temperature kriging

	Method	MAE	MAE(in)	MAE(ex)	PoI	PoI(in)	PoI(ex)	DoI
Winter	OK std. dist	1.233	1.179	1.348	-	-	-	-
	OK PMDS 2d	1.194	1.157	1.272	0.551	0.551	0.551	335
	OK PMDS 3d	1.156	1.019	1.403	0.562	0.580	0.524	394
	OK LMDS 2d	1.185	1.017	1.602	0.642	0.627	0.673	358
	OK LMDS 3d	1.184	1.027	1.420	0.634	0.607	0.691	358
Spring	OK std. dist	1.111	1.063	1.212	-	-	-	-
	OK PMDS 2d	1.071	1.032	1.151	0.550	0.558	0.531	343
	OK PMDS 3d	1.053	0.945	1.250	0.551	0.566	0.518	361
	OK LMDS 2d	1.063	0.902	1.450	0.635	0.619	0.669	376
	OK LMDS 3d	1.061	0.910	1.275	0.630	0.600	0.694	385
Summer	OK std. dist	1.036	0.987	1.141	-	-	-	-
	OK PMDS 2d	0.993	0.940	1.104	0.564	0.578	0.534	357
	OK PMDS 3d	0.971	0.869	1.163	0.553	0.575	0.504	358
	OK LMDS 2d	0.995	0.835	1.385	0.625	0.617	0.644	390
	OK LMDS 3d	0.992	0.842	1.190	0.628	0.608	0.670	389
Autumn	OK std. dist	1.128	1.092	1.204	-	-	-	-
	OK PMDS 2d	1.080	1.039	1.159	0.570	0.568	0.574	311
	OK PMDS 3d	1.042	0.943	1.218	0.552	0.560	0.536	369
	OK LMDS 2d	1.083	0.939	1.443	0.632	0.626	0.645	319
	OK LMDS 3d	1.077	0.933	1.274	0.630	0.614	0.665	338
Winter	EDK std. dist	0.714	0.682	0.782	-	-	-	-
	EDK PMDS 2d	0.726	0.691	0.818	0.487	0.487	0.486	213
	EDK PMDS 3d	0.710	0.679	0.782	0.505	0.506	0.502	280
	EDK LMDS 2d	0.722	0.677	0.854	0.528	0.529	0.525	141
	EDK LMDS 3d	0.715	0.679	0.785	0.539	0.545	0.527	175
Spring	EDK std. dist	0.612	0.589	0.662	-	-	-	-
	EDK PMDS 2d	0.615	0.588	0.683	0.499	0.501	0.494	237
	EDK PMDS 3d	0.609	0.589	0.655	0.510	0.503	0.526	282
	EDK LMDS 2d	0.629	0.593	0.735	0.494	0.500	0.480	127
	EDK LMDS 3d	0.624	0.585	0.697	0.496	0.503	0.483	143
Summer	EDK std. dist	0.626	0.598	0.687	-	-	-	-
	EDK PMDS 2d	0.624	0.594	0.702	0.495	0.496	0.494	231
	EDK PMDS 3d	0.620	0.595	0.681	0.512	0.505	0.527	273
	EDK LMDS 2d	0.637	0.598	0.761	0.499	0.489	0.522	137
	EDK LMDS 3d	0.633	0.576	0.743	0.500	0.494	0.515	155
Autumn	EDK std. dist	0.691	0.663	0.753	-	-	-	-
	EDK PMDS 2d	0.687	0.652	0.774	0.502	0.501	0.505	232
	EDK PMDS 3d	0.676	0.653	0.730	0.504	0.506	0.498	275
	EDK LMDS 2d	0.697	0.661	0.810	0.531	0.532	0.529	148
	EDK LMDS 3d	0.691	0.626	0.815	0.536	0.541	0.526	163

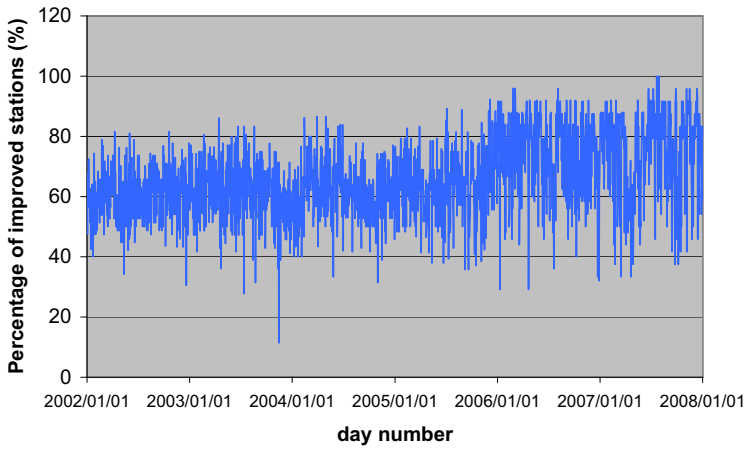

Figure 6.6: PoI for interpolation period from 2002 to 2007

improvement(see Table 6.6). The extrapolation of 3d PMDS gives a very high MAE, but the PoI is also relatively high, which means that few points on the boundary have been extremely distorted by 3d PMDS.

Table 6.6: Comparison of kriging with original and MDS-transformed distances for multi-days (precipitation)

Method	MAE	MAE(in)	MAE(ex)	PoI	PoI(in)	PoI(ex)	DoI
OK std. dist	1.115	1.065	1.367	-	-	-	-
OK PMDS 2d	1.135	1.076	1.423	0.590	0.588	0.600	486
OK PMDS 3d	2.989	1.077	11.442	0.594	0.588	0.620	534
OK LMDS 2d	1.136	1.065	1.470	0.586	0.588	0.577	524
OK LMDS 3d	1.132	1.076	1.284	0.581	0.582	0.576	481
EDK std. dist	1.147	1.102	1.374	-	-	-	-
EDK PMDS 2d	1.192	1.118	1.549	0.580	0.578	0.589	432
EDK PMDS 3d	3.053	1.124	11.582	0.582	0.579	0.599	455
EDK LMDS 2d	1.173	1.098	1.527	0.583	0.585	0.577	445
EDK LMDS 3d	1.169	1.105	1.342	0.582	0.582	0.582	417

The correlograms of the two datasets show that for precipitation, a clear isotropic variogram can be fitted for the time series, while for temperature data, the correlation is more scattered, which means higher non-stationarity (Fig.6.7). The purpose of space transformation with MDS is mainly to assimilate the non-stationarity by changing the distance. If the data is more or less stationary, the method will not provide better results than the standard kriging method. Another reason may lie in the large number of precipitation stations.

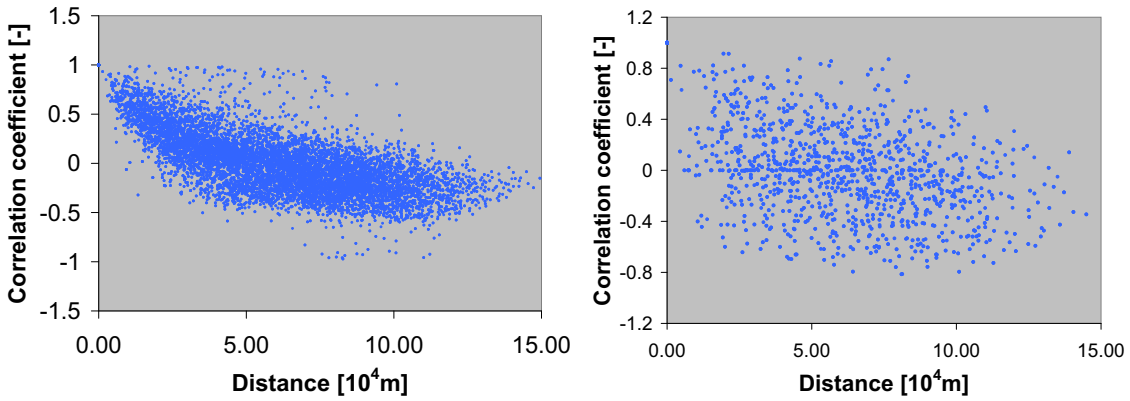

(a) Correlogram precipitation data

(b) Correlogram temperature data

Figure 6.7: Correlograms of precipitation and temperature

6.6 Conclusion and Discussion

In this chapter, the MDS transformed space are applied to reduce the non-stationarity caused by topography for hydrological parameters. Space transformation with global, partial, and local MDS have been checked. Just look at the distances in the transformed space, LMDS provides a more reasonable spaces with less non-stationarity, and PMDS will probably change the order of the points, because the objective function of the metric MDS algorithm is to reduce the overall stress. Although the non-metric MDS is said to be able to preserve the order of the distances, it is impossible when more points with complex dissimilarity are presented in MDS. The point results with both a single station and multiple stations show good improvement with the LMDS method. But to be mentioned, the selected multi-station case is one day with only 24 stations. When the MDS transformations are applied to all stations for 2191 days from 2002 to 2007, no significant improvement can be detected, except for ordinary kriging of temperature data. Still for the last two years when less stations are available, the results are better, which corroborate the results of one-day multi-station case with less stations. The reason might be when more stations are presented, the MDS accounts more for the micro-topography, which has less or nothing to do with the non-stationarity. A solution to remove the micro-topographic effects might be digital elevation model smoothing. The better performance for temperature data than precipitation data shows that the method is only proper for the case, when high non-stationarity are presented. A methodology to check existence of non-stationarity and quantify it are expected, and should be used to evaluate whether the MDS approach is proper or not. An intrinsic problem exists for the MDS algorithm, both metric and non-metric MDS try to minimize the overall stress. Since all the distances are considered equally, the closest points with smaller distance are considered less important in the algorithm. On the other hand, these points are the most important points in the kriging system. A proper MDS scheme, which assigns more weights to the nearest points, are expected to solve this problem.

7 Valley Effects on Precipitation Interpolation

The small-scale ($1\sim10\,\mathrm{km}$) spatial variability of daily precipitation in the alpine region in South Germany is investigated with observed daily precipitation from high-density rain gauges for a period over 40 years, with consideration of the daily general circulation patterns (CPs) defined by SLP(sea level pressure) or alternatively, 500 or $700\,\mathrm{hPa}$ geopotential height anomalies. The daily precipitation at stations located in the narrow-steep valleys is compared with the neighboring stations at the mountain crest in terms of mean value (by one-way ANOVA) and their cumulative probability distribution (Kolmogorov-Smirnov test). The statistical tests are performed specifically for each CP, and also in general without considering CPs. The results reveal that there are two effects governing the spatial precipitation pattern at two different scales - the orographic effect by which the precipitation increases with elevation at a larger scale ($10\sim100\,\mathrm{km}$) and the other, what we call "narrow-valley effect", by which the precipitation in narrow-steep valleys is comparable with the precipitation at the mountain crest at a smaller scale ($1\sim10\,\mathrm{km}$), when the valley is shielded from the moisture flow driven by general circulations. The study confirms the phenomenon that the precipitation is "blind"to the narrow-steep valleys, which is quite often disregarded in hydrological applications, for example, rainfall interpolation from observation data. A kernel smoothing algorithm with different window sizes and directions is applied to smooth the topographic data and fill the narrow-steep valleys, which is consequently used as auxiliary information for external drift kriging (EDK). The cross-validation results show that EDK with DEM smoothed by a certain window size performs better than with the original DEM in terms of both mean square error (MSE) and bias.

7.1 Introduction

Two major topographic effects on precipitation have been reported in the literatures: orographic effects and wind-drift effects. The orographic effects deals with spatial distribution of precipitation at large scale consisting of major mountain-valley topography, and are reflected by an elevation-precipitation relationship at upslope and rain shadowing at leeside. The orographic phenomenon have been confirmed and studied by theory (Houze, 1993; Haven, 2004), modeling (Jiang, 2007), and statistical analysis (Basist et al., 1994; Weisse and Bois, 2001; MarquInez et al., 2003). The wind-drift effects focuses on, instead of the precipitation climatology, the precipitation trajectories affected by topography-conditioned perturbations in the local wind field at fine scale featured by complex terrain, which have also been investigated with both observation data and models (Sharon and Arazi, 1997; Blocken et al.,

2005; Lehning et al., 2008). The orographic effects concerns with precipitation climatology at major mountain-valley areas at the scale of around $100\,\mathrm{km}$, while very few studies look into the climatological precipitation variability at the secondary mountain-valley areas. A climatology study over time scales of years at fine scale of about $25\,\mathrm{km}$ presented by Frei and Schär (1998) already demonstrates that a simple precipitation-height relationship does not exist on the Alpine region, but their study still concerns with regional scale. Wastl and Zängl (2008) have investigated the small scale mountain-valley precipitation difference with selected mountain-valley station pairs, and tried to relate the difference to MM5 simulated wind and vertical moisture profile. They found that in some cases the valley stations receive comparable rainfall as the mountain stations, and in some cases not. Such phenomenon can neither be captured by the orographic effects, nor be reflected in the wind-drift mechanism, forming a spatial gap, as well as a climatological gap that has motivated this work.

The major mountain-valley topography, which will be referred as macro-scale in this paper, is mostly resulted from tectonic movements or glacial carving, is therefore wide and gentle-slope, and reflects the underlying trend in the terrain. The orographic precipitation dominates at this scale and causes mainly a precipitation-height relationship. The secondary mountain-valleys are micro-scale features caused by gully incision, and other secondary surface processes (Jordan, 2007). Yet the distribution of precipitation over mountains at fine scale which is not captured by the precipitation-height relationship, is critically important for flood forecasting (Westrick and Mass, 2001), natural hazard (landslides, avalanches) assessment (Conway and Raymond, 1993), and understanding co-evolution of precipitation and topography (Stolar et al., 2007), which makes statistical and numerical investigation of the rainfall variability at this scale necessary. Meteorological precipitation models can give spatial precipitation distribution, but require detailed input of environmental parameters, such as temperature, lapse rate, wind, and background precipitation, which render the modeling practice rather location- and event-specific (Smith, 2006). Even with most detailed data, current models still have a limited accuracy and capacity in resolving the small scale precipitation. Ultimately model results have to be validated with observation from a dense rain gauge network. Due to the limitation of the modeling approach, statistical studies on topography-altered spatial precipitation have been very popular, which range from pure precipitation-altitude relationship (Sevruk and Nevenic, 1998) to multivariate regression models relating precipitation to more topographic parameters including elevation, slope, orientation and exposure (Prudhomme and Reed, 1998; Sun et al., 2008), and in some cases also wind (Johansson and Chen, 2003) and other climatic factors (Daly et al., 2002). But rain gauge networks seldom have the spatial density that is fine enough to sample the micro-scale variations in precipitation, and the distribution of stations tends to biased towards valley sites. As a consequence, most of these statistical studies are oriented to macro-scale.

In south Germany, a high-density rain gauge network with long time series data enables the investigation of the micro-climatology. In the chapter, the spatial precipitation variability in the mountainous region with a steep relief and narrow valleys in south German State Baden-Württemberg has been analyzed with both parametric and non-parametric statistical approach with consideration of circulation patterns (CPs). The rain gauge stations are first classified into valley and non-valley stations, to assist the comparative statistical analysis and search for a systematic mountain-valley difference. The ultimate goal is to include the

interacting topographic and CP effects in interpolation algorithm to improve spatial interpolation accuracy. So the first part of the paper an introduction of the study domain and the dataset will be given, which will be followed by the presentation of the valley recognition algorithm and the statistical analysis of the precipitation time series. Afterwards an isotropic DEM smoothing as well as an directional DEM smoothing technique will be introduced, and their improvement in improving the cross validation results for EDK will be demonstrated.

7.2 Study Area and Data

7.2.1 Study Domain and Topography

Because this study relies mainly on observational data, the German Federal state with good precipitation data availability and rich topographic features - Baden-Württemberg ($35,751\,\mathrm{km}^2$) is taken as the research areas (see Fig.7.1). Baden-Württemberg locates in south-west Germany, and covers two mountain ranges, black forest in the west and the Swabian Alps in the east. Both the black forest and Swabian Alps extend from southwest to northeast, with the black forest located in the west part and Swabian Alb in the east. The highest peak in the Swabian Alps is $1,015\,\mathrm{m}$, whereas the highest mountain in the black forest stretches to $1,493\,\mathrm{m}$. For the study area, a $30\,\mathrm{m}$ DEM is available from the local environmental agency, and is resampled to $100\,\mathrm{m}$.

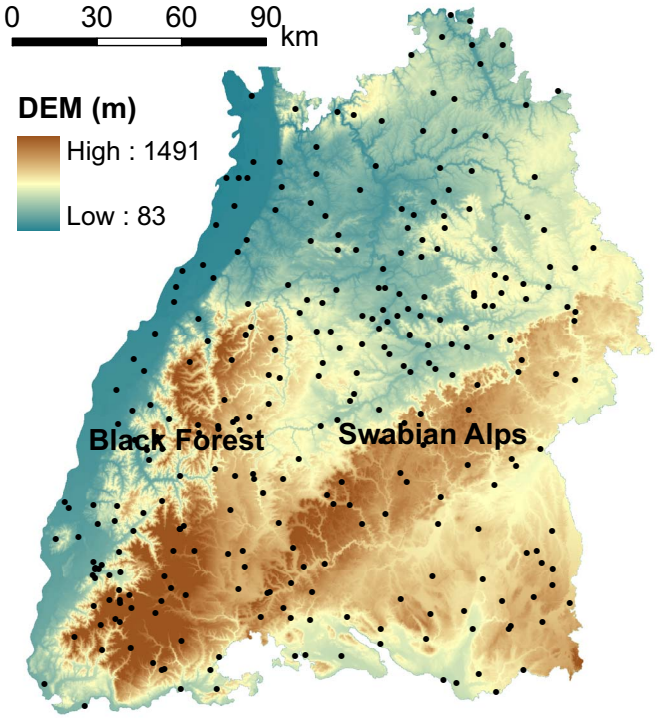

Figure 7.1: Study area and location of rain gauges

7.2.2 Station Data

The basis for the statistical analysis is the rain-gauge observations with high spatial resolution provided by German Weather Service (DWD). In Baden-Württemberg there are in total 294 stations, shown in Fig.7.2a, which is equivalent to a mean gauge distance of around $10\,\mathrm{km}$. In certain regions of study area, the mean gauge distance reaches $2.5\,\mathrm{km}$, with a minimum distance of around $1.5\,\mathrm{km}$. The high density network employed in this study enables the statistical study of mountain-valley precipitation variation at micro-scale. The station data span over 40 years from 1961 to 2007, but during the reference period some stations have been stopped due to the introduction of Radar stations and others newly opened. In general the number of daily stations decreases with time because of the deployment of Radar stations, especially since year 2000. Before 2000, the station density exhibits only slight variations, therefore we take 40 years from 1960 to 1999 as the studying time period.

Fig.7.2b figures shows the altitudinal distribution of the fraction of rain-gauges, the fraction of surface area, and the corresponding mean daily precipitation of stations lying in each elevation band. In the study areas, the number of rain gauges in different elevation belts is in general well correlated to the surface area of the corresponding elevation belt, except for the elevation belt between $1050\,\mathrm{m}$ to $1400\,\mathrm{m}$, where no rain gauge station is available. So no precipitation data is available for this elevation band. Because of the presence of one station at the mountain peek, and several stations on the top of the lower mountain within the study region even the highest peek, are available, which make the comparison of mountain-valley stations possible. The average precipitation of daily mean precipitation shows a increasing trend with the increasing elevation.

7.2.3 Circulation Pattern its Classification

In this work, the station data are analyzed under consideration of the circulation patterns (CPs). CP is the mean air pressure distribution over an area, and is defined using 500 or 700 hPa geo-potential anomalies. Any given circulation type persists for several days and

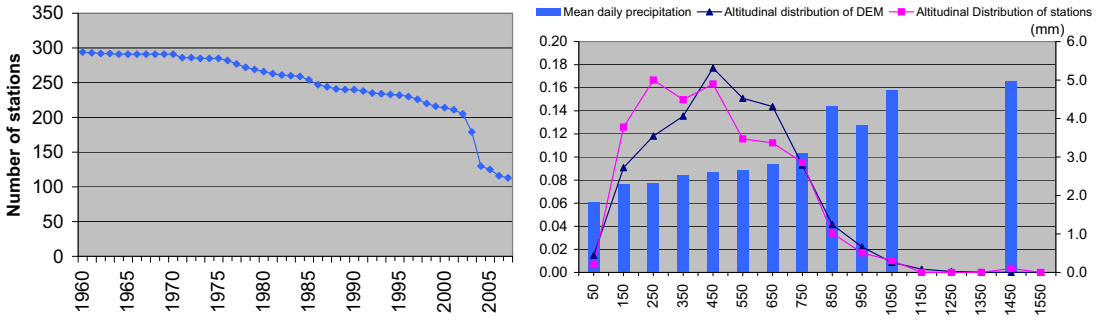

(a) Number of stations

(b) Station statistics

Figure 7.2: Information of rain gauge stations

during this time the main features of weather remain mostly constant across the CP covered region. Then through a rapid transition, another CP will emerge. Similar CPs will generate similar weather conditions, and can be classified by their characteristic pressure field. In this work, the CPs are classified with the automated fuzzy-rule based algorithm by Bárdossy et al. (2002). Fuzzy rules specify the position of high- and low- pressure anomalies, and are then optimized automatically with simulated annealing (SA) algorithm. With the help of the optimized fuzzy rules the pressure fields, i.e. the large-scale atmospheric CPs, can be classified into groups associated with a certain local precipitation fields (Bardossy et al., 2005). For the study area the daily circulation patterns have been classified into 18 groups, and 6 of them are so-called wet CPs, which produce more rainfall than the climatological average (see Table 7.1). Fig.7.3 shows the geopotential anomalies and the Wetness Index of example dry and wet CP respectively. The Wetness Index is the ratio of precipitation associated with each CP to the meteorological mean, with high values indicating wet CPs. CP04 is a dry CP, for which the study region is covered by a high pressure center, whereas CP10 is a wet CP associated with a low pressure center.

Table 7.1: CPs classified by automated fuzzy-rule based algorithm

CP	Direction	Type	CP	Direction	Type
CP01	NE	dry	CP10	NW	wet
CP02	E	dry	CP11	SW	dry
CP03	SE	dry	CP12	SW	dry
CP04	SE,E	dry	CP13	W	dry
CP05	SW	wet	CP14	NW	dry
CP06	W,SW	dry	CP15	SE	dry
CP07	E,SE	wet	CP16	S	dry
CP08	S	dry	CP17	W	wet
CP09	N	wet	CP18	NW	wet

7.3 Statistical Analysis

Because the goal of this chapter is to investigate the effects of narrow-steep valleys, in the first step we will define and identify the target valleys, i.e. separate the station in narrow-steep valleys from the other stations. Then a preliminary study of the mountain-valley station difference will be demonstrated by the scatter plot of station precipitation and elevation. Eventually statistical analysis with Kolmogorov-Smirnov test and One-way ANOVA for selected pairs will give an insight into the spatial precipitation distribution.

7.3.1 Valley Profile Classification

Valleys are formed by river or glacial erosion, or sequential occupation of one after the other. With its erosion, transportation, and sedimentation functions, river will form valleys with

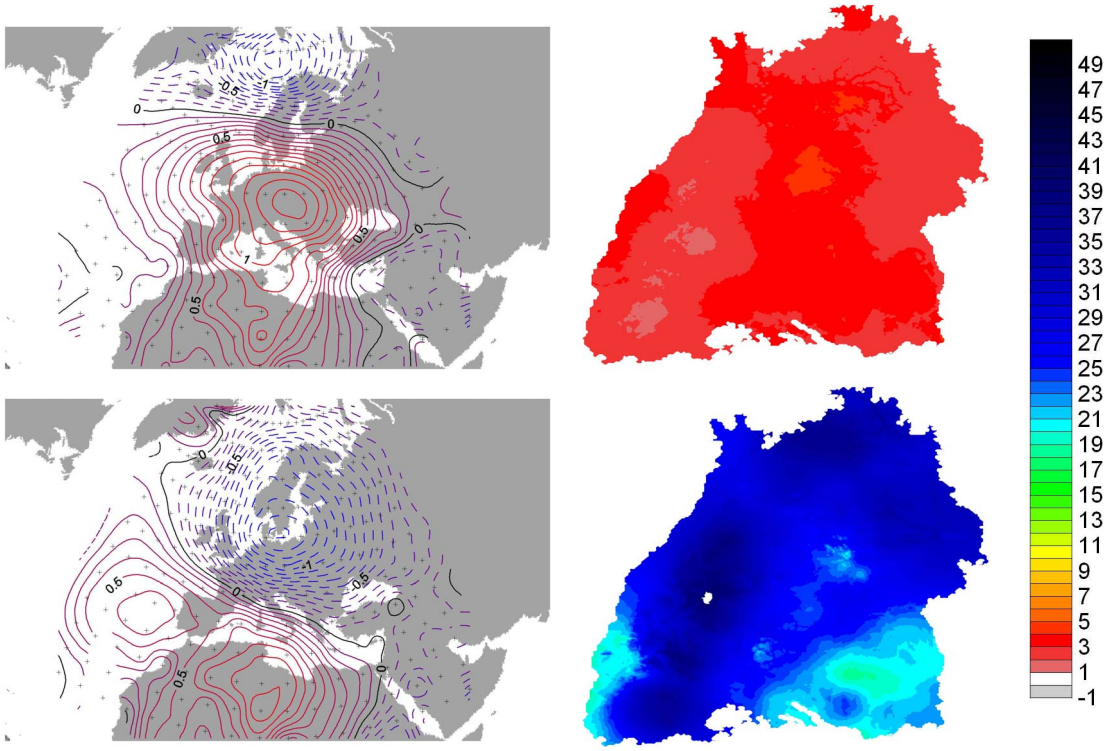

Figure 7.3: Geopotential anomalies and Wetness Index of CP04 (upper) and CP10 (lower)

different cross section shapes depending on the surrounding topography - rivers with steep gradients produce steep walls with a narrow bottom, and rivers with smaller slopes will result in broader and gentler valleys, both resulted valleys are commonly V-shaped. At the lowest reach of a river, a floodplain comes into being by sedimentation. The invasion and recession of the glaciers will form the U-shaped valleys, which does not depend on the floor gradient, but the glacier's size. In addition to the driving force, the underlying topography, rock types and the climate produce a lot of transitional forms between V-, U- and plain valleys. Characteristics, such as bottom width, shoulder width, ridge-crest-to-valley-bottom relief, and cross-sectional area are used to classify the valley shapes. In this study, criteria based on elevation difference for all cross sections passing a given location are selected. Whether a given point P with elevation Z_p is located in valley or non-valley area is justified by the following trial-and-error procedure:

1. A vertical plain passing point P intersect the terrain at a planar curve S. The plain will be rotated N times such that its horizontal angle to the east changes from 0 to 360 at an interval of $\frac{360}{N}$;

2. For each rotation, search on the plain for the lowest elevation (Z_l^l and Z_r^l) on each side of the station along the curve within a horizontal distance l;

3. Search for the highest elevation Z_l^h on the one side of the station within a horizontal distance $L(L > l)$, the actual distance from the highest point to point P is recorded as L_l;

4. Search for the hightest elevation Z_r^h on the other side of the station within a distance of $L - L_l$;

5. For a station to be recognized within narrow-steep valley, n out of N plain should satisfy the following conditions:

$$max(Z_l^h, Z_r^h) - min(Z_l^l, Z_r^l) \geq \Delta h_1 \tag{7.1}$$

$$min(Z_l^h, Z_r^h) - max(Z_l^l, Z_r^l) \geq \Delta h_2 \tag{7.2}$$

$$max(Z_l^h, Z_r^h) - Z_p \geq \Delta h_3 \tag{7.3}$$

$$\tag{7.4}$$

Except N is set to 72, all the other parameters $(L, l, \Delta h_1, \Delta h_2, \Delta h_3, n)$ are determined by trial-and-error procedure started on a reasonable guess, and changed by visual comparison with DEM map. For the study area, a reasonable classification is obtained with the parameter set: $L = 3200m, l = 1000m, \Delta h_1 = 180m, \Delta h_2 = 150m, \Delta h_3 = 150m, n = 30$. Fig.7.4 demonstrated the identified valley stations together with their station numbers.

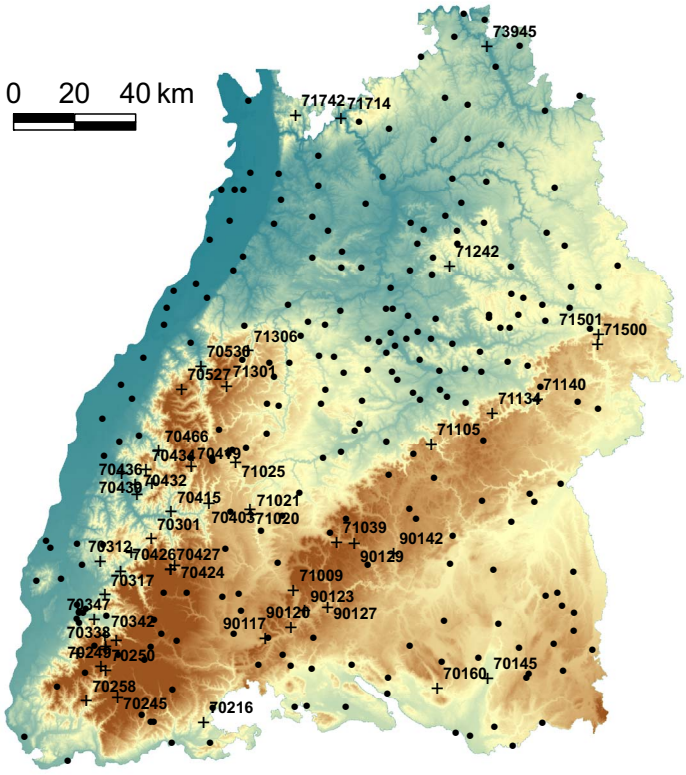

Figure 7.4: Classification of valley and non-valley stations(Valley stations are denoted with cross with station numbers, and circles show the non-valley stations.)

7.3.2 Scatter Plot of Altitude *vs.* Precipitation

Fig.7.5 shows the scatter plot of mean daily precipitation at both the valley and non-valley stations. The valley stations are given as circles with the corresponding station number. The general elevation-precipitation trend of the mixed point clouds demonstrates the orographic effect. One can also detect that the valley stations lie on the upper edge of the scatter cloud, except two clusters (marked by two ovals in Fig.7.5). The upper lying valley stations can be interpreted in two ways: for a valley station and non-valley station located at the same elevation, the valley stations receives more rainfall. Because the valley stations are usually in the mountainous region, it reflects the higher regional precipitation at mountains than in flat areas. Or it can be interpreted in another way that, a valley station receives comparable rainfall as a station which is located at a much higher elevation, i.e. a mountain station. This is also physically reasonable - the orographic precipitation theory states that the precipitation is formed when the rising moist air flow is forced to condense, for example on the windward side, and on the leeside when the moist air can sink down freely, precipitation will stop or reduced. For steep-narrow valleys, there is no enough space for the air to sink down, therefore no reduction in precipitation is to be detected.

As to the outliers, closer investigation shows the two clusters of outlier stations are all located in the two sides of the Swabian Alps, where a smaller regional mean precipitation occurs. If the scatter plot for the regional stations for all stations on each side of the Swabian Alps, the valley stations mixed in the middle of the cloud in Fig.7.5 will appear again on the upper part with regarding to its surrounding stations(see Fig.7.6).

Another single outlier station 73945 is a station in the river valley, which is not actually narrow and steep, and identified as a valley station just because the inaccuracy of the valley identification procedure.

Scatter plots of daily precipitation also demonstrate similar feature, but shows that the distribution of the scatter points seems to related to the CPs. A further look of the scatter plot of each CP is given in Figure. 7.7. For CP07, the valley and non-valley stations are rather mixed. For other wet CPs, valley stations are still somehow on the upper edge, but their position are changing for different CPs, for example, for CP05, the valley and non-valley stations are clearly separated, but in CP07 some of them become mixed, which may imply that, valley stations receiving comparable precipitation as some non-valley stations for CP05 receives less precipitation for CP07. Whether the assumption is true should be checked through detailed comparison of the neighboring valley and non-valley precipitation time series data.

7.3.3 Statistical Test of Pairwise Stations

To confirm whether valley-mountain precipitation difference are affected by CPs, two statistical tests of the precipitation time series are performed for the selected valley-mountain station pairs: non-parametric Kolmogorov-Smirnov (KS) test of the cumulative distribution and One-way ANOVA test of the mean precipitation. Both tests are conducted for daily precipitation of each CP and for all days in general. The Null-hypothesis of KS-test is that the

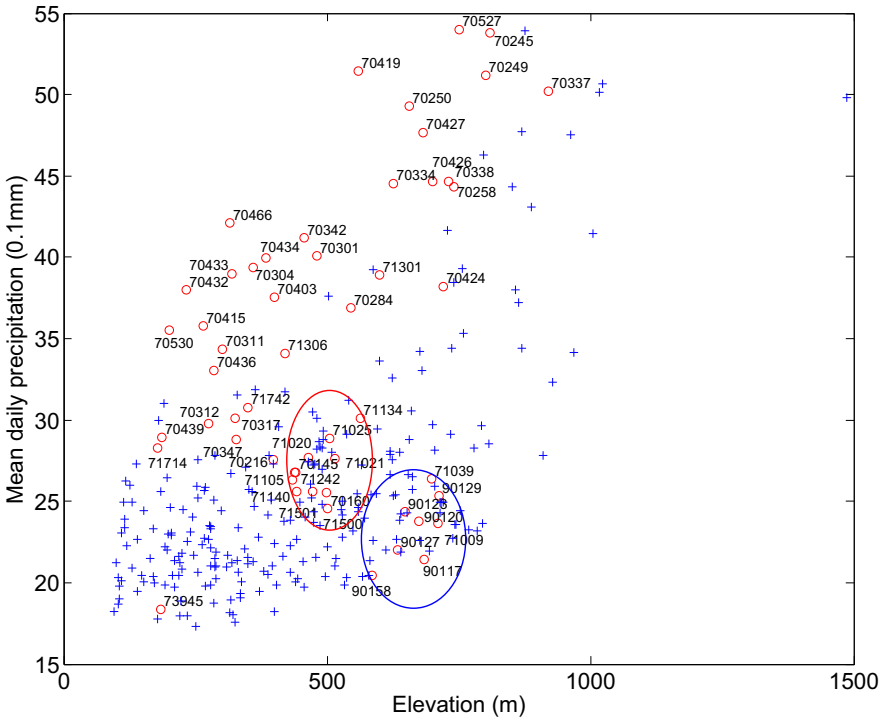

Figure 7.5: Scatter plot of mean daily precipitation vs. elevation

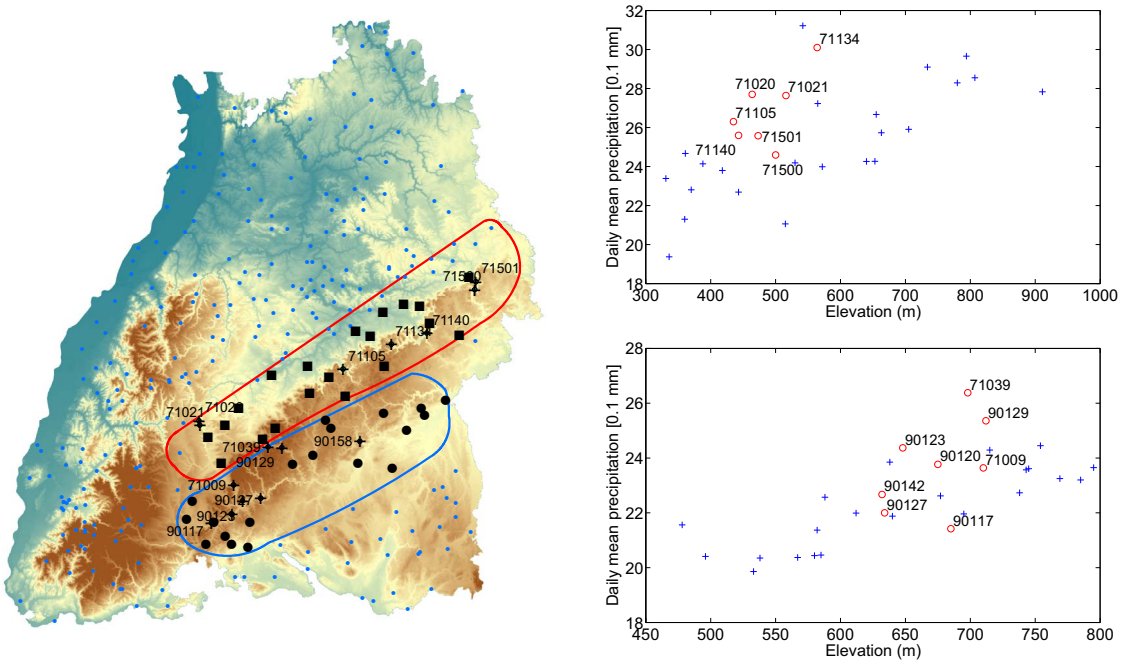

Figure 7.6: Location of outlies and local scatter plot

two stations are drawn from the same continuous distribution, and for One-way ANOVA test is that the mean precipitation of the two station are the same. To eliminate the effect

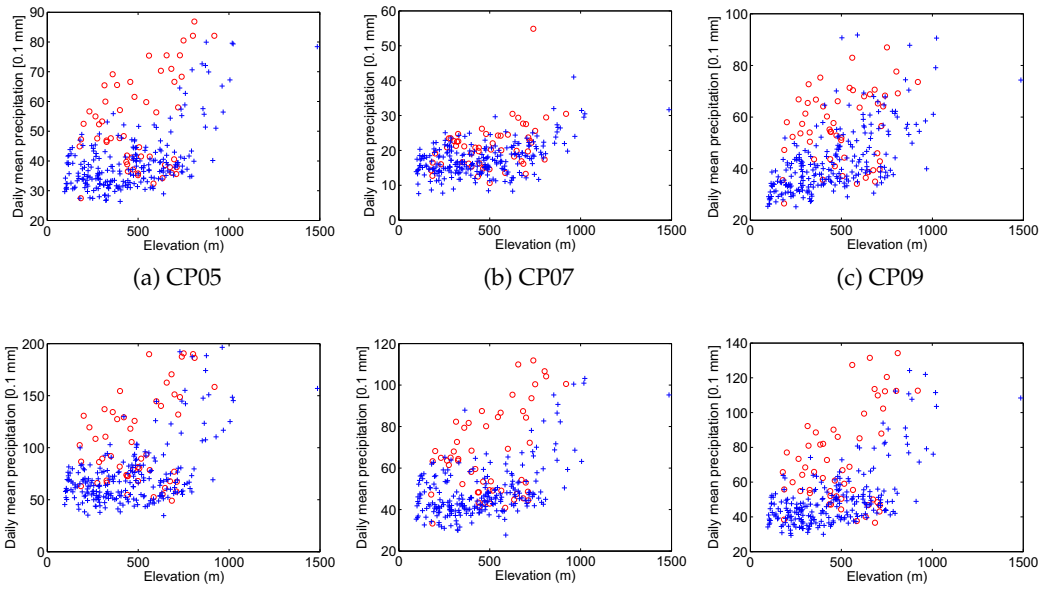

(a) CP05 (b) CP07 (c) CP09

(d) CP10 (e) CP17 (f) CP18

Figure 7.7: Scatter plot of mean daily precipiation of wet CPs

of orographic effects, the selected stations should be close to each other, with some on the mountain and others in the valley. But a general problem for rain gauge is that there are very few stations that are located on the mountains due to the operation and maintenance difficulties. In this work three groups of stations have been selected and studied.

Station 71038 and 71039

The two stations lie in Swabian Alps, a low mountain region. Station 71038 is a mountain station ($911\,\mathrm{m}$ a.s.l.), whereas station 71039 is a valley station ($698\,\mathrm{m}$ a.s.l.) oriented in east direction. Table 7.2 shows the $p-$values of the test results, and the values in parenthesis are to be rejected. For a significance level of $\alpha = 0.05$, except for CP09 and CP17, by which the valley orientation is the same as the CP direction, i.e. the valley is open to the moist air flow. For other CPs, especially the wet CPs, the two stations show little precipitation variation despite the elevation difference. Fig.7.8 shows the comparison results of CP09 and for all days in general.

Station 71306 and 71307

Station 71306 is a valley station with an elevation of $421\,\mathrm{m}$ a.s.l., and station 71307 is a mountain station ($740\,\mathrm{m}$ a.s.l.), both located in the north end of the Black Forest. The valley in which station 71306 is located, is oriented to north. To be mentioned, although the two stations are close, but station 71306 is in a valley surrounded by lower ridges than the station 71307, i.e. it is in a valley of the downslope of the station 71307. Only when the direction of the CP is perpendicular to the direction connecting the two stations, no orographic effects will present, for example, most of CPs with south-east direction over this region are indifferentiable. For other CPs, although the Null-hypothesis can not be rejected, the $p-$value is

Table 7.2: Statistical test results of station 71038 and 71039

CP	KS-p	ANOVA-p	CP	KS-p	ANOVA-p
CP01	0.636	0.382	CP10	0.558	0.643
CP02	0.862	0.786	CP11	0.999	0.803
CP03	0.299	0.771	CP12	1.000	0.935
CP04	0.999	0.941	CP13	0.986	0.637
CP05	0.894	0.473	CP14	0.999	0.953
CP06	0.990	0.816	CP15	1.000	0.959
CP07	0.987	0.913	CP16	1.000	0.429
CP08	0.998	0.829	CP17	(0.027)	(0.006)
CP09	(0.008)	(0.007)	CP18	1.000	0.994
			ALL	0.466	0.141

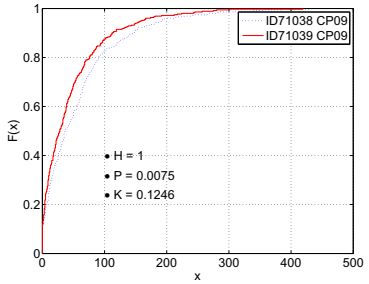

(a) CP09 KS

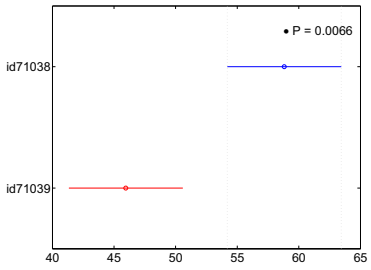

(b) CP09 One-way ANOVA

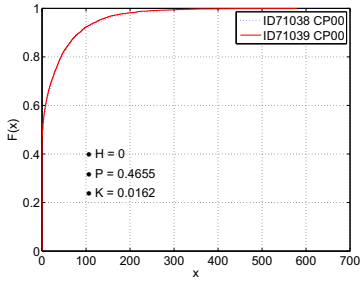

(c) General KS

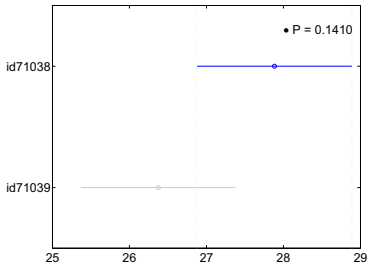

(d) General One-way ANOVA

Figure 7.8: CDF and mean comparison of station 71038 and 71039

relatively low. This means that, because the interference of the orographic effects, the steep-valley effects can be observed, but not so strong as for station pair of 71038 and 71039. Table 7.3 shows the comparison statistics of the station pair.

Station 70334-70340 and 70334-70332

For this comparison, 2 station pairs consisting of 3 stations that are located in the south part of black forest, have been investigated. Data at other nearby stations in this small area are not used, because their precipitation time series are too short to give a strong test result. Station 70332 with an elevation of $1486\,\mathrm{m}$ a.s.l. are lying at the highest peek of this moun-

Table 7.3: Statistical test results of station 71306 and 71307

CP	KS-p	ANOVA-p	CP	KS-p	ANOVA-p
CP01	0.282	0.157	CP10	0.310	0.123
CP02	0.113	0.373	CP11	0.872	0.526
CP03	0.528	0.630	CP12	0.725	0.376
CP04	1.000	0.817	CP13	0.411	0.353
CP05	0.090	(0.012)	CP14	0.052	0.080
CP06	0.068	0.071	CP15	0.962	0.721
CP07	0.643	0.530	CP16	0.810	0.497
CP08	0.560	0.935	CP17	0.277	0.116
CP09	(0.019)	(0.027)	CP18	(0.006)	(0.002)
			ALL	0.000	0.000

tain primary massif, which is in the southwest-northeast direction. Station 70334 ($650\,\mathrm{m}$ a.s.l.)and station 70332 ($1023\,\mathrm{m}$ a.s.l.) are lying on the nearby lower mountain secondary ridges which is somehow perpendicular to the primary massif, with 70334 being a valley station and 70340 being a mountain station. The ridges of the northwest oriented valley where station 70334 is locating has an elevation comparable to station 70340. The rejection of Null-hypothesis for station 70334 and 70332 in all almost all conditions shows a clear orographic effects. Station 70334 and 70340 show difference in case of CP05 and CP09, which is in this case difficult to interpret. One possible reason might be the complex local wind field, which may adjust the direction of moisture flow. The general circulation pattern is the defined at a scale larger than $1000\,\mathrm{km}$, but will be altered by the topography. It gives only a rough estimation of the air flow, the exact air flow is depending on the local air flow directions, which may be very complicated. Since the large scale circulation pattern can explain most of the cases, we will leave such exceptional cases, and not go into detail.

In general, it can be concluded that if the valley is open to the air flow, it will receive less precipitation as the mountain ridges do, whereas if the valley is isolated from the air flow, the valley and mountain ridge will receive comparable precipitation.

7.4 Kriging with Smoothed DEM

The orographic effects, i.e. the precipitation-elevation can not be accounted with traditional interpolation methods, such as inverse distance, spline, and ordinary kriging, etc. Non-stationary kriging methods, such as residual kriging (RK), also called detrended kriging (DTK), or external drift kriging (EDK), can consider the systematic drift of interpolated variables with external variables, but the local valley effects can not be resolved by such approaches. For a proper interpolation method, the results should be unbiased, i.e. although for individual data, the estimation error is unavoidable, but the error should be normally distributed with zero mean. But these methods, when directly applied to precipitation interpolation in complex terrain, will cause systematic bias in the interpolation results. Cross

Table 7.4: Statistical test results of station 70332 and 70334 and 70340

	70334 vs. 70340		70334 vs. 70332	
CP	KS-p	ANOVA-p	KS-p	ANOVA-p
CP01	0.392	0.071	(0.000)	0.232
CP02	0.970	0.218	(0.000)	0.058
CP03	0.925	0.947	(0.000)	0.092
CP04	1.000	0.692	(0.010)	0.564
CP05	(0.007)	(0.031)	(0.000)	(0.017)
CP06	0.205	0.065	(0.000)	0.091
CP07	0.957	0.983	(0.036)	0.745
CP08	0.746	0.319	(0.019)	0.260
CP09	(0.000)	(0.000)	(0.001)	(0.044)
CP10	0.980	0.912	0.222	0.084
CP11	0.935	0.062	(0.013)	0.165
CP12	0.954	0.534	0.005	0.286
CP13	0.990	0.367	(0.000)	0.130
CP14	0.154	0.099	(0.001)	0.060
CP15	0.976	0.233	0.059	0.515
CP16	0.962	1.000	(0.002)	0.651
CP17	0.580	0.213	0.078	0.906
CP18	0.113	0.416	(0.003)	(0.005)
general	(0.000)	(0.000)	(0.000)	(0.000)

validation with both ordinary kriging and external drift kriging has been performed on the 40 years daily precipitation data, and the station mean bias are shown in Fig.7.9. Fig.7.9a shows that the bias of OK shows a systematic trend for both valley and non-valley stations, because of neglection of the orographic effects. Consideration of orographic effects by EDK reduces the bias, leading to a more normally distributed errors, a exaggerated difference between valley and non-valley stations has been generated artificially. For valley stations EDK gives a positive mean bias ($Z - \hat{Z}$) of around $0.4\,\mathrm{mm}$, with a mean bias of around $-0.10\,\mathrm{mm}$ for the non-valley stations, i.e. there is a essential underestimation for valley stations, and a slightly overestimation of non-valley stations. The smoothing techniques have been applied to overcome this problem. First an isotropic smoothing is tried, followed by a directional smoothing technique to consider the CP effects.

7.4.1 Isotropic and Anisotropic DEM smoothing

The statistical precipitation analysis for mountain-valley pairs and groups shows that at small scale the precipitation is "blind"to the topography. Physically it means that for small narrow-steep valleys there is no enough space for the moisture air to sink down, therefore it stays lifted, and produce as much precipitation in the valleys as at the mountain ridges. This raises the question in our rainfall interpolation procedure, especially for external drift krig-

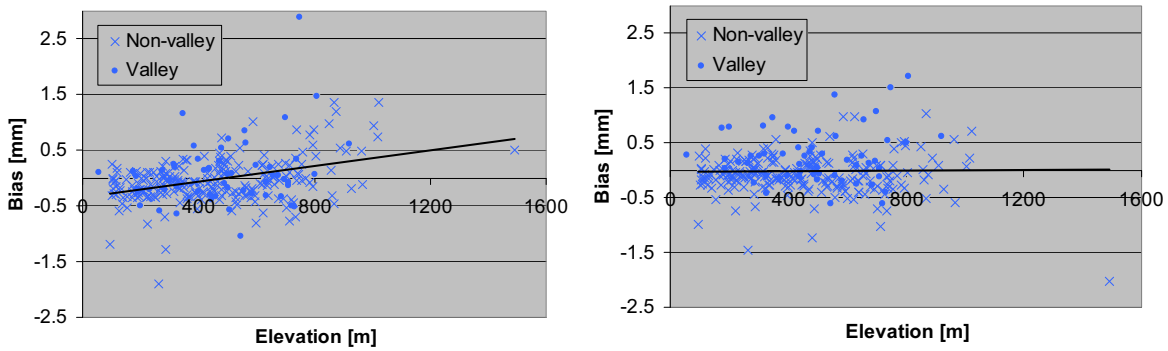

(a) OK (b) EDK

Figure 7.9: Bias of valley and non-valley stations for standard OK and EDK

ing (EDK), which considers the elevation-precipitation orographic effects. While accounting for the orographic effects, it underestimates the rainfall at small scale valleys which receives the similar rainfall as the mountain ridges. One solution to overcome this problem is to smooth the DEM, so that the local topographic change is homogenized out while the topographic trend at larger scale is still kept. We use a kernel smoothing technique to smooth the topography. For a given cell, the elevation is taken as the weighted average of a window centering at the cell, and the weight of the cells within the window is inversely proportional to their distances to the smoothed cell. In case of a square window parallel to the coordinate system, the smoothing is called *isotropic*. Fig.7.10a and 7.10b shows the smoothed DEM with a window size of $2.5 \times 2.5\,\mathrm{km}^2$ and $5 \times 5\,\mathrm{km}^2$. It shows that with the increasing smoothing window size, the micro topographic features disappeared, and the elevation difference is also reduced.

Isotropic smoothing technique will represent the valley stations properly, if the valley stations behave completely the same as the non-valley stations. This holds only when the valley is completely isolated with surrounded mountains. For valleys that are open to the flat region in a given direction, interaction of CP with the topography leads to a CP-dependent precipitation behavior, as shown in Section 7.3. If the air flow direction of a CP is parallel to the open valley, then the moist air will not be lifted in the valley, consequently the valley station will receive less precipitation. The isotropic smoothing can not reflect such cases properly. To overcome this problem, an *anisotropic* smoothing technique, which smooths the DEM in the CP direction, can be applied. For anisotropic smoothing, a rectangular smoothing window with its long edge parallel to the CP direction is taken. The length of long edge is denoted as L_s, and the ratio of the long edge to the short edge is marked as λ_s.

Two different anisotropic smoothing are tried to see whether the differentiation between CPs of two opposite directions, e.g. CP from southwest and CP from northeast, is necessary:

- Two-side anisotropic smoothing: the smoothing rectangle is centered at the point to be smoothed, by which the effects of CPs from two opposite directions are considered identical;
- One-side anisotropic smoothing: the smoothing rectangle is lying on the side behind

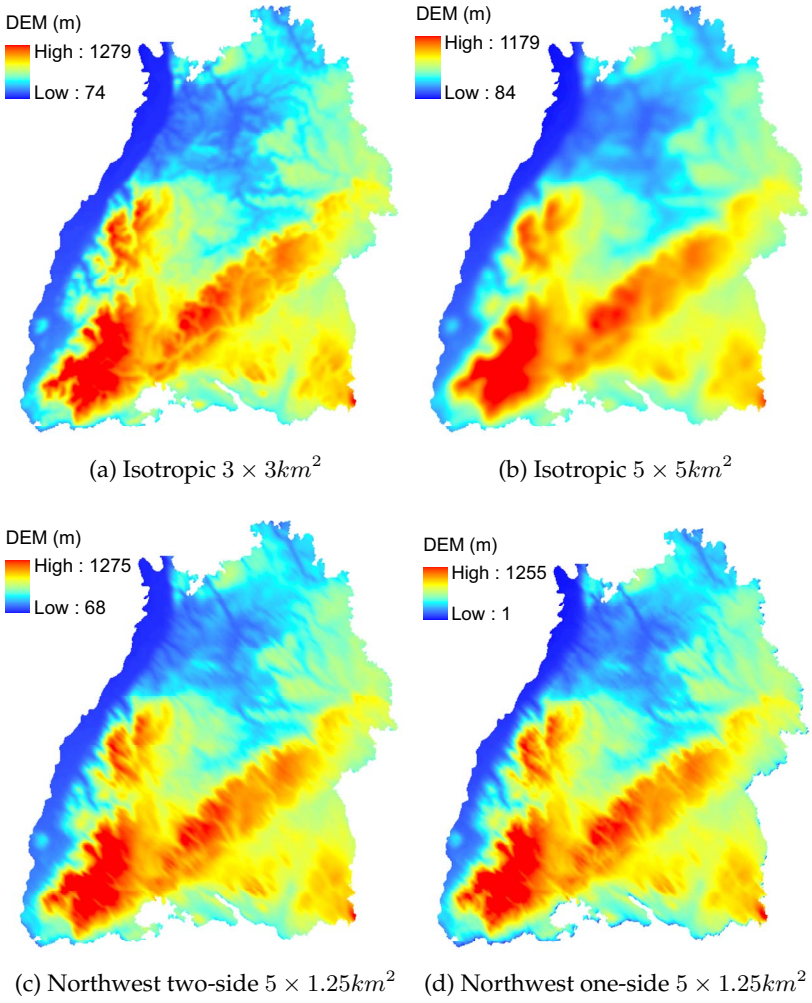

(a) Isotropic $3 \times 3km^2$ (b) Isotropic $5 \times 5km^2$

(c) Northwest two-side $5 \times 1.25km^2$ (d) Northwest one-side $5 \times 1.25km^2$

Figure 7.10: DEM smoothing with different techniques

the point in the CP direction, i.e. DEM is smoothed only within the half window.

Fig.7.10c shows the two-side anisotropic smoothing with a main range L_s equal to $5km$ and λ_s equal to 4. The valleys that are northwest and southeast oriented, are still kept, while valleys in other directions, especially those that are orthognal to the main smoothing direction disappear. Fig.7.10d demonstrates the one-side anisotropic smoothing with the same window size. The pattern of the DEM is very similar to the result two-side smoothing, but the whole DEM seems to shift to the northwest, because the smoothing is done on the southeast side of a point. Theoretically, for a CP coming in the same direction as the valley orientation, the interpolated precipitation in the valley by EDK with anisotropically smoothed DEM will not change much comparing with EDK with original DEM, because of the selected smoothing of DEM does not change the elevation in the valleys open to the CP.

7.4.2 Kriging Results

The different smoothed DEMs have been utilized in EDK and DTK procedure to check whether a desired improvement of the interpolation results can be obtained. Following cases have been compared in this study:

- OK: Ordinary kriging
- EDK STD: External Drift Kriging with original DEM
- EDK ISO: EDK with isotropic smoothing
- EDK ANISO2: EDK with two-side anisotropic smoothing in the CP direction
- EDK ANISO1: EDK with one-side anisotropic smoothing in the CP direction
- DTK STD: Detrended Kriging with original DEM
- DTK ISO: DTK with isotropic smoothing
- DTK ANISO2: DTK with two-side anisotropic smoothing in the CP direction
- DTK ANISO1: DTK with one-side anisotropic smoothing in the CP direction

The results are compared for the cross validation in terms of bias and mean squared error (MSE).

Results for each CP

CPs are specified in 8 directions over 360 degree, by visual inspection of the pressure contour plot. Because CPs are obtained from the large continental scale, it is not very accurate, and certain tolerance is allowed. The DEM is smoothed in 8 directions for two-side smoothing, and 16 directions for one-side smoothing, both at an interval of 22.5°. At each station, cross validation is performed for each DEM smoothing, and the best result from the DEM smoothed in direction α_s, with $|\alpha_s - \alpha_{cp}| \leq 22.5$ is taken as the result of CP direction smoothing.

Table 7.5 shows the daily average of mean squared error (MSE) for each CP for the two-side smoothing.

$$MSE = \sum_{d=1}^{m_{cp_i}} \sum_{i=1}^{n_{obs}} (\hat{z}_i - z_{obs})^2 \tag{7.5}$$

where m_{cp_i} is number of raining days for the ith CP, n_{obs} is number of station observations. In most cases, MSE is very small for OK, but as shown before, a systematic bias is associated with OK. MSE for anisotropic smoothing in different directions changes for different CP, but in general the smoothing in CP direction shows the smallest MSE. The isotropic smoothing with the same smoothing window area shows a better results than standard EDK, but is not as good as the anisotropic CP smoothing. The results for DTK is not as good as the corresponding EDK, but the improvement with the smoothing technique are similar to EDK. The results of individual one-sided smoothing are not listed in the table, but only the smoothing in CP direction, which have shown a better performance for the cross validation comparing

to the two-sided smoothing. If the relative MSE with reference to EDK with original DEM is considered, all the wet CPs show much higher relative improvement. The relative improvements are not listed in the table, but they can be easily calculated from the table. The highest relative improvement is for CP10, around 10%. It may sound not so exciting, but we should keep in mind that, the MSE is evaluated for all stations, including stations located not in the mountainous area, which are not affacted by the smoothing, thus the error reduction at the mountainous stations are deminished by these stations.

Results for Stations

The results are also evaluated for the valley and non-valley stations by looking at the station average of BIAS and MSE. Because the precipiation show strongly season difference, the results are also listed for each season.

$$MSE = \sum_{i=1}^{n_{obs}} \sum_{d=1}^{m} (\hat{z}_i - z_{obs})^2 \tag{7.6}$$

$$BIAS = \sum_{i=1}^{n_{obs}} \sum_{d=1}^{m} (z_{obs} - \hat{z}_i) \tag{7.7}$$

where m is number of days of a given season in case of seasonal result, or all seasons in case of general result. Table 7.6 and 7.7 show the mean squared error and bias respectively. The result of EDK STD is not as good as OK in terms of both average MSE and average bias, but if we look at the error distribution of all stations (see Fig.7.9), EDK is less biased, and in our case, it is even completely random. The lower average bias of OK is resulted from the compensation of the negative errors at lower elevation and positive errors at higher elevation. With smoothing, both the underestimation for valley stations and the overestimation of non-valley stations are reduced (see Fig.7.11). The systematic bias over different elevation is almost removed for both EDK and DTK with smoothing. The best result is obtained by the one-sided anisotropic smoothing. EDK ANISO1 provides not only the smallest average MSE and bias, but also a more randomly distributed error (see Fig.7.11c). For example, the highest station in the study area is slightly underestimated with OK, and strongly overestimated with EDK, but with EDK ANISO1, the error is minimum.

Smoothing with different ranges and ratios of range have also been tried, it seems that the level of improvement is depending on the two smoothing parameters L_s and λ_s. Theoretically, both EDK and DTK will approach the result of OK, when a complete smoothing of DEM is undertaken. Currently, the author suggests to use an optimization or traversing to seek for the best smoothing parameters.

Detailed Results of Station Time Series

A more convincing result is given by the detailed interpolation output of the station time series. Fig.7.12 shows the interpolation result by OK, EDK STD, and EDK ANISO1 for the valley-mountain station pairs 71306-71307. The positive value for the valley station 71306 shows the systematic underestimation with EDK STD, while the negative value shows the

Table 7.5: Comparison of MSE for different kriging methods

CP	days	EDK STD	EDK ANISO 2								EDK ISO	EDK ANISO1
			90°	112.5°	135°	157.5°	0°	22.5°	45°	57.5°	CP		
CP01	413	7.31	7.12	7.14	7.13	7.11	7.13	7.12	7.12	7.12	7.06	7.14	6.97
CP02	296	2.59	2.50	2.51	2.51	2.51	2.53	2.53	2.52	2.51	2.50	2.52	2.53
CP03	350	4.44	4.37	4.38	4.38	4.37	4.37	4.37	4.38	4.38	4.35	4.38	4.30
CP04	149	10.96	10.83	10.81	10.78	10.76	10.79	10.82	10.84	10.84	10.72	10.84	10.63
CP06	524	3.00	2.94	2.96	2.97	2.96	2.94	2.94	2.94	2.94	2.92	2.96	2.88
CP08	285	11.62	11.49	11.47	11.46	11.47	11.48	11.49	11.49	11.50	11.36	11.49	11.41
CP11	321	9.90	9.76	9.76	9.75	9.75	9.76	9.78	9.78	9.76	9.71	9.77	9.60
CP12	384	6.21	6.09	6.10	6.09	6.08	6.08	6.09	6.09	6.09	6.05	6.10	5.98
CP13	350	9.79	9.70	9.69	9.70	9.71	9.71	9.72	9.72	9.71	9.66	9.73	6.90
CP14	452	7.23	6.80	6.84	6.82	6.78	6.80	6.82	6.83	6.82	6.74	6.87	6.54
CP15	126	6.84	6.69	6.69	6.70	6.72	6.74	6.74	6.72	6.71	6.67	6.72	6.66
CP16	366	7.61	7.48	7.49	7.49	7.48	7.49	7.49	7.50	7.49	7.42	7.50	7.41
CP05	1218	8.20	7.93	7.95	7.94	7.91	7.91	7.92	7.93	7.93	7.86	7.96	7.70
CP07	385	8.13	7.95	7.95	7.95	7.95	7.96	7.97	7.98	7.97	7.90	7.98	7.79
CP09	972	10.11	9.76	9.78	9.78	9.76	9.79	9.80	9.80	9.77	9.72	9.82	9.61
CP10	388	14.77	13.73	13.80	13.74	13.63	13.64	13.66	13.70	13.70	13.55	13.79	13.32
CP17	840	10.50	10.10	10.16	10.15	10.08	10.07	10.07	10.09	10.09	10.00	10.13	9.91
CP18	1539	10.51	9.92	9.97	9.94	9.87	9.87	9.88	9.92	9.92	9.82	9.97	9.58

CP	OK	DTK STD	DTK ANISO 2								DTK ISO	DTK ANISO1
			90°	112.5°	135°	157.5°	0°	22.5°	45°	57.5°	CP		
CP01	7.24	7.48	7.26	7.28	7.27	7.25	7.27	7.27	7.27	7.26	7.22	7.29	7.13
CP02	2.53	2.68	2.58	2.58	2.59	2.60	2.62	2.62	2.60	2.59	2.58	2.60	2.61
CP03	4.28	4.51	4.42	4.43	4.43	4.42	4.42	4.42	4.42	4.42	4.40	4.43	4.37
CP04	10.62	11.21	11.02	11.06	11.08	11.06	11.03	11.05	11.05	11.04	11.01	11.09	10.89
CP06	2.95	3.06	2.98	2.99	2.99	2.99	2.97	2.97	2.98	2.98	2.96	2.99	2.92
CP08	11.28	11.92	11.69	11.67	11.66	11.67	11.68	11.70	11.71	11.71	11.58	11.72	11.62
CP11	9.53	10.04	9.86	9.87	9.87	9.86	9.86	9.88	9.88	9.87	9.83	9.90	9.71
CP12	6.09	6.43	6.21	6.22	6.22	6.20	6.19	6.19	6.20	6.20	6.16	6.23	6.09
CP13	9.49	10.06	9.88	9.87	9.86	9.85	9.84	9.87	9.89	9.89	9.80	9.91	6.99
CP14	6.99	7.41	6.87	6.91	6.88	6.84	6.83	6.85	6.88	6.88	6.81	6.93	6.67
CP15	6.67	6.91	6.79	6.80	6.80	6.81	6.81	6.80	6.80	6.80	6.78	6.82	6.73
CP16	7.36	7.76	7.62	7.63	7.62	7.61	7.61	7.62	7.62	7.63	7.58	7.65	7.50
CP05	7.93	8.51	8.14	8.15	8.14	8.11	8.09	8.11	8.13	8.14	8.06	8.17	7.88
CP07	7.85	8.28	8.08	8.08	8.09	8.09	8.09	8.11	8.10	8.09	8.05	8.12	7.94
CP09	9.84	10.29	9.93	9.95	9.96	9.95	9.95	9.97	9.97	9.95	9.90	10.01	9.82
CP10	14.29	15.88	14.31	14.35	14.26	14.12	14.10	14.17	14.28	14.32	14.05	14.41	13.60
CP17	10.00	10.97	10.42	10.46	10.45	10.39	10.36	10.38	10.42	10.43	10.31	10.47	10.15
CP18	10.07	11.11	10.20	10.24	10.20	10.10	10.08	10.11	10.18	10.21	10.06	10.26	9.75

overestimation of station 71307. In contrast to EDK STD, OK provides an underestimation of station 71307. Instead, EDK ANISO1 provieds for both stations the best results with smallest bias in most of the days.

Table 7.6: Comparison of average station MSE

		MSE								
		OK	EDK				DTK			
			STD	ISO	ANSIO1	ANISO2	STD	ISO	ANSIO1	ANISO2
Winter	V*	10.058	10.668	9.774	8.014	8.834	11.566	10.128	8.163	9.093
	NV**	4.805	5.056	4.723	4.089	4.461	5.354	4.844	4.161	4.563
Spring	V	8.921	9.283	8.842	7.707	8.189	9.756	9.123	7.996	8.472
	NV	5.754	5.920	5.742	5.214	5.496	6.122	5.863	5.335	5.620
Summer	V	16.098	16.576	16.234	14.765	15.254	16.975	16.628	15.193	15.666
	NV	13.427	13.725	13.593	12.606	13.092	14.011	13.817	12.870	13.353
Autumn	V	8.513	8.926	8.451	6.995	7.680	9.679	8.831	7.335	8.037
	NV	5.379	5.519	5.327	4.752	5.073	5.766	5.481	4.876	5.217
ALL	V	11.011	11.469	10.942	9.500	10.107	12.081	11.291	9.804	10.435
	NV	7.496	7.711	7.508	6.819	7.188	7.969	7.664	6.967	7.348

$*$ V stands for valley stations. $**$ NV stands for non-valley stations.

Table 7.7: Comparison of average station bias

		Bias								
		OK	EDK				DTK			
			STD	ISO	ANSIO1	ANISO2	STD	ISO	ANSIO1	ANISO2
Winter	V	0.183	0.405	0.273	0.166	0.242	0.484	0.284	0.171	0.251
	NV	-0.068	-0.108	-0.071	-0.038	-0.058	-0.099	-0.057	-0.027	-0.045
Spring	V	0.099	0.258	0.161	0.098	0.144	0.261	0.153	0.101	0.140
	NV	-0.045	-0.073	-0.046	-0.018	-0.034	-0.055	-0.031	-0.009	-0.021
Summer	V	0.033	0.166	0.081	0.046	0.085	0.141	0.064	0.041	0.072
	NV	-0.044	-0.073	-0.051	-0.010	-0.032	-0.059	-0.040	-0.005	-0.025
Autumn	V	0.090	0.296	0.186	0.091	0.162	0.303	0.182	0.095	0.160
	NV	-0.052	-0.082	-0.054	-0.026	-0.043	-0.067	-0.040	-0.016	-0.031
ALL	V	0.099	0.276	0.172	0.099	0.155	0.292	0.124	0.167	0.153
	NV	-0.052	-0.083	-0.055	-0.022	-0.041	-0.069	-0.042	-0.014	-0.030

7.5 Conclusion and Discussion

In this chapter, the precipitation variability in complex terrain are analyzed with statistical methods based on high-density rain gauge network data. The study have confirmed the interaction of topography and circulation patterns, and demonstrated that, when a narrow-steep valley is isolated from the CP, the valley will receive comparable precipitation as the mountain station does, whereas when the valley is open to the CP, then the orographic precipitation will take effect. Due to the neglection of such phenomenon occurring at small scale, standard interpolation algorithm will produce systematic bias, thus fail to provide a reasonable interpolation for complex terrain. A solution is suggested by this chapter to apply DEM smoothing techniques. Both external drift kriging and detrended kriging with isotropic, two-sided anisotropic, and one-sided anisotropic smoothing, all have shown the

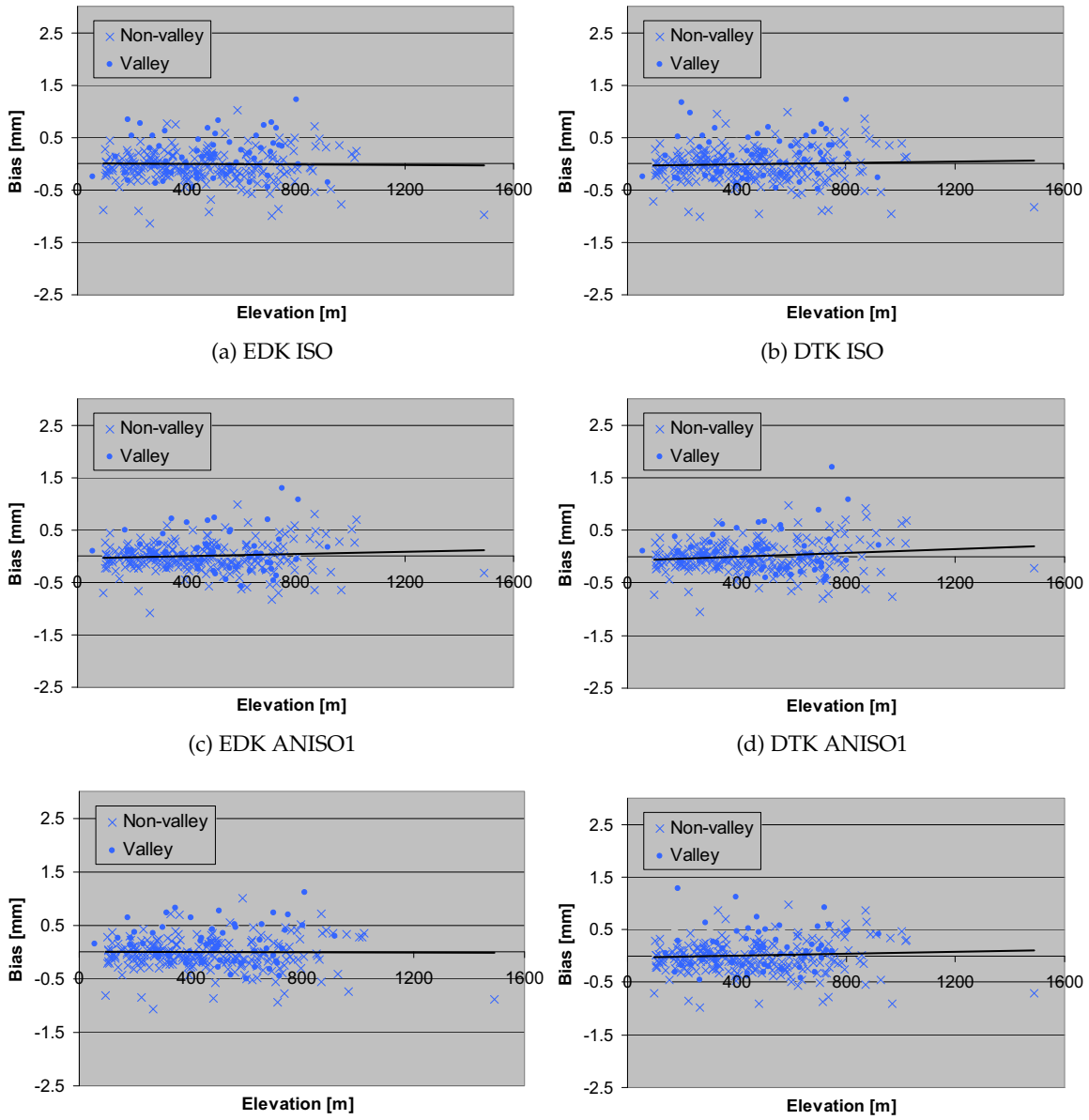

(a) EDK ISO

(b) DTK ISO

(c) EDK ANISO1

(d) DTK ANISO1

(e) EDK ANISO2

(f) DTK ANISO2

Figure 7.11: Bias of valley and non-valley stations for kriging with smoothed DEM

capability to remove the systematic error in the cross validation procedure. In addition to a more randomly distributed error, the anisotropic smoothing techniques also gives smaller errors values, with the best results provided by one-sided anisotropic smoothing. It is also shown that, the improvement of anisotropic smoothing for cross validation results are depending on the smoothing parameters - the smoothing range and ratio of ranges, which may be restricted by some physical processes. At the moment, the author suggest to use optimization or traversing to search for the best parameters.

In this work, the valley classification is very subjective. An automatic and more subjec-

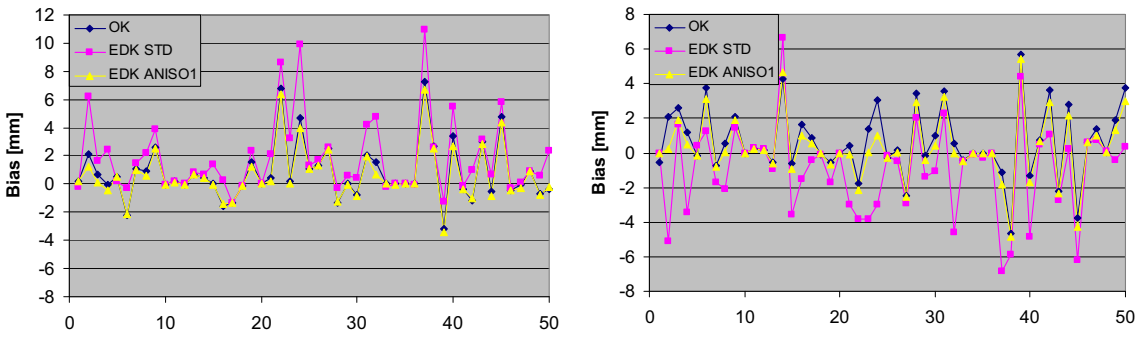

(a) Valley station 71306

(b) Mountain station 71307

Figure 7.12: Time series of bias for valley-mountain station pair

tive approach should be developed, which is applicable to any region. A potential method might be the automatic optimized fuzzy-rule by simulated annealing. Due to the smoothing, the elevation of mountainous region are reduced, which may lead to an overshoot, i.e. an underestimation of the mountain area instead of overestimation. Instead of smoothing, a valley-filling algorithm may be applied. Analogy to the Strahler stream order, valleys can be assigned to an order. Depending on the scope of the valley effect, to which order the valley should be filled can be specified. Implementation of the approach is beyond the scope of this work, and will be tried in the following-up work.

8 Summary and Outlook

8.1 Summary

This work is motivated by an occasional comparison of overland flow patterns of the saturated-overland-flow based TOPMODEL and the Hortonian-overland-flow based CASC2D model. The similarity of simulated overland flow patterns from the two models with distinct mechanism directed our attention to the control of topography over hydrological responses and the resulted spatial variabilities, in other words, patterns. A short review of the topographic effects and hydrological patterns shows that the topographic influence on hydrological cycle is extensive. Besides its governing on horizontal water transfer, DEM also control the water transfer in vertical direction. Because DEM is a readily available information, the thesis is dedicated to investigate the DEM effects on hydrological processes in vertical direction and search for hydrological patterns resulted from topography. It started from the primary topographic effects on solar radiation, wind, and precipitation, and addresses several special aspects of the secondary effects:

- physically based spatial radiation and wind mapping;
- the spatial ET/SMC variability caused by heterogeneous vertical water transfer originated from topography, as a supplement of numerous studies on the spatial variability caused by lateral soil water flow;
- conceptualizing of the topographic effects into the snowmelt model;
- Improvement of interpolation techniques by accounting for the local anisotropy caused by regional mountains and precipitation patterns resulted from local valleys.

The study has exploited the topographic effects with three different means: physically-based model, conceptual model, and statistical analysis. This work has also applied a wide variety of operational remote sensing data, from the cloud data from geostationary satellite Meteosat to vegetation and snow data from MODIS, and demonstrated the benefit of application of such data in hydrological research.

Although the wind simulation is not the central topic of this work, the utilization of mesoscale wind model in this work is a step further to the coupling of meteorological and hydrological model. It shows that introduction of meteorological elements into hydrology will open a much broader view for the hydrologists. The future is expecting an interdisciplinary research, a more compact integration of meteorology, hydrology, and ecology is desired.

In summary, the work will contribute to hydrological research in the following aspects:

- The study will deepen our understanding of spatial hydrology, i.e. hydrological responses to any spatial changes, such as land use;
- Knowledge of spatial variability can be used for downscaling of results of large scale models, such as land surface model, and more accurate interpolation of station observations;
- The topographic effects can be abstracted into hydrological models to improve the model concept;
- Some approaches applied in this work themselves can be regarded as modeling procedures with less data requirements, and can be applied to ungauged basin. In one word, the work also contribute to the PUB initiative.

8.2 Outlook

This work has provided an insight into the topographic effects on hydrological processes, some of which are rather complex. Beside the improvement in understanding the topographic effects, there is also a demand to develop simple and operational techniques and models which are able to include these effects. The conceptualized snow model incorporating the radiation index is just one example. An index similar to the topographic wetness index, but including the topographic induced spatial radiation and wind variations may be developed in further study.

So far, this work has dealt with radiation, wind, ET/SMC, snowmelt, and interpolation, spatial soil variability is left by this work, therefore a homogeneous soil condition is assumed for the ET/SMC mapping in Chapter 4. Actually spatial soil type and depth is also subjected to the influence of topography, therefore to some extent, soil properties can also be predicted with modeling approach. Actually, several models have been developed as mentioned in Chapter 1. A proper model maybe selected and adapted to be applied together with the radiation and wind model to implement a realistic and complete observation free ET/SMC mapping approach. A validation of the simulated ET/SMC map is desired, if advanced remote sensing data of soil moisture at fine scale is available in the future.

Besides some small improvements for the individual studies as mentioned in the discussion part of each chapter, an interesting work might be correction of remote sensing data from different satellite sources. For example, the cloud cover from Meteosat (fixed view angle) and MODIS (changing view angle), the vegetation and snow data from MODIS (finer resolution) and AVHRR (coarser resolution), how to combine the data and minimize the uncertainty of both data set is a very important and interesting issue.

Appendix I: Solar-Earth Geometry and Analytical Radiation Modeling

Earth's revolution around the sun changes the solar declination angle δ as well as the sun-earth distance (represented by the eccentricity correction factor ϵ), both being function of the day number of the year d_n (see Eq.8.1), ranging from 1 on 1 January to 365 on 31 December. February is always assumed to have 28 days. The earth self-revolution leads to a change of hour angle ω with time t (the hour angle is zero at noon, and positive in the morning.), as well as the sun-earth distance. The eccentricity correction factor

$$\delta = 0.409 sin(\frac{2\pi}{365} d_{\mathrm{n}} - 1.39) \tag{8.1}$$

$$\epsilon = 1 + 0.033 \; cos(2\pi d_n \; /365) \tag{8.2}$$

$$\omega = \frac{2\pi}{24}(12 - t) \tag{8.3}$$

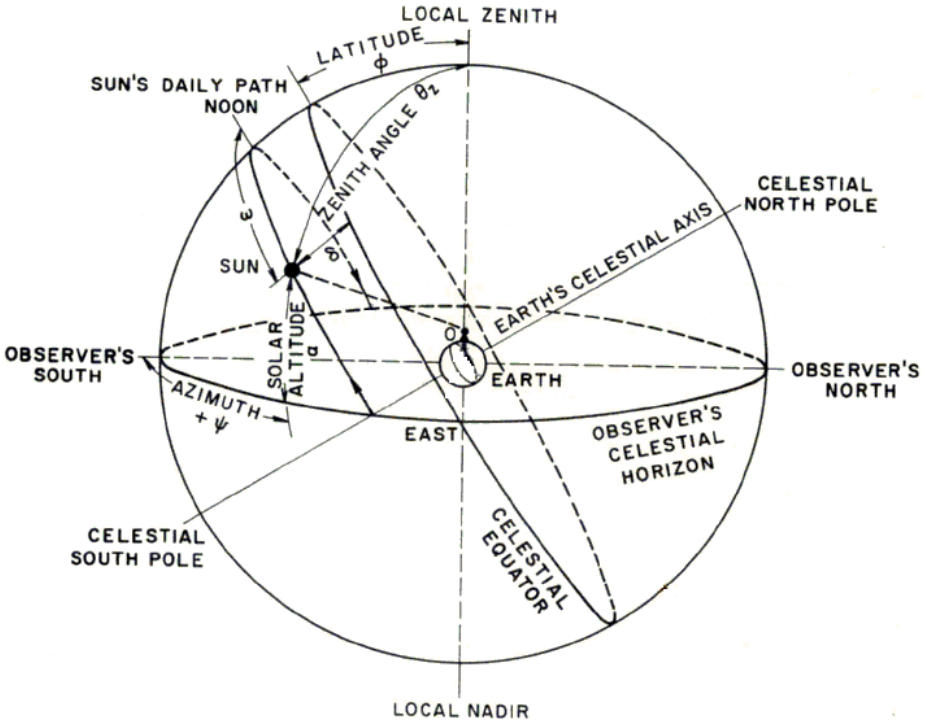

Figure 8.1: Celestial coordinate system of sun-earth system (used from Iqbal (1983))

The SPA described here is based on the celestial horizontal coordinate system with a imaginary celestial sphere concentric with the earth (see Fig.8.1). The zenith is the direction normal to a horizontal surface at a particular point. The horizon is the plane which passes through the center of the earth orthogonal to the zenith. The plane that intersects the zenith and the north direction of the horizon and perpendicular to the horizon is called the local meridian. The solar is positioned with the solar zenith θ_z and azimuth angle ϕ. Solar zenith is the complement of the solar altitude α, i.e. $\alpha = 90 - \theta_z$, which is the sun's angular height above the horizon. The azimuth angle ϕ is the horizontal angle between the sun and the meridian.

$$cos\theta_z = sin\delta\ sin\phi + cos\delta\ cos\phi\ cos\omega = sin\alpha \tag{8.4}$$

$$cos\phi = (sin\alpha\ sin\phi - sin\delta)/cos\alpha\ cos\phi \tag{8.5}$$

Here ψ is the geographic latitude. The sunrise hour angle ω_s for the horizontal surface can be obtained by solution of Eq.8.4.

$$\omega_s = cos^{-1}(-tan\phi\ tan\delta) \tag{8.6}$$

On the horizontal surface, sunset hour angle and sunrise hour angle are symmetrical. The day length is $2\omega_s$, and can be expressed as:

$$N_{dh} = \frac{2}{15}cos^{-1}(-tan\phi\ tan\delta) \tag{8.7}$$

For a horizontal surface, the zenith angle is also the solar incidence angle, i.e. the angle between the solar beam and the normal of the surface. The irradiance on a horizontal surface can be written as

$$\dot{I}_{0h} = \dot{I}_{SC}\ cos\theta_z = \dot{I}_{SC}\ \epsilon\ (sin\delta\ sin\phi + cos\delta\ cos\phi\ \omega). \tag{8.8}$$

The irradiation I_0 from $t1$ to $t2$ ($t1$ and $t2$ are counted in 24-hour format) is

$$I_{0h} = \int_{t1}^{t2} \dot{I}_{SC}(sin\delta\ sin\phi + cos\delta\ cos\phi\ cos\omega)dt. \tag{8.9}$$

The hourly irradiation for 1 h centered around the hour angle ω_i is then

$$\begin{aligned} I_{0h} &= \dot{I}_{SC}\ \epsilon\ \int_{\omega_i-\pi/24}^{\omega_i+\pi/24} (sin\delta\ sin\phi + cos\delta\ cos\phi\ cos\omega)d\omega \\ &\approx \dot{I}_{SC}(sin\delta\ sin\phi + cos\delta\ cos\delta\ cos\omega_i). \end{aligned} \tag{8.10}$$

The daily irradiation is then

$$\begin{aligned} H_{0h} &= \dot{I}_{SC}\ \epsilon\ \int_{sr}^{ss} (sin\delta\ sin\phi + cos\delta\ cos\phi\ cos\omega)d\omega \\ &= \frac{24}{\pi}\dot{I}_{SC}\ \epsilon\ (\omega_{ss}\ sin\delta\ sin\phi + cos\delta\ cos\delta\ cos\omega_s). \end{aligned} \tag{8.11}$$

On an inclined surface with slope β and surface azimuth angle γ, the solar incidence angle θ is different (see Eq.8.12). To be mentioned, the surface azimuth angle γ is the deviation between the projection of the normal of the surface and the local meridian, south zero, east positive(counter clockwise). The aspect γ_{arcgis} in GIS software are defined differently. In ArcGIS, the aspect is defined clockwise from zero at north to 2π, therefore $\gamma = \pi - \gamma_{arcgis}$.

$$\begin{aligned} cos\theta = &(sin\phi\ cos\beta - cos\phi\ sin\beta\ cos\gamma)\ sin\delta \\ &+ (cos\phi\ cos\beta + sin\phi\ sin\beta\ cos\gamma)\ cos\delta\ cos\omega \\ &+ (cos\delta\ sin\beta\ sin\gamma\ sin\omega) \end{aligned} \tag{8.12}$$

By setting $\theta = \pi/2$ in Eq.8.12, the sunrise angle ω_{sr} and sunset angle ω_{ss} can be obtained.

$$0 = A\ sin\omega + B\ cos\omega + C \tag{8.13}$$

where

$$A = cos\delta\ sin\beta\ sin\gamma, \tag{8.14}$$

$$B = cos\delta\ cos\phi\ cos\beta + cos\delta\ sin\phi\ sin\beta\ cos\gamma, \tag{8.15}$$

$$C = sin\delta\ sin\phi\ cos\beta - sin\delta\ cos\phi\ sin\beta\ cos\gamma. \tag{8.16}$$

By solving this equation, we get

$$cos\omega = \frac{-BC \pm \sqrt{A^4 + A^2B^2 - A^2C^2}}{B^2 + A^2} \tag{8.17}$$

For east oriented surface, $0 < \gamma < \pi$:

$$\omega_{sr} = min\left\{\omega_s, cos^{-1}\left(\frac{-BC - \sqrt{A^4 + A^2B^2 - A^2C^2}}{B^2 + A^2}\right)\right\} \tag{8.18}$$

$$\omega_{ss} = -min\left\{\omega_s, cos^{-1}\left(\frac{-BC + \sqrt{A^4 + A^2B^2 - A^2C^2}}{B^2 + A^2}\right)\right\} \tag{8.19}$$

For west oriented surface, $\pi < \gamma < 2\pi$:

$$\omega_{sr} = min\left\{\omega_s, cos^{-1}\left(\frac{-BC + \sqrt{A^4 + A^2B^2 - A^2C^2}}{B^2 + A^2}\right)\right\} \tag{8.20}$$

$$\omega_{ss} = -min\left\{\omega_s, cos^{-1}\left(\frac{-BC - \sqrt{A^4 + A^2B^2 - A^2C^2}}{B^2 + A^2}\right)\right\} \tag{8.21}$$

The day length on the inclined surface $N_{d\beta}$ is

$$N_{d\beta} = \frac{12}{\pi}\left(\omega_{sr} - \omega_{ss}\right) \tag{8.22}$$

By the same procedure as for the horizontal surface, the hourly irradiation $I_{0\beta}$ for inclined surface can be obtained as

$$\begin{aligned} I_{0\beta} &= \frac{12}{\pi}\dot{I}_{SC}\,\epsilon\,\int_{\omega_i-\pi/24}^{\omega_i+\pi/24}(A\;sin\omega + B\;cos\omega + C)d\omega \\ &= (12/\pi)\dot{I}_{SC}\,\epsilon\,(0.26A\;sin\omega_i + 0.26B\;cos\omega_i + (\pi/12)C) \end{aligned} \tag{8.23}$$

The daily irradiation $H_{0\beta\gamma}$ is

$$H_{0\beta} = (12/\pi)\dot{I}_{SC}\,\epsilon\,(C\|\omega_{ss} - \omega_{sr}\| + B\,\|sin\omega_{ss} - sin\omega_{sr}\| + A\|cos\omega_{ss} - cos\omega_{sr}\|) \tag{8.24}$$

$$\xi = H_{0h}/H_{0\beta} = \frac{C\|\omega_{ss} - \omega_{sr}\| + B\,\|sin\omega_{ss} - sin\omega_{sr}\| + A\|cos\omega_{ss} - cos\omega_{sr}\|}{\omega_{ss}\;sin\delta\;sin\phi + cos\delta\;cos\delta\;cos\omega_s} \tag{8.25}$$

Appendix II: Penman-Monteith Equation and Longwave Radiation Estimation

The most widely used Penman-Monteith approach to estimate evapotranspiration from land surface is expressed in the following form:

$$ET = \frac{\Delta_v \ (G_n + L_n) + \rho_a c_a C_{at}(e_s - e_a)}{\rho_w \lambda_v (\Delta_v + \gamma_{pc}(1 + C_{at}/C_{can}))} \tag{8.26}$$

with

ET	:	evapotranspiration rate [LT^{-1}]
Δ_v	:	slope of the vapor pressure curve [$\mathrm{ML}^{-1}\mathrm{T}^{-3}$]
G_n	:	net shortwave radiation [$\mathrm{EL}^{-2}\mathrm{T}^{-1}$]
L_n	:	net longwave radiation [$\mathrm{EL}^{-2}\mathrm{T}^{-1}$]
ρ_a	:	air density [ML^{-3}]
c_a	:	heat capacity of air [$\mathrm{EM}^{-2}\mathrm{T}^{-1}$]
e_s	:	the saturation vapor pressure [$ML^{-1}T^{-2}$]
e_a	:	actual vapor pressure [$ML^{-1}T^{-2}$]
ρ_w	:	water density [ML^{-3}]
λ_v	:	latent heat of vaporization [$\mathrm{EL}^{-2}\mathrm{T}^{-1}$]
γ_{pc}	:	psychrometric constant [$\mathrm{ML}^{-1}\mathrm{T}^{-3}$]
C_{at}	:	atmospheric conductance [LT^{-1}]
C_{can}	:	canopy conductance [LT^{-1}]

The net short wave radiation G_n depends on the ground surface albedo ρ_g [-], which is related to the land cover.

$$G_n = G(1 - \rho_g) \tag{8.27}$$

The longwave radiation L_n, as demonstrated in Chapter 2, is a result of the outgoing longwave radiation and the downward longwave radiation emitted by the atmosphere and clouds.

$$L_n = L\downarrow - L\uparrow = f_c(\epsilon_{vs}(1 - \epsilon_a))\sigma_{sb}T_a^4 \approx f_c(\epsilon_{vs} - \epsilon_a)\sigma_{sb}T_a^4 \tag{8.28}$$

with

$$\epsilon_a - \epsilon_g = 0.261 \ e^{-7.77*10^{-4}T_a^2 - 0.02} \tag{8.29}$$

$$f_c = 0.9n_{rel} + 0.1 \tag{8.30}$$

$$\tag{8.31}$$

with
$L\downarrow$: downward longwave radiation [$\mathrm{EL}^{-2}\mathrm{T}^{-1}$]
$L\uparrow$: upward longwave radiation [$\mathrm{EL}^{-2}\mathrm{T}^{-1}$]
f_c : adjustment coefficient for cloud cover [$-$]
ϵ_{vs} : emissivity of vegetation and soil, ≈ 0.98 [$-$]
ϵ_a : emissivity of the atmosphere [$-$]
σ_{sb} : Stefan-Boltzmann constant [$\mathrm{E\,L}^{-2}\Theta^{-4}$]
T_a : mean air temperature [Θ]

Bibliography

Allen, R. G.: Self-Calibrating Method for Estimating Solar Radiation from Air Temperature, Journal of Hydrological Engineering, 2, 56–67, 1997.

Allen, R. G., Tasumi, M., and Trezza, R.: Satellite-based energy balance for mapping evapotranspiration with internalized calibration (METRIC) - Model, JOURNAL OF IRRIGATION AND DRAINAGE ENGINEERING-ASCE, 133, 380–394, 2007.

Andersen, J., Sandholt, I., Jensen, K. H., Refsgaard, J. C., and Gupta, H.: Perspectives in using a remotely sensed dryness index in distributed hydrological models at the river-basin scale, Hydrological Processes, 2987, 2973– 2987, doi:10.1002/hyp.1080, 2002.

Anderson, E.: National weather service river forecast system/snow accumulation and ablation modelNOAA Technical Memorandum NWS HYDRO-17, US Department of Commerce, Silver Spring, p. 217pp, 1973.

Anderton, S. P., White, S. M., and Alvera, B.: Micro-scale spatial variability and the timing of snow melt runoff in a high mountain catchment, Journal of Hydrology, 268, 158 – 176, 2002.

Andreadis, K. M. and Lettenmaier, D. P.: Assimilating remotely sensed snow observations into a macroscale hydrology model, Advances in Water Resources, 29, 872 – 886, 2006.

Angström, A.: Solar and terrestrial radiation. Report to the international commission for solar research on actinometric investigations of solar and atmospheric radiation, Quarterly Journal of the Royal Meteorological Society, 50, 121–126, 1924.

Ayotte, K. W.: Computational modelling for wind energy assessment, Journal of Wind Engineering and Industrial Aerodynamics, 96, 1571 – 1590, 4th International Symposium on Computational Wind Engineering (CWE2006), 2008.

Bahel, V., Bakhsh, H., and Srinivasan, R.: A correlation for estimation of global solar radiation, Energy, 12, 131 – 135, 1987.

Bárdossy, A., Stehlík, J., and Caspary, H.-j.: Automated objective classification of daily circulation patterns for precipitation and temperature downscaling based on optimized fuzzy rules, Climate Research, 23, 11–22, 2002.

Bardossy, A., Bogardi, I., and Matyasovszky, I.: Fuzzy rule-based downscaling of precipitation, Theor. Appl. Climatol., 82, 119–129, doi:10.1007/s00704-004-0121-0, 2005.

Basist, A., Bell, G. D., and Meentemeyer, V.: Statistical relationships between topography and precipitation patterns, Journal of Climate, 7, 1305–1315, 1994.

Bastiaanssen, W. G. M., Menenti, M., Feddes, R. A., and Holtslag, A. A. M.: A remote sensing surface energy balance algorithm for land (SEBAL). 1. Formulation, Journal of Hydrology, 212-213, 198 – 212, doi:10.1016/S0022-1694(98)00253-4, 1998.

Batlles, F., Bosch, J., Tovar-Pescador, J., Martínez-Durbán, M., Ortega, R., and Miralles, I.: Determination of atmospheric parameters to estimate global radiation in areas of complex topography: Generation of global irradiation map, Energy Conversion and Management, 49, 336 – 345, 2008.

Bergström, S.: Computer Models of Watershed Hydrology, chap. The HBV model, pp. 443–476, Water Resources Publications, Highlands Ranch, CO., 1995.

Betson, R. P.: "What is watershed runoff?", Journal of Geophysical Research, 69, 1541–1551, 1964.

Beven, K.: A sensitivity analysis of the Penman-Monteith actual evapotranspiration estimates, Journal of Hydrology, 44, 169 – 190, doi:10.1016/0022-1694(79)90130-6, 1979.

Beven, K.: TOPMODEL: A critique, Hydrological Processes, 11, 1069–1085, 1997.

Beven, K. J.: Rainfall-Runoff Modelling - the Primer, Wiley, Chichester, 2001.

Beven, K. J., Lamb, R., Quinn, P., Romanowicz, R., and Freer, J.: TOPMODEL, in: Computer models of watershed hydrology, edited by Singh, V. P., Highlands Ranch, Colo.: Water Resources Publications, 1995.

Bird, R. and Huldstrom, R.: Direct insolation models, Transactions ASME Journal of Solar Energy Engineering, 103, 182–192, 1980.

Black, T. A., Gardner, W. R., and Thurtell, G. W.: The prediction of evaporation, drainage and soil water storage for a bare soil, Soil Science Society of America, 33, 655–660, 1969.

Blocken, B., Carmeliet, J., and Poesen, J.: Numerical simulation of the wind-driven rainfall distribution over small-scale topography in space and time, Journal of Hydrology, 315, 252 – 273, doi:10.1016/j.jhydrol.2005.03.029, 2005.

Blöschl, G. and Sivapalan, M.: Scale issues in hydrological modelling: A review, Hydrological Processes, 9, 251–290, doi:10.1002/hyp.3360090305, 1995.

Bø ggild, C. E., Knudby, C. J., Knudsen, M. B., and Starzer, W.: Snowmelt and runoff modelling of an Arctic hydrological basin in west Greenland, Hydrological Processes, 13, 1989–2002, 1999.

Boesten, J. and Stroosnijder, L.: Simple model for daily evaporation from fallow tilled soil under spring conditions in a temperate climate, Netherlands Journal of Agricultural Science, 34, 75–90, 1986.

Bois, B., Pieri, P., Leeuwen, C. V., Wald, L., Huard, F., Gaudillere, J.-P., and Saur, E.: Using remotely sensed solar radiation data for reference evapotranspiration estimation at a daily time step, Agricultural and Forest Meteorology, 148, 619 – 630, doi:10.1016/j.agrformet.2007.11.005, 2008.

Boisvert, J. and Deutsch, C. V.: Geostatistics with Locally Varying Anisotropy, in: Frontiers+Innovation, 2009 CSPG CSEG CWLS Convention, pp. 816–819, Calgary, Alberta, Canada, 2009.

Boland, J., Scott, L., and Luther, M.: Modelling the diffuse fraction of global solar radiation on a horizontal surface, Environmetrics, 12, 103–116, 2001.

Borg, I. and Groenen, P.: Modern Multidimensional Scaling: theory and applications, Springer-Verlag, New York, 2005.

Braun, L. N., Allen, M., Funk, M., Hock, R., Rohrer, M. B., Steinegger, U., Kappenberger, G., and Müller-Lehmans, H.: Measurement and simulation of high alpine water balance components in the Linth-Limmern head watershed, Zeitschrift für Gletscherkunde und Glazialgeologie, 30, 161–185, 1994.

Bárdossy, A. and Lehmann, W.: Spatial distribution of soil moisture in a small catchment. Part 1: geostatistical analysis, Journal of Hydrology, 206, 1 – 15, doi:10.1016/S0022-1694(97)00152-2, 1998.

Bresnahan, P. A. and Miller, D. R.: Choice of data scale: predicting resolution error in a regional evapotranspiration model, Agricultural and Forest Meteorology, 84, 97 – 113, 1997.

Bristow, K. L. and Campbell, G. S.: On the relationship between incoming solar radiation and daily maximum and minimum temperature, Agricultural and Forest Meteorology, 31, 159 – 166, doi:10.1016/0168-1923(84)90017-0, 1984.

Brubaker, K., albert Rango, and Kustas, W.: Incorporating radiation inputs into the snowmelt runoff models, Hydrological Processes, 10, 1329–1343, 1996.

Cano, D., Monget, J. M., Albuisson, M., and. N. Regas, H. G., and Wald, L.: A method for the determination of the global solar radiation from meteorological satellite data, Solar Energy, 37, 31–39, 1986.

Carlson, T. N., Capehart, W. J., and Gillies, R. R.: A new look at the simplified method for remote sensing of daily evapotranspiration, Remote Sensing of Environment, 54, 161 – 167, doi:10.1016/0034-4257(95)00139-R, 1995.

Cassardo, C., Balsamo, G. P., Cacciamani, C., Cesari, D., Paccagnella, T., and Pelosini, R.: Impact of soil surface moisture initialization on rainfall in a limited area model: a case study of the 1995 South Ticino flash flood, Hydrological Processes, 16, 1301–1317, 2002.

Cazorzi, F. and Fontana, G. D.: Snowmelt modelling by combining air temperature and a distributed radiation index, Journal of Hydrology, 181, 169 – 187, doi:10.1016/0022-1694(95)02913-3, 1996.

Clark, I.: The art of cross validation in geostatistical application, in: Proceedings of the 19th International APCOM Symposium, pp. 211–220, 1986.

Cleugh, H. A., Leuning, R., Mu, Q., and Running, S. W.: Regional evaporation estimates from flux tower and MODIS satellite data, Remote Sensing of Environment, 106, 285 – 304, 2007.

Conway, H. and Raymond, C.: Snow stability during rain, Journal of Glaciology, 39, 636–642, 1993.

Corbari, C., Ravazzani, G., Martinelli, J., and Mancini, M.: Elevation based correction of snow coverage retrieved from satellite images to improve model calibration, Hydrology and Earth System Sciences, 13, 639–649, 2009.

Cullen, A. and H.C., F.: Probabilistic techniques in exposure assessment, Plenum Press, 1999.

Daly, C., Gibson, W. P., Taylor, G. H., Johnson, G. L., and Pasteris, P.: A knowledge-based approach to the statistical mapping of climate, Climate Research, 22, 99–113, 2002.

Danny Marks, Tim Link, A. W. and Garen, D.: Simulating snowmelt processes during rain-on-snow over a semi-arid mountain basin, Anuuals of Glaciology, 32, 2001.

Debele, B., Srinivasan, R., and Gosain, A. K.: Comparison of Process-Based and Temperature-Index Snowmelt Modeling in SWAT, Water Resources Management, 24, 1065–1088, 2009.

Deutsch, C. and Journel, A.: Geostatistical Software Library and User s Guide, Oxford University Press, New York, 1998.

Devlin, K.: Mathematics: The Science of Patterns, Scientific American Liberary, New York, 1997.

DeWalle, D. R. and Rango, A.: Principles of snow hydrology, Cambridge University Press, New York, http://www.cambridge.org/catalogue/catalogue.asp?isbn=0521823625, 2008.

Dingman, S. L.: Physical Hydrology, Prentice-Hall, Inc., second edn., 2002.

Downer, C. W., Ogden, F. L., Martin, W. D., and Harmon, R. S.: Theory, development, and applicability of the surface water hydrologic model, Hydrological Processes, 16, 1085–1099, doi:10.1002/hyp.338, 2002.

Dozier, J. and Frew, J.: Rapid calculation of terrain parameters for radiation modeling from digital elevation model data, IEEE Transactions on Geoscience and Remote Sensing, 28, 1769–1774, 1990.

Dubayah, R. and Loechel, S.: Modeling Topographic Solar Radiation Using GOES Data, Journal of Applied Meteorology, 36, 141–154, 1997.

Dunn, S. M. and Colohan, R. J. E.: Developing the snow component of a distributed hydrological model: a step-wise approach based on multi-objective analysis, Journal of Hydrology, 223, 1 – 16, 1999.

Dunne, T. and Black, R.: An experimental investigation of runoff production in permeable soils, Water Resources Research, 6, 478–499, 1970.

Durand, M., Molotch, N. P., and Margulis, S. A.: Merging complementary remote sensing datasets in the context of snow water equivalent reconstruction, Remote Sensing of Environment, 112, 1212 – 1225, 2008.

Dymond, C. C. and Johnson, E. A.: Mapping vegetation spatial patterns from modeled water, temperature and solar radiation gradients, ISPRS Journal of Photogrammetry and Remote Sensing, 57, 69 – 85, doi:10.1016/S0924-2716(02)00110-7, 2002.

Evseev, E. G. and Kudish, A. I.: The assessment of different models to predict the global solar radiation on a surface tilted to the south, Solar Energy, 83, 377 – 388, doi:10.1016/j.solener.2008.08.010, 2009.

FAO: Expert consultation on revision of FAO methodologies for crop water requirements, ANNEX V: FAO Penman-Monteith Formula, Tech. rep., FAO, Rome, Italy, 1990.

Finardi, S., Tinarelli, G., Faggian, P., and Brusasca, G.: Evaluation of different wind field modeling techniques for wind energy applications over complex topography, Journal of Wind Engineering and Industrial Aerodynamics, 74-76, 283 – 294, 1998.

Fox, N. I., Saich, P., and Collier, C. G.: Estimating the surface water and radiation balance in an upland area from space, International Journal of Remote Sensing, 21, 2985–3002, 2000.

Frank, H. and Landberg, L.: Modelling waving crops in a wind tunnel, Boundary-Layer Meteorology, 85, 359–377, 1997.

Frei, C. and Schär, C.: A precipitation climatology of the Alps from high-resolution rain-gauge observations, International Journal of Climatology, 18, 873–900, 1998.

Frey, H. C. and Patil, S. R.: Identification and review of sensitivity analysis methods, Risk Analysis, 22, 553–578, doi:10.1111/0272-4332.00039, 2002.

Fu, P. and Rich, P. M.: A geometric solar radiation model with applications in agriculture and forestry, Computers and Electronics in Agriculture, 37, 25 – 35, doi:10.1016/S0168-1699(02)00115-1, 2002.

Fuentes, M.: A high frequency kriging approach for non-stationary environmental processes, EnvironMetrics, 12, 469–483, 2001.

Gafurov, A. and Bárdossy, A.: Cloud removal methodology from MODIS snow cover product, Hydrology and Earth System Sciences, 13, 1361–1373, 2009.

Garen, D. C. and Marks, D.: Spatially distributed energy balance snowmelt modelling in a mountainous river basin: estimation of meteorological inputs and verification of model results, Journal of Hydrology, 315, 126 – 153, 2005.

Gerstengarbe, F. and Werner, P.: Precipitation Pattern, pp. 2916 – 2923, doi:10.1016/B978-008045405-4.00591-7, 2008.

Glover, J. and McCulloch, J. S. G.: The empirical relation between solar radiation and hours of sunshine, Quarterly Journal of the Royal Meteorological Society, 84, 172–175, 1958.

Goovaerts, P., Avruskin, G., Meliker, J., Slotnick, M., Jacquez, G., and Nriagu, J.: Geostatistical modeling of the spatial variability of arsenic in groundwater of southeast Michigan, Water Resources Research, 41, doi:10.1029/2004WR003705, 2005.

Grayson, R. B. and Blöschl, G.: Spatial Patterns in Catchment Hydrology: Observations and Modelling, Cambridge University Press, Cambridge, 2000.

Grayson, R. B., Blöschl, G., Western, A. W., and McMahon, T. A.: Advances in the use of observed spatial patterns of catchment hydrological response, Advances in Water Resources, 25, 1313 – 1334, doi:10.1016/S0309-1708(02)00060-X, 2002a.

Grayson, R. B., Blöschl, G., Western, A. W., and McMahon, T. A.: Advances in the use of observed spatial patterns of catchment hydrological response, Advances in Water Resources, 25, 1313 – 1334, doi:10.1016/S0309-1708(02)00060-X, 2002b.

Green, W. H. and Ampt, G.: Studies of soil physics. Part1. The flow of air and water through soils, Journal of the Agricultural Society, 4, 1–24, 1911.

Gueymard, C.: Mathermatically integrable parameterization of clear-sky beam and global irradiances and its use in daily irradiation applications, Solar Energy, 50, 385 – 397, 1993.

Haas, T. C.: Kriging and automated variogram modeling within a moving window, Atmospheric Environment. Part A. General Topics, 24, 1759 – 1769, doi:10.1016/0960-1686(90)90508-K, 1990.

Hallet, B.: Spatial self-organization in geomorphology: from periodic bedforms and patterned ground to scale-invariant topography, Earth-Science Reviews, 29, 57 – 75, doi:10.1016/0012-8252(0)90028-T, 1990.

Hammer, A.: Solar energy assessment using remote sensing technologies, Remote Sensing of Environment, 86, 423–432, doi:10.1016/S0034-4257(03)00083-X, 2003.

Hargreaves, G. L., Hargreaves, G. H., and Riley, J. P.: Irrigation water requirements for Senegal river basin, Journal of Irrigation and Drainage Engineering, 111, 265–275, 1985.

Harr, R. D.: Water flux in soil and subsoil on a steep forested slope, Journal of Hydrology, 33, 37 – 58, doi:10.1016/0022-1694(77)90097-X, 1977.

Haven, N.: A Linear Theory of Orographic Precipitation, Journal of the Atmospheric Sciences, 61, 1377–1391, 2004.

Hay, J. E.: Study of shortwave radiation on non-horizontal surfaces, Tech. Rep. Rept. 79-12, Atmospheric Environment Service, Downsview, Ontario, 1979.

Heidke, P.: Berechnung des Erfolges und der Gute der Windstarkevorhersagen im Sturmwarnungsdienst, Geografiska Annaler, 8, 301–349, 1926.

Hewlett, J. D. and Hibbert, A. R.: Factors affecting the response of small watersheds to precipitation in humid areas, pp. 275–290, Forest hydrology, Pergamon Press, 1967.

Hock, R.: A distributed temperature-index ice- and snowmelt model including potential direct solar radiation, Journal of Glaciology, 45, 101–111, 1999.

Hock, R.: Temperature index melt modelling in mountain areas, Journal of Hydrology, 282, 104 – 115, 2003.

Hofierka, J. and Suri, M.: The solar radiation model for Open source GIS: implementation and application, in: Proceddings of the Open source GIS - GRASS users conference 2002, Trento, Italy, 2002.

Horton, R. E.: The Role of Infiltration in Hydrology, vol. 14 of *Transactions*, pp. 446–460, American Geoscience Union, 1933.

Hosking, J. R. M. and Wallis, J. R.: Regional frequency analysis: an approach based on L-moments, Cambridge University Press, Cambridge, U.K., 1997.

Houze, R.: Cloud Dynamics, chap. Orograpic clouds, pp. 502–238, Academic Press, 1993.

Hunt, L. A., Kuchar, L., and Swanton, C. J.: Estimation of solar radiation for use in crop modelling, Agricultural and Forest Meteorology, 91, 293 – 300, 1998.

Immerzeel, W., Droogers, P., de Jong, S., and Bierkens, M.: Large-scale monitoring of snow cover and runoff simulation in Himalayan river basins using remote sensing, Remote Sensing of Environment, 113, 40 – 49, 2009.

Ineichen, P.: Comparison of eight clear sky broadband models against 16 independent data banks, Solar Energy, 80, 468 – 478, 2006.

Ineichen, P. and Perez, R.: A new airmass independent formulation for the Linke turbidity coefficient, Solar Energy, 73, 151 – 157, doi:10.1016/S0038-092X(02)00045-2, 2002.

Iqbal, M.: An introduction to solar radiation, Academic Press Canada, 1983.

Iziomon, M. G. and Mayer, H.: Assessment of some global solar radiation parameterizations, Journal of Atmospheric and Solar-Terrestrial Physics, 64, 1631 – 1643, 2002.

Janjai, S., Laksanaboonsong, J., Nunez, M., and Thongsathitya, A.: Development of a method for generating operational solar radiation maps from satellite data for a tropical environment, Solar Energy, 78, 739 – 751, doi:10.1016/j.solener.2004.09.009, 2005.

Jenny, H.: Factors of Soil Formation: A System of Quantitative Pedology, McGraw Hill Book Company, New York, NY, USA, 1941.

Jiang, Q.: Precipitation over multiscale terrain, Tellus, 59a, 321–335, doi:10.1111/j.1600-0870.2007.00232.x, 2007.

Johansson, B. and Chen, D.: The influence of wind and topograpy on precipitation distribution in Sweden: statistical analysis and modelling, International Journal of Climatology, 23, 1523–1535, doi:10.1002/joc.951, 2003.

Johnson, R. A. and Wichern, D. W.: Applied multivariate statistical analysis, Prentice Hall, Englewood Cliffs, New Jersey, 1992.

Jordan, G.: Adaptive smoothing of valleys in DEMs using TIN interpolation from ridgeline elevations: An application to morphotectonic aspect analysis, Computers & Geosciences, 33, 573 – 585, doi:10.1016/j.cageo.2006.08.010, 2007.

Julien, P. Y., Saghafian, B., and Ogden, F. L.: Raster-based hydrologic modeling of spatially-varied surface runfoff, Water Resources Bulletin, 31, 523–536, doi:10.1111/j.1752-1688.1995.tb04039.x, 1995.

Kafle, H. K. and Yamaguchi, Y.: Effects of topography on the spatial distribution of evapotranspiration over a complex terrain using two-source energy balance model with ASTER data, Hydrological Processes, 23, 2295–2306, 2009.

Kalnay, E., Kanamitsu, M., Kistler, R., Collins, W., Deaven, D., Gandin, L., Iredell, M., Saha, S., White, G., Woollen, J., Zhu, Y., Leetmaa, A., Reynolds, R., Chelliah, M., Ebisuzaki, W., Higgins, W., Janowiak, J., Mo, K. C., Ropelewski, C., Wang, J., Jenne, R., and Joseph, D.: The NCEP/NCAR 40-Year Reanalysis Project, Bulletin of the American Meteorological Society, 77, 437–471, 1996.

Kane, D. L., Gieck, R. E., and Hinzman, L. D.: Snowmelt Modeling at Small Alaskan Arctic Watershed, Journal of Hydrologic Engineering, 2, 204, 1997.

Kasten, F.: Parametriserung der Globalstrahlung durch Bedeckungsgrad und Trübungsfaktor, Annalen der Meteorologie, 20, 49–50, 1983.

Kasten, F.: The linke turbidity factor based on improved values of the integral Rayleigh optical thickness, Solar Energy, 56, 239 – 244, doi:10.1016/0038-092X(95)00114-7, 1996.

Kasten, F. and Czeplak, G.: Solar and terrestrial radiation dependent on the amount and type of cloud, Solar Energy, 24, 177 – 189, 1980.

K.H.Schlünzen and Bigalke, K.: Abschlussbericht: Entwicklung und Evaluierung eines meteorologischen Modellsystems zur Folgenabschätzung von Umwelteingriffen auf Klima und Luftqualität, Band 2: Anhänge 6 bis 10, Tech. rep., METCON Umweltmeteorologische Beratung, Pinneberg, aktenzeichen der Deutschen Bundesstiftung Umwelt: 16839, 2001a.

K.H.Schlünzen and Bigalke, K.: Abschlussbericht: Entwicklung und Evaluierung eines meteorologischen Modellsystems zur Folgenabschätzung von Umwelteingriffen auf Klima und Luftqualität, Band 1: Anhänge 1 bis 5, Tech. rep., METCON Umweltmeteorologische Beratung, Pinneberg, aktenzeichen der Deutschen Bundesstiftung Umwelt: 16839, 2001b.

Klein, A. G. and Barnett, A. C.: Validation of daily MODIS snow cover maps of the Upper Rio Grande River Basin for the 2000-2001 snow year, Remote Sensing of Environment, 86, 162 – 176, 2003.

Kustas, W. P., Rango, A., and Uijlenhoet, R.: A simple energy budget algorithm for the snowmelt runoff model, Water Resources Research, 30, 1515–1527, 1994.

Landberg, L., Myllerup, L., Rathmann, O., Petersen, E. L., Jø rgensen, B. H., Badger, J., and Mortensen, N. G.: Wind Resource Estimation - An Overview, Wind Energy, 6, 261–271, 2003.

Lehner, B., Umlauf, G., Hamann, B., and Ustin, S.: Topographic distance functions for interpolation of meteorological data, in: GI Lecture Notes in Informatics, Visualization of Large and Unstructured Data Sets, edited by Hagen, H., Kerren, A., and Dannenmann, P., pp. 119–131, 2006.

Lehning, M., Völksch, I., Gustafsson, D., Nguyen, T. A., Stähli, M., and Zappa, M.: ALPINE3D: a detailed model of mountain surface processes and its application to snow hydrology, Hydrological Processes, 20, 2111–2128, 2006.

Lehning, M., Lo, H., Ryser, M., and Raderschall, N.: Inhomogeneous precipitation distribution and snow transport in steep terrain, Water Resources Research, 44, 1–19, doi: 10.1029/2007WR006545, 2008.

Liang, S., Zheng, T., Liu, R., Fang, H., Tsay, S.-C., and Running, S.: Estimation of incident photosynthetically active radiation from Moderate Resolution Imaging Spectrometer data, Journal of Geophysical Research, 111, 1–13, doi:10.1029/2005JD006730, 2006.

Liang, X., Ettenmaier, D. P., Wood, E. F., and Buges, S. J.: A simple hydrologically based model of land surface water and energy fluxes for general circulation models, JOURNAL OF GEOPHYSICAL RESEARCH-ATMOSPHERES, 99, 14 415–14 428, 1994.

Liu, B. Y. H. and Jordan, R. C.: Daily insolation on surfaces tilted towards to equator, Transactions ASHARE, 67, 526–541, 1961.

Liu, D. L. and Scott, B. J.: Estimation of solar radiation in Australia from rainfall and temperature observations, Agricultural and Forest Meteorology, 106, 41 – 59, 2001.

Livezey, R. E.: Forecast Verification: A Practitioner's Guide in Atmospheric Science, chap. Categorical Events, pp. 77–96, John Wiley & Sons, Inc, 2003.

Male, D. and Gray, D.: Handbook of Snow, Principles, Processes, Management and Use, chap. Snowcover ablation and runoff, pp. 360–436, Pergamon Press, New York, 1981.

Marks, D., Domingo, J., Susong, D., Link, T., and Garen, D.: A spatially distributed energy balance snowmelt model for application in mountain basins, Hydrological Processes, 13, 1935–1959, 1999.

MarquInez, J., Lastra, J., and GarcIa, P.: Estimation models for precipitation in mountainous regions: the use of GIS and multivariate analysis, Journal of Hydrology, 270, 1 – 11, doi: 10.1016/S0022-1694(02)00110-5, 2003.

Marsik, M. and Waylen, P.: An application of the distributed hydrologic model CASC2D to a tropical montane watershed, Journal of Hydrology, 330, 481 – 495, doi:10.1016/j.jhydrol.2006.04.003, 2006.

Martinec, J.: Hour-to-hour snowmelt rates and lysimeter outflow during an entire ablation period, in: Snow Cover and Glacier Variations (Proceddings of Baltimore Symposium), 183, pp. 19–28, IAHS Publ. no. 183, Maryland, 1989.

Martinec, J. and Rango, A.: Parameter values for snowmelt runoff modelling, Journal of Hydrology, 84, 197 – 219, 1986.

Martínez-Durbán, M., Zarzalejo, L., Bosch, J., Rosiek, S., Polo, J., and Batlles, F.: Estimation of global daily irradiation in complex topography zones using digital elevation models and meteosat images: Comparison of the results, Energy Conversion and Management, 50, 2233 – 2238, 2009.

Maxwell, E. L.: A quasi physical model for converting hourly global horizontal to direct normal insolation, Tech. rep., Solar Energy Research Institute, Golden, Colorado, 1987.

Mckenney, D.: Calibration and sensitivity analysis of a spatially-distributed solar radiation model, International Journal of Geographical Information Science, 13, 49–65, doi:10.1080/136588199241454, 1999.

Melloch, R. A.: A synopsis and comparison of selected snowmelt algorithms, U.S. Army Corps of Engineers, Washington, DC 20314-1000, crrel report 99-8 edn., 1999.

Minasny, B. and McBratney, A. B.: A rudimentary mechanistic model for soil production and landscape development, Geoderma, 90, 3 – 21, doi:10.1016/S0016-7061(98)00115-3, 1999.

Mohanty, B. P. and Skaggs, T. H.: Spatio-temporal evolution and time-stable characteristics of soil moisture within remote sensing footprints with varying soil, slope, and vegetation, Advances in Water Resources, 24, 1051 – 1067, doi:10.1016/S0309-1708(01)00034-3, 2001.

Monestiez, P., Dubroca, L., Bonnin, E., Durbec, J.-P., and Guinet, C.: Geostatistical modelling of spatial distribution of Balaenoptera physalus in the Northwestern Mediterranean Sea from sparse count data and heterogeneous observation efforts, Ecological Modelling, 193, 615 – 628, doi:10.1016/j.ecolmodel.2005.08.042, 2006.

Moore, I. D., Grayson, R. B., and Ladson, A. R.: Digital terrain modelling: A review of hydrological, geomorphological, and biological applications, Hydrological Processes, 5, 3–30, 1991.

Moore, I. D., Gallant, J. C., and Guerra, L.: Modelling the spatial variability of hydrological process using GIS, in: HydroGIS 93: Application of Geographic Information System in Hydrology and Water Resources, Proceedings of Viena Conference, IAHS Publication, 1993.

Mu, Q., Heinsch, F. A., Zhao, M., and Running, S. W.: Development of a global evapotranspiration algorithm based on MODIS and global meteorology data, Remote Sensing of Environment, 111, 519 – 536, doi:10.1016/j.rse.2007.04.015, 2007.

Mueller, R. W., Dagestad, K. F., Ineichen, P., Schroedter-Homscheidt, M., Cros, S., Dumortier, D., Kuhlemann, R., Olseth, J. A., Piernavieja, G., Reise, C., Wald, L., and Heinemann, D.: Rethinking satellite-based solar irradiance modelling: The SOLIS clear-sky module, Remote Sensing of Environment, 91, 160 – 174, 2004.

Muneer, T.: Solar radiation model for Europe, Building Services Engineering Research and Technology, 11, 153–163, 1990.

Muneer, T. and Gul, M. S.: Evaluation of sunshine and cloud cover based models for generating solar radiation data, Energy Conversion and Management, 41, 461 – 482, 2000.

Nagler, T., Rott, H., Malcher, P., and Müller, F.: Assimilation of meteorological and remote sensing data for snowmelt runoff forecasting, Remote Sensing of Environment, 112, 1408 – 1420, 2008.

Norbiato, D., Borga, M., Esposti, S. D., Gaume, E., and Anquetin, S.: Flash flood warning based on rainfall thresholds and soil moisture conditions: An assessment for gauged and ungauged basins, Journal of Hydrology, 362, 274 – 290, 2008.

Page, J. K.: Proposed quality control procedures for the Meteorological Office data tapes relating to global solar radiation, difuse solar radiation, sunshine and cloud in the UK, Tech. rep., FCIBSE, 1997.

Parajka, J. and Blöschl, G.: Spatio-temporal combination of MODIS images – potential for snow cover mapping, Water Resources Research, 44, 1–13, 2008.

Parajka, J. and Blöschl, G.: Validation of MODIS snow cover images over Austria, Hydrology and Earth System Sciences, 10, 679–689, 2006.

Paulescu, M., Fara, L., and Tulcan-Paulescu, E.: Models for obtaining daily global solar irradiation from air temperature data, Atmospheric Research, 79, 227 – 240, 2006.

Penman, H. L.: Natural evaporation from open water, bare soil and grass, Proc. Roy. Soc., A193, 120–146, 1948.

Perez, R., Ineichen, P., Seals, R., Michalsky, J. J., and Stewart, R.: Modelling daylight availability and irradiance components from direct and global irradiance, Solar Energy, 44, 271–289, 1990.

Perez, R., Ineichen, P., Maxwell, E., Seals, R., and Zelenka, A.: Dynamic global-to-direct irradiance conversion models, ASHRAE Transactions, 98, 354–369, 1992.

Perez, R., Ineichen, P., Moore, K., Kmiecik, M., Chain, C., George, R., and Vignola, F.: A new operational model for satellite-derived irradiances: description and validation, Solar Energy, 73, 307 – 317, 2002.

Philip, J. R.: The theory of infiltration. 1. The Infiltration equation and its solution, Soil Science, 83, 345–357, 1957.

Phillips, J. D.: Stability implications of the state factor model of soils as a nonlinear dynamical system, Geoderma, 58, 1 – 15, doi:10.1016/0016-7061(93)90082-V, 1993.

Pielke, R. A. and Uliasz, M.: Use of meteorological models as input to regional and mesoscale air quality models–limitations and strengths, Atmospheric Environment, 32, 1455 – 1466, 1998.

Prescott, J. A.: Evaporation from a water surface in relation to solar radiation, Transactions of Royal Society, 64, 114–118, 1940.

Price, J.: Using Spatial Context in Satellite Data to Infer Regional Scale Evapotranspiration, IEEE Transactions on Geoscience and Remote Sensing, 28, 940–948, 1990.

Prudhomme, C. and Reed, D. W.: Relationships between extreme daily precipitation and topography in a mountainous region: A case study in Scotland, Int. J. Climatol, 18, 1439–1453, 1998.

Reda, I., Gotseff, P. A., Stoffel, T. L., , and Webb, C.: Evaluation of improved pyrgeometer calibration method, in: Thirteenth ARM Science Team Meeting Proceedings, Broomfield, colorado, 2003.

Reijmer, C. H. and Hock, R.: Internal accumulation on Storglaciären, Sweden, in a multi-layer snow model coupled to a distributed energy- and mass-balance model, Journal of Glaciology, 54, 61–72, 2008.

Rich, P. M., Hetrick, W. A., Saving, S. C., and Dubayah, R.: Viewshed analysis for calculation of incident solar radiation: applications in ecology, Proceedings of the ASPRS-ACSM Convention ASPRS, pp. 524–529, 1994.

Ridley, B., Boland, J., and Lauret, P.: Modelling of diffuse solar fraction with multiple predictors, Renewable Energy, 35, 478 – 483, 2010.

Rigollier, C., Lefèvre, M., and Wald, L.: On the clear sky model of the ESRA - European Solar Radiation Atlas - with respect to the Heliosat method, Solar Energy, 68, 33–48, 2000.

Rigollier, C., Lefèvre, M., and Wald, L.: The method Heliosat-2 for deriving shortwave solar radiation from satellite images, Solar Energy, 77, 159 – 169, 2004.

Rousseeuw, P. J. and Ruts, I.: Algorithm AS 307: Bivariate Location Depth, Journal of the Royal Statistical Society. Series C (Applied Statistics), 45, 516–526, 1996.

Ruiz-Arias, J. A., Tovar-Pescador, J., Pozo-Vazquez, D., and Alsamamra, H.: A comparative analysis of DEM-based models to estimate the solar radiation in mountainous terrain, International Journal of Geographical Information Science, 23, 1049–1076, doi:10.1080/13658810802022806, 2009.

Ruth, D. W. and Chant, R. E.: The relationship of difffuse radiation to total radiation in Canada, Solar Energy, 18, 153–154, 1976.

Saltelli, A., Ratto, M., Tarantola, S., and Campolongo, F.: Sensitivity analysis practices: Strategies for model-based inference, Reliability Engineering & System Safety, 91, 1109 – 1125, doi:10.1016/j.ress.2005.11.014, 2006.

Saltelli, A., Tarantola, S., Campolongo, F., and Ratto, M.: Sensitivity analysis in practices: A guide to assessing scientific models, Wiley, 2007.

Sampson, P., Damian, D., and Guttorp, P.: Advances in Modeling and Inference for Environmental Processes with Nonstationary Spatial Covariance, pp. 17–32, 061, Kluwer, Dordrecht, 2001.

Sampson, P. D. and Guttorp, P.: Nonparametric Estimation of Nonstationary Spatial Covariance Structure, Journal of the American Statistical Association, 87, 108–119, 1992.

Schlünzen, K. H., Bigalke, K., Lüpkes, C., and Panskus, H.: Documentation of the mesoscale transport- and fluid model METRAS PC as part of model system METRAS+, Tech. rep., Meteorologisches Institut, Universität Hamburg, mETRAS Technical Rep. 11, 2001.

Schmugge, T. J., Kustas, W. P., Ritchie, J. C., Jackson, T. J., and Rango, A.: Remote sensing in hydrology, Advances in Water Resources, 25, 1367 – 1385, 2002.

Schröder, B.: Pattern, process, and function in landscape ecology and catchment hydrology - how can quantitative landscape ecology support predictions in ungauged basins?, Hydrology and Earth System Sciences, 10, 967–979, 2006.

Schulla, J. and Jasper, K.: Model Description WaSiM-ETH, Tech. rep., Eidgenössische Technische Hochschule Zürich, 2007.

Schumann, G. and Lauener, G.: Application of a degree-day snow depth model to a Swiss glacierised catchment to improve neural network discharge forecasts, Nordic Hydrology, 36, 99–111, 2005.

Semádeni-Davies, A.: Monthly snowmelt modelling for large-scale climate change studies using the degree day approach, Ecological Modelling, 101, 303 – 323, 1997.

Sevruk, B. and Nevenic, M.: The geography and topography effects on the areal pattern of precipitation in a small prealpine basin, Water Science and Technology, 37, 163 – 170, doi:10.1016/S0273-1223(98)00329-1, 1998.

Sharon, D. and Arazi, A.: The distribution of wind-driven rainfall in a small valley: an empirical basis for numerical model verification, Journal of Hydrology, 201, 21 – 48, doi: 10.1016/S0022-1694(97)00034-6, 1997.

Singh, P., Kumar, N., and Arora, M.: Degree-day factors for snow and ice for Dokriani Glacier, Garhwal Himalayas, Journal of Hydrology, 235, 1 – 11, 2000.

Smith, R. B.: Progress on theory of orographic precipitation, Geological Society of America special paper 398, Tectonics, Climate and Landscape Evolution, pp. 1–16, 2006.

Smith, R. E. and Parlange, J. Y.: A parameter efficient infiltration model, Water Resources Research, 14, 533–538, 1978.

Sánchez, R. R.: GIS-based upland erosion modeling, geovisualization and grid size effects on errosion simulations with CASC2D-SED, Ph.D. thesis, Colorado State University, 2002.

Steen, L. A.: The Science of Patterns, Science, 240, 611–616, doi:10.1126/science.240.4852.611, 1988.

Stolar, D., Roe, G., and Willett, S.: Controls on the patterns of topography and erosion rate in a critical orogen, Water Resources Research, 112, 1–17, doi:10.1029/2006JF000713, 2007.

Strahler, A. N.: Hypsometric (Area-Altitude) analysis of erosional topography, Geological Society of America Bulletin, 63, 1117–1142, 1952.

Su, Z.: The Surface Energy Balance System (SEBS) for estimation of turbulent heat fluxes, Hydrology and Earth System Sciences, 6, 85–100, doi:10.5194/hess-6-85-2002, 2002.

Sun, R., Zhang, B., and Tan, J.: A Multivariate Regression Model for Predicting Precipitation in the Daqing Mountains, Mountain Research and Development, 28, 318–325, doi: 10.1659/mrd.0944, 2008.

Tan, P.-N., Steinbach, M., and Kumar, V.: Introduction to Data Mining, (First Edition), Addison-Wesley Longman Publishing Co., Inc., Boston, MA, USA, 2005.

Tappeiner, U., Tappeiner, G., Aschenwald, J., Tasser, E., and Ostendorf, B.: GIS-based modelling of spatial pattern of snow cover duration in an alpine area, Ecological Modelling, 138, 265 – 275, 2001.

Tarboton, D. G., Chowdhury, T. G., and Jackson, T. H.: A spatially distributed energy balance snowmelt model, in: In: Tonnessen, K.A., Williams, M.W., Tranter, M. (Eds.), Biogeochemistry of Seasonally Snow-Covered Catchments, IAHS Publication No., pp. 141–155, 1995.

Tekeli, A. E., Akyürek, Z., Sorman, A. A., Sensoy, A., and Ünal Sorman, A.: Using MODIS snow cover maps in modeling snowmelt runoff process in the eastern part of Turkey, Remote Sensing of Environment, 97, 216 – 230, 2005.

Thornthwaite, C. W. and Mather, J. R.: The Water Balance, Publications in Climatology, 8, 188, 1955.

Thornton, P. E., Running, S. W., and White, M. A.: Generating surfaces of daily meteorological variables over large regions of complex terrain, Journal of Hydrology, 190, 214 – 251, doi:10.1016/S0022-1694(96)03128-9, 1997.

Tong, J., Déry, S. J., Jackson, P. L., and Derksen, C.: Snow distribution from SSM/I and its relationships to the hydroclimatology of the Mackenzie River Basin, Canada, Advances in Water Resources, In Press, Corrected Proof, –, 2010.

Torres, J., Blas, M. D., García, A., and de Francisco, A.: Comparative study of various models in estimating hourly diffuse solar irradiance, Renewable Energy, 35, 1325 – 1332, 2010.

Trnka, M., Zalud, Z., Eitzinger, J., and Dubrovský, M.: Global solar radiation in Central European lowlands estimated by various empirical formulae, Agricultural and Forest Meteorology, 131, 54 – 76, 2005.

Urban, D. L., Miller, C., Halpin, P. N., and Stephenson, N. L.: Forest gradient response in Sierran landscapes: the physical template, Landscape Ecology, 15, 603–620, doi:10.1023/A:1008183331604, 2000.

van Dam, J., Huygen, J., Wesseling, J., R.A., F., Kabat, P., van Walsum, P., Groenendijk, P., and van Diepen, C.: Theory of SWAP version 2.0, Tech. rep., Department of Water Resources, Wageningen Agricultural University, Wageningen, the Netherlands, 1997.

Verstraeten, W. W., Veroustraete, F., and Feyen, J.: Assessment of Evapotranspiration and Soil Moisture Content Across Different Scales of Observation, Sensors, 8, 70–117, 2008.

Vertessy, R., Wilson, C., Silburn, D., Connolly, R., and Ciesiolka, C.: Predicting erosion hazard areas using digital terrain analysis, AHS AISH Publication, 192, 298–308, 1990.

Wagner, W., Blöschl, G., Pampaloni, P., Calvet, J.-c., Bizzarri, B., Wigneron, J.-P., and Kerr, Y.: Operational readiness of microwave remote sensing of soil moisture for hydrologic applications, Nordic Hydrology, 38, 1–20, 2007.

Walter, M. T., Brooks, E. S., McCool, D. K., King, L. G., Molnau, M., and Boll, J.: Process-based snowmelt modeling: does it require more input data than temperature-index modeling?, Journal of Hydrology, 300, 65 – 75, 2005.

Wang, K., Wang, P., Li, Z., Cribb, M., and Sparrow, M.: A simple method to estimate actual evapotranspiration from a combination of net radiation , vegetation index , and temperature, Journal of Geophysical Research, 112, 1–14, doi:10.1029/2006JD008351, 2007.

Wang, Q., Tenhunen, J., Schmidt, M., and Kolcun, O.: A Model to Estimate Global Radiation in Complex Terrain, Boundary-Layer Meteorology, 119, 409–429, doi:10.1007/s10546-005-9000-1, 2006.

Wang, S., Chen, W., and Cihlar, J.: New calculation methods of diurnal distribution of solar radiation and its interception by canopy over complex terrain, Ecological Modelling, 155, 191 – 204, 2002.

Wastl, C. and Zängl, G.: Analysis of mountain-valley precipitation differences in the Alps, Meteorologisch Zeitschrift, 17, 311–321, doi:10.1127/0941-2948/2008/0291, 2008.

Watson, F. G., Anderson, T. N., Kramer, M., Detka, J., Masek, T., Cornish, S. S., and Moore, S. W.: Chapter 5 Effects of Wind, Terrain, and Vegetation on Snow Pack, 3, 67 – 84, doi:10.1016/S1936-7961(08)00205-4, 2008.

Weisse, A. K. and Bois, P.: Topographic Effects on Statistical Characteristics of Heavy Rainfall and Mapping in the French Alps, Journal of Applied Meteorology, 40, 720–740, 2001.

Western, A. W. and Grayson, R. B.: The Tarrawarra Data Set: Soil Moisture Patterns, Soil Characteristics, and Hydrological Flux Measurements, Water Resources Research, 34, 2765–2768, doi:10.1029/98WR01833, 1998.

Western, A. W., Grayson, R. B., and Blöschl, G.: Scaling of Soil Moisture: A Hydrologic Perspective, Annual Review of Earth and Planetary Sciences, 30, 149–180, 2002.

Westrick, K. J. and Mass, C. F.: An Evaluation of a High-Resolution Hydrometeorological Modeling System for Prediction of a Cool-Season Flood Event in a Coastal Mountainous Watershed, Journal of Hydrometeorology, 2, 161–180, 2001.

Weyman, D.: Measurements of the downslope flow of water in a soil, Journal of Hydrology, 20, 267 – 288, doi:10.1016/0022-1694(73)90065-6, 1973.

Wilson, J. P. and Gallant, J. C., eds.: Terrain analysis: principles and applications, John Wiley & Sons, Inc, 2000.

Winstral, A., Marks, D., and Gurney, R.: An efficient method for distributing wind speeds over heterogeneous terrain, Hydrological Processes, 2535, 2526– 2535, doi:10.1002/hyp, 2009.

WMO: Intercomparison of models of snowmelt runoff, Tech. Rep. 23, World Meteorological Organization, Geneva, 1986.

WMO: Guide to Meteorological Instruments and Methods of Observation, World Meteorological Organization, seventh edn., 2008.

Wu, G., Liu, Y., and Wang, T.: Methods and strategy for modeling daily global solar radiation with measured meteorological data - A case study in Nanchang station, China, Energy Conversion and Management, 48, 2447 – 2452, doi:10.1016/j.enconman.2007.04.011, 2007.

Xu, C. Y. and Singh, V. P.: Evaluation and generalization of radiation-based methods for calculating evaporation, Hydrol. Process., 14, 339–349, 2000.

Yang, K. and Koike, T.: Estimating surface solar radiation from upper-air humidity, Solar Energy, 72, 177 – 186, 2002.

Yang, W., Tan, B., Huang, D., Rautiainen, M., Shabanov, N. V., Wang, Y., Privette, J. L., Huemmrich, K. F., Fensholt, R., Sandholt, I., Weiss, M., Ahl, D. E., Gower, S. T., Nemani, R. R., Knyazikhin, Y., and Myneni, R. B.: MODIS Leaf Area Index Products : From Validation to Algorithm Improvement, IEEE Transactions on Geoscience and Remote Sensing, 44, 1885–1898, 2006.

Zehe, E. and Flühler, H.: Slope scale variation of flow patterns in soil profiles, Journal of Hydrology, 247, 116 – 132, doi:10.1016/S0022-1694(01)00371-7, 2001.

Zehe, E., Maurer, T., Ihringer, J., and Plate, E.: Modeling water flow and mass transport in a loess catchment, Physics and Chemistry of the Earth, Part B: Hydrology, Oceans and Atmosphere, 26, 487 – 507, 2001.

Zehe, E., Graeff, T., Morgner, M., Bauer, A., and Bronstert, A.: Plot and field scale soil moisture dynamics and subsurface wetness control on runoff generation in a headwater in the Ore Mountains, Hydrology and Earth System Sciences, 14, 873–889, 2010.

Zuzel, J. F. and Cox, L. M.: Relative Importance of Meteorological Variables in Snowmelt, Water Resources Research, 11, 174–176, 1975.

Curriculum Vitae

Personal Information

Name:	Min Liu
Date of Birth:	06.01.1978
Place of Birth:	Hubei, China

Educational Background

10/2006 - 10/2010 :	Doctoral study
	Dept. of Hydrology and Geohydrology, Institute of Hydraulic Engineering
	Universität Stuttgart, Germany
	Member of the International Doctoral Program ENWAT (http://www.phd.envwater.uni-stuttgart.de/)
04/2006 - 03/2008:	Master of Business Administration (MBA)
	Hochschule für Wirtschaft und Umwelt, Nürtingen-Geislingen
09/2003 - 11/2005:	Master of Science
	International Program of Water Resources Engineering and Management
	Universität Suttgart, Germany
09/1995 - 07/2000:	Bachelor of Science
	Dept. of Civil and Environmental Engineering
	Tongji University, Shanghai, China

Working Experience

10/2006 - 10/2010 :	Research Assistant
	Dept. of Hydrology and Geohydrology, Institute of Hydraulic Engineering
	Universität Suttgart, Germany
07/2000 - 08/2003:	Water/Wastewater Engineer
	Shanghai Urban Construction Design and Research Institute
	Shanghai, China

Institut für Wasserbau
Universität Stuttgart

Pfaffenwaldring 61
70569 Stuttgart (Vaihingen)
Telefon (0711) 685 - 64717/64749/64752/64679
Telefax (0711) 685 - 67020 o. 64746 o. 64681
E-Mail: iws@iws.uni-stuttgart.de
http://www.iws.uni-stuttgart.de

Verzeichnis der Mitteilungshefte

5 Plate, Erich: *Beitrag zur Bestimmung der Windgeschwindigkeitsverteilung in der durch eine Wand gestörten bodennahen Luftschicht*,
und
Röhnisch, Arthur; Marotz, Günter: *Neue Baustoffe und Bauausführungen für den Schutz der Böschungen und der Sohle von Kanälen, Flüssen und Häfen; Gestehungskosten und jeweilige Vorteile*, sowie Unny, T.E.: *Schwingungsuntersuchungen am Kegelstrahlschieber*, 1967

6 Seiler, Erich: *Die Ermittlung des Anlagenwertes der bundeseigenen Binnenschiffahrtsstraßen und Talsperren und des Anteils der Binnenschiffahrt an diesem Wert*, 1967

7 *Sonderheft anläßlich des 65. Geburtstages von Prof. Arthur Röhnisch mit Beiträgen von* Benk, Dieter; Breitling, J.; Gurr, Siegfried; Haberhauer, Robert; Honekamp, Hermann; Kuz, Klaus Dieter; Marotz, Günter; Mayer-Vorfelder, Hans-Jörg; Miller, Rudolf; Plate, Erich J.; Radomski, Helge; Schwarz, Helmut; Vollmer, Ernst; Wildenhahn, Eberhard; 1967

8 Jumikis, Alfred: *Beitrag zur experimentellen Untersuchung des Wassernachschubs in einem gefrierenden Boden und die Beurteilung der Ergebnisse*, 1968

9 Marotz, Günter: *Technische Grundlagen einer Wasserspeicherung im natürlichen Untergrund*, 1968

10 Radomski, Helge: *Untersuchungen über den Einfluß der Querschnittsform wellenförmiger Spundwände auf die statischen und rammtechnischen Eigenschaften*, 1968

11 Schwarz, Helmut: *Die Grenztragfähigkeit des Baugrundes bei Einwirkung vertikal gezogener Ankerplatten als zweidimensionales Bruchproblem*, 1969

12 Erbel, Klaus: *Ein Beitrag zur Untersuchung der Metamorphose von Mittelgebirgsschneedecken unter besonderer Berücksichtigung eines Verfahrens zur Bestimmung der thermischen Schneequalität*, 1969

13 Westhaus, Karl-Heinz: *Der Strukturwandel in der Binnenschiffahrt und sein Einfluß auf den Ausbau der Binnenschiffskanäle*, 1969

14 Mayer-Vorfelder, Hans-Jörg: *Ein Beitrag zur Berechnung des Erdwiderstandes unter Ansatz der logarithmischen Spirale als Gleitflächenfunktion*, 1970

15 Schulz, Manfred: *Berechnung des räumlichen Erddruckes auf die Wandung kreiszylindrischer Körper*, 1970

16 Mobasseri, Manoutschehr: *Die Rippenstützmauer. Konstruktion und Grenzen ihrer Standsicherheit*, 1970

17 Benk, Dieter: *Ein Beitrag zum Betrieb und zur Bemessung von Hochwasserrückhaltebecken*, 1970

18 Gàl, Attila: *Bestimmung der mitschwingenden Wassermasse bei überströmten Fischbauchklappen mit kreiszylindrischem Staublech*, 1971, vergriffen

19 Kuz, Klaus Dieter: *Ein Beitrag zur Frage des Einsetzens von Kavitationserscheinungen in einer Düsenströmung bei Berücksichtigung der im Wasser gelösten Gase*, 1971, vergriffen

20 Schaak, Hartmut: *Verteilleitungen von Wasserkraftanlagen*, 1971

21 *Sonderheft zur Eröffnung der neuen Versuchsanstalt des Instituts für Wasserbau der Universität Stuttgart mit Beiträgen von* Brombach, Hansjörg; Dirksen, Wolfram; Gàl, Attila; Gerlach, Reinhard; Giesecke, Jürgen; Holthoff, Franz-Josef; Kuz, Klaus Dieter; Marotz, Günter; Minor, Hans-Erwin; Petrikat, Kurt; Röhnisch, Arthur; Rueff, Helge; Schwarz, Helmut; Vollmer, Ernst; Wildenhahn, Eberhard; 1972

22 Wang, Chung-su: *Ein Beitrag zur Berechnung der Schwingungen an Kegelstrahlschiebern*, 1972

23 Mayer-Vorfelder, Hans-Jörg: *Erdwiderstandsbeiwerte nach dem Ohde-Variationsverfahren*, 1972

24 Minor, Hans-Erwin: *Beitrag zur Bestimmung der Schwingungsanfachungsfunktionen überströmter Stauklappen*, 1972, vergriffen

25 Brombach, Hansjörg: *Untersuchung strömungsmechanischer Elemente (Fluidik) und die Möglichkeit der Anwendung von Wirbelkammerelementen im Wasserbau*, 1972, vergriffen

26 Wildenhahn, Eberhard: *Beitrag zur Berechnung von Horizontalfilterbrunnen*, 1972

27 Steinlein, Helmut: *Die Eliminierung der Schwebstoffe aus Flußwasser zum Zweck der unterirdischen Wasserspeicherung, gezeigt am Beispiel der Iller*, 1972

28 Holthoff, Franz Josef: *Die Überwindung großer Hubhöhen in der Binnenschiffahrt durch Schwimmerhebewerke*, 1973

29 Röder, Karl: *Einwirkungen aus Baugrundbewegungen auf trog- und kastenförmige Konstruktionen des Wasser- und Tunnelbaues*, 1973

30 Kretschmer, Heinz: *Die Bemessung von Bogenstaumauern in Abhängigkeit von der Talform*, 1973

31 Honekamp, Hermann: *Beitrag zur Berechnung der Montage von Unterwasserpipelines*, 1973

32 Giesecke, Jürgen: *Die Wirbelkammertriode als neuartiges Steuerorgan im Wasserbau*, und Brombach, Hansjörg: *Entwicklung, Bauformen, Wirkungsweise und Steuereigenschaften von Wirbelkammerverstärkern*, 1974

33 Rueff, Helge: *Untersuchung der schwingungserregenden Kräfte an zwei hintereinander angeordneten Tiefschützen unter besonderer Berücksichtigung von Kavitation*, 1974

34 Röhnisch, Arthur: *Einpreßversuche mit Zementmörtel für Spannbeton - Vergleich der Ergebnisse von Modellversuchen mit Ausführungen in Hüllwellrohren*, 1975

35 *Sonderheft anläßlich des 65. Geburtstages von Prof. Dr.-Ing. Kurt Petrikat mit Beiträgen von*: Brombach, Hansjörg; Erbel, Klaus; Flinspach, Dieter; Fischer jr., Richard; Gàl, Attila; Gerlach, Reinhard; Giesecke, Jürgen; Haberhauer, Robert; Hafner Edzard; Hausenblas, Bernhard; Horlacher, Hans-Burkhard; Hutarew, Andreas; Knoll, Manfred; Krummet, Ralph; Marotz, Günter; Merkle, Theodor; Miller, Christoph; Minor, Hans-Erwin; Neumayer, Hans; Rao, Syamala; Rath, Paul; Rueff, Helge; Ruppert, Jürgen; Schwarz, Wolfgang; Topal-Gökceli, Mehmet; Vollmer, Ernst; Wang, Chung-su; Weber, Hans-Georg; 1975

36 Berger, Jochum: *Beitrag zur Berechnung des Spannungszustandes in rotationssymmetrisch belasteten Kugelschalen veränderlicher Wandstärke unter Gas- und Flüssigkeitsdruck durch Integration schwach singulärer Differentialgleichungen*, 1975

37 Dirksen, Wolfram: *Berechnung instationärer Abflußvorgänge in gestauten Gerinnen mittels Differenzenverfahren und die Anwendung auf Hochwasserrückhaltebecken*, 1976

38 Horlacher, Hans-Burkhard: *Berechnung instationärer Temperatur- und Wärmespannungsfelder in langen mehrschichtigen Hohlzylindern*, 1976

39 Hafner, Edzard: *Untersuchung der hydrodynamischen Kräfte auf Baukörper im Tiefwasserbereich des Meeres*, 1977, ISBN 3-921694-39-6

40 Ruppert, Jürgen: *Über den Axialwirbelkammerverstärker für den Einsatz im Wasserbau*, 1977, ISBN 3-921694-40-X

41 Hutarew, Andreas: *Beitrag zur Beeinflußbarkeit des Sauerstoffgehalts in Fließgewässern an Abstürzen und Wehren*, 1977, ISBN 3-921694-41-8, vergriffen

42 Miller, Christoph: *Ein Beitrag zur Bestimmung der schwingungserregenden Kräfte an unterströmten Wehren*, 1977, ISBN 3-921694-42-6

43 Schwarz, Wolfgang: *Druckstoßberechnung unter Berücksichtigung der Radial- und Längsverschiebungen der Rohrwandung*, 1978, ISBN 3-921694-43-4

44 Kinzelbach, Wolfgang: *Numerische Untersuchungen über den optimalen Einsatz variabler Kühlsysteme einer Kraftwerkskette am Beispiel Oberrhein*, 1978, ISBN 3-921694-44-2

45 Barczewski, Baldur: *Neue Meßmethoden für Wasser-Luftgemische und deren Anwendung auf zweiphasige Auftriebsstrahlen*, 1979, ISBN 3-921694-45-0

46 Neumayer, Hans: *Untersuchung der Strömungsvorgänge in radialen Wirbelkammerverstärkern*, 1979, ISBN 3-921694-46-9

47 Elalfy, Youssef-Elhassan: *Untersuchung der Strömungsvorgänge in Wirbelkammerdioden und -drosseln*, 1979, ISBN 3-921694-47-7

48 Brombach, Hansjörg: *Automatisierung der Bewirtschaftung von Wasserspeichern*, 1981, ISBN 3-921694-48-5

49 Geldner, Peter: *Deterministische und stochastische Methoden zur Bestimmung der Selbstdichtung von Gewässern*, 1981, ISBN 3-921694-49-3, vergriffen

50 Mehlhorn, Hans: *Temperaturveränderungen im Grundwasser durch Brauchwassereinleitungen*, 1982, ISBN 3-921694-50-7, vergriffen

51 Hafner, Edzard: *Rohrleitungen und Behälter im Meer*, 1983, ISBN 3-921694-51-5

52 Rinnert, Bernd: *Hydrodynamische Dispersion in porösen Medien: Einfluß von Dichteunterschieden auf die Vertikalvermischung in horizontaler Strömung*, 1983, ISBN 3-921694-52-3, vergriffen

53 Lindner, Wulf: *Steuerung von Grundwasserentnahmen unter Einhaltung ökologischer Kriterien*, 1983, ISBN 3-921694-53-1, vergriffen

54 Herr, Michael; Herzer, Jörg; Kinzelbach, Wolfgang; Kobus, Helmut; Rinnert, Bernd: *Methoden zur rechnerischen Erfassung und hydraulischen Sanierung von Grundwasserkontaminationen*, 1983, ISBN 3-921694-54-X

55 Schmitt, Paul: *Wege zur Automatisierung der Niederschlagsermittlung*, 1984, ISBN 3-921694-55-8, vergriffen

56 Müller, Peter: *Transport und selektive Sedimentation von Schwebstoffen bei gestautem Abfluß*, 1985, ISBN 3-921694-56-6

57 El-Qawasmeh, Fuad: *Möglichkeiten und Grenzen der Tropfbewässerung unter besonderer Berücksichtigung der Verstopfungsanfälligkeit der Tropfelemente*, 1985, ISBN 3-921694-57-4, vergriffen

58 Kirchenbaur, Klaus: *Mikroprozessorgesteuerte Erfassung instationärer Druckfelder am Beispiel seegangsbelasteter Baukörper*, 1985, ISBN 3-921694-58-2

59 Kobus, Helmut (Hrsg.): *Modellierung des großräumigen Wärme- und Schadstofftransports im Grundwasser*, Tätigkeitsbericht 1984/85 (DFG-Forschergruppe an den Universitäten Hohenheim, Karlsruhe und Stuttgart), 1985, ISBN 3-921694-59-0, vergriffen

60 Spitz, Karlheinz: *Dispersion in porösen Medien: Einfluß von Inhomogenitäten und Dichteunterschieden*, 1985, ISBN 3-921694-60-4, vergriffen

61 Kobus, Helmut: *An Introduction to Air-Water Flows in Hydraulics*, 1985, ISBN 3-921694-61-2

62 Kaleris, Vassilios: *Erfassung des Austausches von Oberflächen- und Grundwasser in horizontalebenen Grundwassermodellen*, 1986, ISBN 3-921694-62-0

63 Herr, Michael: *Grundlagen der hydraulischen Sanierung verunreinigter Porengrundwasserleiter*, 1987, ISBN 3-921694-63-9

64 Marx, Walter: *Berechnung von Temperatur und Spannung in Massenbeton infolge Hydratation*, 1987, ISBN 3-921694-64-7

65 Koschitzky, Hans-Peter: *Dimensionierungskonzept für Sohlbelüfter in Schußrinnen zur Vermeidung von Kavitationsschäden*, 1987, ISBN 3-921694-65-5

66 Kobus, Helmut (Hrsg.): *Modellierung des großräumigen Wärme- und Schadstofftransports im Grundwasser*, Tätigkeitsbericht 1986/87 (DFG-Forschergruppe an den Universitäten Hohenheim, Karlsruhe und Stuttgart) 1987, ISBN 3-921694-66-3

67 Söll, Thomas: *Berechnungsverfahren zur Abschätzung anthropogener Temperaturanomalien im Grundwasser*, 1988, ISBN 3-921694-67-1

68 Dittrich, Andreas; Westrich, Bernd: *Bodenseeufererosion, Bestandsaufnahme und Bewertung*, 1988, ISBN 3-921694-68-X, vergriffen

69 Huwe, Bernd; van der Ploeg, Rienk R.: *Modelle zur Simulation des Stickstoffhaushaltes von Standorten mit unterschiedlicher landwirtschaftlicher Nutzung*, 1988, ISBN 3-921694-69-8, vergriffen

70 Stephan, Karl: *Integration elliptischer Funktionen*, 1988, ISBN 3-921694-70-1

71 Kobus, Helmut; Zilliox, Lothaire (Hrsg.): *Nitratbelastung des Grundwassers, Auswirkungen der Landwirtschaft auf die Grundwasser- und Rohwasserbeschaffenheit und Maßnahmen zum Schutz des Grundwassers*. Vorträge des deutsch-französischen Kolloquiums am 6. Oktober 1988, Universitäten Stuttgart und Louis Pasteur Strasbourg (Vorträge in deutsch oder französisch, Kurzfassungen zweisprachig), 1988, ISBN 3-921694-71-X

72 Soyeaux, Renald: *Unterströmung von Stauanlagen auf klüftigem Untergrund unter Berücksichtigung laminarer und turbulenter Fließzustände*,1991, ISBN 3-921694-72-8

73 Kohane, Roberto: *Berechnungsmethoden für Hochwasserabfluß in Fließgewässern mit überströmten Vorländern*, 1991, ISBN 3-921694-73-6

74 Hassinger, Reinhard: *Beitrag zur Hydraulik und Bemessung von Blocksteinrampen in flexibler Bauweise*, 1991, ISBN 3-921694-74-4, vergriffen

75 Schäfer, Gerhard: *Einfluß von Schichtenstrukturen und lokalen Einlagerungen auf die Längsdispersion in Porengrundwasserleitern*, 1991, ISBN 3-921694-75-2

76 Giesecke, Jürgen: *Vorträge, Wasserwirtschaft in stark besiedelten Regionen; Umweltforschung mit Schwerpunkt Wasserwirtschaft*, 1991, ISBN 3-921694-76-0

77 Huwe, Bernd: *Deterministische und stochastische Ansätze zur Modellierung des Stickstoffhaushalts landwirtschaftlich genutzter Flächen auf unterschiedlichem Skalenniveau*, 1992, ISBN 3-921694-77-9, vergriffen

78 Rommel, Michael: *Verwendung von Kluftdaten zur realitätsnahen Generierung von Kluftnetzen mit anschließender laminar-turbulenter Strömungsberechnung*, 1993, ISBN 3-92 1694-78-7

79 Marschall, Paul: *Die Ermittlung lokaler Stofffrachten im Grundwasser mit Hilfe von Einbohrloch-Meßverfahren*, 1993, ISBN 3-921694-79-5, vergriffen

80 Ptak, Thomas: *Stofftransport in heterogenen Porenaquiferen: Felduntersuchungen und stochastische Modellierung*, 1993, ISBN 3-921694-80-9, vergriffen

81 Haakh, Frieder: *Transientes Strömungsverhalten in Wirbelkammern,* 1993, ISBN 3-921694-81-7

82 Kobus, Helmut; Cirpka, Olaf; Barczewski, Baldur; Koschitzky, Hans-Peter: *Versucheinrichtung zur Grundwasser und Altlastensanierung VEGAS, Konzeption und Programmrahmen*, 1993, ISBN 3-921694-82-5

83 Zang, Weidong: *Optimaler Echtzeit-Betrieb eines Speichers mit aktueller Abflußregenerierung*, 1994, ISBN 3-921694-83-3, vergriffen

84 Franke, Hans-Jörg: *Stochastische Modellierung eines flächenhaften Stoffeintrages und Transports in Grundwasser am Beispiel der Pflanzenschutzmittelproblematik*, 1995, ISBN 3-921694-84-1

85 Lang, Ulrich: *Simulation regionaler Strömungs- und Transportvorgänge in Karstaquiferen mit Hilfe des Doppelkontinuum-Ansatzes: Methodenentwicklung und Parameteridentifikation*, 1995, ISBN 3-921694-85-X, vergriffen

86 Helmig, Rainer: *Einführung in die Numerischen Methoden der Hydromechanik*, 1996, ISBN 3-921694-86-8, vergriffen

87 Cirpka, Olaf: *CONTRACT: A Numerical Tool for Contaminant Transport and Chemical Transformations - Theory and Program Documentation* -, 1996, ISBN 3-921694-87-6

88 Haberlandt, Uwe: *Stochastische Synthese und Regionalisierung des Niederschlages für Schmutzfrachtberechnungen*, 1996, ISBN 3-921694-88-4

89 Croisé, Jean: *Extraktion von flüchtigen Chemikalien aus natürlichen Lockergesteinen mittels erzwungener Luftströmung*, 1996, ISBN 3-921694-89-2, vergriffen

90 Jorde, Klaus: *Ökologisch begründete, dynamische Mindestwasserregelungen bei Ausleitungskraftwerken*, 1997, ISBN 3-921694-90-6, vergriffen

91 Helmig, Rainer: *Gekoppelte Strömungs- und Transportprozesse im Untergrund - Ein Beitrag zur Hydrosystemmodellierung*-, 1998, ISBN 3-921694-91-4, vergriffen

92 Emmert, Martin: *Numerische Modellierung nichtisothermer Gas-Wasser Systeme in porösen Medien,* 1997, ISBN 3-921694-92-2

93 Kern, Ulrich: *Transport von Schweb- und Schadstoffen in staugeregelten Fließgewässern am Beispiel des Neckars*, 1997, ISBN 3-921694-93-0, vergriffen

94 Förster, Georg: *Druckstoßdämpfung durch große Luftblasen in Hochpunkten von Rohrleitungen 1997*, ISBN 3-921694-94-9

95 Cirpka, Olaf: *Numerische Methoden zur Simulation des reaktiven Mehrkomponententransports im Grundwasser*, 1997, ISBN 3-921694-95-7, vergriffen

96 Färber, Arne: *Wärmetransport in der ungesättigten Bodenzone: Entwicklung einer thermischen In-situ-Sanierungstechnologie*, 1997, ISBN 3-921694-96-5

97 Betz, Christoph: *Wasserdampfdestillation von Schadstoffen im porösen Medium: Entwicklung einer thermischen In-situ-Sanierungstechnologie*, 1998, ISBN 3-921694-97-3

98 Xu, Yichun: *Numerical Modeling of Suspended Sediment Transport in Rivers*, 1998, ISBN 3-921694-98-1, vergriffen

99 Wüst, Wolfgang: *Geochemische Untersuchungen zur Sanierung CKW-kontaminierter Aquifere mit Fe(0)-Reaktionswänden,* 2000, ISBN 3-933761-02-2

100 Sheta, Hussam: *Simulation von Mehrphasenvorgängen in porösen Medien unter Einbeziehung von Hysterese-Effekten*, 2000, ISBN 3-933761-03-4

101 Ayros, Edwin: *Regionalisierung extremer Abflüsse auf der Grundlage statistischer Verfahren*, 2000, ISBN 3-933761-04-2, vergriffen

102 Huber, Ralf: *Compositional Multiphase Flow and Transport in Heterogeneous Porous Media*, 2000, ISBN 3-933761-05-0

103 Braun, Christopherus: *Ein Upscaling-Verfahren für Mehrphasenströmungen in porösen Medien*, 2000, ISBN 3-933761-06-9

104 Hofmann, Bernd: *Entwicklung eines rechnergestützten Managementsystems zur Beurteilung von Grundwasserschadensfällen*, 2000, ISBN 3-933761-07-7

105 Class, Holger: *Theorie und numerische Modellierung nichtisothermer Mehrphasenprozesse in NAPL-kontaminierten porösen Medien,* 2001, ISBN 3-933761-08-5

106 Schmidt, Reinhard: *Wasserdampf- und Heißluftinjektion zur thermischen Sanierung kontaminierter Standorte*, 2001, ISBN 3-933761-09-3

107 Josef, Reinhold:, *Schadstoffextraktion mit hydraulischen Sanierungsverfahren unter Anwendung von grenzflächenaktiven Stoffen*, 2001, ISBN 3-933761-10-7

108 Schneider, Matthias: *Habitat- und Abflussmodellierung für Fließgewässer mit unscharfen Berechnungsansätzen*, 2001, ISBN 3-933761-11-5

109 Rathgeb, Andreas: *Hydrodynamische Bemessungsgrundlagen für Lockerdeckwerke an überströmbaren Erddämmen*, 2001, ISBN 3-933761-12-3

110 Lang, Stefan: *Parallele numerische Simulation instätionärer Probleme mit adaptiven Methoden auf unstrukturierten Gittern*, 2001, ISBN 3-933761-13-1

111 Appt, Jochen; Stumpp Simone: *Die Bodensee-Messkampagne 2001, IWS/CWR Lake Constance Measurement Program 2001*, 2002, ISBN 3-933761-14-X

112 Heimerl, Stephan: *Systematische Beurteilung von Wasserkraftprojekten,* 2002, ISBN 3-933761-15-8

113 Iqbal, Amin: *On the Management and Salinity Control of Drip Irrigation,* 2002, ISBN 3-933761-16-6

114 Silberhorn-Hemminger, Annette: *Modellierung von Kluftaquifersystemen: Geostatistische Analyse und deterministisch-stochastische Kluftgenerierung,* 2002, ISBN 3-933761-17-4

115 Winkler, Angela: *Prozesse des Wärme- und Stofftransports bei der In-situ-Sanierung mit festen Wärmequellen,* 2003, ISBN 3-933761-18-2

116 Marx, Walter: *Wasserkraft, Bewässerung, Umwelt - Planungs- und Bewertungsschwerpunkte der Wasserbewirtschaftung,* 2003, ISBN 3-933761-19-0

117 Hinkelmann, Reinhard: *Efficient Numerical Methods and Information-Processing Techniques in Environment Water,* 2003, ISBN 3-933761-20-4

118 Samaniego-Eguiguren, Luis Eduardo: *Hydrological Consequences of Land Use / Land Cover and Climatic Changes in Mesoscale Catchments*, 2003, ISBN 3-933761-21-2

119 Neunhäuserer, Lina: *Diskretisierungsansätze zur Modellierung von Strömungs- und Transportprozessen in geklüftet-porösen Medien*, 2003, ISBN 3-933761-22-0

120 Paul, Maren: *Simulation of Two-Phase Flow in Heterogeneous Poros Media with Adaptive Methods*, 2003, ISBN 3-933761-23-9

121 Ehret, Uwe: *Rainfall and Flood Nowcasting in Small Catchments using Weather Radar*, 2003, ISBN 3-933761-24-7

122 Haag, Ingo: *Der Sauerstoffhaushalt staugeregelter Flüsse am Beispiel des Neckars - Analysen, Experimente, Simulationen -,* 2003, ISBN 3-933761-25-5

123 Appt, Jochen: *Analysis of Basin-Scale Internal Waves in Upper Lake Constance,* 2003, ISBN 3-933761-26-3

124 Hrsg.: Schrenk, Volker; Batereau, Katrin; Barczewski, Baldur; Weber, Karolin und Koschitzky, Hans-Peter: *Symposium Ressource Fläche und VEGAS - Statuskolloquium 2003, 30. September und 1. Oktober 2003,* 2003, ISBN 3-933761-27-1

125 Omar Khalil Ouda: *Optimisation of Agricultural Water Use: A Decision Support System for the Gaza Strip,* 2003, ISBN 3-933761-28-0

126 Batereau, Katrin: *Sensorbasierte Bodenluftmessung zur Vor-Ort-Erkundung von Schadensherden im Untergrund*, 2004, ISBN 3-933761-29-8

127 Witt, Oliver: *Erosionsstabilität von Gewässersedimenten mit Auswirkung auf den Stofftransport bei Hochwasser am Beispiel ausgewählter Stauhaltungen des Oberrheins*, 2004, ISBN 3-933761-30-1

128 Jakobs, Hartmut: *Simulation nicht-isothermer Gas-Wasser-Prozesse in komplexen Kluft-Matrix-Systemen*, 2004, ISBN 3-933761-31-X

129 Li, Chen-Chien: *Deterministisch-stochastisches Berechnungskonzept zur Beurteilung der Auswirkungen erosiver Hochwasserereignisse in Flussstauhaltungen,* 2004, ISBN 3-933761-32-8

130 Reichenberger, Volker; Helmig, Rainer; Jakobs, Hartmut; Bastian, Peter; Niessner, Jennifer: *Complex Gas-Water Processes in Discrete Fracture-Matrix Systems: Upscaling, Mass-Conservative Discretization and Efficient Multilevel Solution,* 2004, ISBN 3-933761-33-6

131 Hrsg.: Barczewski, Baldur; Koschitzky, Hans-Peter; Weber, Karolin; Wege, Ralf: *VEGAS - Statuskolloquium 2004,* Tagungsband zur Veranstaltung am 05. Oktober 2004 an der Universität Stuttgart, Campus Stuttgart-Vaihingen, 2004, ISBN 3-933761-34-4

132 Asie, Kemal Jabir: *Finite Volume Models for Multiphase Multicomponent Flow through Porous Media*. 2005, ISBN 3-933761-35-2

133 Jacoub, George: *Development of a 2-D Numerical Module for Particulate Contaminant Transport in Flood Retention Reservoirs and Impounded Rivers,* 2004, ISBN 3-933761-36-0

134 Nowak, Wolfgang: *Geostatistical Methods for the Identification of Flow and Transport Parameters in the Subsurface,* 2005, ISBN 3-933761-37-9

135 Süß, Mia: *Analysis of the influence of structures and boundaries on flow and transport processes in fractured porous media*, 2005, ISBN 3-933761-38-7

136 Jose, Surabhin Chackiath: *Experimental Investigations on Longitudinal Dispersive Mixing in Heterogeneous Aquifers,* 2005, ISBN: 3-933761-39-5

137 Filiz, Fulya: *Linking Large-Scale Meteorological Conditions to Floods in Mesoscale Catchments,* 2005, ISBN 3-933761-40-9

138 Qin, Minghao: *Wirklichkeitsnahe und recheneffiziente Ermittlung von Temperatur und Spannungen bei großen RCC-Staumauern*, 2005, ISBN 3-933761-41-7

139 Kobayashi, Kenichiro: *Optimization Methods for Multiphase Systems in the Subsurface - Application to Methane Migration in Coal Mining Areas*, 2005, ISBN 3-933761-42-5

140 Rahman, Md. Arifur: *Experimental Investigations on Transverse Dispersive Mixing in Heterogeneous Porous Media,* 2005, ISBN 3-933761-43-3

141 Schrenk, Volker: *Ökobilanzen zur Bewertung von Altlastensanierungsmaßnahmen,* 2005, ISBN 3-933761-44-1

142 Hundecha, Hirpa Yeshewatesfa: *Regionalization of Parameters of a Conceptual Rainfall-Runoff Model*, 2005, ISBN: 3-933761-45-X

143 Wege, Ralf: *Untersuchungs- und Überwachungsmethoden für die Beurteilung natürlicher Selbstreinigungsprozesse im Grundwasser,* 2005, ISBN 3-933761-46-8

144 Breiting, Thomas: *Techniken und Methoden der Hydroinformatik - Modellierung von komplexen Hydrosystemen im Untergrund*, 2006, 3-933761-47-6

145 Hrsg.: Braun, Jürgen; Koschitzky, Hans-Peter; Müller, Martin: *Ressource Untergrund: 10 Jahre VEGAS: Forschung und Technologieentwicklung zum Schutz von Grundwasser und Boden,* Tagungsband zur Veranstaltung am 28. und 29. September 2005 an der Universität Stuttgart, Campus Stuttgart-Vaihingen, 2005, ISBN 3-933761-48-4

146 Rojanschi, Vlad: *Abflusskonzentration in mesoskaligen Einzugsgebieten unter Berücksichtigung des Sickerraumes,* 2006, ISBN 3-933761-49-2

147 Winkler, Nina Simone: *Optimierung der Steuerung von Hochwasserrückhaltebecken-systemen,* 2006, ISBN 3-933761-50-6

148 Wolf, Jens: *Räumlich differenzierte Modellierung der Grundwasserströmung alluvialer Aquifere für mesoskalige Einzugsgebiete*, 2006, ISBN: 3-933761-51-4

149 Kohler, Beate: *Externe Effekte der Laufwasserkraftnutzung*, 2006, ISBN 3-933761-52-2

150 Hrsg.: Braun, Jürgen; Koschitzky, Hans-Peter; Stuhrmann, Matthias: *VEGAS-Statuskolloquium 2006,* Tagungsband zur Veranstaltung am 28. September 2006 an der Universität Stuttgart, Campus Stuttgart-Vaihingen, 2006, ISBN 3-933761-53-0

151 Niessner, Jennifer: *Multi-Scale Modeling of Multi-Phase - Multi-Component Processes in Heterogeneous Porous Media*, 2006, ISBN 3-933761-54-9

152 Fischer, Markus: *Beanspruchung eingeerdeter Rohrleitungen infolge Austrocknung bindiger Böden,* 2006, ISBN 3-933761-55-7

153 Schneck, Alexander: *Optimierung der Grundwasserbewirtschaftung unter Berücksichtigung der Belange der Wasserversorgung, der Landwirtschaft und des Naturschutzes*, 2006, ISBN 3-933761-56-5

154 Das, Tapash: *The Impact of Spatial Variability of Precipitation on the Predictive Uncertainty of Hydrological Models,* 2006, ISBN 3-933761-57-3

155 Bielinski, Andreas: *Numerical Simulation of CO_2 sequestration in geological formations*, 2007, ISBN 3-933761-58-1

156 Mödinger, Jens: *Entwicklung eines Bewertungs- und Entscheidungsunterstützungssystems für eine nachhaltige regionale Grundwasserbewirtschaftung*, 2006, ISBN 3-933761-60-3

157 Manthey, Sabine: *Two-phase flow processes with dynamic effects in porous media - parameter estimation and simulation,* 2007, ISBN 3-933761-61-1

158 Pozos Estrada, Oscar: *Investigation on the Effects of Entrained Air in Pipelines,* 2007, ISBN 3-933761-62-X

159 Ochs, Steffen Oliver: *Steam injection into saturated porous media – process analysis including experimental and numerical investigations*, 2007, ISBN 3-933761-63-8

160 Marx, Andreas: *Einsatz gekoppelter Modelle und Wetterradar zur Abschätzung von Niederschlagsintensitäten und zur Abflussvorhersage, 2007,* ISBN 3-933761-64-6

161 Hartmann, Gabriele Maria: *Investigation of Evapotranspiration Concepts in Hydrological Modelling for Climate Change Impact Assessment*, 2007, ISBN 3-933761-65-4

162 Kebede Gurmessa, Tesfaye: *Numerical Investigation on Flow and Transport Characteristics to Improve Long-Term Simulation of Reservoir Sedimentation*, 2007, ISBN 3-933761-66-2

163 Trifković, Aleksandar: *Multi-objective and Risk-based Modelling Methodology for Planning, Design and Operation of Water Supply Systems*, 2007, ISBN 3-933761-67-0

164 Götzinger, Jens: *Distributed Conceptual Hydrological Modelling - Simulation of Climate, Land Use Change Impact and Uncertainty Analysis*, 2007, ISBN 3-933761-68-9

165 Hrsg.: Braun, Jürgen; Koschitzky, Hans-Peter; Stuhrmann, Matthias: *VEGAS – Kolloquium 2007,* Tagungsband zur Veranstaltung am 26. September 2007 an der Universität Stuttgart, Campus Stuttgart-Vaihingen, 2007, ISBN 3-933761-69-7

166 Freeman, Beau: *Modernization Criteria Assessment for Water Resources Planning; Klamath Irrigation Project, U.S.*, 2008, ISBN 3-933761-70-0

167 Dreher, Thomas: *Selektive Sedimentation von Feinstschwebstoffen in Wechselwirkung mit wandnahen turbulenten Strömungsbedingungen*, 2008, ISBN 3-933761-71-9

168 Yang, Wei: *Discrete-Continuous Downscaling Model for Generating Daily Precipitation Time Series*, 2008, ISBN 3-933761-72-7

169 Kopecki, Ianina: *Calculational Approach to FST-Hemispheres for Multiparametrical Benthos Habitat Modelling,* 2008*,* ISBN 3-933761-73-5

170 Brommundt, Jürgen: *Stochastische Generierung räumlich zusammenhängender Niederschlagszeitreihen*, 2008, ISBN 3-933761-74-3

171 Papafotiou, *Alexandros: Numerical Investigations of the Role of Hysteresis in Heterogeneous Two-Phase Flow Systems*, 2008, ISBN 3-933761-75-1

172 He, Yi: *Application of a Non-Parametric Classification Scheme to Catchment Hydrology*, 2008, ISBN 978-3-933761-76-7

173 Wagner, Sven: *Water Balance in a Poorly Gauged Basin in West Africa Using Atmospheric Modelling and Remote Sensing Information*, 2008, ISBN 978-3-933761-77-4

174 Hrsg.: Braun, Jürgen; Koschitzky, Hans-Peter; Stuhrmann, Matthias; Schrenk, Volker: *VEGAS-Kolloquium 2008 Ressource Fläche III*, Tagungsband zur Veranstaltung am 01. Oktober 2008 an der Universität Stuttgart, Campus Stuttgart-Vaihingen, 2008, ISBN 978-3-933761-78-1

175 Patil, Sachin: *Regionalization of an Event Based Nash Cascade Model for Flood Predictions in Ungauged Basins*, 2008, ISBN 978-3-933761-79-8

176 Assteerawatt, Anongnart: *Flow and Transport Modelling of Fractured Aquifers based on a Geostatistical Approach,* 2008, ISBN 978-3-933761-80-4

177 Karnahl, Joachim Alexander: *2D numerische Modellierung von multifraktionalem Schwebstoff- und Schadstofftransport in Flüssen*, 2008, ISBN 978-3-933761-81-1

178 Hiester, Uwe: *Technologieentwicklung zur In-situ-Sanierung der ungesättigten Bodenzone mit festen Wärmequellen,* 2009, ISBN 978-3-933761-82-8

179 Laux, Patrick: *Statistical Modeling of Precipitation for Agricultural Planning in the Volta Basin of West Africa,* 2009, ISBN 978-3-933761-83-5

180 Ehsan, Saqib: *Evaluation of Life Safety Risks Related to Severe Flooding,* 2009, ISBN 978-3-933761-84-2

181 Prohaska, Sandra: *Development and Application of a 1D Multi-Strip Fine Sediment Transport Model for Regulated Rivers,* 2009, ISBN 978-3-933761-85-9

182 Kopp, Andreas: *Evaluation of CO_2 Injection Processes in Geological Formations for Site Screening,* 2009, ISBN 978-3-933761-86-6

183 Ebigbo, Anozie: *Modelling of biofilm growth and its influence on CO_2 and water (two-phase) flow in porous media,* 2009, ISBN 978-3-933761-87-3

184 Freiboth, Sandra: *A phenomenological model for the numerical simulation of multiphase multicomponent processes considering structural alterations of porous media*, 2009, ISBN 978-3-933761-88-0

185 Zöllner, Frank: *Implementierung und Anwendung netzfreier Methoden im Konstruktiven Wasserbau und in der Hydromechanik*, 2009, ISBN 978-3-933761-89-7

186 Vasin, Milos: *Influence of the soil structure and property contrast on flow and transport in the unsaturated zone*, 2010, ISBN 978-3-933761-90-3

187 Li, Jing: *Application of Copulas as a New Geostatistical Tool*, 2010, ISBN 978-3-933761-91-0

188 AghaKouchak, Amir: *Simulation of Remotely Sensed Rainfall Fields Using Copulas*, 2010, ISBN 978-3-933761-92-7

189 Thapa, Pawan Kumar: *Physically-based spatially distributed rainfall runoff modelling for soil erosion estimation*, 2010, ISBN 978-3-933761-93-4

190 Wurms, Sven: *Numerische Modellierung der Sedimentationsprozesse in Retentionsanlagen zur Steuerung von Stoffströmen bei extremen Hochwasserabflussereignissen*, 2011, ISBN 978-3-933761-94-1

191 Merkel, Uwe: *Unsicherheitsanalyse hydraulischer Einwirkungen auf Hochwasserschutzdeiche und Steigerung der Leistungsfähigkeit durch adaptive Strömungsmodellierung*, 2011, ISBN 978-3-933761-95-8

192 Fritz, Jochen: *A Decoupled Model for Compositional Non-Isothermal Multiphase Flow in Porous Media and Multiphysics Approaches for Two-Phase Flow*, 2010, ISBN 978-3-933761-96-5

193 Weber, Karolin (Hrsg.): *12. Treffen junger WissenschaftlerInnen an Wasserbauinstituten*, 2010, ISBN 978-3-933761-97-2

194 Bliefernicht, Jan-Geert: *Probability Forecasts of Daily Areal Precipitation for Small River Basins,* 2011, ISBN 978-3-933761-98-9

195 Hrsg.: Koschitzky, Hans-Peter; Braun, Jürgen: *VEGAS-Kolloquium 2010 In-situ-Sanierung - Stand und Entwicklung Nano und ISCO -,* Tagungsband zur Veranstaltung am 07. Oktober 2010 an der Universität Stuttgart, Campus Stuttgart-Vaihingen*, 2010, ISBN 978-3-933761-99-6*

196 Gafurov, Abror: *Water Balance Modeling Using Remote Sensing Information - Focus on Central Asia,* 2010, ISBN 978-3-942036-00-9

197 Mackenberg, Sylvia: *Die Quellstärke in der Sickerwasserprognose: Möglichkeiten und Grenzen von Labor- und Freilanduntersuchungen,* 2010, ISBN 978-3-942036-01-6

198 Singh, Shailesh Kumar: *Robust Parameter Estimation in Gauged and Ungauged Basins,* 2010, ISBN 978-3-942036-02-3

199 Doğan, Mehmet Onur: *Coupling of porous media flow with pipe flow,* 2011, ISBN 978-3-942036-03-0

200 Liu, Min: *Study of Topographic Effects on Hydrological Patterns and the Implication on Hydrological Modeling and Data Interpolation,* 2011, ISBN 978-3-942036-04-7

Die Mitteilungshefte ab der Nr. 134 (Jg. 2005) stehen als pdf-Datei über die Homepage des Instituts: www.iws.uni-stuttgart.de zur Verfügung.